Technical University of Munich
TUM School of Natural Sciences

A symmetric universe: matter-antimatter asymmetry and dark matter from baryon number conservation

Mar Císcar-Monsalvatje

Complete reprint of the dissertation approved by the TUM School of Natural Sciences of the Technical University of Munich for the award of the

Doktorin der Naturwissenschaften (Dr. rer. nat.)

Chair: Prof. Dr. Stefan Schönert

Examiners:

1. Prof. Dr. Alejandro Ibarra
2. Prof. Dr. Björn Garbrecht

The dissertation was submitted to the Technical University of Munich on 25.02.2025 and accepted by the TUM School of Natural Sciences on 30.04.2025.

A symmetric universe:
matter-antimatter asymmetry and dark matter from baryon number conservation

Thesis advisor: Prof. Dr. Alejandro Ibarra Mar Císcar-Monsalvatje

A symmetric universe: matter-antimatter asymmetry and dark matter from baryon number conservation

Abstract

We present a minimal, baryon-conserving scenario that simultaneously explains dark matter and the quark-antiquark asymmetry. Since the observed baryon asymmetry only accounts for Standard Model particles, dark matter could carry baryon number and exhibit an equal but opposite asymmetry, eliminating the need for baryon number violation and, consequently, the first Sakharov condition. Our model introduces a complex scalar χ (dark matter), which is naturally stable as the lightest spin-0 particle carrying baryon number, and a Dirac fermion N, both initially carrying equal but opposite asymmetries. The asymmetry in N is transferred to the Standard Model via a neutron portal, generating the observed baryon asymmetry, while χ remains asymmetric today. We propose a mechanism for generating the initial asymmetry in the dark sector through CP-violating decays of heavy Majorana fermions. Additionally, we present a UV completion of the neutron portal via a colored scalar mediator Φ, which can be probed in collider searches through missing energy signatures from the long-lived N. We also explore an alternative scenario where dark matter annihilates into an ultralight scalar S, leaving a detectable imprint on future N_{eff} measurements.

Thesis advisor: Prof. Dr. Alejandro Ibarra Mar Císcar-Monsalvatje

Ein symmetrisches Universum: Materie-Antimaterie-Asymmetrie und Dunkle Materie durch Baryonenzahlerhaltung

Zusammenfassung

Wir präsentieren ein minimales, baryonenerhaltendes Szenario, das gleichzeitig Dunkle Materie und die Quark-Antiquark-Asymmetrie erklärt. Da die beobachtete Baryonasymmetrie nur Teilchen des Standardmodells umfasst, könnte Dunkle Materie eine Baryonenzahl tragen und eine gleich große, aber entgegengesetzte Asymmetrie aufweisen. Dies würde die Notwendigkeit einer Baryonenzahlverletzung und somit die erste Sakharov-Bedingung eliminieren. Unser Modell führt einen komplexen Skalar χ (als Dunkle Materie) ein, der als das leichteste Spin-0-Teilchen mit Baryonenzahl natürlich stabil ist, sowie ein Dirac-Fermion N, wobei beide anfangs gleich große, aber entgegengesetzte Asymmetrien tragen. Die Asymmetrie in N wird über ein Neutronen-Portal auf das Standardmodell übertragen und erzeugt die beobachtete Baryonasymmetrie, während χ bis heute asymmetrisch bleibt. Wir schlagen einen Mechanismus vor, durch den die anfängliche Asymmetrie im dunklen Sektor durch CP-verletzende Zerfälle schwerer Majorana-Fermionen erzeugt wird. Zudem präsentieren wir eine UV-Vervollständigung des Neutronen-Portals mittels eines farb-geladenen skalaren Mediators Φ, der in Beschleuniger-Suchen durch fehlende Energie-Signaturen des langlebigen N getestet werden kann. Schlussendlich untersuchen wir ein alternatives Szenario, in dem die Dunkle Materie in einen ultraleichten Skalar S annihiliert und so eine nachweisbare Spur in zukünftigen N_{eff}-Messungen hinterlassen würde.

Statement of collaboration and publications

This dissertation was carried out under the supervision of Prof. Dr. Alejandro Ibarra at TUM. Additionally, it was developed in close collaboration with Dr. Jérôme Vandecasteele, whose contributions were essential in shaping this work.

The research presented in Chapters 5 and 6 is based on work published in the Journal of Cosmology and Astroparticle Physics (JCAP 01 (2024) 028) and the associated erratum (JCAP 10 (2024) E01). Chapter 7 contains research that remains unpublished at the time of writing.

Acknowledgements

I would like to start by thanking Prof. Alejandro Ibarra. Already from my master thesis, he trusted my capabilities more than I did myself. Thank you for providing me with the opportunity to pursue a PhD, for supporting me in attending many schools and conferences, for proposing interesting topics to me, and for the freedom with which you supervised my thesis.

Then, I would like to thank Jérôme. Really, Jérôme, thank you so much for everything. Collaborating with you and being mentored by you made this process a thousand times easier. Thank you for always being available to discuss, for your patience, and for always explaining things to me without making me feel stupid. This thesis is also greatly yours.

I am also grateful to Miguel Escudero, who, after supervising my master thesis, continued to collaborate with me and support me whenever I needed it during my PhD. Both you and Gonzalo were my mentors in navigating academia during my early stages, and I truly appreciate it.

Many thanks to all the other members of T30d who accompanied me on this journey and provided me with a lot of support. Thank you Motoko, Di, Nico, Robert, Merlin, Simon, Alessia, Nick, Boris, Yu, Lukas, Janni, and the rest. Thank you for the lunches, the long coffee breaks, the geoguessr, the dinners, for the times you asked me how I was doing.

My days in Garching were immensely more enjoyable thanks to the friends I made there. Thank you to my office mates, Kai, Javier, Romy, and Asmaa, for creating such a nice environment and for always being willing to listen and support me. Thank you to my bouldering friends, Javier, Andrea, Gael, Lollo, Giovanni and Kai. Bouldering was truly one of the highlights of this time, largely because of how much you encouraged me and made me feel part of it. I am also very grateful for the many afternoon ping-pong breaks, thank you to my teachers! And thanks to Raúl for always being there with a smile and a hug when I needed it.

Thank you to the friends I made in schools and conferences. Toni, Jack, Leonie, Pavlo, and many more.

Outside academia, I want to thank my Munich friends, who supported my PhD by improving my mental health through talk and laughter and crochet. Thank you, Marta, Ana, Nicole and Sara. Thank you, Henrike for the talks in the kitchen. Thank you, Tirso for the breakfasts.

I am also grateful to the friends who were there for me from the distance, especially Alejandra, Saretta, and Paula. I could write many things here, but you already know.

Muchas gracias a mis padres. Cada vez más me doy cuenta de la suerte que he tenido y que tengo por tenerlos. Estoy aquí gracias a ellos. Siempre me han apoyado en todo, me han aconsejado y me han animado cuando lo necesitaba. Iríanhasta el fin del mundo por mí. Gracias.

Por último, estoy realmente agradecida a Gonzalo. Gracias por todo tu apoyo, en persona en la primera mitad del doctorado, y en la distancia durante la segunda. Gracias por estar ahí mientras navegaba las dificultades de la academia, por ser mi aliado. Gracias por siempre querer lo mejor para mí. Gracias por tu inmensa paciencia, Por sacar siempre tiempo para mí. Gracias por llenar mi vida de cosas bonitas. Te quiero.

Contents

Chapter 1

Introduction

The Standard Model of Particle Physics (SM), combined with Quantum Field Theory, provides a theoretical framework that has been remarkably successful as a low-energy effective model. Its predictions have been confirmed with astonishing precision across numerous laboratory tests. Experiments at the Large Hadron Collider have probed its validity up to TeV-scale energies, with no evidence for new particles. The model has also successfully anticipated key discoveries, such as the electroweak gauge bosons, the necessity of a third quark generation to explain CP-violation in the quark sector, and the Higgs boson, which plays a crucial role in mass generation.

Despite its success in explaining a vast array of physical phenomena, the SM remains incomplete. Several fundamental questions remain unresolved, highlighting the need for physics beyond the SM. These include the formulation of a quantum theory of gravity [1], the hierarchy problem [2], the origin of neutrino masses [3], the strong CP problem [4], and, notably, the nature of dark matter and the matter-antimatter asymmetry. This work focuses on addressing the last two.

Observations from the Cosmic Microwave Background, in combination with the ΛCDM cosmological model, reveal that approximately 85% of the universe's matter content is dark matter [5]. There is overwhelming evidence supporting the presence of an invisible form of matter that interacts gravitationally yet remains undetected in laboratory experiments. The most plausible explanation is the existence of a new stable particle (or set of particles) that interacts very weakly with SM particles. While numerous dark matter candidates have been proposed, searches for them have so far yielded no results. A complete dark matter theory must not only introduce a viable candidate but also provide a production mechanism that accounts for the observed relic density. These aspects will be discussed in Chapter 2.

Another major puzzle in modern physics is the matter-antimatter asymmetry of the universe. Everything we observe is predominantly composed of matter rather than antimatter, with no evidence for large regions of antimatter. This asymmetry has been precisely measured, yet the SM fails to provide an explanation. The most plausible scenario is that an excess of baryons over antibaryons was generated in the early universe through a process known as baryogenesis. This issue will be examined in detail in Chapter 3.

Motivated by the fact that the measured energy densities of dark matter and SM baryons are of the same order of magnitude ($\Omega_{\mathrm{DM}}/\Omega_{\mathrm{b}} \simeq 5$) [5], it has been suggested that dark matter may be asymmetric and linked to the matter-antimatter asymmetry.

We explore this connection in Chapter 4, where we review various proposed classes of models that relate these two problems.

In Chapter 5, we introduce our model: a minimal baryon-conserving scenario in which dark matter carries baryon number and compensates the observed baryon asymmetry. The model is formulated within an effective field theory framework. We highlight its key features and analyze the resulting dynamics arising from the set of coupled Boltzmann equations governing the evolution of all particle abundances and asymmetries.

In Chapter 6, we explore the phenomenology of the interaction portals connecting the dark and visible sectors, focusing on the constraints and potential signatures that could allow for the detection of dark matter and the dark fermion N. We analyze the parameter space of the neutron portal, considering the various phenomenological factors that influence it, including cosmology, collider searches, freeze-out dynamics, and nucleon decay constraints.

Then, in Chapter 7, we explore the ultraviolet (UV) completion of the model. First, we propose a mechanism for generating the initial asymmetry in the dark sector, inspired by thermal leptogenesis, where two heavy Majorana fermions φ_1 and φ_2 produce a particle-antiparticle asymmetries through CP-violating decays. We analyze the impact of washout processes and determine the viable parameter space.

In this chapter, we also present the UV completion of the neutron portal, which is realized through the introduction of a colored scalar mediator Φ. This mediator is expected to be abundantly produced in colliders due to its gauge interactions, allowing for promising detection prospects. The key signature consists of monojet events with missing energy, which has not yet been consistently explored in experimental searches. A dedicated analysis of this signature could significantly enhance the discovery potential of our scenario.

Additionally, we explore the UV completion of dark matter freeze-out and propose an alternative realization in which dark matter annihilates into a very light dark scalar S, which remains as a hot subcomponent of dark matter. We show that the contribution of this scalar to N_{eff} is within current experimental uncertainties but could be detected by next-generation CMB experiments.

Finally, in Chapter 8, we summarize the proposed model, highlighting its implications and main results.

Chapter 2

Dark matter and the dark sector

Dark matter remains one of the most pressing unresolved questions in modern physics, playing a fundamental role in the standard cosmological model. Its existence implies new physics beyond the Standard Model of particle physics, which lacks a viable candidate to explain the observed phenomena. The leading hypothesis suggests that dark matter consists of one or more novel particles that are weakly coupled to visible matter and remain stable over cosmological timescales. These particles must also possess the necessary properties to account for the formation of large-scale structures in the universe, evolving from small density fluctuations in the early cosmos.

2.1 Observational evidence for dark matter

The existence of dark matter in the universe is supported by robust evidence spanning a wide range of phenomena, scales, and sources. Collectively, these observations reveal the presence of non-luminous matter that constitutes approximately 85% of the universe's total matter content. Below, we briefly comment on the key observations that demonstrate the existence of dark matter. For a more comprehensive review, we refer the reader to Refs. [6, 7].

The first evidence for dark matter emerged in 1933, when Fritz Zwicky applied the virial theorem to the Coma Cluster [8]. His analysis revealed that the cluster's total mass density was at least 400 times greater than what could be accounted for by its visible matter. This discrepancy could only be explained by the presence of an abundant, non-luminous component dominating the cluster's dynamics. Zwicky's discovery marked the beginning of dark matter research, and subsequent studies of other galaxy clusters have consistently verified this phenomenon.

In the 1970s, Vera Rubin and Kent Ford conducted measurements and analyses of the rotation curves of spiral galaxies [9], uncovering that these curves remain unexpectedly flat beyond a certain radius. Rotation curves represent the circular velocities of stars as a function of their distance to the center of the galaxy. According to classical dynamics, when the integrated visible mass $M(r)$ ceases to increase with radius r, the circular velocity $v(r) = \sqrt{GM(r)/r}$ should decrease as $v \propto \sqrt{1/r}$. However, observations, such as the rotation curve shown in Fig. 2.1, reveal that $v(r)$ remains constant, indicating the presence of an extended, non-luminous halo where $M(r) \propto r$. This phenomenon provides some of the most direct evidence for dark matter at galactic scales.

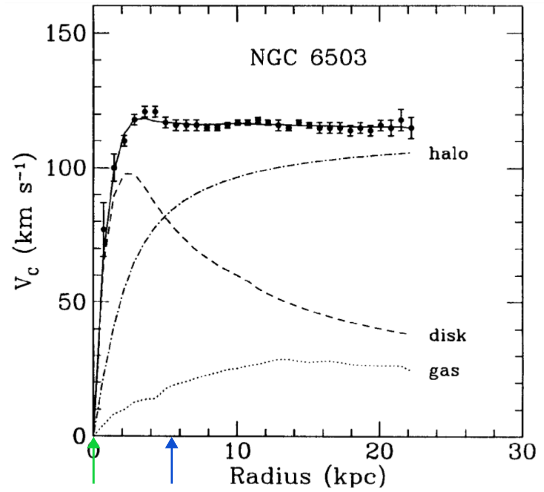

a)

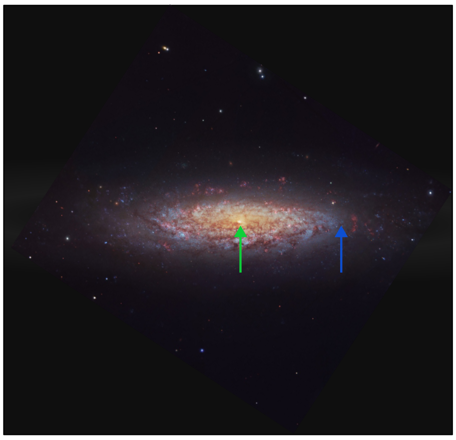

b)

Fig. 2.1: *a*) Galactic rotation curve of NGC 6503, from Ref. [10]. The contributions from the gas and disk components are shown as dotted and dashed lines, respectively. The rotation curve remains flat even at radii where visible matter is no longer present, providing evidence for the presence of an extended dark matter halo, represented as a dash-dotted line. *b*) Optical image of NGC 6503, taken from the Subaru Telescope (NAOJ) and the Hubble Legacy Archive. The galaxy's visible radius is 5.35 kpc [11] and the arrow markers are placed in both figures for size comparison.

At extragalactic scales, gravitational lensing provides compelling evidence for the existence of dark matter. According to General Relativity, light traveling near intense gravitational fields bends due to the curvature of spacetime caused by massive objects, which act as gravitational lenses. This bending results in observable distortions, such as the formation of multiple images of the same source or increased brightness of distant objects. Notably, the degree of distortion depends solely on the total mass distribution within the lens, regardless of whether it is luminous or dark matter. Lensing measurements have confirmed the presence of significant amounts of dark matter in galaxies and galaxy clusters. For a comprehensive review of weak gravitational lensing, see Ref. [12].

Collisions of galaxy clusters, such as the Bullet Cluster, offer additional insights into the nature of dark matter through lensing analyses. Reconstructed gravitational potential maps, such as the one in Fig. 2.2, show how most of the total mass density remains aligned with the original cluster locations, while the visible matter, dominated by hot gas, is concentrated in the collision region. This spatial separation demonstrates that dark matter does not interact significantly with visible matter nor with itself, a key property that distinguishes it from baryonic matter and further supports its role as

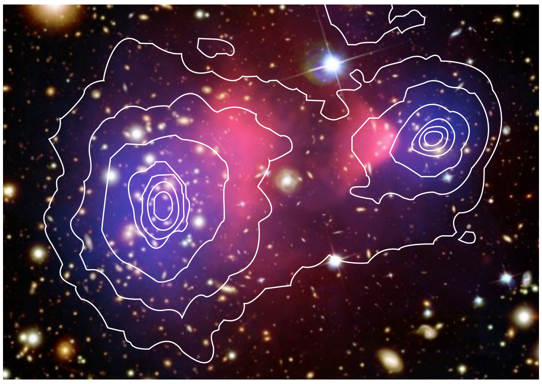

Fig. 2.2: Composite image of the Bullet Cluster. The white contours represent the gravitational lensing density reconstructions, reproduced from Ref. [13]. The pink region corresponds to the hot baryonic gas observed in the X-ray spectrum [14], while the blue region depicts the dark matter distribution as inferred from lensing maps [13]. Notably, the baryonic matter does not align with the centers of the gravitational potential, highlighting the weak interaction of dark matter with both visible matter and itself, as evidenced by its unaffected distribution following the collision.

a dominant but elusive component of the universe.

Moving to cosmological scales, some of the most compelling evidence for dark matter comes from the small anisotropies observed in the Cosmic Microwave Background (CMB). The position and shape of the peaks in the CMB power spectrum provide insights into photon-baryon oscillations that occurred just before the decoupling of light and matter (recombination), approximately 3.8×10^5 years after the Big Bang. These features cannot be explained without the presence of dark matter. The density anisotropies at the time of recombination, of the order of $\sim 10^{-5}$, would not have evolved sufficiently to form the galaxies observed today without the presence of cold dark matter component which does not significantly couple to photons. While evidence from galaxy dynamics, rotation curves, and gravitational lensing provides insights into the presence of dark matter, they do not measure the total amount of dark matter in the universe. In contrast, CMB observations serve as highly precise probes of cosmological parameters, including the dark matter energy density. Analysis of CMB data by the Planck collaboration, within the framework of the standard ΛCDM model, indicates that approximately 26% of the total energy density of the universe is comprised of dark matter [5]:

$$\Omega_{\mathrm{DM}} = \frac{\rho_{\mathrm{DM}}}{\rho_{\mathrm{crit}}} = 0.265(7). \tag{2.1}$$

Finally, on large scales, further evidence for dark matter emerges from the study of structure formation in the universe. Within the ΛCDM paradigm, the large-scale structures we observe today, such as galaxies and galaxy clusters, originate

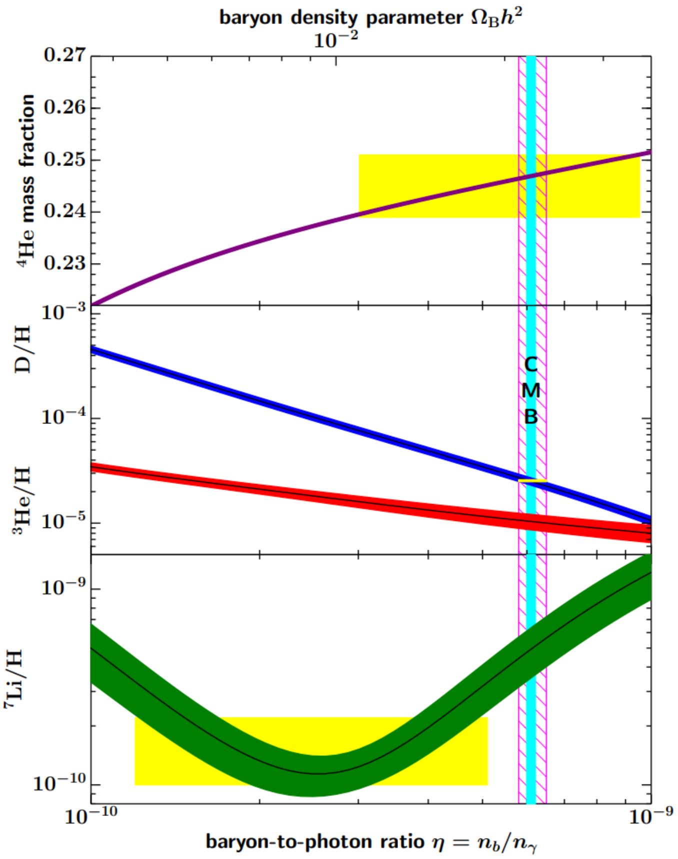

Fig. 2.3: The primordial abundances of ^{4}He, D, ^{3}He, and ^{7}Li as predicted by BBN [16]. The bands represent the 95% CL range. The yellow boxes indicate the measured abundances. The vertical blue band corresponds to the CMB measure of the baryon density [5], while the vertical pink band corresponds to the BBN D+^{4}He concordance range at 95% CL. Figure taken from [17].

from primordial density fluctuations generated during cosmic inflation. Cosmological simulations demonstrate that dark matter is essential for these initial anisotropies to grow and evolve into the current distribution of matter in the universe. Without the gravitational influence of dark matter, the observed large-scale structure could not have formed within the time elapsed since the Big Bang. For a detailed discussion, see Ref. [15].

It is worth highlighting that Big Bang Nucleosynthesis (BBN), although not a direct probe of dark matter, provides a powerful and independent cross-check of early-universe physics that reinforces the findings from the CMB measurements. BBN describes the formation of light nuclei (D, ^{3}He, ^{4}He, and ^{7}Li), approximately three minutes after the Big Bang and is highly sensitive to the baryon density at that time, as illustrated in Fig. 2.3. BBN provides a robust and reliable probe of the early universe, achieving remarkable agreement between its theoretical predictions and the observed abundances of these elements. The baryon energy density inferred from the observed abundances of deuterium and helium aligns extremely well with the value extracted from CMB data. Specifically, BBN constraints yield [18]

$$\Omega_{\mathrm{b}} h^2 = 0.02205(43), \tag{2.2}$$

where h is the dimensionless scaling factor for Hubble expansion rate defined as $h \equiv H_0/(100\ \mathrm{km\ s^{-1}\ Mpc^{-1}})$. For $h = 0.674(5)$ [5], this corresponds to $\Omega_{\mathrm{b}} = 0.0485(12)$. In contrast, the total matter density inferred from the CMB is much larger ($\Omega_{\mathrm{m}} \simeq 0.3$), implying that most of the matter must be non-baryonic, consistent with the existence of dark matter. For further analysis of this topic, see Refs. [17, 19].

In summary, the evidence for dark matter spans a vast range of scales and phenomena, from the dynamics of galaxy clusters and the rotation curves of spiral galaxies to the large-scale structures of the universe and the precise anisotropies in the CMB. Each piece of evidence independently confirms the existence of a significant non-luminous matter component that cannot be explained by ordinary baryonic matter alone. Additionally, BBN and its concordance with CMB measurements provide stringent constraints on the nature and abundance of the dark matter.

2.2 Dark matter candidates

The list of potential dark matter candidates is extensive. The possible mass range of dark matter is remarkably broad, from approximately 10^{-30} to 10^{57} GeV. Some of the most compelling candidates are those connected to other unresolved issues in particle physics, such as the electroweak hierarchy problem, the strong CP problem, neutrino mass generation, or the baryon asymmetry of the universe.

A variety of candidates have been proposed, ranging from Weakly Interacting Massive Particles (WIMPs), Asymmetric Dark Matter (ADM), axions, sterile neutrinos, and dark sectors, which we briefly review below, and other possibilities like Feebly Interacting Massive Particles (FIMPs) [20], Strongly Interacting Massive Particles (SIMPs) [21], and gravitinos [22]. Some non-particle candidates include primordial black holes [23]. Additionally, alternative theories, such as modifications of gravity, have been considered to explain phenomena like spiral galaxy rotation curves, but fail to account for the CMB [24, 25].

For comprehensive reviews of dark matter candidates, see Refs. [6, 26].

- **WIMPs**. Weakly Interacting Massive Particles are hypothetical particles with masses in the MeV–TeV range. They interact with other particles at rates comparable to or weaker than the weak nuclear force. In the early universe, WIMPs would have annihilated into lighter particles via $2 \leftrightarrow 2$ interactions, keeping them in thermal equilibrium with the cosmic plasma. As the universe expanded and cooled, the interaction rates dropped below the Hubble expansion rate, leading to the decoupling of WIMPs and the freeze-out of their relic abundance, as detailed in Section 2.4.1.

The relic density of WIMPs is primarily determined by their annihilation cross section, $\langle\sigma v\rangle_{\text{ann}}$. For WIMPs to account for the observed dark matter abundance, this value must be approximately $\langle\sigma v\rangle \simeq 2.6 \times 10^{-9}$ GeV^{-2}, which coincides with the scale of weak interactions, and stays almost constant for a wide range of masses [27]. This coincidence, often called the "WIMP miracle", has made WIMPs highly attractive candidates, as it hints a connection between the dark and visible sectors. They also arise naturally in several extensions of the SM, such as the Minimal Supersymmetric Standard Model, where the lightest neutralino is a natural WIMP candidate. For detailed reviews, see Refs. [6, 28].

Despite extensive searches which we review in Section 2.3, no definitive evidence for WIMPs has been found. For an overview of the current experimental status, see Ref. [29].

- **ADM**. Asymmetric Dark Datter proposes a dark sector where the particle and antiparticle abundances are unequal, analogous to the matter-antimatter asymmetry in the visible sector. This asymmetry could have a common origin with the baryon asymmetry or could have been transmitted from one sector to the other through some interactions. The symmetric component of dark matter would annihilate away, leaving behind the asymmetric relic density, as detailed in Section 2.4.2. ADM provides a compelling explanation for the observed similarity in dark matter and baryon energy densities, $\Omega_{\text{DM}} \simeq 5\,\Omega_{\text{b}}$. We will delve deeper into ADM and the leading classes of models in Chapter 4.

- **Axions**. This candidate arises as a consequence of the Peccei-Quinn mechanism, a solution to the strong CP problem in Quantum Chromodynamics (QCD) [30]. They are pseudo-Goldstone bosons resulting from the spontaneous breaking of a new global symmetry, $U(1)_{\text{PQ}}$, which dynamically enforces CP conservation in the QCD vacuum.

  While the mass and relic abundance of axions depend on their production mechanism and the symmetry-breaking scale, they are considered strong candidates for dark matter. Observational constraints, such as those from stellar cooling and supernova dynamics, place upper limits on their mass, typically $m_a \lesssim 0.1$ eV [17, 31]. Axion couplings to matter and photons are model-dependent, but in some scenarios, they fall within ranges in agreement with the observational constraints for dark matter. For reviews on axion dark matter and ongoing experimental efforts, see Refs. [32–34].

- **Sterile neutrinos**. Evidence for neutrino flavor oscillations, first proposed by Bruno Pontecorvo [35], indicates that at least two of the SM neutrinos possess mass. Sterile neutrinos, N_R, are hypothetical right-handed particles introduced to account for these small but nonzero masses. They carry no quantum numbers under any SM symmetry groups. In the seesaw mechanism [36], sterile neutrinos acquire large Majorana masses, leading to tiny masses for the active neutrinos.

  Sterile neutrinos with masses in the keV range could serve as dark matter candidates [37], originating in the early universe through oscillations with active neutrinos. This scenario is theoretically appealing but faces stringent constraints from cosmology and X-ray searches, which have excluded much of the parameter space for sterile neutrino dark matter. For a review of the current status of this candidate, see Ref. [38].

- **Dark sector models**. They suggest that dark matter exists in a hidden sector with little or no interaction with SM particles. They introduce new particles and forces, often connected to the visible sector through mediator portals. Common portal mechanisms include kinetic mixing with the photon (resulting in dark photons [39]) or scalar mixing with the Higgs boson (resulting in dark Higgs [40]). These interactions allow for indirect connections between the dark and visible sectors, providing testable predictions in certain regimes. Self-interacting dark matter models, which introduce strong interactions within the dark sector, have been proposed to address discrepancies in small-scale structure formation, such as the core-cusp problem, the diversity problem for rotation curves, and the missing satellite problem, see Refs. [41, 42].

2.3 Searches for dark matter

Here, we will explore various detection methods proposed to search for the dark matter candidates introduced in the previous section.

2.3.1 Colliders

Collider searches are experimental techniques used to detect dark matter by attempting to produce it directly in high-energy particle collisions. These experiments replicate conditions similar to those of the early universe by accelerating particles to extremely high speeds using electromagnetic fields and then colliding them. The goal is to generate dark matter particles during these collisions.

Dark matter particles cannot be observed directly because they interact very weakly with ordinary matter. Key observables in collider dark matter searches provide indirect evidence of invisible particles and their interactions. Missing transverse energy (MET) is one of the most critical observables, representing the non-conservation of measured energy in the transverse plane of a collision. It arises when invisible particles escape detection, leaving behind an apparent energy deficit. Building on MET, Mono-X signatures describe specific event topologies where a single visible particle (such as a photon, jet, or W/Z boson) is detected, balancing the momentum carried by invisible particles and providing a distinctive signal to differentiate potential dark matter events from SM backgrounds. Another key observable involves mediator resonances, where a mediator particle from the dark sector is produced resonantly and promptly decays into detectable particles, such as dijets or dileptons, creating peaks in invariant mass distributions that differ from SM predictions. These approaches allow researchers to study dark matter properties in a controlled environment and test theoretical models of its production and interactions.

Some of the most important existing colliders include the Large Hadron Collider (LHC) at CERN, a proton-proton collider operating at energies up to 13–14 TeV. The LHC hosts major experiments such as CMS (Compact Muon Solenoid) [43] and ATLAS (A Toroidal LHC ApparatuS) [44], which are general-purpose detectors designed to investigate a wide range of physics phenomena. Both experiments play a crucial role in dark matter searches, focusing on MET signals. Another significant collider is SuperKEKB [45] in Japan, an electron-positron collider dedicated to studying light dark matter candidates, particularly through potential interactions involving dark photons. Looking to the future, the High-Luminosity LHC (HL-LHC) [46], an upgraded version of the LHC expected to begin operations in 2028, aims to increase luminosity by a factor of 10, significantly enhancing its sensitivity to rare processes and weakly interacting particles.

Theoretical frameworks are important to guide experimental searches. Modern strategies for detecting GeV–TeV dark matter at the LHC are grounded in several of these theoretical frameworks, including Effective Field Theories (EFTs), simplified models [47], and more comprehensive theories like Supersymmetry (SUSY) [48–52]. EFTs offer a model-independent approach with minimal parameters, such as the interaction scale and dark matter mass, allowing comparisons with direct detection experiments. However, they are valid only when the mediator is significantly heavier than the energy scales probed by the collider, limiting their applicability in specific scenarios [53, 54]. Simplified models address this limitation by explicitly including the mediator particle, introducing additional parameters such as mediator and dark matter masses and their couplings to the SM and the dark sector. This makes them ideal for collider searches where the mediator can be produced directly, enabling detailed studies of dark matter interactions. Still, they are less general than EFTs and rely on some assumptions [55].

Collider searches for dark matter face several experimental challenges. High background noise from SM processes can mimic the signatures of dark matter, making it difficult to isolate potential signals. Precise calibration and sophisticated data analysis techniques are required to differentiate between signal and background. Additionally, the limited energy range of current colliders may not be sufficient to probe very heavy mediators or weakly interacting particles, and the production rates for dark matter candidates are often extremely low, requiring large datasets to achieve meaningful constraints. These challenges need advanced detector technologies and innovative search strategies to maximize the potential for discovery.

Constraints from colliders depend heavily on the choice of couplings of interactions with dark matter and SM particles. Fixing these couplings allows comparisons with the dark matter relic density and direct and indirect detection results in the mass-cross section plane, see for example Fig. 2.4. For instance, collider bounds are more stringent than direct detection limits for low dark matter masses in the case of standard spin-independent interactions. However, translating collider limits to direct or indirect detection limits is not straightforward due to their dependence on specific mediators and coupling assumptions. Still, these searches are crucial because they provide

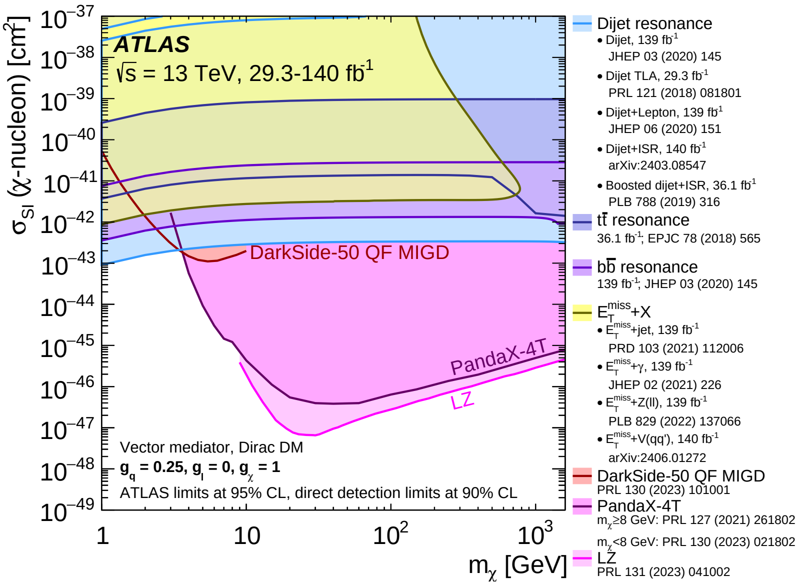

Fig. 2.4: Comparison of collider (ATLAS) and direct detection (DarkSide-50 [56], PandaX-4T [57, 58] and LZ [59]) upper limits on the spin-independent dark matter-nucleon scattering cross section for a Z' mediator that couples only to quarks. Figure taken from Ref. [60].

complementary tests for thermal dark matter models.

For comprehensive reviews on the search of dark matter in colliders, we refer the reader to Refs. [40, 61, 62].

2.3.2 Direct detection

Direct detection experiments aim to observe interactions between dark matter particles and atomic nuclei, providing a complementary approach to collider and indirect searches. The underlying concept is based on the expectation that dark matter, as it passes through the Earth, may occasionally scatter off nuclei, transferring a small amount of energy to the nucleus in the process, inducing a detectable nuclear recoil. Direct detection is motivated by its ability to probe dark matter interactions at extremely low energy scales and test dark matter properties, such as mass and coupling strength, in a way independent of collider-specific assumptions.

The concept of directly detecting dark matter particles in the form of WIMPs was first proposed by Goodman and Witten [63]. Soon after, two low-background germanium ionization experiments placed the first direct constraints on spin-independent and spin-dependent dark matter-nucleon couplings [64, 65], based on the lack of a significant excess of recoil events above the expected background. Around the same time, the idea of annual modulation in the dark matter signal rate was introduced [66], proposing that the Earth's orbit around the Sun, combined with the Sun's motion through the

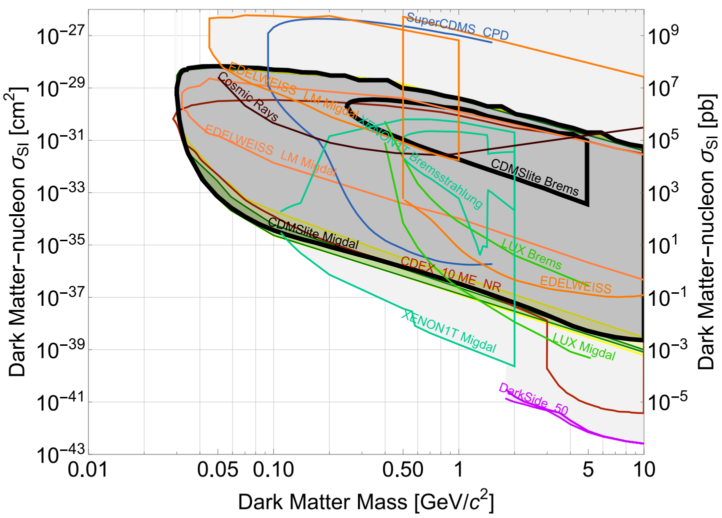

Fig. 2.5: Direct detection constraints on the dark matter-nucleon scattering cross section in the low-mass regime. The plot includes limits from elastic interaction searches conducted by SuperCDMS-CPD [75], DAMIC [76], cosmic-ray constraints from Collar [77], and DarkSide-50 [56], together with bounds from the Migdal effect, from LUX [78], EDELWEISS [68, 79], XENON1T [80], CDEX [81], CDEX-10 [82], and SuperCDMS [83]. Figure taken from Ref. [83].

dark matter halo, could produce seasonal variations in detection rates. Since then, a variety of experiments have employed diverse detection technologies to explore the parameter space of dark matter-nucleon interactions, using both total scattering rates and modulation signals. These include light scintillators, such as the NaI crystal-based DAMA/LIBRA [67]; cryogenic ionization detectors, like EDELWEISS [68] and SuperCDMS [69], which use germanium crystals; liquid noble gas detectors, such as XENON1T [70] and PandaX [57], which utilize xenon and LUX-ZEPLIN (LZ) [59], and DarkSide-50 [71], which utilize argon; and bubble chambers, like PICO [72], which are filled with C_3F_8 to detect spin-dependent interactions. The sensitivity of these experiments has improved dramatically over the years, approaching the threshold required to detect coherent elastic scattering of solar neutrinos, which would represent an irreducible background for WIMP searches [73, 74].

Direct detection experiments face significant challenges in detecting sub-GeV dark matter due to their energy thresholds and the velocity of dark matter particles reaching the detector, typically assumed to be the escape velocity of the Milky Way. While some experiments aim to lower their energy thresholds to probe scatterings of lighter dark matter particles with nucleons [84], alternative methods have also been proposed to extend sensitivity without requiring substantial advances in existing technologies. One such approach focuses on dark matter interactions with electrons in the detector [85, 86]. These interactions could ionize electrons for sufficiently light dark matter without producing detectable nuclear recoils. Additionally, measuring the ionization signal from the Migdal effect, where nuclear recoil indirectly ionizes electrons, has been suggested to enhance the sensitivity of current experiments to lower mass dark matter particles [87, 88]. The ultimate sensitivity of these searches is also limited by the so-called neutrino floor, where neutrino scattering events become an irreducible background [89–91]. Fig. 2.5 shows the current experimental limits for the dark matter-nucleon scattering cross section in the low-mass regime for elastic interaction searches and Migdal effect.

2.3.3 Indirect detection

Indirect detection aims to identify dark matter by observing the byproducts of its annihilation or decay in astrophysical environments.

The field was opened in 1978 with two seminal articles [92, 93], which proposed searching for dark matter through the products of its self-annihilations or decays that reach Earth. Early studies focused on gamma-ray signals from regions of high dark matter density, such as the galactic center, where gradients distinguishable from the astrophysical background could be detected for thermal values of the WIMP annihilation cross section. A few years later, the potential of antiproton and positron flux measurements to constrain self-annihilating dark matter was recognized [94], along with the possibility that dark matter particles could be gravitationally captured by the Sun and annihilate in its core, producing neutrinos detectable at Earth [95].

More recently, dwarf spheroidal galaxies have emerged as critical targets for indirect detection due to their high dark matter densities and low baryonic contamination, offering some of the strongest constraints on dark matter annihilation [96, 97]. Fig. 2.6 provides the limits obtained by these kind of searches for different annihilation channels.

By analyzing excesses in these astrophysical signals beyond what is expected from known processes, indirect detection provides a complementary strategy to probe the nature of dark matter, offering insights into its annihilation cross section, decay lifetime, and interaction channels.

Another promising approach in indirect detection involves observations of neutron star temperatures as a potential probe for dark matter interactions [98–101]. Dark matter particles may be gravitationally captured by neutron stars, accumulating in their cores and annihilating into SM particles. This process could deposit energy, preventing the star from cooling at the expected rate. Deviations in the thermal evolution of neutron stars, particularly in old or isolated systems, provide a potential indirect signal of dark matter interactions, such as annihilation cross sections and scattering rates. This method, while still in its early stages, offers a complementary avenue to explore dark matter properties, especially for particles with low interaction rates or masses that are difficult to access through other indirect detection strategies.

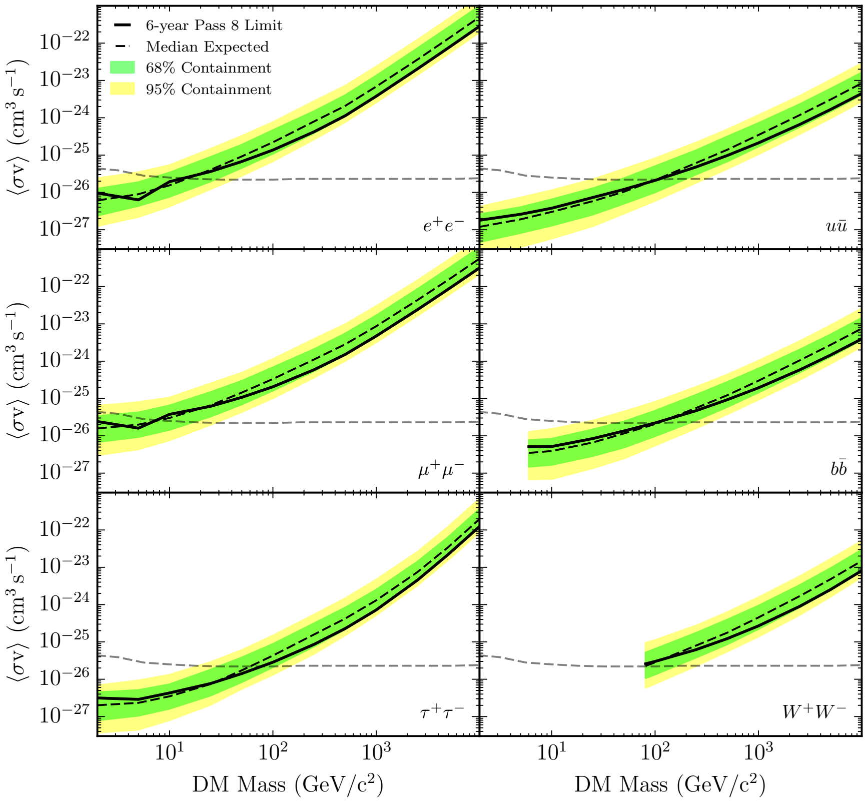

Fig. 2.6: Indirect detection constraints on the dark matter annihilation cross section for various channels derived from the combined analysis of 15 dwarf spheroidal satellite galaxies by Fermi-LAT [97]. The dashed gray line corresponds to the thermal relic cross section derived by Ref. [27].

2.4 Dark matter production

The production of dark matter in the early universe is a key aspect for understanding its nature and properties. While various mechanisms have been proposed to explain how dark matter was generated, this section focuses on the freeze-out mechanism, which is central to many well-motivated dark matter models, including WIMPs.

Before delving into the details of freeze-out, it is worth briefly mentioning other proposed production mechanisms:

- **Freeze-in.** Dark matter may have never reached thermal equilibrium with the cosmic plasma, as proposed in the freeze-in mechanism [20]. This scenario involves feebly interacting massive particles (FIMPs) that are decoupled from the thermal bath. Initially, the abundance of dark matter is negligible. Over time, rare interactions with the plasma gradually produce dark matter particles, but as the universe expands and cools, these interactions become increasingly infrequent. Eventually, the production ceases, and the dark matter abundance freezes in, remaining constant thereafter. Unlike the freeze-out mechanism, freeze-in results in a final abundance that increases with the interaction strength.

- **Super-WIMP mechanism.** It proposes a non-thermal production scenario for dark matter, where dark matter particles are generated as decay products of a heavier, weakly interacting particle after its freeze-out [102]. In this framework, the parent particle freezes out in thermal equilibrium and subsequently decays into a lighter, stable dark matter particle. Unlike traditional freeze-out scenarios, the super-WIMP dark matter inherits the relic abundance from its parent particle rather than being produced directly via thermal processes. This mechanism is particularly interesting because the resulting dark matter interacts even more weakly with the SM, making it more challenging to detect directly. However, it offers distinct signals, such as delayed decays of the parent particle, which could be probed through indirect detection or cosmological observations.
- **Misalignment mechanism.** Associated with scalar fields like axions. This mechanism involves coherent oscillations of the axion field, which result in zero-momentum bosonic condensates behaving as cold dark matter [103–105].
- **Other scenarios.** Additional mechanisms, such as gravitational production during inflation [106] or scenarios involving topological defects such as cosmic strings [107], are also discussed in the literature.

These alternatives provide viable explanations under different assumptions, but the freeze-out mechanism remains the leading candidate due to its strong theoretical foundation and connection to experimental searches. In this framework, a particle species initially in thermal equilibrium with the cosmic plasma decouples as the universe expands and cools, leaving behind a relic abundance that persists to the present day.

2.4.1 Freeze-out

A particle species is in thermal equilibrium with the plasma when interactions involving this species occur frequently enough to maintain coupling with the rest of the thermal bath. This condition is expressed as

$$\begin{cases} \Gamma \gtrsim H & \text{coupled}, \\ \Gamma \lesssim H & \text{decoupled}, \end{cases} \tag{2.3}$$

where Γ is the interaction rate of the particle and H is the Hubble expansion rate at a given temperature T. The equilibrium distribution depends on the plasma temperature T, the particle mass m_i and chemical potential μ_i. For a particle species in the Maxwell-Boltzmann approximation, the number density n_i^{eq} is given by

$$n_i^{\text{eq}} = \frac{g_i}{2\pi^2} m_i^2 T K_2\left(\frac{m_i}{T}\right) e^{\mu_i/T} = \begin{cases} \frac{g_i}{\pi^2} e^{\mu_i/T}\, T^3 & T \gg m_i, \\ g_i\, e^{\mu_i/T} e^{-m_i/T} \left(\frac{m_i T}{2\pi}\right)^{3/2} & T \lesssim m_i, \end{cases} \tag{2.4}$$

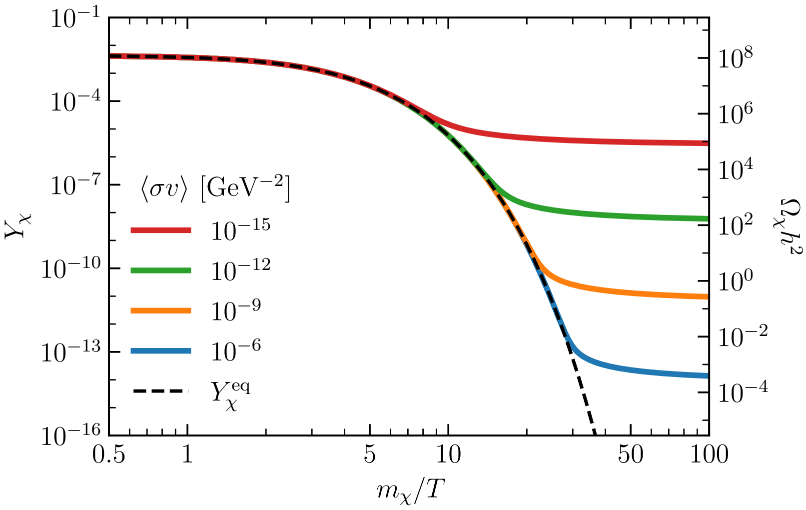

Fig. 2.7: Evolution of the abundance of a massive particle species χ during freeze-out for different annihilation cross sections $\langle\sigma v\rangle$ and a mass of $m_\chi = 100$ GeV. The dashed black line represents the equilibrium abundance, while the solid lines show the actual abundance as obtained from solving the Boltzmann equation. The relic abundance today (right side of the plot) decreases with increasing $\langle\sigma v\rangle$. The analysis assumes s-wave annihilation, where $\langle\sigma v\rangle$ is velocity-independent.

as derived in Appendix A.1. It is usual to define the dimensionless quantity "yield", as:

$$Y \equiv n/\mathfrak{s}, \tag{2.5}$$

where $\mathfrak{s}$ is the entropy density of the universe

$$\mathfrak{s} = \frac{2\pi^2}{45} g_{\star S}(T)\, T^3. \tag{2.6}$$

Here, $g_{\star S}$ is the effective number of relativistic degrees of freedom at temperature of the thermal plasma T, defined in Appendix A.2. Then, the equilibrium distribution in terms of the yield is given by

$$\begin{aligned} Y_i^{\rm eq} &= \frac{45}{2\pi^4}\frac{g_i}{g_{\star S}(T)}\frac{m_i^2}{T^2} K_2\left(\frac{m_i}{T}\right) e^{\mu_i/T} \\ &= \begin{cases} \frac{45}{2\pi^4}\frac{g_i}{g_{\star S}(T)} e^{\mu_i/T} & T \gg m_i, \\ \frac{45}{4\sqrt{2}\pi^{7/2}}\frac{g_i}{g_{\star S}(T)}\, e^{\mu_i/T}\left(\frac{m_i}{T}\right)^{3/2} e^{-m_i/T} & T \lesssim m_i. \end{cases} \end{aligned} \tag{2.7}$$

For relativistic particles ($T \gg m_i$), the yield is practically constant with temperature. When the particles become non-relativistic ($T \lesssim m_i$), their abundance drops exponentially, as shown by the dashed line in Fig. 2.7.

As the universe expands and cools, interaction rates decrease due to both reduced particle densities and kinematic suppression. Once the interaction rate Γ falls below the Hubble expansion rate H, the particle species decouples from the plasma and its abundance ceases to track the equilibrium distribution. From that point onward, the particle yield Y_i remains effectively constant, in the absence of additional interactions or decays at later times.

When a particle species decouples from the plasma non-relativistically, the final relic abundance depends on the efficiency of the interactions maintaining thermal equilibrium. Stronger interactions result in later decoupling and a lower relic abundance, as more particles annihilate before freeze-out. On the contrary, weaker interactions lead to earlier decoupling and a higher relic abundance. This results in the relic abundance being inversely proportional to the thermally averaged interaction cross section, $\langle \sigma v \rangle$. Fig. 2.7 illustrates this behavior: each solid line represents the evolution of the particle abundance for a different value of $\langle \sigma v \rangle$.

In the case of dark matter, we consider particles χ that are stable, massive, and weakly interacting with SM particles. The annihilation and production processes for such a symmetric dark matter candidate can be described as

$$\chi \, \bar{\chi} \longleftrightarrow \psi \, \bar{\psi}, \tag{2.8}$$

where ψ denotes all the SM species into which χ can annihilate. At the temperatures relevant to dark matter freeze-out, SM particles are assumed to remain in thermal equilibrium with the plasma due to their additional interactions. Consequently, ψ and $\bar{\psi}$ will follow thermal distributions. Including these processes in the Boltzmann equation formalism described in Appendix B.1, leads to the following differential equation for the yield Y_χ, as derived in Appendix B.2:

$$\frac{dY_\chi}{dx} = \frac{dY_{\bar{\chi}}}{dx} = -\frac{x\mathfrak{s}\langle \sigma v \rangle_{\mathrm{ann}}}{H(T = m_\chi)} \left(Y_\chi^2 - Y_\chi^{\mathrm{eq}\,2} \right), \tag{2.9}$$

where $x \equiv m_\chi / T$ is a dimensionless parameter, $\langle \sigma v \rangle_{\mathrm{ann}}$ is the thermally averaged annihilation cross section, summed over all possible final states. We have assumed equal number of particles and antiparticles, so that $Y_\chi = Y_{\bar{\chi}}$, as their chemical potentials are zero.

Numerical solutions to this equation, as shown in Fig. 2.7, track the evolution of the number density Y_χ. Before freeze-out, Y_χ closely follows its equilibrium value Y_χ^{eq}. After freeze-out, the yield becomes constant, as number-changing interactions cease. By comparing the relic yield with the observed dark matter density today, we can extract information about the dark matter mass m_χ and the interaction cross section $\langle \sigma v \rangle_{\mathrm{ann}}$.

2.4.2 Asymmetric dark matter freeze-out

We discuss now the freeze-out mechanism in the case of ADM. In this framework, the dark matter particle, is distinct from its antiparticle, making it possible for their abundances to differ. It is generally assumed that this asymmetry between the number of particles and antiparticles is generated well before the annihilation processes for dark matter freeze-out. As will be discussed in Section 4.1, ADM is motivated by the observed similarity between the dark matter and baryon densities in the universe, suggesting that a common mechanism could have generated both the baryon asymmetry and the hypothetical dark matter asymmetry.

To describe the evolution of such a scenario, we consider a dark matter particle χ, and its antiparticle $\bar{\chi}$, assuming that only $\chi\bar{\chi}$ pairs can annihilate into SM particles. Now, without the equal abundance assumption, $Y_\chi \neq Y_{\bar{\chi}}$, and the Boltzmann equations take the general form [108]:

$$\frac{dY_\chi}{dx} = -\frac{\lambda \langle \sigma v \rangle_{\text{ann}}}{x^2} \left(Y_\chi \, Y_{\bar{\chi}} - Y_\chi^{\text{eq}} \, Y_{\bar{\chi}}^{\text{eq}} \right) , \tag{2.10}$$

$$\frac{dY_{\bar{\chi}}}{dx} = -\frac{\lambda \langle \sigma v \rangle_{\text{ann}}}{x^2} \left(Y_\chi \, Y_{\bar{\chi}} - Y_\chi^{\text{eq}} \, Y_{\bar{\chi}}^{\text{eq}} \right) , \tag{2.11}$$

where we have defined the quantity

$$\lambda \equiv \frac{4\pi}{\sqrt{90}} \, m_\chi M_{\text{Pl}} \, \sqrt{g_{\star S}} \, , \tag{2.12}$$

with $g_{\star S}$ being the effective number of relativistic degrees of freedom for entropy. The equilibrium yields Y_χ^{eq} and $Y_{\bar{\chi}}^{\text{eq}}$ in the Maxwell-Boltzmann distribution are given in Eq. (2.7). Note that the chemical potentials for particles and antiparticles cancel out in the product $Y_\chi^{\text{eq}} Y_{\bar{\chi}}^{\text{eq}}$, as in chemical equilibirum $\mu_\chi = -\mu_{\bar{\chi}}$.

Since the annihilation process is symmetric, subtracting the two Boltzmann equations gives:

$$\frac{dY_\chi}{dx} - \frac{dY_{\bar{\chi}}}{dx} = 0 \, , \tag{2.13}$$

which implies

$$Y_\chi - Y_{\bar{\chi}} = C \, , \tag{2.14}$$

where C is a constant. This shows that the difference in the comoving number densities of particles and antiparticles remains conserved, as expected for a symmetric annihilation process. This conserved difference could be related to the conservation of a dark matter charge associated with a global symmetry.

Using this conserved asymmetry, the Boltzmann equations can be rewritten in a decoupled form:

$$\frac{dY_\chi}{dx} = -\frac{\lambda \langle \sigma v \rangle_{\text{ann}}}{x^2} \left(Y_\chi^2 - C Y_\chi - Y_\chi^{\text{eq}} \, Y_{\bar{\chi}}^{\text{eq}} \right) , \tag{2.15}$$

$$\frac{dY_{\bar{\chi}}}{dx} = -\frac{\lambda \langle \sigma v \rangle_{\text{ann}}}{x^2} \left(Y_{\bar{\chi}}^2 + C Y_{\bar{\chi}} - Y_\chi^{\text{eq}} \, Y_{\bar{\chi}}^{\text{eq}} \right) . \tag{2.16}$$

These equations can be solved numerically to obtain the evolution of the number densities of χ and $\bar{\chi}$, as shown in Fig. 2.8. The independent parameters are the initial

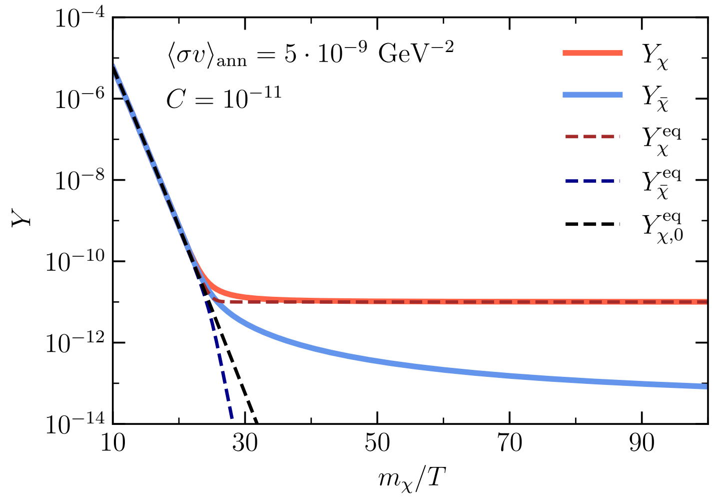

Fig. 2.8: Evolution of the χ and $\bar\chi$ abundances for $m_\chi = 100$ GeV, $\langle\sigma v\rangle_{\rm ann} = 5 \times 10^{-9}$ GeV^{-2} and $C = 10^{-11}$. The dashed black line represents the equilibrium abundance in the absence of asymmetry ($C = 0$), while the red and blue dashed lines correspond to the equilibrium abundances of χ and $\bar\chi$ for $C = 10^{-11}$. The solid red and blue lines show the actual abundances of χ and $\bar\chi$. The results in this plot are consistent with those reported in Ref. [108].

asymmetry C, which remains constant as shown in Eq. (2.14), the mass m_χ, and the annihilation cross section $\langle\sigma v\rangle_{\rm ann}$, assumed to be constant (s-wave).

This scenario differs significantly from the WIMP or symmetric freeze-out case shown in Fig. 2.7. In the asymmetric case, the equilibrium abundances for χ and $\bar\chi$ differ due to their dependence on the chemical potential. This leads to distinct dynamics for each species. The yield Y_χ (solid red line in Fig. 2.8) is bounded from below by $Y_\chi^{\rm eq}$ (dashed red line) to the value of the asymmetry C. This reflects the excess of χ particles that cannot find $\bar\chi$ partners for annihilation.

One can also explore the dependence of the final relic abundance on the annihilation cross section. Fig. 2.9 shows the relic densities Ωh^2 as a function of $\langle\sigma v\rangle_{\rm ann}$ for two different values of the asymmetry, $C = 10^{-11}$ and $C = 3 \times 10^{-12}$, assuming constant s-wave annihilation.

As expected, lower annihilation cross sections lead to higher relic densities. For small values of $\langle\sigma v\rangle_{\rm ann}$, the asymmetry C has little effect since Y_χ and $Y_{\bar\chi}$ are not depleted efficiently enough to be affected by the lower bound set by the asymmetry. For larger $\langle\sigma v\rangle_{\rm ann}$, however, C significantly influences the relic abundance. Beyond a certain cross section value, the relic abundance of χ no longer varies, as it reaches the minimum value determined by the asymmetry. As expected, higher values of C lead to a larger disparity between the relic abundances of χ and $\bar\chi$.

As it will be further explored in Chapter 4, in standard ADM scenarios, the dark matter asymmetry is often linked to the baryon asymmetry. If the asymmetries are

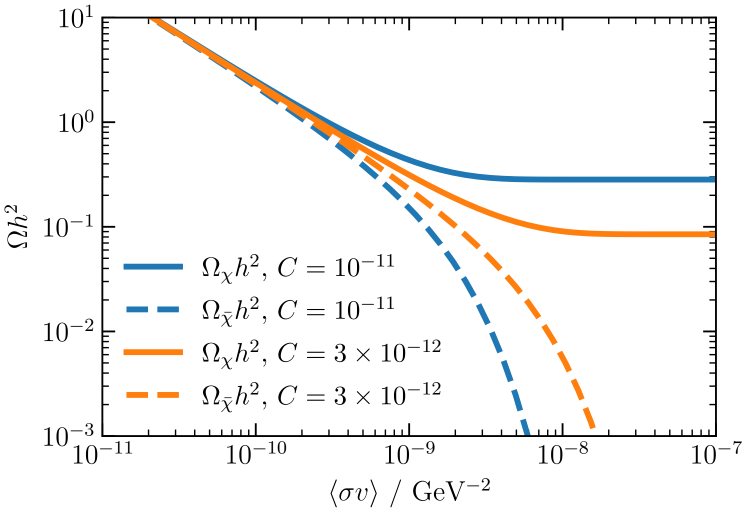

Fig. 2.9: Relic densities Ωh^2 for χ and $\bar{\chi}$ with $m_\chi = 100$ GeV, plotted as a function of $\langle \sigma v \rangle_{\rm ann}$ for two different asymmetry values. The calculations assume s-wave annihilation. The results shown in this plot are consistent with those reported in Ref. [108].

of the same magnitude, a natural prediction emerges for the dark matter mass to be $m_{\rm DM} \simeq 5$ GeV.

Chapter 3

An asymmetric visible sector: the matter-antimatter asymmetry

The overwhelming dominance of visible matter over antimatter in the universe, a phenomenon referred to as the baryon asymmetry, presents a profound challenge in modern physics. Observations of CP symmetry, which appears nearly perfect in collider experiments, seem to contradict this imbalance. Resolving the question of the matter-antimatter asymmetry remains one of the most pressing problems in contemporary physics, and finding a viable mechanism for baryogenesis is far from straightforward.

3.1 Evidence for a baryon asymmetry in the visible sector

Despite being rare in our surroundings, antimatter has been observed in small amounts on Earth. It is produced through the decay of certain radioactive nuclei and can also be created and stored in particle physics laboratories. Furthermore, it is evident that the solar system is composed of matter, as the survival of space exploration probes visiting other planets relies on this fact. Additionally, solar cosmic rays confirm that the Sun itself consists of matter.

On a larger scale, cosmic rays allow us to investigate the composition of our galaxy and beyond. Among these rays, minute amounts of antiprotons are detected, at a level of roughly $\sim 10^{-4}$ relative to protons [109]. However, these antiprotons are likely the result of interactions between cosmic rays and interstellar material.[1] This finding underscores a significant asymmetry between baryons and antibaryons in the galaxy.

The nucleon-antinucleon annihilation process has a remarkably high cross section, maintaining these particles in thermal equilibrium with the cosmic plasma down to low temperatures ($T \sim 22$ MeV). If the universe had been locally symmetric with respect to SM baryons and antibaryons, such annihilation processes would have reduced their abundance drastically during its thermal evolution. The predicted relic density of nucleons and antinucleons would then be about $n_{\mathrm{b}}/\mathfrak{s} = n_{\bar{\mathrm{b}}}/\mathfrak{s} \approx 7 \times 10^{-20}$ [111], nine orders of magnitude smaller than what is observed.

One might hypothesize that the visible universe is baryon symmetric but divided into isolated regions of matter and antimatter. However, this idea is ruled out, as annihilation at the boundaries of these regions would produce observable signals that

[1] They may also originate from dark matter annihilations [110].

exceed current experimental constraints [112]. These observations strongly support the conclusion that the visible universe is inherently baryon asymmetric.

The simplest explanation for this asymmetry is that the early universe already contained an excess of quarks over antiquarks. During matter-antimatter annihilation, this excess ensured that quarks remained after the annihilation process exhausted the antiquarks. It is highly improbable, however, that this asymmetry originated as an initial condition, since inflation would have erased it. Therefore, it is assumed that a specific unknown mechanism generated this quark excess in the early universe. This mechanism is referred to as baryogenesis.

The degree of quark-antiquark asymmetry in the universe is most precisely quantified by the ratio of the baryon number density to the photon number density, η_B, as derived from the amplitude of the peaks in the cosmic microwave background power spectrum [5]:

$$\eta_B \equiv \frac{n_{\mathrm{b}}}{n_\gamma} = (6.12 \pm 0.04) \times 10^{-10}. \tag{3.1}$$

Since the amount of antibaryons is negligible compared the amount of baryons, this ratio also serves as a measure of the matter-antimatter imbalance

$$\eta_B \equiv \frac{n_{\mathrm{b}}}{n_\gamma} \approx \frac{n_{\mathrm{b}} - n_{\bar{\mathrm{b}}}}{n_\gamma}. \tag{3.2}$$

The smallness of this measured value highlights the subtlety of the asymmetry: in the early universe ($t \lesssim 10^{-6}$ s), the excess amounted to just one extra quark per 30 million antiquarks [111]. We can also express this measurement in terms of the yield, defined in Eq. (2.5), as

$$Y_B = (8.71 \pm 0.06) \times 10^{-11}\,. \tag{3.3}$$

3.2 The Sakharov conditions

In 1967, Sakharov published his famous work on baryogenesis [113], building on the recent discovery of CP violation in K^0 decays. In this paper, he proposed a framework identifying the three essential conditions required for the generation of a baryon asymmetry in the universe. These three conditions are still today the guideline that physicists follow when developing baryogenesis mechanisms. The three conditions are

1. **Baryon number violation.** To generate a net baryon asymmetry, $B \neq 0$, interactions that violate baryon number seem to be essential. Inflationary dynamics reset any pre-existing baryon asymmetry, leaving $B = 0$ afterwards. If all interactions in the universe conserved baryon number, there would be no mechanism able to produce a net asymmetry starting from this neutral state.

   One known source of baryon number violation within the SM are electroweak sphaleron processes, studied in Section 3.3.

2. **C and CP violation.** The symmetries of charge conjugation (C) and the combination of charge conjugation and parity (CP) play a critical role. If these symmetries are conserved, the rates of particle and antiparticle processes are identical:
$$\Gamma\big(X \to YB\big) = \Gamma\left(\bar{X} \to \bar{Y}\bar{B}\right). \tag{3.4}$$
Even with B-violating interactions, conservation of C and CP would result in equal rates of baryon and antibaryon production (positive and negative baryon number), preventing any net asymmetry. Therefore, a violation of C and CP is required to introduce the necessary imbalance between baryons and antibaryons.

   The SM includes CP violation in weak interactions, but the effect is small and insufficient to explain the observed baryon asymmetry.

3. **Departure from thermal equilibrium.** Thermal equilibrium imposes equal phase-space densities for baryons and antibaryons, effectively erasing any potential asymmetry. From a kinetic perspective, equilibrium implies that the rates of forward and inverse reactions are equal:
$$\Gamma\big(X \to YB\big) = \Gamma\big(YB \to X\big). \tag{3.5}$$
This ensures that any baryon asymmetry generated is immediately washed out, resulting in a net baryon number of zero. To circumvent this, some interaction must depart from thermal equilibrium, allowing different rates for the forward and inverse reactions and enabling the generation of an asymmetry.

3.3 Electroweak sphalerons

3.3.1 Theoretical foundations of sphaleron transitions

In the SM, baryon number (B) and lepton number (L) are conserved quantities associated with the global symmetries $U(1)_B$ and $U(1)_L$. These symmetries are considered "accidental" because their conservation arises not from any fundamental principle but rather from the structure of the SM itself. At the tree level, these quantities are conserved, as expressed by:

$$\partial_\mu J^\mu_B = \partial_\mu J^\mu_L = 0\,, \tag{3.6}$$

where J^μ_B and J^μ_L are the corresponding baryon and lepton number currents.

However, as 't Hooft demonstrated in 1976 [114], quantum effects introduce a chiral anomaly that violates B and L through non-perturbative processes. The resulting anomaly equation is:

$$\partial_\mu J^\mu_B = \partial_\mu J^\mu_L = \frac{N_\mathrm{F}}{32\pi^2}\left(g^2 W^a_{\mu\nu}\widetilde{W}^{a\mu\nu} - g'^2 B_{\mu\nu}\widetilde{B}^{\mu\nu}\right), \tag{3.7}$$

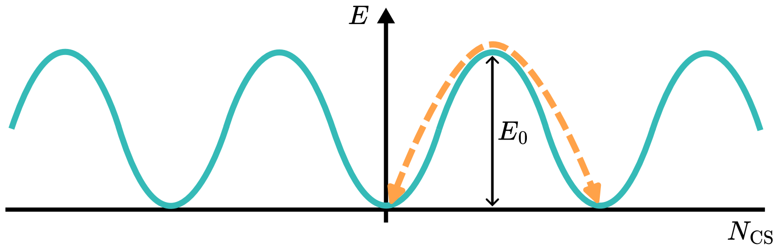

Fig. 3.1: Schematic representation of the vacuum structure in the SM, showing the infinite set of degenerate vacuum states characterized by different integer values of the Chern-Simons number, N_{CS}. These vacua are separated by energy barriers of height E_0, corresponding to the sphaleron configuration. Transitions between vacua lead to violations of baryon and lepton number of three units.

where $N_{\text{F}} = 3$ represents the number of fermion families, $W_{\mu\nu}$ and $B_{\mu\nu}$ denote the field strengths of the $SU(2)_L$ and $U(1)_Y$ gauge groups, and g and g' are their respective coupling constants. The dual field tensor $\widetilde{A}^{\mu\nu}$ is defined as $\widetilde{A}^{\mu\nu} \equiv \frac{1}{2}\epsilon^{\mu\nu\sigma\rho}A_{\sigma\rho}$.

Notably, within the SM, the difference $B - L$ remains a conserved symmetry, even in the presence of quantum effects:

$$\partial_\mu\big(J_B^\mu - J_L^\mu\big) = \partial_\mu J_B^\mu - \partial_\mu J_L^\mu = 0, \tag{3.8}$$

while the orthogonal combination $B + L$ is not conserved,

$$\partial_\mu\big(J_B^\mu + J_L^\mu\big) \neq 0. \tag{3.9}$$

The change in B and L is connected to the variation in the topological charge, or the so-called Chern-Simons number, N_{CS}, as described by:

$$B(t) - B(0) = N_{\text{F}}\big[N_{\text{CS}}(t) - N_{\text{CS}}(0)\big]. \tag{3.10}$$

As illustrated schematically in Fig. 3.1, the vacuum structure of the theory consists of an infinite set of degenerate vacuum states, each distinguished by a different integer value of N_{CS}. These vacua are separated by an energy barrier of height E_0, determined by the static solutions to the classical equations of motion known as "sphalerons" [115, 116]. To transition from one vacuum state to another, the system must overcome this energy barrier, resulting in a change of N_{CS} by one unit. As can be seen in Eq. (3.10), such a transition leads to a change in baryon and lepton numbers by a multiple of $N_{\text{F}} = 3$.

At low energies, transitions that alter the Chern-Simons number occur through quantum tunneling. However, at high temperatures, thermal fluctuations provide sufficient energy for the system to cross over the sphaleron barriers. The rate at which these transitions occur, per unit time and volume, is known as the Chern-Simons diffusion rate, or sphaleron rate, Γ_{sph}. This rate has been computed using large-scale lattice simulations in [117].

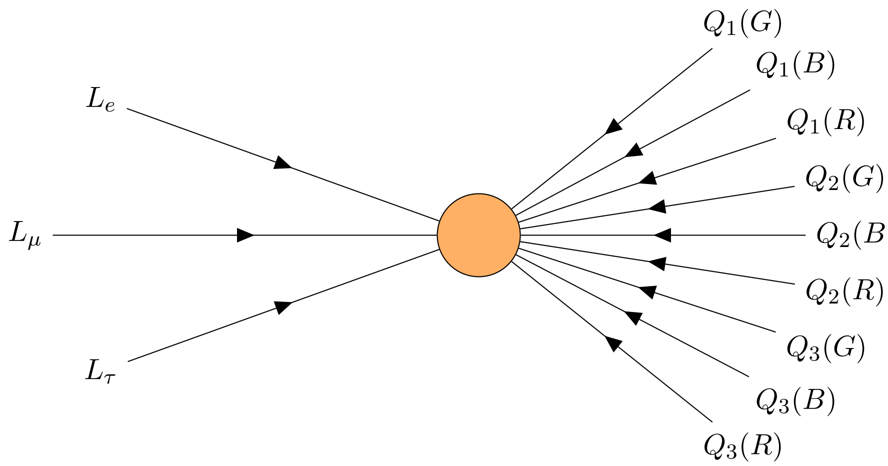

Fig. 3.2: Diagram illustrating a sphaleron transition, which involves interactions between twelve left-handed fermions: nine quarks (three from each generation) and three leptons (one from each generation). These processes violate B and L in three units while conserving $B-L$.

Sphaleron transitions involve interactions that include twelve left-handed fermions: nine quarks and three leptons, as illustrated in Fig. 3.2. For a comprehensive discussion of electroweak sphalerons in the context of quantum field theory, we direct the reader to Refs. [111, 118, 119].

3.3.2 Dynamics of asymmetry redistribution by sphalerons

When a net $B-L$ asymmetry is generated in the SM through a mechanism that violates this combination of quantum numbers, sphalerons redistribute the asymmetry between B and L according to their equilibrium distribution. This relationship is given by:

$$B = c\,(B-L), \tag{3.11}$$

where the constant c takes the value 12/37 [120]. The derivation of this constant, considering the chemical potential relations in the thermal plasma, is presented in Appendix C.1.

This equilibrium relation implies that a net baryon asymmetry in the visible sector cannot arise from a mechanism that does not violate $B-L$, as constrained by Eq. (3.11). This is illustrated schematically in Fig. 3.3, which shows the B vs. L plane. The diagonal gray dotted lines correspond to conserved $B-L$, along which sphaleron processes redistribute B and L. The dashed purple line represents the equilibrium relationship imposed by Eq. (3.11). The panel on the left demonstrates an example of baryon asymmetry generation in two steps: first, a positive asymmetry is injected into B (green arrow); second, sphalerons redistribute this asymmetry between the baryon and lepton sectors along the gray diagonal until equilibrium is reached (orange arrow).

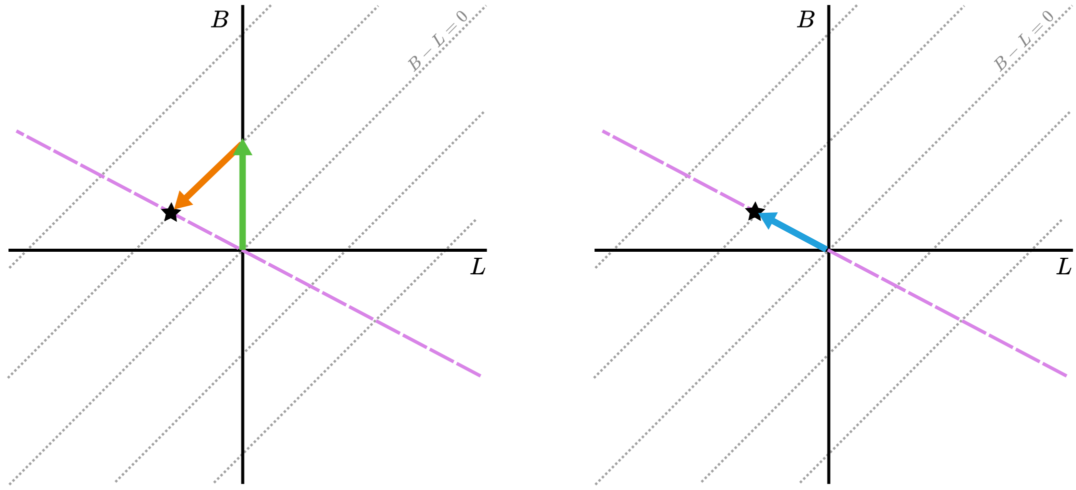

Fig. 3.3: Schematic representation of the B vs. L plane, illustrating the redistribution of asymmetry by sphaleron processes. The gray dotted lines correspond to conserved $B-L$, while the dashed purple line represents the equilibrium relationship between B and $B-L$ given by Eq. (3.11). In the left panel, the generation of baryon asymmetry is depicted in two steps: 1.) a positive asymmetry is injected into B (green arrow), and 2.) sphalerons redistribute the asymmetry along the gray diagonal to reach the equilibrium line (orange arrow). In the right panel, the dynamic evolution is shown, where the system moves directly along the equilibrium line (blue arrow) due to sphalerons being in thermal equilibrium. The final state (black star) exhibits a net positive B asymmetry, a negative L asymmetry, and a positive $B-L$ asymmetry.

In reality, these steps occur dynamically and simultaneously. This is shown in the right panel, where the system moves directly along the equilibrium line (blue arrow) as long as sphaleron processes remain in thermal equilibrium. The final state is marked by the black star, where there is a net positive asymmetry in B, smaller than the injected $B-L$ asymmetry, along with a corresponding negative asymmetry in L. As expected, the final state possesses a non-zero $B-L$ asymmetry.

The electroweak sphaleron processes will become relevant later in this thesis, as they represent an unavoidable effect to consider when generating a baryon asymmetry in the visible sector at high temperatures.

3.4 Main mechanisms for baryogenesis

Several mechanisms have been proposed to explain the origin of the baryon asymmetry in the universe. While these scenarios satisfy the Sakharov conditions, they differ in how and when the asymmetry is generated. In this section, we focus on two of the most widely studied mechanisms: Electroweak Baryogenesis (EWBG) (3.4.1) and Leptogenesis (3.4.2). EWBG relies on a first-order electroweak phase transition to

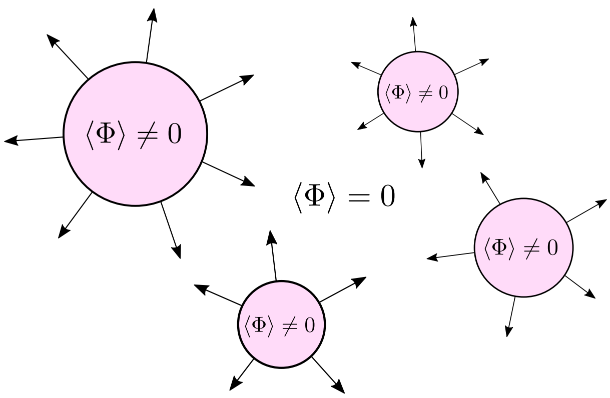

Fig. 3.4: First-order electroweak phase transition: Bubbles from the broken phase, characterized by $\langle\Phi\rangle \neq 0$, expand into the surrounding plasma, which remains in the symmetric phase with $\langle\Phi\rangle = 0$.

generate the asymmetry, while leptogenesis produces a lepton asymmetry that is later converted into a baryon asymmetry via sphaleron processes.

Another approach is based on Grand Unified Theories [121], where baryon number violation naturally arises due to the unification of quarks and leptons into common representations of a larger gauge group. In these models, interactions mediated by heavy gauge bosons violate baryon number at high energies. While proton stability today requires these mediators to have masses exceeding 10^{14} GeV [122], making B-violating interactions negligible at present temperatures, such processes could have played a significant role in the early universe.

Other proposals, like the Affleck-Dine mechanism [123], offer alternative explanations. This framework involves the dynamics of scalar fields that carry baryon or lepton number. In supersymmetric theories, certain flat directions in the potential allow these fields to acquire large vacuum expectation values during inflation. As the universe evolves, these fields undergo coherent oscillations and eventually decay, transferring their asymmetry to the baryon and/or lepton sectors.

3.4.1 Electroweak Baryogenesis

EWBG refers to mechanisms where the baryon asymmetry is generated during the electroweak phase transition (EWPT). While many variations of EWBG have been proposed, they all share foundational features [118]. These scenarios assume initial conditions of a baryon-symmetric, radiation-dominated universe governed by the electroweak symmetry group $SU(2)_L \times U(1)_Y$.

For EWBG to successfully produce the baryon asymmetry, the EWPT must be of first order [124]. In this type of transition, bubbles with a non-zero Higgs vacuum expectation value, $\langle\Phi\rangle \neq 0$, nucleate and expand within a symmetric phase space where $\langle\Phi\rangle = 0$,

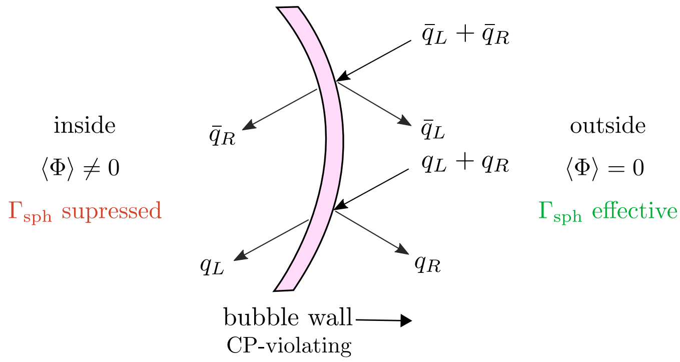

Fig. 3.5: Schematic representation of baryon asymmetry generation near the bubble walls. CP violation leads to asymmetric scattering for right- and left-handed quarks and antiquarks.

as depicted in Fig. 3.4. Eventually, these bubbles collide and fill the universe. During this process, the sphaleron rate, highly active in the symmetric phase, is exponentially suppressed within the bubbles (broken phase). The baryon asymmetry is generated near the bubble walls through the following three steps:

1. Particles in the plasma interact with the advancing bubble walls. CP violation in the walls results in asymmetric scattering, leading to unequal reflection and transmission probabilities for right- and left-handed quarks and antiquarks. This creates a chiral asymmetry near the bubble walls, where the number of $(\bar{q}_L + q_R)$ exceeds that of $(\bar{q}_R + q_L)$. This process is schematically illustrated in Fig. 3.5.

2. Electroweak sphalerons, which remain effective in the symmetric phase outside the bubbles, convert the chiral asymmetry into a baryon asymmetry. These processes affect only left-handed quarks, and due to the asymmetry generated in Step 1, the interaction rate $\Gamma(\bar{q}_L \to 8q_L + 3l_L)$ with $\Delta B = +3$ exceeds the reverse process $\Gamma(q_L \to 8\bar{q}_L + 3\bar{l}_L)$ with $\Delta B = -3$. This imbalance results in a net baryon number.

3. The baryon asymmetry diffuses into the expanding bubbles. Once inside, the sphaleron rate is strongly suppressed in the broken phase, preventing the asymmetry from being washed out. The universe thus transitions into a broken phase with a net baryon asymmetry.

These steps collectively satisfy Sakharov's conditions for baryogenesis. While all the necessary ingredients for EWBG are present in the SM, they are insufficient to explain the observed baryon asymmetry. For the EWPT to be of first order, the Higgs boson mass would need to be $m_h \lesssim 70$ GeV [125], far below its experimentally measured value of $m_h = (125.10 \pm 0.14)$ GeV [17]. Additionally, the CP violation induced by the CKM phase in the SM quark sector produces a baryon asymmetry of only $\eta_B \sim 10^{-20}$, which

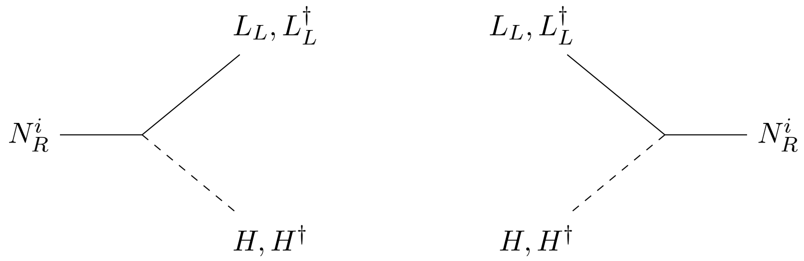

Fig. 3.6: Tree-level decay and inverse decay processes of sterile neutrinos mediated by the Dirac mass term. These interactions result in $\Delta L = 1$ transitions, essential for leptogenesis.

is negligible compared to the observed value in Eq. (3.1) [126]. For further discussions and detailed reviews on EWBG, see Refs. [119, 127].

3.4.2 Leptogenesis

Thermal leptogenesis, proposed by Fukugita and Yanagida in 1986 [128], is a mechanism where a lepton asymmetry is first generated and later converted into a baryon asymmetry through electroweak sphaleron processes.

The introduction of right-handed sterile neutrinos, N_R^i (with i denoting the generation index), plays a central role in addressing neutrino masses. The seesaw mechanism [129–132] combines Dirac and Majorana mass terms in the Lagrangian to explain the smallness of light neutrino masses, provided the Majorana mass is much larger than the electroweak scale.

The key property of N_R^i for leptogenesis is their participation in L-violating interactions. Their decays and inverse decays into the lepton doublet L_L and the Higgs field H, mediated by the Dirac mass term, result in a change of lepton number $\Delta L = 1$. These decays are shown at tree level in Fig. 3.6.

The conditions for a successful Leptogenesis are:

- **Generation of a $B - L$ Asymmetry.** For leptogenesis to yield a baryon asymmetry, it is crucial that N_R^i decays and inverse decays violate $B - L$. Sphaleron processes transfer the $B - L$ asymmetry to a net baryon number, as described by the equilibrium relation in Eq. (3.11). If the generated $B - L$ asymmetry is zero, the resulting baryon asymmetry will also vanish.

- **C and CP violation.** CP violation in N_R^i decays occurs at the one-loop level when at least two generations of sterile neutrinos are present. The one-loop diagrams contributing to CP violation are shown in Fig. 3.7. The CP violation parameter ϵ_i is defined as

$$\epsilon_i \equiv \frac{\Gamma(N_R^i \to L_L H) - \Gamma(N_R^i \to L_L^\dagger H^\dagger)}{\Gamma(N_R^i \to L_L H) + \Gamma(N_R^i \to L_L^\dagger H^\dagger)}. \tag{3.12}$$

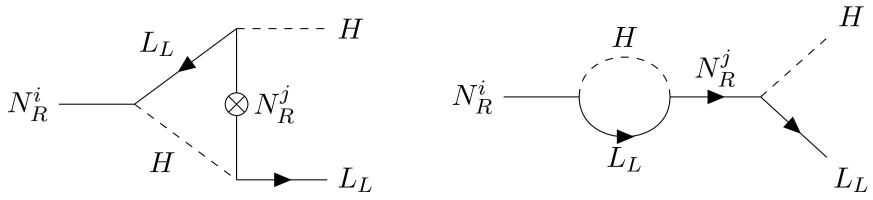

Fig. 3.7: One-loop contributions to the tree-level decay $N_R^i \to L_L H$. These diagrams, which interfere with the tree-level process, are essential for generating CP violation in leptogenesis.

At one-loop order, ϵ_i is computed to be

$$\epsilon_i = \frac{1}{8\pi|\lambda_i|^2} \sum_{j \neq i} \mathrm{Im}\left[(\lambda_j^* \lambda_i)^2\right] \left[f\left(\frac{M_j^2}{M_i^2}\right) + g\left(\frac{M_j^2}{M_i^2}\right)\right], \tag{3.13}$$

where M_i is the mass of N_R^i, λ_i is the Dirac coupling, and the functions $f(a)$ and $g(a)$ are defined as

$$f(a) \equiv \sqrt{a}\left[1 - (1+a)\ln\left(\frac{1+a}{a}\right)\right], \tag{3.14}$$

$$g(a) \equiv \frac{\sqrt{a}}{1-a}. \tag{3.15}$$

- **Avoiding washout.** Some scattering processes with $\Delta L = 1$ or $\Delta L = 2$ may erase the generated lepton asymmetry. It is important to ensure that these processes do not fully wash out the asymmetry before it is transferred to the baryon sector.
- **Departure from thermal equilibrium.** The expansion of the universe naturally provides the departure from thermal equilibrium required for leptogenesis, particularly for Majorana masses in the range of 10^{10}–10^{16} GeV.

The evolution of the sterile neutrino abundance, $Y_{N_R^i}$, and the $B-L$ asymmetry, Y_{B-L}, is governed by the following Boltzmann equations

$$\frac{dY_{N_R^i}}{dx} = -\frac{x}{H(1)} \langle\Gamma\rangle_{\mathrm{D}}^{\mathrm{tot},i} \left(Y_{N_R^i} - Y_{N_R^i}^{\mathrm{eq}}\right), \tag{3.16}$$

$$\frac{dY_{B-L}}{dx} = -\sum_i \frac{x}{H(1)} \left[\epsilon_i \langle\Gamma\rangle_{\mathrm{D}}^{\mathrm{tot},i}\left(Y_{N_R^i} - Y_{N_R^i}^{\mathrm{eq}}\right) + \mathfrak{s}\langle\sigma v\rangle_{\mathrm{scatts}}^i Y_{B-L}\right], \tag{3.17}$$

where $\langle\Gamma\rangle_{\mathrm{D}}^{\mathrm{tot},i}$ is the thermally averaged decay rate of N_R^i, and $\langle\sigma v\rangle_{\mathrm{scatts}}^i$ is the thermally averaged cross section for scattering processes violating $B-L$.

For a comprehensive discussion on leptogenesis, refer to Ref. [119].

Chapter 4

An asymmetric dark sector

In Chapter 2, we discussed the dark sector, a component of the universe supported by overwhelming evidence but whose nature remains unknown. In Chapter 3, we examined the matter-antimatter asymmetry in the visible sector. This observation naturally suggests the possibility of a dark sector with unequal particle and antiparticle abundances, a concept referred to as Asymmetric Dark Matter (ADM).

4.1 Ratio of dark matter and baryon densities

Another compelling reason to consider an asymmetric dark sector is the observational similarity between the dark matter and baryon abundances [5]:

$$\Omega_{\mathrm{DM}} \simeq 5\,\Omega_{\mathrm{b}}, \tag{4.1}$$

which hints at the possibility of a shared mechanism linking the two sectors. A priori, these two quantities are unrelated. The relic density of dark matter in the freeze-out framework depends on the point at which the interaction rate falls below the Hubble expansion rate. In contrast, the baryon relic density is governed by CP-violation parameters and the out-of-equilibrium dynamics associated with baryon number-violating processes during baryogenesis. Given that these mechanisms are seemingly independent, the fact that the energy densities of dark matter and baryons are of the same order of magnitude is striking.

A way to establish a connection between these two sectors is to consider an asymmetry in the dark sector that is directly linked to the baryon asymmetry. The two asymmetries could either have a common origin or have been transferred from one sector to the other.

4.2 Asymmetric dark matter models

The idea that dark matter and the baryon asymmetry might be related dates back to the late 1980s, around the same time as the emergence of the WIMP paradigm. One of the earliest motivations for a dark matter asymmetry was to explain the relation in Eq. (4.1), as suggested in Ref. [133]. Additionally, it was proposed as a solution to the solar neutrino problem, where dark matter could accumulate in the Sun and impact heat transport [134], but the annihilation inside the Sun's core could be avoided if only particles of asymmetric nature would be present [135].

Building on these early ideas, the ADM paradigm [136] provided a framework to connect the baryon and dark matter number densities via higher-dimensional operators. This paradigm encompasses a wide range of realizations while naturally avoiding all experimental constraints, and led to significant research activity in developing ADM models and exploring their phenomenology. Generally, the ADM mechanism works as follows:

1. An asymmetry arises in the visible sector, the dark sector, or both. It may originate in the visible sector and be transferred to the dark sector, emerge in the dark sector and subsequently be communicated to baryons and leptons in the visible sector, or be generated simultaneously in both sectors.

2. The process which communicates the asymmetry between the two sectors decouples or becomes inefficient, leaving the asymmetries in each sector fixed.

3. If dark matter had a thermal abundance during the asymmetry generation process, its symmetric component must annihilate, leaving only the asymmetric component. This can occur through ADM freeze-out, as discussed in Section 2.4.2.

We will briefly review in the following some of the most common asymmetry transfer and asymmetry generation mechanisms.

4.2.1 Asymmetry transfer mechanisms

The transfer of a pre-existing asymmetry between the dark and visible sectors can occur through various mechanisms, including sphalerons, higher-dimensional operators and oscillations.

Sphaleron transfer models exploit electroweak sphalerons. In these models, dark matter carries a global symmetry (D), analogous to B and L, which is classically conserved but is violated by sphalerons if D is anomalous under $SU(2)$. As a result, the dark matter asymmetry freezes in when sphalerons decouple. However, these models often require modifications to the electroweak sector, leading to strict experimental constraints. An alternative is to introduce a new gauge group where D, along with B or L, is anomalous, avoiding these constraints while maintaining the same mechanism. Some proposals which use electroweak sphalerons to relate baryon and dark matter asymmetries are Refs. [137–141].

The second class of transfer mechanisms avoids precision electroweak constraints by using higher-dimensional operators to link the baryon, lepton, and dark matter asymmetries. As the universe cools and the operator decouples, the asymmetries freeze in separately in each sector. Alternatively, renormalizable interactions can achieve the same effect, particularly in models with additional fields, where the interaction naturally decouples as heavy particles are integrated out, providing a connection between higher-dimensional and renormalizable approaches. Higher-dimensional operators can arise naturally in Grand Unified Theories through the integration of heavy fields [142], or in string theory via higher-dimensional effects [143]. Other models make use of operators such as $\bar{L}HX^2$ [144–146] or alternative higher-dimensional interactions [147] to facilitate asymmetry transfer between sectors.

Another asymmetry transfer mechanism relies on particle oscillations to redistribute a pre-existing asymmetry between the visible and dark sectors. Similar to neutrino oscillations, these mechanisms involve a mass mixing term between a SM particle and a dark sector state carrying baryon or lepton number. If oscillations occur after an initial asymmetry has been established, they allow for a late-time transfer of the asymmetry before freezing out [148].

4.2.2 Asymmetry generation mecanisms

Since ADM models can transfer a pre-existing asymmetry, they naturally integrate with standard mechanisms for generating the cosmological lepton or baryon asymmetry, like those mentioned in Section 3.4. In addition, some models occur through "darkogenesis", where the asymmetry originates in the dark sector and is later transferred to the SM through the previously discussed mechanisms, or through "cogenesis", where a single source generates asymmetries in both the dark and visible sectors simultaneously.

4.2.2.1 Darkogenesis

In dark baryogenesis (or darkogenesis), an asymmetry is first generated in the dark sector and later transferred to the visible sector, either through sphalerons or other interactions.

In some models, asymmetry generation in the dark sector follows frameworks analogous to EWBG, which was introduced in Section 3.4.1. In the dark sector, a dark Higgs can have C- and CP-violating interactions and undergo a first-order phase transition, enabling asymmetry generation. Additionally, if the dark sector includes a dark non-Abelian gauge group, under which the dark matter number D has a chiral anomaly, then dark sphalerons can violate D. Since the dynamics of the dark sector remain largely unknown, most constraints on these models arise from the asymmetry transfer mechanism rather than its generation. Viable models of dark EWBG include Refs. [149, 150].

Other models are based on spontaneous baryogenesis, described in Refs. [151, 152]. Here, instead of relying on a dark phase transition, spontaneous dark baryogenesis can generate a dark matter asymmetry via spontanous symmetry breaking. In this framework, the usual C and CP violation required by the Sakharov conditions is replaced by a spontaneous violation of CPT and T symmetry. This mechanism introduces a term in the Lagrangian of the form [153]:

$$\mathcal{L} \supset \frac{\partial_\mu \phi}{f} J^\mu_X \,, \tag{4.2}$$

where f is a decay constant, and J^μ_X is the current associated to the symmetry X, which in this case is $X = D$. If the scalar field ϕ acquires a vacuum expectation value, its time derivative induces spontaneous CPT and T violation, generating a chemical potential $\mu_X = \dot{\phi}/f$ and leading to a net dark asymmetry.

Additionally, the literature includes mechanisms inspired in leptogenesis, such as Ref. [154] and in Affleck-Dine dynamics, both of which can operate exclusively within the dark sector before transferring the asymmetry.

4.2.2.2 Cogenesis

A common class of cogenesis models involves the decay of a parent particle that simultaneously generates asymmetries in both the visible and dark sectors. This is particularly well illustrated in extensions of the classic leptogenesis mechanism. In this scenario, heavy sterile neutrinos N_i decay into both SM particles (L and H) and dark sector particles (χ and ϕ) [155]:

$$\mathcal{L} = -\frac{1}{2} M_i N_i^2 - y_i N_i L H - \lambda_i N_i \chi \phi \,. \tag{4.3}$$

Since N_i violate both $B-L$ and D, the resulting asymmetries in these sectors are generally not identical. Each asymmetry is determined by CP violation in the decay channels, which is governed by the Yukawa couplings y_i or λ_i. This leptogenesis-inspired framework can be realized in many different ways, including those proposed in Refs. [156–164].

Another class of cogenesis models relies on CP-violating oscillations of neutral mesons before their decay into both visible and dark sector particles. In these scenarios, mesons such as neutral B mesons undergo CP-violating oscillations before decaying into baryons and dark matter candidates, leading to a dynamically generated asymmetry [165, 166]. This approach allows for a testable, low-energy realization of cogenesis [167].

Other cogenesis models are also based on the Affleck-Dine mechanism, where a potential-flat direction in field space carrying both $B-L$ and D generates asymmetries in both sectors simultaneously [168–172].

Additional possibilities include EWBG scenarios extended to incorporate both the dark matter sector and the SM [139, 173–175], as well as spontaneous cogenesis, such as in Ref. [176], where Eq. (4.2) features the combination $X = B - L - D$.

4.3 A baryon-symmetric universe

We typically refer to the baryon asymmetry in the visible sector as if it implies a baryon-asymmetric universe. However, from an observational standpoint, there is no direct evidence that the universe as a whole is baryon asymmetric. As previously discussed, the visible sector, the portion of matter we can directly observe, constitutes only a small fraction of the total matter in the universe. The vast majority remains unobservable, meaning that our evidence for a baryon asymmetry is confined to the visible sector alone. Specifically, what we observe is an asymmetry between quarks and antiquarks, quantified as

$$Y_{\Delta q,0} = (2.613 \pm 0.018) \times 10^{-10} \,, \tag{4.4}$$

which is obtained by multiplying by 3 the commonly reported value in terms of the asymmetry in baryon number, given in Eq. (3.3).

This raises a crucial possibility: dark matter itself could carry baryon number. If the excess of quarks in the visible sector were exactly compensated by an opposite baryon charge hidden in the dark sector, then there would be no net baryon asymmetry in the universe.[1]

In this scenario, the first Sakharov condition, which expresses the requirement of baryon number violation, would no longer be necessary for generating the observed quark-antiquark asymmetry.[2]

The remainder of this thesis is structured as follows: we first introduce the fundamental aspects of this scenario, followed by an exploration of its dynamics, in Chapter 5. Then, we discuss the expected experimental constraints and observational signatures in Chapter 6, before concluding with a discussion of its potential UV completion in Chapter 7.

[1] Since sphalerons violate B but conserve $B-L$, we must talk about a universe which is $B-L$ symmetric. This topic will be formally addressed in the following chapter.

[2] Other works that consider a $B-L$ symmetric universe are Refs. [156, 157, 162, 165, 174, 177–179].

Chapter 5

Baryon number conserving model

5.1 A simple scenario

At the end of the previous chapter, we established that the universe could be baryon-symmetric, with the counterpart of the apparent baryon asymmetry concealed in the dark sector. We now present the proposed model which explains the nature of dark matter and the matter-antimatter asymmetry in a baryon number conserving scenario.

We introduce a dark sector with two new particles: a complex scalar χ, which is charged under baryon number as $B(\chi) = -1$, and a Dirac fermion N, which is charged with an opposite baryon number $B(N) = +1$. Both particles are singlets under any other SM gauge groups. The SM quarks are charged as usual with fractional baryon number $B(q) = 1/3$.

The revised conditions required for the generation of a quark-antiquark asymmetry in this scenario are as follows:

1. C and CP violation within the dark sector,
2. a departure from thermal equilibrium,
3. a portal interaction between the dark sector and the quarks.

The first two conditions are essential for creating an asymmetry between the number of particles N and $\overline{N}$, and therefore a baryon asymmetry within this particle species. The third condition is then necessary to transfer this asymmetry generated in the N sector to the quarks.

5.1.1 Lagrangian and interactions

The scenario follows the principle of baryon number conservation, as we ensure that the global $U(1)_B$ symmetry is strictly conserved in the new interactions, just as it is in the SM. Following this principle, we will use it as a guideline when writing the interaction terms in the Lagrangian for the dark sector particles.

The kinetic and mass terms in the Lagrangian of the dark sector baryons read

$$\mathcal{L} \supset |\partial_\mu \chi|^2 + m_\chi^2 \chi^* \chi + \overline{N} \left(i\partial\!\!\!/ - m_N \right) N. \tag{5.1}$$

Additionally, two baryon number-conserving interaction terms involving these dark sector particles can be introduced using dimension-5 operators in Effective Field Theory (EFT), each associated with a different energy scale Λ:

$$\mathcal{L} \supset \frac{1}{\Lambda_0}\chi\chi^*\overline{N}N + \frac{1}{\Lambda_2}\left(\chi\chi\overline{N^c}N + h.c.\right), \tag{5.2}$$

where the superscript c denotes charge conjugation. Both of these terms conserve baryon number, but the first term, with energy scale Λ_0, does not change baryon number in the fermionic current or within each particle species sector. In contrast, the second type of term, with energy scale Λ_2, changes the baryon number within each species in two units, as the subscript denotes.

The connection between the dark sector and the SM is realized through a term connecting the particle N with first-family quarks, called the "neutron portal":

$$\mathcal{L} \supset \frac{1}{{\Lambda_n}^2}\left(\overline{N}d_R\,\overline{u^c_R}d_R + h.c.\right), \tag{5.3}$$

with u_R and d_R the right-handed up and down quarks.[1] The energy scale associated with this dimension-6 term is Λ_n.

We can also introduce a Higgs-type portal of the form

$$\mathcal{L} \supset \lambda_{\chi H}|\chi|^2|H|^2, \tag{5.4}$$

with H the SM Higgs doublet, and $\lambda_{\chi H}$ a dimensionless coupling constant. This portal will not impact the dynamics of the scenario, as it does not transfer baryon number from the dark sector to the visible sector. Moreover, $\lambda_{\chi H}$ is experimentally constrained, and it would only feebly contribute to the freeze-out of the dark matter. More details about the phenomenology of this portal will be addressed in Section 6.1.

Table 5.1 provides a summary of all particle-number-changing processes corresponding to each interaction term and energy scale presented in Eqs. (5.2) and (5.3).

Annihilations mediated by Λ_0 either increase or decrease the total abundance of the species χ and N. Since these processes always involve one particle and one antiparticle, they do not alter any asymmetry stored within each particle species.

The processes associated with the energy scale Λ_2, including both annihilations and scatterings, impact any asymmetry stored in these particle species, as they transfer baryon number between the species while still conserving the total baryon number.

Finally, we have the processes associated with the neutron portal, characterized by the energy scale Λ_n. These processes link the dark sector, specifically the particle species N, to the quark sector, allowing baryon number to flow between them. Through the scatterings, an initial asymmetry in N will be quickly partially converted into an asymmetry within the quark sector. At later times, the decays of N and $\overline{N}$ will transfer any remaining asymmetry to the quarks as they disappear from the universe. The neutron portal interactions do not violate baryon number but will appear to do so in experiments, as only SM particles are detectable.

[1] Portals involving heavier generation quarks are also possible, and will be commented in Section 7.2.3. Portals involving left-handed quarks are do not present any phenomenological advantage.

Table 5.1: Relevant processes arising from the different EFT interaction terms in the Lagrangian (5.2) and (5.3), associated to the different energy scales.

Energy scale	**Relevant interactions**	
Λ_0	Annihilations:	$\chi\chi^* \leftrightarrow N\overline{N}$
Λ_2	Annihilations:	$\chi\chi \leftrightarrow \overline{N}\overline{N}$, $\chi^*\chi^* \leftrightarrow NN$
	Scatterings:	$\chi N \leftrightarrow \chi^*\overline{N}$
Λ_n	Scatterings:	$N\bar{d} \leftrightarrow ud$, $\overline{N}d \leftrightarrow \bar{u}\bar{d}$ $N\bar{u} \leftrightarrow dd$, $\overline{N}u \leftrightarrow \bar{d}\bar{d}$
	Decays:	$N \to udd$, $\overline{N} \to \bar{u}\bar{d}\bar{d}$

5.1.2 Initial condition

As mentioned earlier, we need an asymmetry to be generated between particles N and antiparticles $\overline{N}$. To conserve the overall baryon number, a corresponding asymmetry between particles χ and antiparticles χ^* is also required. Fig. 5.1 illustrates this initial condition. The boxes represent the different particles involved, their size proportional to their abundance. Yellow represents negative baryon number, while blue represents positive baryon number. The interactions between the different particle species are shown as connecting pipes.

The generation of this asymmetry in each dark sector species, can be realized though different mechanisms. For now, we assume an initial condition where the asymmetry is already present. Later, we explore the dynamic generation via a leptogenesis-like mechanism, involving two heavy Majorana fermions that decay into the dark sector particles, with CP violation occurring at the loop level. For a detailed description of this mechanism, see section 7.1.

5.1.3 Dark matter

Let us now focus on the complex scalar χ. This particle is the lightest scalar charged under baryon number. This implies that, in the case of baryon and lepton number conservation, χ and χ^* are not allowed to decay, making them absolutely stable. In typical dark matter models, stability is imposed ad hoc by making them odd with respect to a $\mathbb{Z}_2$ symmetry. Here, however, stability is a natural consequence of baryon and lepton number conservation, without the need to impose any new symmetries.[2] Furthermore, dark matter stability is also strongly linked to the quark-antiquark asymmetry in this scenario: if dark matter decayed into SM particles, it would erase the visible net baryon

[2] In the model presented in Eq. (5.1–5.4), the dark matter particle exhibits an accidental $\mathbb{Z}_2$ symmetry, $\chi \to -\chi$, which however has no influence on the dark matter stability.

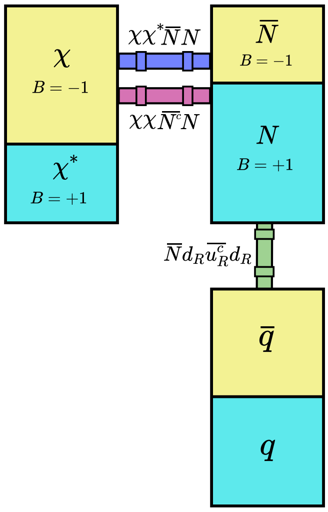

Fig. 5.1: Simplified sketch of the initial condition in our scenario. The particles and antiparticles charged under baryon number in the dark and visible sectors are represented as boxes, with box size indicating particle abundance and color representing the sign of the baryonic charge. There is an equal but opposite asymmetry in the dark sector particles. The overall baryon number of the universe is zero.

asymmetry. The fact that this particle is stable and neutral under the SM gauge symmetries, makes it a good dark matter candidate.

The present-day abundance of this partice species must match the observed relic abundance of dark matter. This can be achieved, for instance, through the asymmetric freeze-out of χ and χ^* via annihilations of the type $\chi\chi^* \to N\overline{N}$, mediated by Λ_0, provided this energy scale is sufficiently low. The freeze-out processes might result in the complete depletion of the asymmetric component, leaving only the excess of particles, as represented in the left panel of Fig. 5.2. Alternatively, it might result in a partial depletion of the asymmetric component, leaving also an abundance of antiparticles, as represented in the right panel of Fig. 5.2. The asymmetry present in the dark matter sets th depletion e limit for the asymmetric freeze-out scenario: even with the strongest cross section, it is impossible to annihilate the excess particles once all antiparticles are depleted. We will explore the dark matter freeze-out in our scenario in more detail in Section 5.2.4.

It is important to note that while freeze-out dynamics require the scale Λ_0 to be low to enable efficient $\chi\chi^* \to N\overline{N}$ annihilations, the opposite is true for the interaction scale Λ_2. As mentioned earlier, interactions mediated by this scale tend to erase the asymmetry within each particle species, earning the name of "washout processes". If these interactions are too strong, they will erase the asymmetry between χ and χ^* as well as between N and $\overline{N}$, preventing any asymmetry from being transferred to the quarks. Therefore, Λ_2 needs to be larger than a certain value. A more detailed analysis of the washout dynamics is provided in Section 5.2.2.

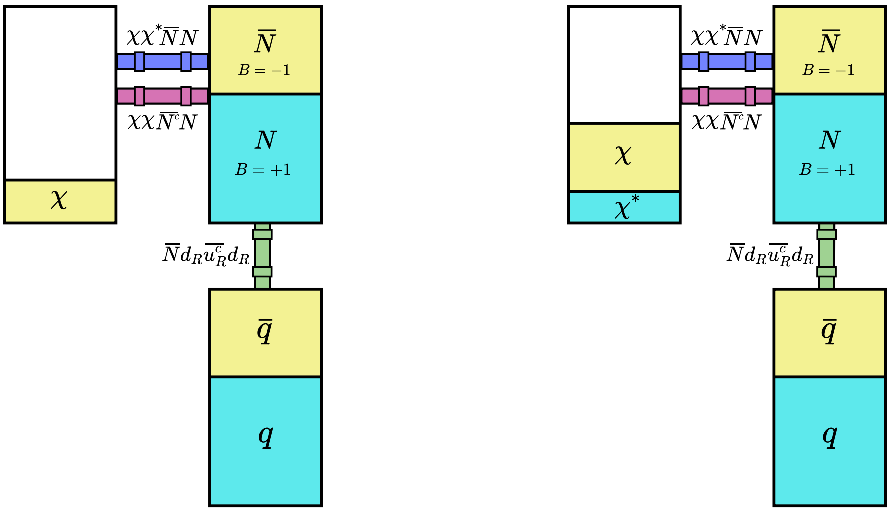

Fig. 5.2: Possible states after dark matter freeze-out starting from the initial condition in Fig. 5.1, corresponding to the scenario where dark matter antiparticles have efficiently annihilated (left panel), or only partially annihilated (right panel).

Assuming that the asymmetry is not completely washed out (a partial washout can be compensated with a larger initial asymmetry), any remaining asymmetry between N and $\overline{N}$ will be transferred to the quarks through scatterings and decays. This results in a final state with equal and opposite baryon number in the visible and dark sectors today, $n^0_{\Delta\chi} = n^0_{\Delta \mathrm{b}}$. This final state is depicted in Fig. 5.3, where the two sketches correspond to the case where the asymmetric component of dark matter is totally annihilated (left) or only partially annihilated (right).

In this setup, we find that the maximum dark matter mass is $m_{\mathrm{DM}} = 5$ GeV, corresponding to the case where Λ_0 is sufficiently large for dark matter to be fully asymmetric today. This value comes from the relation between the dark matter and baryon energy densities, given in Eq. (4.1), and the fact that there are practically no SM antibaryons today ($n^0_{\mathrm{b}} = n^0_{\Delta\mathrm{b}}$):

$$m_{\mathrm{DM}}\, n^0_{\mathrm{DM}} = 5\, n^0_{\mathrm{b}}\, m_p, \tag{5.5}$$

$$m_{\mathrm{DM}} = 5\,\mathrm{GeV}\,\frac{n^0_{\mathrm{b}}}{n^0_{\mathrm{DM}}}, \tag{5.6}$$

$$m_{\mathrm{DM}} = 5\,\mathrm{GeV}\,\frac{n^0_{\Delta\mathrm{b}}}{n^0_{\Delta\chi} + 2n^0_{\chi^*}}, \tag{5.7}$$

where $m_p \simeq 1$ GeV is the mass of the proton. If the relic dark matter abundance is fully asymmetric, $n^0_{\chi^*} = 0$ and $m_{\mathrm{DM}} = 5$ GeV. If it is not fully asymmetric, then $n^0_{\chi^*} \neq 0$, and the dark matter mass will be lower to compensate its excess of abundance relative to the SM baryons.

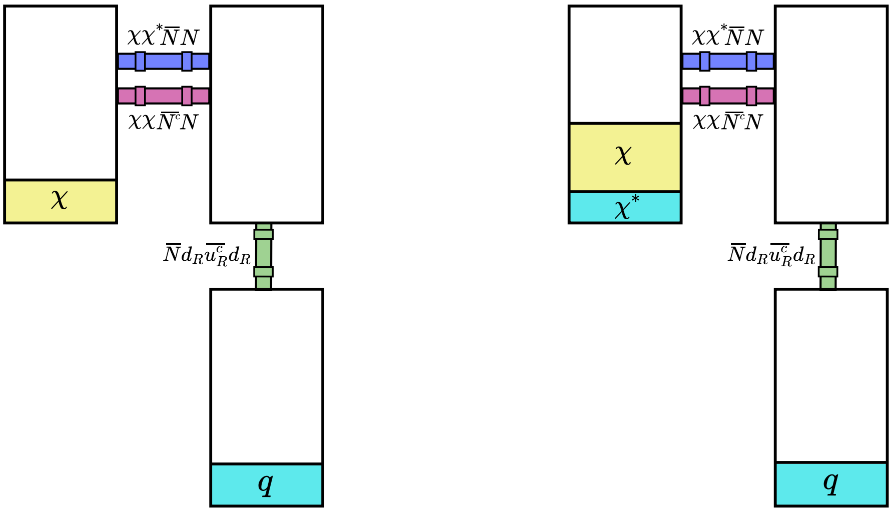

Fig. 5.3: Possible final states from the initial condition in Fig. 5.1, corresponding to the scenario where dark matter antiparticles have efficiently annihilated (left panel), or only partially annihilated (right panel). All N have decayed into quarks. The effect of sphalerons is not considered in this sketch. In both cases, the total baryon number of the Universe is conserved and equal to zero.

5.1.4 Effect of sphalerons

So far, we have presented a somewhat simplified picture of the actual scenario. One important factor to consider is the effect of sphalerons, introduced in Section 3.3. Sphalerons are processes that remained active in the universe up to temperatures of $T \sim 130$ GeV [117], and which involve SM quarks and leptons in a manner that conserves $B - L$ but violates B and L individually.

If the asymmetry in the dark sector particles is generated while sphaleron processes are still in equilibrium, then, given that neutron portal scatterings will transfer immediately part of this asymmetry to the quarks, sphalerons will in turn transfer part of this asymmetry from the quarks to the leptons. Once sphalerons go out of thermal equilibrium any asymmetry stored in leptons will remain fixed, altering the scenario shown in Fig. 5.3.

After the particles N and $\overline{N}$ decay into quarks, the asymmetry in the dark matter particles will differ from that present in the quarks, as part of it has been transferred to the leptons: $n^0_{\Delta\chi} > n^0_{\Delta b}$. Now, in the totally asymmetric case ($n^0_{\chi^*} = 0$), the mass of the dark matter is lower than 5 GeV, see Eq. (5.7). A careful analysis of the fraction of asymmetry transferred to leptons, performed in Section 5.2.3, reveals that the maximum dark matter mass for $T_{\rm in} > 130$ GeV is $m_{\rm DM} = 1.9$ GeV. The effect of sphalerons will be included from now on.

5.1.5 Viable energy scales

It is worth noting that the requirements for the the introduced energy scales are not overly restrictive, as they allow for broad parameter ranges rather than specific values. We impose an upper limit on Λ_0 to ensure it can deplete the thermal abundances of dark matter, and a lower limit on Λ_2 to prevent washout of the asymmetry. A wide range of values is also permitted for Λ_n. Specific analysis and numerical values for these limits can be found in Sections 5.2.2, 5.2.4 and 6.2.2.

5.2 Dynamics

5.2.1 Boltzmann equations

We have presented in the previous section the different particles and interactions that conform the dark sector in our scenario. To assess the evolution of the abundances of these particles, we use the Boltzmann equation formalism described in Appendices B.1 and B.2. We write an equation for the yield of each particle and antiparticle, accounting for the various interactions that impact it (see Table 5.1). The equations read

$$\begin{aligned}\frac{dY_\chi}{dx} = -\frac{\lambda}{x^2}\Bigg[&\langle\sigma v\rangle_{\chi\chi^*\to N\bar{N}}\left(Y_\chi Y_{\chi^*} - \frac{Y_\chi^{\rm eq}Y_{\chi^*}^{\rm eq}}{Y_N^{\rm eq}Y_{\bar{N}}^{\rm eq}}Y_N Y_{\bar{N}}\right) + 2\langle\sigma v\rangle_{\chi\chi\to\bar{N}\bar{N}}\left(Y_\chi^2 - \left(\frac{Y_\chi^{\rm eq}}{Y_{\bar{N}}^{\rm eq}}\right)^2 Y_{\bar{N}}^2\right) \\ &+ \langle\sigma v\rangle_{\chi N\to\chi^*\bar{N}}\left(Y_\chi Y_N - \frac{Y_\chi^{\rm eq}Y_N^{\rm eq}}{Y_{\chi^*}^{\rm eq}Y_{\bar{N}}^{\rm eq}}Y_{\chi^*}Y_{\bar{N}}\right)\Bigg], \end{aligned} \tag{5.8}$$

$$\begin{aligned}\frac{dY_{\chi^*}}{dx} = -\frac{\lambda}{x^2}\Bigg[&\langle\sigma v\rangle_{\chi\chi^*\to N\bar{N}}\left(Y_\chi Y_{\chi^*} - \frac{Y_\chi^{\rm eq}Y_{\chi^*}^{\rm eq}}{Y_N^{\rm eq}Y_{\bar{N}}^{\rm eq}}Y_N Y_{\bar{N}}\right) + 2\langle\sigma v\rangle_{\chi^*\chi^*\to NN}\left(Y_{\chi^*}^2 - \left(\frac{Y_{\chi^*}^{\rm eq}}{Y_N^{\rm eq}}\right)^2 Y_N^2\right) \\ &- \langle\sigma v\rangle_{\chi N\to\chi^*\bar{N}}\left(Y_\chi Y_N - \frac{Y_\chi^{\rm eq}Y_N^{\rm eq}}{Y_{\chi^*}^{\rm eq}Y_{\bar{N}}^{\rm eq}}Y_{\chi^*}Y_{\bar{N}}\right)\Bigg], \end{aligned} \tag{5.9}$$

$$\begin{aligned}\frac{dY_N}{dx} = -\frac{\lambda}{x^2}\Bigg[&-\langle\sigma v\rangle_{\chi\chi^*\to N\bar{N}}\left(Y_\chi Y_{\chi^*} - \frac{Y_\chi^{\rm eq}Y_{\chi^*}^{\rm eq}}{Y_N^{\rm eq}Y_{\bar{N}}^{\rm eq}}Y_N Y_{\bar{N}}\right) - 2\langle\sigma v\rangle_{\chi^*\chi^*\to NN}\left(Y_{\chi^*}^2 - \left(\frac{Y_{\chi^*}^{\rm eq}}{Y_N^{\rm eq}}\right)^2 Y_N^2\right) \\ &+ \langle\sigma v\rangle_{\chi N\to\chi^*\bar{N}}\left(Y_\chi Y_N - \frac{Y_\chi^{\rm eq}Y_N^{\rm eq}}{Y_{\chi^*}^{\rm eq}Y_{\bar{N}}^{\rm eq}}Y_{\chi^*}Y_{\bar{N}}\right) + \frac{1}{\mathfrak{s}}\langle\Gamma_N\rangle\left(Y_N - Y_N^{\rm eq}\right) \\ &+ \langle\sigma v\rangle_{N\bar{d}\to ud}Y_{\bar{d}}^{\rm eq}\left(Y_N - Y_N^{\rm eq}\right) + \langle\sigma v\rangle_{N\bar{u}\to dd}Y_{\bar{u}}^{\rm eq}\left(Y_N - Y_N^{\rm eq}\right)\Bigg], \end{aligned} \tag{5.10}$$

$$\begin{aligned}\frac{dY_{\bar{N}}}{dx} = -\frac{\lambda}{x^2}\Bigg[&-\langle\sigma v\rangle_{\chi\chi^*\to N\bar{N}}\left(Y_\chi Y_{\chi^*} - \frac{Y_\chi^{\rm eq}Y_{\chi^*}^{\rm eq}}{Y_N^{\rm eq}Y_{\bar{N}}^{\rm eq}}Y_N Y_{\bar{N}}\right) - 2\langle\sigma v\rangle_{\chi\chi\to\bar{N}\bar{N}}\left(Y_\chi^2 - \left(\frac{Y_\chi^{\rm eq}}{Y_{\bar{N}}^{\rm eq}}\right)^2 Y_{\bar{N}}^2\right) \\ &- \langle\sigma v\rangle_{\chi N\to\chi^*\bar{N}}\left(Y_\chi Y_N - \frac{Y_\chi^{\rm eq}Y_N^{\rm eq}}{Y_{\chi^*}^{\rm eq}Y_{\bar{N}}^{\rm eq}}Y_{\chi^*}Y_{\bar{N}}\right) + \frac{1}{\mathfrak{s}}\langle\Gamma_N\rangle\left(Y_{\bar{N}} - Y_{\bar{N}}^{\rm eq}\right) \\ &+ \langle\sigma v\rangle_{\bar{N}d\to\bar{u}\bar{d}}Y_d^{\rm eq}\left(Y_{\bar{N}} - Y_{\bar{N}}^{\rm eq}\right) + \langle\sigma v\rangle_{\bar{N}u\to\bar{d}\bar{d}}Y_u^{\rm eq}\left(Y_{\bar{N}} - Y_{\bar{N}}^{\rm eq}\right)\Bigg]. \end{aligned} \tag{5.11}$$

Here, $x \equiv m_\chi/T$, $\mathfrak{s}$ is the entropy density of the universe at the temperature T, defined in Eq. (2.6), and the overall numerical factor λ is given in Eq. (2.12). To simplify the equations, we have applied detailed balance to relate the thermally averaged cross section of each process to that of its inverse.

The explicit expressions in the EFT for the cross sections and rates of the involved annihilations, scatterings, and decays read:

$$\sigma_{\chi\chi^*\to N\overline{N}} = \frac{\left(s-4m_N^2\right)^{3/2}}{8\pi\, s\sqrt{s-4m_\chi^2}\,\Lambda_0{}^2}\,, \tag{5.12}$$

$$\sigma_{\chi\chi\to\overline{N}\overline{N}} = \sigma_{\chi^*\chi^*\to NN} = \frac{\left(s-4m_N^2\right)^{3/2}}{8\pi\, s\sqrt{s-4m_\chi^2}\,\Lambda_2{}^2}\,, \tag{5.13}$$

$$\sigma_{\chi N\to\chi^*\overline{N}} = \frac{m_N^4-2m_N^2\left(m_\chi^2-3s\right)+\left(m_\chi^2-s\right)^2}{32\pi\, s^2\Lambda_2{}^2}\,, \tag{5.14}$$

$$\sigma_{N\bar{d}\to ud} = \sigma_{\overline{N}d\to\bar{u}\bar{d}} = \frac{m_N^2+14s}{192\pi\Lambda_n{}^4}\,, \tag{5.15}$$

$$\sigma_{N\bar{u}\to dd} = \sigma_{\overline{N}u\to\bar{d}\bar{d}} = \frac{2m_N^2+s}{192\pi\Lambda_n{}^4}\,, \tag{5.16}$$

$$\Gamma_{N\to udd} = \Gamma_{\overline{N}\to\bar{u}\bar{d}\bar{d}} = \frac{1}{768\pi^3}\frac{m_N^5}{\Lambda_n{}^4}\,, \tag{5.17}$$

with s the square of the center of mass energy. To obtain the thermally averaged cross sections and thermally averaged decay rates which appear in the Boltzmann equations, see the formalism detailed in Appendix A.4.

To simplify the discussion, we will assume that the neutron portal interaction is sufficiently strong to bring the dark sector baryons into thermal equilibrium with the visible sector, bringing the temperature of both sectors to be the same. At a given temperature T, this condition requires:

$$\Lambda_n \lesssim 6.1\times 10^7\left(\frac{T}{10^5\ \text{GeV}}\right)^{3/4}\ \text{GeV}, \tag{5.18}$$

coming from the imposition that the rate of the neutron portal scatterings is faster than the expansion of the universe, $\langle\sigma v\rangle\, n_N \geq H$. We can see in Fig. 6.6 how this is a reasonable assumption.

It will be convenient to work with the total yields of the different particle species, along with their corresponding asymmetries, defined as:

$$Y_\chi^{\text{tot}} = Y_\chi + Y_{\chi^*}\,, \qquad Y_{\Delta\chi} = Y_\chi - Y_{\chi^*}\,, \tag{5.19}$$

$$Y_N^{\text{tot}} = Y_N + Y_{\overline{N}}\,, \qquad Y_{\Delta N} = Y_N - Y_{\overline{N}}\,. \tag{5.20}$$

The Boltzmann equations describing their temperature evolution are then

$$\frac{dY_\chi^{\rm tot}}{dx} = -\frac{\lambda}{x^2}\Bigg[2\langle\sigma v\rangle_{\chi\chi^*\to N\overline{N}}\Big(Y_\chi Y_{\chi^*} - P Y_N Y_{\overline{N}}\Big) + 2\langle\sigma v\rangle_{\chi\chi\to\overline{N}\,\overline{N}}\Big(Y_\chi^2 + Y_{\chi^*}^2 - P\left(Y_N^2 + Y_{\overline{N}}^2\right)\Big)\Bigg], \tag{5.21}$$

$$\frac{dY_{\Delta\chi}}{dx} = -\frac{\lambda}{x^2}\Bigg[2\langle\sigma v\rangle_{\chi\chi\to\overline{N}\,\overline{N}}\Big(Y_\chi^2 - Y_{\chi^*}^2 + P\left(Y_N^2 - Y_{\overline{N}}^2\right)\Big) + 2\langle\sigma v\rangle_{\chi N\to\chi^*\overline{N}}\Big(Y_\chi Y_N - Y_{\chi^*} Y_{\overline{N}}\Big)\Bigg], \tag{5.22}$$

$$\begin{aligned}\frac{dY_N^{\rm tot}}{dx} = -\frac{\lambda}{x^2}\Bigg[& -2\langle\sigma v\rangle_{\chi\chi^*\to N\overline{N}}\Big(Y_\chi Y_{\chi^*} - P Y_N Y_{\overline{N}}\Big) - 2\langle\sigma v\rangle_{\chi\chi\to\overline{N}\,\overline{N}}\Big(Y_\chi^2 + Y_{\chi^*}^2 - P\left(Y_N^2 + Y_{\overline{N}}^2\right)\Big) \\ & + \langle\sigma v\rangle_{N\bar{d}\to ud}\Big(Y_N Y_{\bar{d}}^{\rm eq} + Y_{\overline{N}} Y_d^{\rm eq} - Y_N^{\rm eq} Y_{\bar{d}}^{\rm eq} - Y_{\overline{N}}^{\rm eq} Y_d^{\rm eq}\Big) \\ & + \langle\sigma v\rangle_{N\bar{u}\to dd}\Big(Y_N Y_{\bar{u}}^{\rm eq} + Y_{\overline{N}} Y_u^{\rm eq} - Y_N^{\rm eq} Y_{\bar{u}}^{\rm eq} - Y_{\overline{N}}^{\rm eq} Y_u^{\rm eq}\Big) \\ & + \frac{1}{\mathfrak{s}}\langle\Gamma_N\rangle\Big(Y_N + Y_{\overline{N}} - Y_N^{\rm eq} - Y_{\overline{N}}^{\rm eq}\Big)\Bigg],\end{aligned} \tag{5.23}$$

$$\begin{aligned}\frac{dY_{\Delta N}}{dx} = -\frac{\lambda}{x^2}\Bigg[& 2\langle\sigma v\rangle_{\chi\chi\to\overline{N}\,\overline{N}}\Big(Y_\chi^2 - Y_{\chi^*}^2 + P\left(Y_N^2 - Y_{\overline{N}}^2\right)\Big) + 2\langle\sigma v\rangle_{\chi N\to\chi^*\overline{N}}\Big(Y_\chi Y_N - Y_{\chi^*} Y_{\overline{N}}\Big) \\ & + \langle\sigma v\rangle_{N\bar{d}\to ud}\Big(Y_N Y_{\bar{d}}^{\rm eq} - Y_{\overline{N}} Y_d^{\rm eq} - Y_N^{\rm eq} Y_{\bar{d}}^{\rm eq} + Y_{\overline{N}}^{\rm eq} Y_d^{\rm eq}\Big) \\ & + \langle\sigma v\rangle_{N\bar{u}\to dd}\Big(Y_N Y_{\bar{u}}^{\rm eq} - Y_{\overline{N}} Y_u^{\rm eq} - Y_N^{\rm eq} Y_{\bar{u}}^{\rm eq} + Y_{\overline{N}}^{\rm eq} Y_u^{\rm eq}\Big) \\ & + \frac{1}{\mathfrak{s}}\langle\Gamma_N\rangle\Big(Y_N - Y_{\overline{N}} - Y_N^{\rm eq} + Y_{\overline{N}}^{\rm eq}\Big)\Bigg],\end{aligned} \tag{5.24}$$

where we have already made use of the fact that the cross sections related by charge conjugation are identical, see Eqs. (5.13), (5.15), (5.16) and (5.17). The yields Y_χ, Y_{χ^*}, Y_N and $Y_{\overline{N}}$ are implicit functions of the total yields and of the asymmetries.

Further, in the derivation of the above equations we have made the approximation

$$\frac{Y_\chi^{\rm eq} Y_N^{\rm eq}}{Y_{\chi^*}^{\rm eq} Y_{\overline{N}}^{\rm eq}} \simeq 1, \tag{5.25}$$

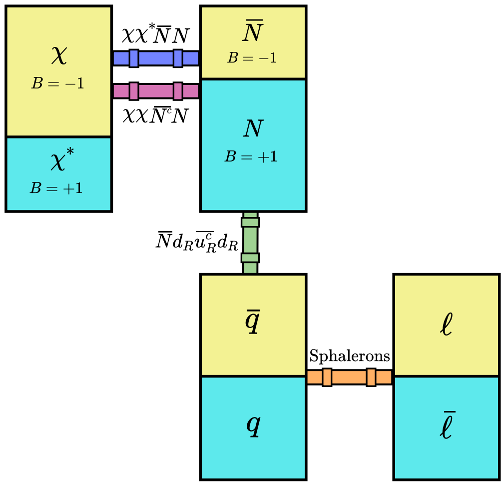

Fig. 5.4: Initial condition in our scenario, now including the standard model leptons. The baryon-number-charged particles and antiparticles in the dark and visible sectors are represented as boxes, with box size indicating particle abundance and color representing the sign of the baryonic charge. There is an equal but opposite asymmetry in the dark sector particles. The overall baryon number is zero.

and we have introduced the function P:

$$P \equiv \frac{Y_\chi^{\text{eq}} Y_{\chi^*}^{\text{eq}}}{Y_N^{\text{eq}} Y_{\overline{N}}^{\text{eq}}} \simeq \left(\frac{Y_\chi^{\text{eq}}}{Y_{\overline{N}}^{\text{eq}}}\right)^2 \simeq \left(\frac{Y_{\chi^*}^{\text{eq}}}{Y_N^{\text{eq}}}\right)^2 \simeq \left(\frac{g_\chi}{g_N}\right)^2 \left(\frac{m_\chi}{m_N}\right)^4 \left(\frac{K_2\left(m_\chi/T\right)}{K_2\left(m_N/T\right)}\right)^2. \tag{5.26}$$

Here, the dependence on the chemical potentials has been neglected. At high temperatures, this is justified by using the Maxwell-Boltzmann approximation, and at low temperatures, the chemical potentials of the χ and N particles are expected to be of the same order of magnitude, canceling out.

Additionally, we also write the Boltzmann equation for the asymmetry in the visible sector, affected by the scatterings and decays mediated by the neutron portal. The asymmetry between the total number of quarks and antiquarks, $\Delta q \equiv \sum_i \Delta q_i$, evolves as:

$$\frac{dY_{\Delta q}}{dx} = c\,\frac{3\lambda}{x^2}\Bigg[\frac{1}{\mathfrak{s}}\langle\Gamma_N\rangle\Big(Y_N - Y_{\overline{N}} - Y_N^{\text{eq}} + Y_{\overline{N}}^{\text{eq}}\Big) \tag{5.27}$$

$$+ \langle\sigma v\rangle_{N\bar{d}\to ud}\Big(Y_N Y_{\bar{d}}^{\text{eq}} - Y_{\overline{N}} Y_d^{\text{eq}} - Y_N^{\text{eq}} Y_{\bar{d}}^{\text{eq}} + Y_{\overline{N}}^{\text{eq}} Y_d^{\text{eq}}\Big)$$

$$+ \langle\sigma v\rangle_{N\bar{u}\to dd}\Big(Y_N Y_{\bar{u}}^{\text{eq}} - Y_{\overline{N}} Y_u^{\text{eq}} - Y_N^{\text{eq}} Y_{\bar{u}}^{\text{eq}} + Y_{\overline{N}}^{\text{eq}} Y_u^{\text{eq}}\Big)\Bigg]. \tag{5.28}$$

The constant c, introduced in Eq. (3.11), quantifies the efficiency of the conversion of the baryon asymmetry stored in the left-handed quarks into a lepton asymmetry stored

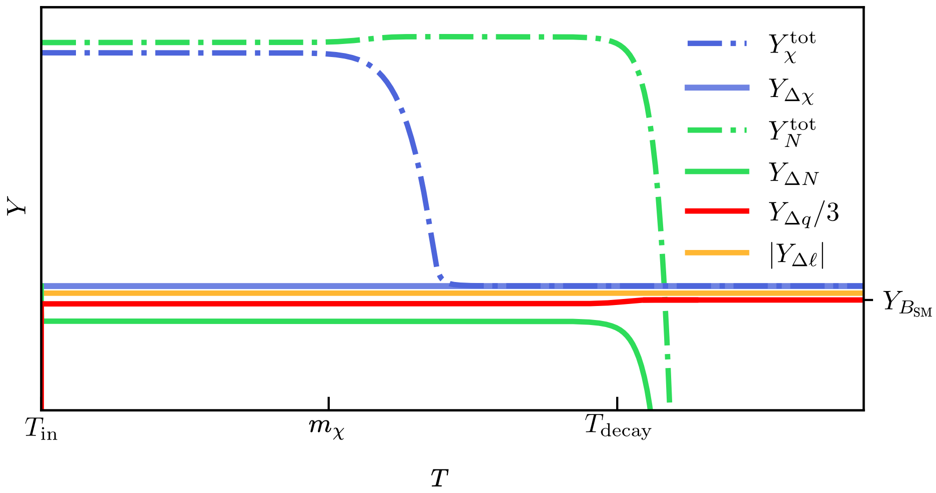

Fig. 5.5: Representative evolution of the total yields of $\chi + \chi^*$ and $N + \overline{N}$ (dash-dotted) and the yields of the different asymmetries between particles and antiparticles (solid) for the initial condition depicted in Fig. 5.4, as a function of decreasing temperature. See the main text for details.

in the left-handed leptons via sphaleron processes. The integration of this effect into the Boltzmann equations is derived in Appendix B.3. If the asymmetry in the dark sector is generated at temperatures above 130 GeV, before sphalerons drop out of thermal equilibrium [117], then $c = 12/37$ [120]. In turn, the asymmetry between the total number of leptons and antileptons, $\Delta\ell \equiv \sum_i \Delta\ell_i$ can be calculated from

$$\frac{dY_{\Delta\ell}}{dx} = -\frac{1}{3}\frac{1-c}{c}\frac{dY_{\Delta q}}{dx}. \tag{5.29}$$

If the initial asymmetry is instead generated after sphaleron freeze-out, then we set $c = 1$ and no asymmetry is transferred to the leptons.

The initial condition is sketched in Fig. 5.4. At the high temperature $T_{\rm in}$, all particle species are ultra-relativistic, so their equilibrium yields depend only on the internal degrees of freedom, see Eq. (A.7). For the particles in the hidden sector, this implies $Y_N^{\rm eq} = 2Y_\chi^{\rm eq}$. Additionally, the yields of the asymmetries satisfy

$$Y_{\Delta N}^{\rm in} = Y_{\Delta\chi}^{\rm in}, \tag{5.30}$$

$$Y_{\Delta q}^{\rm in} = Y_{\Delta\ell}^{\rm in} = 0. \tag{5.31}$$

With these ingredients, we can now numerically solve our system of Boltzmann equations for any chosen set of parameters. Fig. 5.5 presents a qualitative example of the solution. The total abundance of dark sector particles is shown with dashed lines, while the particle-antiparticle asymmetries for dark sector particles, quarks, and leptons are shown with solid lines. The scale Λ_2 is chosen large enough to avoid washout, and Λ_0 is set so that the asymmetric component of dark matter is completely depleted during freeze-out. The figure also illustrates how the asymmetry $Y_{\Delta N}$ is immediately redistributed into quarks and leptons. In the following sections, we provide a detailed explanation of the dynamics in each temperature regime.

5.2.2 Washout of the asymmetry

At temperatures close to $T_{\rm in}$, the processes $\chi\chi \leftrightarrow \overline{N}\overline{N}$ and $\chi N \leftrightarrow \chi^*\overline{N}$ (with rates depending on Λ_2) contribute to the washout of the asymmetry within the hidden sector, thereby influencing the size of the asymmetries transferred to the visible sector. Let us study quantitatively the effect of the washout processes.

The effect of the washout in $\Delta\chi$ follows from Eq. (5.22). We recall

$$\frac{dY_{\Delta\chi}}{dx} \simeq -\frac{\lambda}{x^2}\Bigg[2\langle\sigma v\rangle_{\chi\chi\to\overline{N}\overline{N}}\left(Y_\chi^2 - Y_{\chi^*}^2 + P\left(Y_N^2 - Y_{\overline{N}}^2\right)\right) + 2\langle\sigma v\rangle_{\chi N\to\chi^*\overline{N}}\left(Y_\chi Y_N - Y_{\chi^*}Y_{\overline{N}}\right)\Bigg]. \tag{5.32}$$

We can approximate now the yields of each particle and antiparticle i to first order in terms of their equilibrium values when the asymmetry is zero, $Y_{i,\,\rm eq}^{\mu=0}$, and their asymmetry, $Y_{\Delta i}$, for each temperature:

$$Y_\chi \simeq Y_{\chi,\,\rm eq}^{\mu=0} + \frac{Y_{\Delta\chi}}{2}, \qquad Y_{\chi^*} \simeq Y_{\chi,\,\rm eq}^{\mu=0} - \frac{Y_{\Delta\chi}}{2}, \tag{5.33}$$

$$Y_N \simeq Y_{N,\,\rm eq}^{\mu=0} + \frac{Y_{\Delta N}}{2}, \qquad Y_{\overline{N}} \simeq Y_{N,\,\rm eq}^{\mu=0} - \frac{Y_{\Delta N}}{2}. \tag{5.34}$$

At high temperatures, the function P, defined in Eq. (5.26), approximates well to $P \simeq 1/4$. The relation between the equilibrium yields is $Y_{N,\,\rm eq}^{\mu=0} = 2Y_{\chi,\,\rm eq}^{\mu=0}$. Assuming for simplicity $Y_{\Delta N} = Y_{\Delta\chi}$, which corresponds to neglecting the effect of the nuetron portal scatterings, we can arrive to the simple equation

$$\frac{dY_{\Delta\chi}}{dx} \simeq -\frac{6\lambda}{x^2}\left(\langle\sigma v\rangle_{\chi\chi\to\overline{N}\overline{N}} + \langle\sigma v\rangle_{\chi N\to\chi^*\overline{N}}\right) Y_{\chi,\,\rm eq}^{\mu=0}\, Y_{\Delta\chi}, \tag{5.35}$$

and similarly for $Y_{\Delta N}$. If we take into account the immediate redistribution of the asymmetries in ΔN and the quark sector due to the neutron portal being in equilibrium, then the relation $Y_{\Delta N} = Y_{\Delta\chi}$ no longer holds. Instead, if sphalerons are also active, we have $122Y_{\Delta N} = 11Y_{\Delta\chi}$, as will be explicitly derived in the next section and shown in Eq. (5.51). Then, Eq. (5.32) becomes

$$\frac{dY_{\Delta\chi}}{dx} \simeq -\frac{255\lambda}{61x^2}\left(\langle\sigma v\rangle_{\chi\chi\to\overline{N}\overline{N}} + \langle\sigma v\rangle_{\chi N\to\chi^*\overline{N}}\right) Y_{\chi,\,\rm eq}^{\mu=0}\, Y_{\Delta\chi}. \tag{5.36}$$

Additionally, if the neutron portal is in equilibrium but the shalerons are not at the time the asymmetry is generated, we use $31Y_{\Delta N} = 7Y_{\Delta\chi}$, derived in Appendix C.2, see

Eq. (C.36). The equation would then become

$$\frac{dY_{\Delta\chi}}{dx} \simeq -\frac{90\lambda}{7x^2}\left(\langle\sigma v\rangle_{\chi\chi\to\bar{N}\bar{N}} + \langle\sigma v\rangle_{\chi N\to\chi^*\bar{N}}\right) Y^{\mu=0}_{\chi,\,\mathrm{eq}}\, Y_{\Delta\chi}. \tag{5.37}$$

Taking the most realistic case where both the neutron portal and sphalerons are active at high temperatures, shown in Eq. (5.36), the analytical solution reads

$$Y_{\Delta\chi}(T) \simeq Y^{\mathrm{in}}_{\Delta\chi} \exp\left\{\frac{255}{61}\left[\frac{n^{\mu=0}_{\chi,\,\mathrm{eq}}}{H(T)}\left(\langle\sigma v\rangle_{\chi\chi\to\bar{N}\bar{N}} + \langle\sigma v\rangle_{\chi N\to\chi^*\bar{N}}\right)\right]\Bigg|_{T=T_{\mathrm{in}}} \frac{T-T_{\mathrm{in}}}{T_{\mathrm{in}}}\right\}. \tag{5.38}$$

Here, $n^{\mu=0}_{\chi,\,\mathrm{eq}}$ denotes the equilibrium number density of χ particles in the absence of an asymmetry. Finally, to further simplify this expression, we can make use of the following approximations for the averaged cross sections at high temperatures

$$\langle\sigma v\rangle_{\chi\chi\to\bar{N}\bar{N}} \simeq \frac{1}{8\pi{\Lambda_2}^2}, \tag{5.39}$$

$$\langle\sigma v\rangle_{\chi N\to\chi^*\bar{N}} \simeq \frac{1}{32\pi{\Lambda_2}^2}, \tag{5.40}$$

and write

$$Y_{\Delta\chi}(T) \simeq Y^{\mathrm{in}}_{\Delta\chi} \exp\left(\frac{1275}{1952\pi{\Lambda_2}^2}\frac{n^{\mu=0}_{\chi,\,\mathrm{eq}}}{H(T)}\frac{T-T_{\mathrm{in}}}{T_{\mathrm{in}}}\right). \tag{5.41}$$

In Fig. 5.6 we compare the numerically solved Boltzmann equations with the analytical expression from Eq. (5.41), for various values of Λ_2. Here, the initial condition $Y^{\mathrm{in}}_{\Delta\chi}$, at $T_{\mathrm{in}} = 10^5$ GeV, has been taken such that the asymmetry after washout matches the observed asymmetry $Y_{B_{\mathrm{SM}}}$. The figure shows that both solutions align with very good accuracy.

We can also estimate the scale Λ_2 at which efficient washout occurs for a given T_{in}. To efficiently erase the existing asymmetry, the erasing processes ($\chi\chi \to \bar{N}\bar{N}$ and $\chi N \to \chi^*\bar{N}$) must be slightly more efficient than its CP-conjugates ($\chi^*\chi^* \to NN$ and $\chi^*\bar{N} \to \chi N$). This difference in the rates arises from the difference in number densities between the initial states of such processes, rather than from differences in their cross sections. This requirement imposes the condition

$$\frac{\langle\Gamma\rangle_{\chi\chi\to\bar{N}\bar{N}} - \langle\Gamma\rangle_{\chi^*\chi^*\to NN}}{H} > \beta\, Y^{\mathrm{in}}_{\Delta\chi}, \tag{5.42}$$

where for simplicity we have only denoted the annihilations but also must take into account the scatterings. The factor β corresponds to the fraction of asymmetry erased. Using the relations

$$\langle\Gamma\rangle_{\chi\chi\to\bar{N}\bar{N}} = \langle\sigma v\rangle_{\chi\chi\to\bar{N}\bar{N}}\, n_\chi, \tag{5.43}$$

$$\langle\Gamma\rangle_{\chi^*\chi^*\to NN} = \langle\sigma v\rangle_{\chi^*\chi^*\to NN}\, n_{\chi^*}, \tag{5.44}$$

$$\langle\sigma v\rangle_{\chi\chi\to\bar{N}\bar{N}} \simeq \langle\sigma v\rangle_{\chi^*\chi^*\to NN}, \tag{5.45}$$

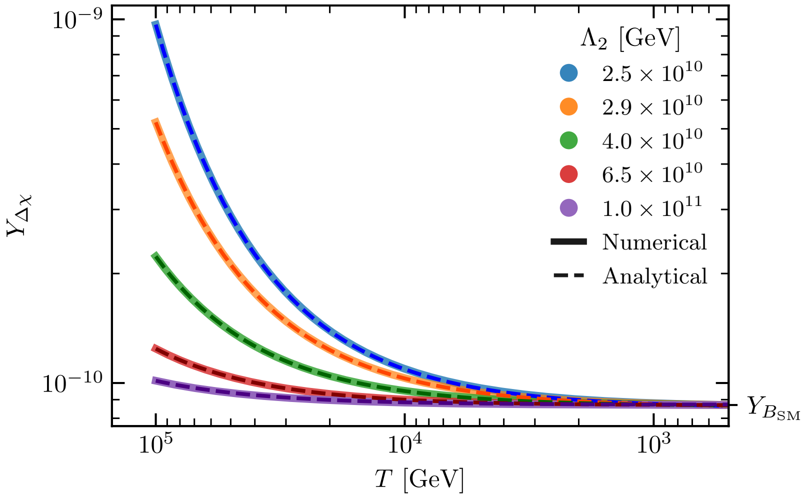

Fig. 5.6: Evolution of the abundance of the asymmetry $Y_{\Delta\chi}$ at high temperatures in the presence of washout, for different values of Λ_2. The initial condition $Y_{\Delta\chi}^{\rm in}$, at $T_{\rm in} = 10^5$ GeV, has been taken such that the asymmetry after washout matches the observed asymmetry $Y_{B_{\rm SM}}$. The solid lines correspond to the numerically solved Boltzmann equations, and the dashed lines to the analytical approximation from Eq. (5.41).

and analogously for the scatterings, we reach

$$\frac{\langle \sigma v \rangle_{\rm washout} \mathfrak{s}}{H} > \beta. \tag{5.46}$$

where $\langle \sigma v \rangle_{\rm washout} \equiv \langle \sigma v \rangle_{\chi\chi \to \bar{N}\bar{N}} + \langle \sigma v \rangle_{\chi N \to \chi^* \bar{N}}$. The requirement that no more than 50% of the asymmetry is washed out implies the lower limit

$$\Lambda_2 \gtrsim 6 \times 10^{10} \left(\frac{T_{\rm in}}{10^5 \text{ GeV}} \right)^{1/2} \text{ GeV}, \tag{5.47}$$

where we used the definitions in Eq. (A.16) for $\mathfrak{s}$ and in Eq. (B.10) for H.

In order to simplify our discussion, we will assume in what follows that Λ_2 satisfies this lower limit and that the initial asymmetry $Y_{\Delta\chi}$ (and $Y_{\Delta N}$) is very weakly washed out.

For a visual representation of the consequences of complete washout, see Fig. 5.7. In the left sketch, the asymmetry within the dark sector has been entirely washed out at high temperatures, and in the right we see what this would imply in the universe today: an absence of asymmetry in both the visible and dark sectors, and a negligible amount of quarks, which would have efficiently annihilated.

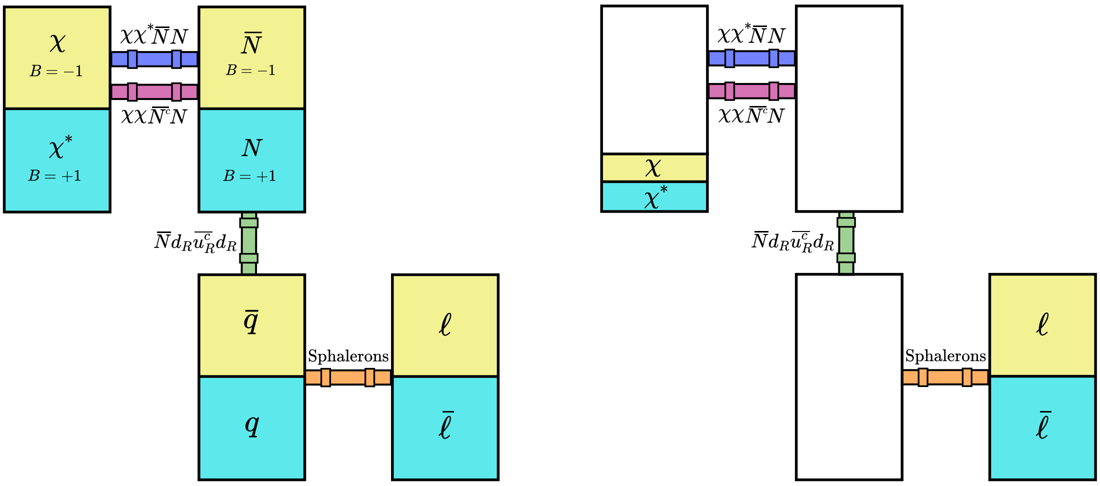

Fig. 5.7: Illustration of the effects of complete washout on the particle asymmetries of the dark sector. The left panel shows a universe where the initial asymmetry has been fully washed out. The right panel depicts the resulting universe today, with no remaining asymmetry in either the visible sector or the dark sector.

5.2.3 Redistribution of the asymmetry

As mentioned earlier, neutron portal scatterings, $N\bar{u} \leftrightarrow dd$ and $N\bar{d} \leftrightarrow ud$, are generally efficient at the temperatures where the asymmetry is generated, see Eq. (5.18). This implies that, at temperatures close to T_{in}, these scatterings effectively transfer a portion of the baryon asymmetry from the dark sector to the visible sector, which is then distributed between leptons and quarks via sphaleron transitions. In this section we will see exactly which fraction of asymmetry is transferred to each sector at high temperatures.

To determine the equilibrium relationships between the asymmetries $Y_{\Delta\chi}$, $Y_{\Delta N}$, $Y_{B_{\text{SM}}}$ and $Y_{L_{\text{SM}}}$, we will analyze the constraints imposed by the chemical potentials in chemical equilibrium. We consider the interactions mediated by the neutron portal, electroweak sphalerons, and all SM interactions, assuming that no washout takes place. For a complete derivation of the fractions presented in this section, go to Appendix C.2. Mo The neutron portal interaction, introduced in Eq. (5.3), involves only right-handed quarks and imposes the relation $\mu_N = 2\mu_{d_R} + \mu_{u_R}$. The SM quark interactions with the Higgs establish additional relations between right- and left-handed quarks. Finally, sphalerons impose relations between the chemical potentials of left-handed quarks and the left-handed leptons. Solving the system of equations and translating the chemical potentials to yields, we find

$$Y_{\Delta N} = \frac{11}{36}\frac{1}{3}Y_{\Delta q} = \frac{11}{36}Y_{B_{\text{SM}}}, \tag{5.48}$$

where $Y_{\Delta q}$ includes all the quarks. The relation that sphalerons impose between the

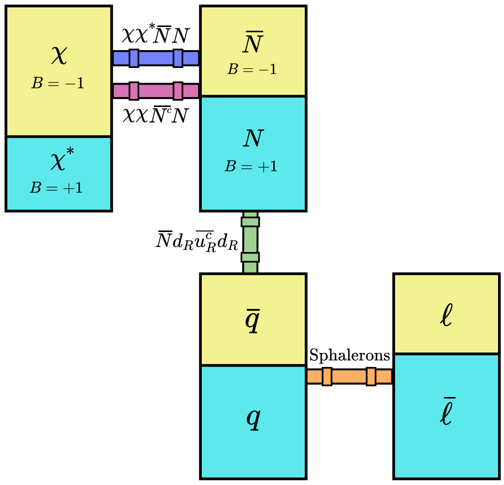

Fig. 5.8: Illustration of the redistribution of asymmetries at high temperatures between the dark and visible sectors, driven by neutron portal scatterings and electroweak sphaleron processes. Yellow represents negative $B-L$ and blue represents positive $B-L$. The total $B-L$ is conserved across the entire system.

baryon and lepton numbers in the SM is [120]

$$Y_{\Delta B} = -\frac{12}{25} Y_{L_{\rm SM}}. \tag{5.49}$$

Finally, the $B-L$ conservation across all species in our scenario implies that the initial asymmetry in N will be equal to the sum of the final baryon asymmetry in N and the quarks, minus the lepton asymmetry in the SM leptons

$$Y^{\rm in}_{\Delta N} = Y_{\Delta N} + Y_{B_{\rm SM}} - Y_{L_{\rm SM}}. \tag{5.50}$$

We can solve this system of three equations to obtain:

$$Y_{\Delta N}(T) = \frac{11}{122} Y^{\rm in}_{\Delta N}, \tag{5.51}$$

$$Y_{\Delta q}(T) = \frac{54}{61} Y^{\rm in}_{\Delta N}, \tag{5.52}$$

$$Y_{\Delta \ell}(T) = -\frac{75}{122} Y^{\rm in}_{\Delta N}, \tag{5.53}$$

which indicates the redistribution after the initial condition is set.[3] We see this redistribution in the numerically solved abundances in Fig. 5.5, and schematically in Fig. 5.8.

The fractions corresponding to the case where sphalerons are already inefficient by the time the asymmetry is generated are also shown in Appendix C.2.

[3] In reality, the sphaleron relation Eq. (5.49) changes slightly before and after electroweak symmetry breaking. The numbers shown correspond to the equilibrium relations after the phase transition, as these will be the ones that persist.

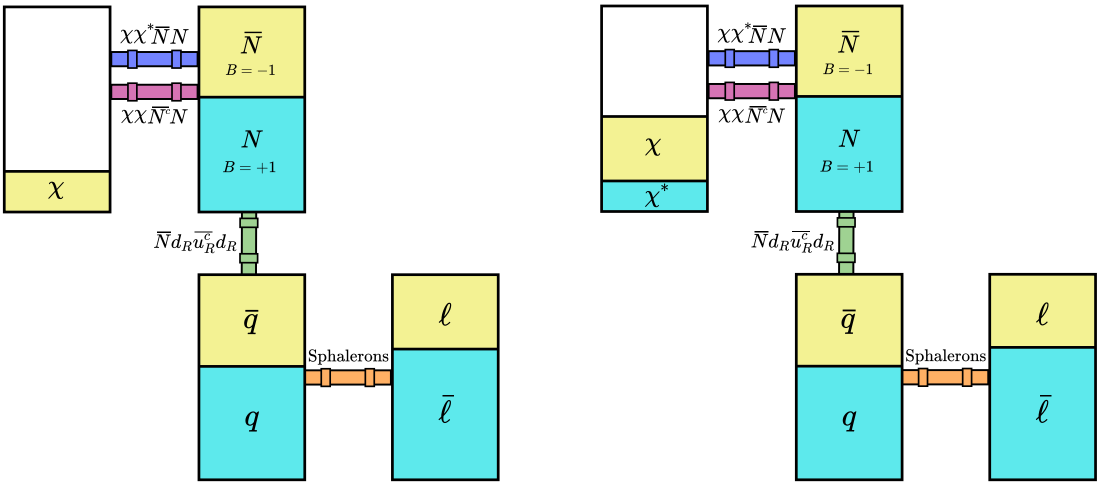

Fig. 5.9: Representation of the system after freeze-out. The left panel shows the scenario of complete annihilation of the asymmetric component, resulting in only dark matter particles. The right panel illustrates a partial depletion case, where some antiparticles also remain in addition to dark matter particles.

5.2.4 Freeze-out of dark matter

In this section, we explore the dynamics of dark matter freeze-out. We focus on the evolution of the total yields Y_χ^{tot} and Y_N^{tot}, given in Eqs. (5.21) and (5.23). For simplicity, we assume that Λ_2 satisfies the condition in Eq. (5.47) to prevent a total washout of the asymmetry.

Additionally, we assume $\Lambda_0 \ll \Lambda_n$, so that the conversion of N and $\overline{N}$ into quarks is slower than the conversion of χ and χ^* into N and $\overline{N}$. This implies that, when the main annihilation channel of dark matter is into N and $\overline{N}$, as we have been assuming, the dark matter abundance is determined by the process $\chi\chi^* \to N\overline{N}$. The Boltzmann equations (5.21) and (5.23) then simplify to

$$\frac{dY_\chi^{\text{tot}}}{dx} = -\frac{\lambda}{x^2}\left[2\langle\sigma v\rangle_{\chi\chi^*\to N\overline{N}}\left(Y_\chi Y_{\chi^*} - PY_N Y_{\overline{N}}\right)\right], \tag{5.54}$$

$$\frac{dY_N^{\text{tot}}}{dx} = -\frac{\lambda}{x^2}\left[-2\langle\sigma v\rangle_{\chi\chi^*\to N\overline{N}}\left(Y_\chi Y_{\chi^*} - PY_N Y_{\overline{N}}\right)\right]. \tag{5.55}$$

We can solve these equations numerically. The qualitative behavior of Y_χ^{tot} and Y_N^{tot} during freeze-out can be seen in Fig. 5.5. Additionally, Fig. 5.9 presents a schematic of the system after freeze-out: on the left, for the case of complete annihilation of the asymmetric component, where only dark matter particles remain; and on the right, for the case where depletion is less effective, leaving some antiparticles as well.

In Fig. 5.10, we compare the final yields of the particle χ for three different freeze-out scenarios, as a function of the scale Λ_0. In light blue, we show the standard asymmetric

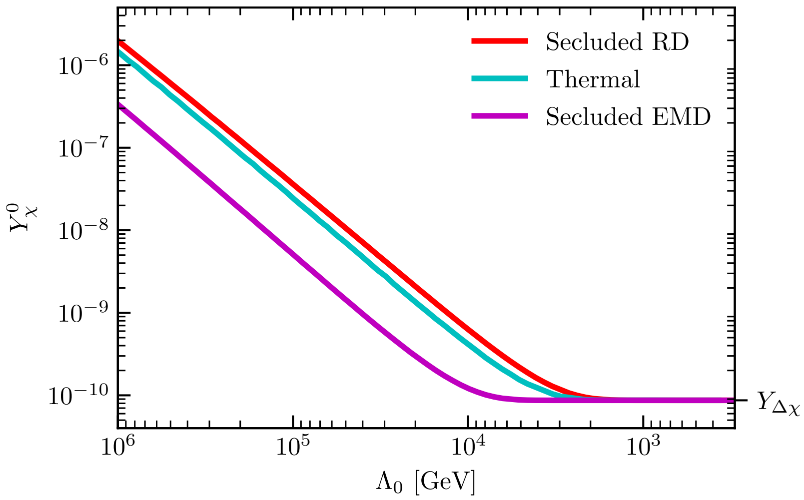

Fig. 5.10: Comparison of the final yields of the particle χ for different dark matter freeze-out scenarios, as a function of the scale Λ_0. The results come from solving numerically Eqs. (5.54) and (5.55) for a set of different assumptions. In light blue, the standard thermal scenario [108] is shown. In red, the freeze-out occurs in a secluded sector scenario during the radiation-dominated era. In pink, freeze-out takes place in a secluded sector scenario during an early matter-dominated era. For low values of Λ_0, all the antiparticles are effectively depleted and $Y_\chi^0 = Y_{\Delta\chi}$.

dark matter case, where the particles produced during dark matter freeze-out are in thermal equilibrium with the SM plasma. In this scenario, described in Ref. [108] and in Section 2.4.2, the freeze-out Eqs. (5.54) and (5.55) simplify to (2.10). This case applies when N and $\overline{N}$ are in thermal equilibrium with quarks at the time of dark matter freeze-out ($T \sim m_\chi$), or when dark matter annihilates directly into SM particles.

If the effective scale of the neutron portal is above $\Lambda_n \geq 4 \times 10^3$ GeV, N scatterings with quarks drop out of equilibrium before dark matter freeze-out, which, given the experimental constraints (see Section 6.2), is likely. Here, the scenario differs from a thermal freeze-out and resembles a secluded sector freeze-out, though with a hidden sector temperature identical to that of the visible sector. There are two possible situations: 1) freeze-out occurring during the usual radiation-dominated era, shown in red in Fig. 5.10, or 2) during an early matter-dominated era, shown in pink, where N and $\overline{N}$ become non-relativistic before decaying and dominate the energy density of the universe [180–182]. This early matter domination alters the universe's expansion rate, affecting freeze-out dynamics. For further details on early matter domination, see Section 6.2.2.1.

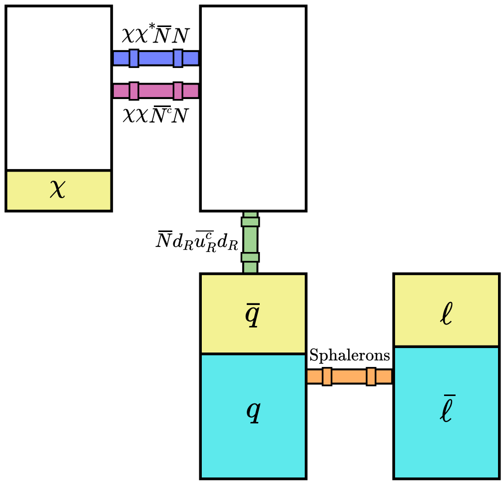

Fig. 5.11: Illustration of the system state after N and $\overline{N}$ decays are complete. Following the decays, the asymmetry from the N sector is fully transferred to the quarks in the visible sector, while the lepton asymmetry remains unchanged.

5.2.5 Decay of N and $\overline{N}$

At temperatures close to or below the mass of N, depending on the scale Λ_n, the particles N and $\overline{N}$ will decay through the neutron portal, disappearing from the thermal plasma. Fig. 5.11 illustrates the state of the system after the decays are complete.

These decays must occur before Big Bang Nucleosynthesis ($T_{\rm BBN} \sim 100$ KeV) to preserve the observed primordial element abundances, as discussed further in Section 6.2.2.1. If the decays occur before the QCD phase transition ($T_{\rm QCD} \sim 150$ MeV), the rate is given by Eq. (5.17), and the decay products will be quarks. However, if the decays occur after $T_{\rm QCD}$, they will proceed via a mass mixing term of the form $\delta m\, \bar{n}N$, as described later in Eq. (6.5).

After decaying away, all remaining asymmetry in the N sector is transferred to the quarks, while the asymmetry in the leptons remains unchanged. Since sphalerons are already out of equilibrium, there is no transfer between baryon and lepton asymmetries. Starting from Eqs. (5.51–5.53), we obtain the present-time asymmetries in the visible sector:

$$Y^0_{\Delta q} = 3\frac{11}{122}Y^{\rm in}_{\Delta N} + \frac{54}{61}Y^{\rm in}_{\Delta N} = \frac{141}{122}Y^{\rm in}_{\Delta N}, \tag{5.56}$$

$$Y^0_{\Delta\ell} = -\frac{75}{122}Y^{\rm in}_{\Delta N}. \tag{5.57}$$

Note that lepton asymmetries are significantly less constrained than baryon asymmetries [183–185]:

$$|\eta_L| \lesssim 4\times 10^{-3}, \tag{5.58}$$

so the size of the lepton asymmetry generated in our scenario is not a concern.

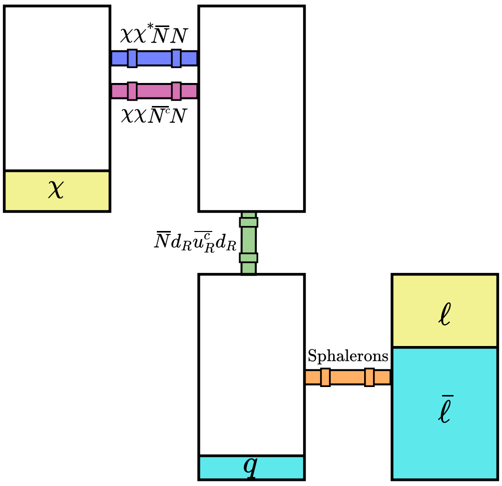

Fig. 5.12: Possible final states from the initial state Fig. 5.4, corresponding to a scenario where dark matter antiparticles have efficiently annihilated (left panel), or only partially annihilated (right panel). All N have decayed into quarks. We have assumed that the initial asymmetry within the dark sector is generated while sphalerons are still in thermal equilibrium. Today, most leptons are in the form of neutrinos and anti-neutrinos, with a small relative asymmetry, leaked via sphaleron processes. In both cases, the total $B-L$ number of the Universe is conserved and equal to zero.

5.2.6 Today

We now have all the necessary elements to link the dynamics of the early universe to present-day observations, allowing us to infer information about key parameters, such as the dark matter mass m_χ and the required initial asymmetry in the dark sector.

The total dark matter abundance today can be determined from measurements using standard analytical methods (see, for example, [186]), leading to

$$\Omega^0_{\mathrm{DM}}h^2 \simeq 2.8\times 10^8\, Y_\chi^{\mathrm{tot}}(x_{\mathrm{f.o.}})\frac{m_\chi}{\mathrm{GeV}}, \tag{5.59}$$

where the freeze-out temperature is determined by the condition $\Gamma_{\chi\chi^*\to N\overline{N}}(x_{\mathrm{f.o.}}) = H(x_{\mathrm{f.o.}})$, and $Y_\chi^{\mathrm{tot}}(x_{\mathrm{f.o.}})$ can be well approximated by its equilibrium value at freeze-out.

In the simplest scenario, all dark matter antiparticles annihilate, leading to the final state depicted in the left diagram of Fig. 5.12. In this case, the total yield of dark matter particles and antiparticles is equal to the dark matter asymmetry. Assuming no washout, this is also equal to the initial asymmetry:

$$Y_\chi^{\mathrm{tot}}(x_{\mathrm{f.o.}}) = Y_{\Delta\chi}(x_{\mathrm{f.o.}}) = Y^{\mathrm{in}}_{\Delta\chi} = Y^{\mathrm{in}}_{\Delta N}. \tag{5.60}$$

Thus, in this simple scenario, the dark matter abundance and the quark-antiquark asymmetry are both determined by the same parameter: the initial asymmetry in the dark sector, $Y^{\rm in}_{\Delta\chi}$ or $Y^{\rm in}_{\Delta N}$. Specifically, using Eqs. (5.56) and (5.59), we find the relation

$$\Omega^0_{\rm DM}h^2 \simeq 2.4\times 10^8\, Y_{\Delta q,0}\frac{m_\chi}{\rm GeV}\,. \tag{5.61}$$

One can then adjust the initial condition $Y^{\rm in}_{\Delta N}$ to generate the observed quark-antiquark asymmetry, $Y^0_{\Delta q}\simeq 2.6\times10^{-10}$, using Eq. (5.56). Additionally, the dark matter mass can be chosen to reproduce the observed dark matter abundance, $\Omega^0_{\rm DM}h^2 \simeq 0.12$, as per Eq. (5.61). This yields:[4]

$$Y^{\rm in}_{\Delta\chi} \simeq 2.3\times 10^{-10}, \tag{5.62}$$

$$m_\chi \simeq 1.9\,{\rm GeV}. \tag{5.63}$$

In the case where not all dark matter antiparticles annihilate, we have

$$Y^{\rm tot}_\chi(x_{\rm f.o.}) = Y_{\Delta\chi}(x_{\rm f.o.}) + 2Y_{\chi^*}(x_{\rm f.o.}), \tag{5.64}$$

and Eq. (5.61) must be replaced by

$$\Omega^0_{\rm DM}h^2 = 2.8\times 10^8\left(2Y_{\chi^*}(x_{\rm f.o.}) + \frac{122}{144}Y_{\Delta q,0}\right)\frac{m_\chi}{\rm GeV}\,. \tag{5.65}$$

This scenario is illustrated in the right diagram of Fig. 5.12. This does not change the initial asymmetry required to reproduce the quark-antiquark asymmetry, which remains as given by Eq. (5.62). However, because the total dark matter yield is larger, the observed dark matter abundance is achieved with a lower dark matter mass,

$$m_\chi\Big|_{Y_{\chi^*}(x_{\rm f.o.})\neq 0} = \frac{Y_{\Delta\chi}(x_{\rm f.o.})}{Y_{\Delta\chi}(x_{\rm f.o.}) + 2Y_{\chi^*}(x_{\rm f.o.})}\, m_\chi\Big|_{Y_{\chi^*}(x_{\rm f.o.})=0}\,. \tag{5.66}$$

Here, $Y_{\chi^*}(x_{\rm f.o.})$ can be determined by using Eq. (5.9) under the assumption of weak washout,

$$\frac{dY_{\chi^*}(x)}{dx} = -\frac{\lambda}{x^2}\langle\sigma v\rangle_{\chi\chi^*\to N\overline{N}}\Big[Y_{\chi^*}(x)\left(Y_{\chi^*}(x) + Y^{\rm in}_{\Delta\chi}\right) - 9\,P(x)\,Y_N Y_{\overline{N}}\Big]. \tag{5.67}$$

Now, assuming that χ, χ^* pairs can only annihilate into N, $\overline{N}$ pairs, after freeze-out, we can approximate the total yield of $N+\overline{N}$ particles after freeze-out as the sum of the equilibrium values of all dark sector particles before they become non-relativistic,

$$Y^{\rm tot}_N(x_{\rm f.o.}) \simeq Y^{\rm in}_{N,\,\rm eq} + Y^{\rm in}_{\overline{N},\,\rm eq} + Y^{\rm in}_{\chi,\,\rm eq} + Y^{\rm in}_{\chi^*,\,\rm eq}. \tag{5.68}$$

Using the relation $Y^{\rm in}_{N,\,\rm eq} = 2Y^{\rm in}_{\chi,\,\rm eq}$ coming from $g_N = 2g_\chi$, and neglecting the asymmetry $Y_{\Delta N}$ compared to the total abundance, we find $Y^{\rm tot}_N(x_{\rm f.o.}) \simeq 6Y^{\rm in}_{\chi,\,\rm eq}$ and therefore

$$Y_N(x_{\rm f.o.}) \simeq Y_{\overline{N}}(x_{\rm f.o.}) \simeq 3Y^{\rm in}_{\chi,\,\rm eq}. \tag{5.69}$$

[4] Note that the value provided for $Y^{\rm in}_{\Delta\chi}$ is expressed in terms of the corresponding yield that would be measured today. However, since the yield scales inversely with $g_{\star S}$, its value at high temperatures would be reduced by a factor of $g_{\star S}(T_{\rm today})/g_{\star S}(T_{\rm in}) \simeq 0.04$.

Since dark matter antiparticles are still in thermal equilibrium at freeze-out, we can approximate $Y_{\chi^*}(x_{\text{f.o.}}) = Y_{\chi^*}^{\text{eq}}(x_{\text{f.o.}})$. The yield at freeze-out, which remains practically constant until today, can then be obtained analytically by setting the right-hand side of Eq. (5.67) to zero. We obtain

$$Y_{\chi^*}(x_{\text{f.o.}}) \simeq \frac{-Y_{\Delta\chi}^{\text{in}}}{2} + \sqrt{\frac{\left(Y_{\Delta\chi}^{\text{in}}\right)^2}{4} + 9P(x_{\text{f.o.}})\left(Y_{\chi,\,\text{eq}}^{\text{in}}\right)^2}\,. \tag{5.70}$$

It is worth emphasizing that these conclusions are fairly robust against the specific values of the portal strengths Λ_2, Λ_0, and Λ_n, as long as (i) washout of the asymmetry is weak, (ii) Λ_n is low enough to keep the hidden sector thermalized with the visible sector at high temperatures, and (iii) $\Lambda_0 \ll \Lambda_n$, so that N remains stable over the freeze-out timescale. Alternative scenarios can be explored by adjusting the initial conditions in the Boltzmann equations. A key assumption in our model is the presence of a neutron portal to transfer the asymmetry from the dark sector to the visible sector. This neutron portal may lead to experimental signatures, which will be discussed in detail in the next section.

Chapter 6

Phenomenology

This chapter explores the experimental implications and the potential observational signatures of the dark matter model developed in the previous chapter. Through the different portal interactions between the dark and the visible sectors, dark sector particles could influence early-universe cosmology and might be detectable in collider experiments. We also consider the possibility of signals in direct detection experiments and even in neutron star observations.

6.1 Phenomenology of the Higgs portal

One possible way to detect the dark matter in our scenario is through a Higgs-type interaction term $\lambda_{\chi H}|\chi|^2|H|^2$, introduced in Eq. (5.4). This term is allowed by baryon number conservation and, therefore, could be present in the model. Potential signals from this interaction include invisible Higgs decays in collider experiments, recoil events in direct detection experiments, and indirect detection signals if a relic population of dark matter antiparticles exists (see right panel of Fig. 5.12).

The absence of observed events arising from the Higgs portal in collider and direct detection experiments allows us to place constraints on the coupling constant $\lambda_{\chi H}$ associated to this interaction term.

In our scenario, the predicted dark matter mass is $m_{\rm DM} \simeq 1.9$ GeV; therefore, the Higgs portal could induce the invisible decay of the Higgs into a dark matter particle-antiparticle pair, $h \to \chi\chi^*$. The decay rate for this decay is given by

$$\Gamma_{h\to\chi\chi^*} \simeq \frac{\lambda_{\chi H}^2 v^2}{32\pi m_h} \, , \tag{6.1}$$

where $v \simeq 246$ GeV is the Higgs vacuum expectation value and $m_h \simeq 125$ GeV is the Higgs mass. Current experimental searches constraint the Higgs branching ratio into invisible final states to $\mathrm{Br}\,(h \to \text{ invisible}) \lesssim 20\%$ [188,189]. Given that the Higgs width into visible particles is approximately $\Gamma_{\rm vis} \simeq 3.7$ MeV [17], this implies $\lambda_{\chi H} \lesssim 10^{-2}$ [187], as shown in Fig. 6.1.

The Higgs portal interaction also enables the scattering of dark matter particles off nuclei, which could be detected in direct detection experiments. The spin-independent

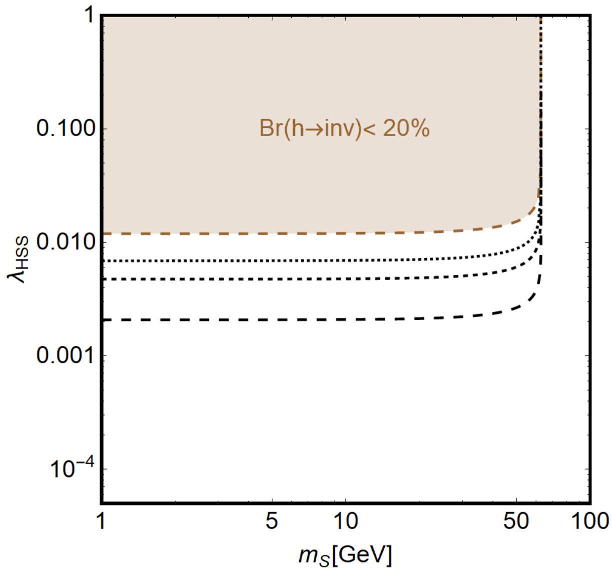

Fig. 6.1: Summary of constraints on the invisible Higgs branching ratio in the $(m_\chi, \lambda_{\chi H})$ plane for the Higgs portal dark matter scenario in the scalar case, from Ref. [187]. The brown area indicates the region excluded by the present limit $\mathrm{Br}(H \to \mathrm{inv}) < 20\%$ [188,189], while the black lines show projected sensitivities for branching ratios of 10%, 5% and 1%, respectively.

scattering cross section with a nucleon $\mathcal{N}$ reads [191, 192]

$$\sigma_{\chi\mathcal{N}\to\chi\mathcal{N}} \simeq \frac{\lambda_{\chi H}^2 f_{\mathcal{N}}^2}{\pi} \frac{\mu^2 m_{\mathcal{N}}^2}{m_h^4 m_\chi^2}, \tag{6.2}$$

where $\mu = m_{\mathcal{N}} m_\chi/(m_{\mathcal{N}} + m_\chi)$ is the dark matter-nucleon reduced mass, and $f_{\mathcal{N}} \approx 0.3$ is the Higgs-nucleon coupling [191]. For dark matter in the GeV mass range, the best current sensitivity is provided by the DarkSide-50 experiment [190], which excludes cross sections larger than $\sim 2 \times 10^{-42}$ cm^2 for a dark matter mass of 1.9 GeV, as shown in Fig. 6.2. This constraint translates to $\lambda_{\chi H} \lesssim 0.07$, which is less stringent than the limit from the invisible Higgs decay constraint.

In addition to these phenomenological constraints on the Higgs portal coupling, there is a theoretical constraint based on the naturalness of the dark matter mass. After electroweak symmetry breaking, the dark matter mass term receives an additional contribution:

$$\delta m_\chi^2 = \lambda_{\chi H} v^2. \tag{6.3}$$

With our favored value of $m_\chi \simeq 1.9$ GeV, this implies $\lambda_{\chi H} < 6 \times 10^{-5}$, unless there is a fine-tuned cancellation between the bare mass term in the Lagrangian and the mass contribution from electroweak symmetry breaking. This strong constraint would make detecting any Higgs portal-induced dark matter signal very challenging.

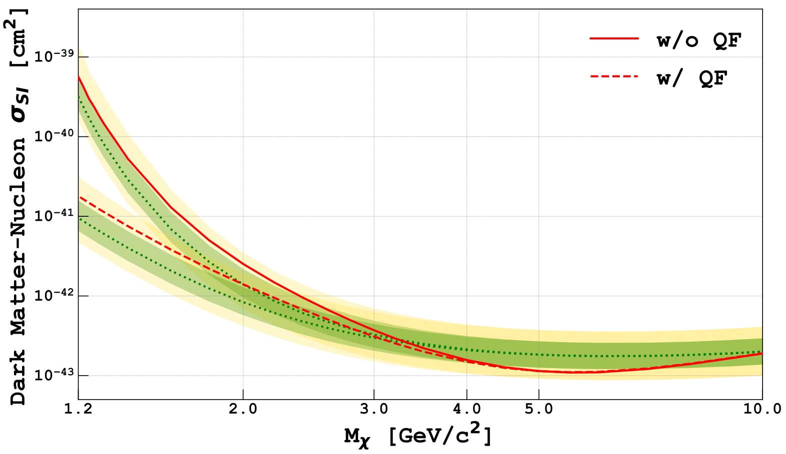

Fig. 6.2: 90% upper limits on spin-independent WIMP-nucleon cross sections from DarkSide-50 [190]. Both non-quenching and quenching fluctuations models are considered.

6.2 Phenomenology of the neutron portal

Another interaction linking the SM to the dark sector is the neutron portal, introduced in Eq. (5.3).

In the contemporary universe, at energies below the QCD confinement scale, quarks are no longer free but hadronize into nucleons and mesons. This hadronization causes the neutron portal term to induce a small mass mixing between the dark sector particles N, $\overline{N}$, and neutrons:

$$\mathcal{L}_{\text{eff}} \supset \delta m \left(\bar{n}N + n\overline{N}\right), \tag{6.4}$$

where δm is a model dependent mixing parameter with mass dimension one, expressed as $\delta m = \beta/\Lambda_n^2$ [193]. Here, $\beta = 0.014\ \text{GeV}^3$ is obtained from lattice QCD calculations [194], leading to

$$\delta m \simeq 1.4 \times 10^{-8} \left(\frac{10^3\ \text{GeV}}{\Lambda_n}\right)^2\ \text{GeV}. \tag{6.5}$$

Next, we examine the different experimental searches that might lead to a signal through the neutron portal interaction term.

6.2.1 Dark matter searches

The mass mixing induced by the neutron portal can mediate interactions between dark matter and nucleons via the intermediary particles N, $\overline{N}$. Here, we explore the various diagrams that contribute to the direct or indirect detection of dark matter in this scenario through such interactions. For an introduction to dark matter searches, see Section 2.3.

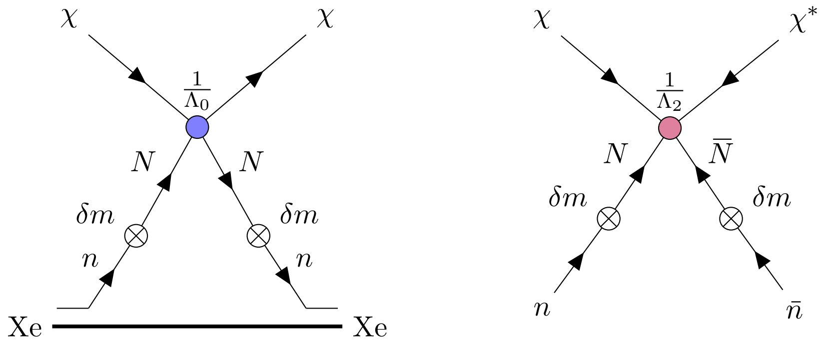

Fig. 6.3: Dark matter direct detection processes induced by the neutron portal: dark matter scattering off nuclei (left panel) and dark matter-induced transmutation of a neutron into an antineutron (right panel).

6.2.1.1 Direct detection

In direct detection searches, this type of interaction could result in the scattering of dark matter particles off neutrons or the transmutation of neutrons into antineutrons. These two possibilities are illustrated in Fig. 6.3.

In the diagram on the left, we see the scattering of dark matter particles off neutrons within the atoms of the detector material, such as Xenon, in the process $\chi n \to \chi n$. The neutrons mix with the particles N and $\overline{N}$ via the mass mixing in Eq. (6.5), represented in the diagram by a crossed dot. The interaction between N or $\overline{N}$ and the dark matter particles occurs through the first interaction term in Eq. (5.2), mediated by Λ_0.

This combination of interactions could also give rise to similar processes such as $\chi^* n \to \chi^* n$, $\chi \bar{n} \to \chi \bar{n}$, $\chi^* \bar{n} \to \chi^* \bar{n}$. However, these are heavily suppressed either due to the lack of dark matter antiparticles in the universe today (resulting from asymmetric freeze-out), the absence of antineutrons in nuclei, or both factors.

We can estimate the rate of dark matter scattering off neutrons in the rest frame within the EFT framework as[1]

$$\begin{aligned}\sigma_{\chi n \to \chi n} &\simeq \frac{1}{4\pi}\left(\frac{\delta m}{m_N}\right)^4 \frac{m_n^2}{(m_n+m_\chi)^2}\frac{1}{\Lambda_0{}^2} \\ &\simeq 10^{-61}\ \mathrm{cm}^2 \left(\frac{\mathrm{GeV}}{m_N}\right)^4 \left(\frac{\mathrm{GeV}}{\Lambda_0}\right)^2 \left(\frac{10^3\,\mathrm{GeV}}{\Lambda_n}\right)^8 ,\end{aligned} \tag{6.6}$$

where m_n is the mass of the neutron. The estimated cross section is many orders of magnitude below the current sensitivity of the DarkSide-50 experiment [190] which is approximately 10^{-42} cm^2 for a dark matter mass of 1.9 GeV, as shown in Fig. 6.2. It also lies below the sensitivity of any foreseeable dark matter direct detection experiment. Consequently, no signals from this type of scattering are expected.

[1] An $\mathcal{O}(1)$ rescaling factor is expected to convert the calculated scattering rate into an average dark matter-nucleon scattering cross section, which is the quantity typically reported by experiments.

In the right diagram of Fig. 6.3, we see another possible interaction that could produce a direct detection signal: $\chi n \to \chi^* \bar{n}$. This process would imply the transmutation of a neutron into an antineutron. Such an interaction could potentially destroy the nucleus, leading to a distinctive and highly specific signal.[2] This diagram combines the mass mixing term with the second interaction term in Eq. (5.2), which is mediated by Λ_2 and connects dark matter particles to N and $\overline{N}$.

Another possible process arising from this combination of interaction terms is $\chi^* \bar{n} \to \chi n$. However, this process is again further suppressed due to the lower abundance (or absence) of dark matter antiparticles in the universe today and the lack of antinuclei in direct detection experiments.

Unfortunately, the interaction $\chi n \to \chi^* \bar{n}$ is expected to be significantly more suppressed than the one mediated by Λ_0. This is because the scale Λ_2 must be very high to prevent asymmetry washout (see Section. 5.2.2). Analogously to Eq. (6.6), but substituting Λ_0 by Λ_2, we find

$$\begin{aligned}\sigma_{\chi n \to \chi^* \bar{n}} &\simeq \frac{1}{4\pi} \left(\frac{\delta m}{m_N}\right)^4 \frac{m_n^2}{(m_n + m_\chi)^2} \frac{1}{{\Lambda_2}^2} \\ &\simeq 10^{-83}\ \mathrm{cm}^2 \left(\frac{\mathrm{GeV}}{m_N}\right)^4 \left(\frac{10^{11}\,\mathrm{GeV}}{\Lambda_2}\right)^2 \left(\frac{10^3\,\mathrm{GeV}}{\Lambda_n}\right)^8, \end{aligned} \tag{6.7}$$

in terms of some benchmark values for m_N, Λ_2 and Λ_n. The normalization $\Lambda_2 = 10^{11}$ GeV represents a typical value at which the particle-antiparticle asymmetries are not significantly washed out, see Eq. (5.47).

The searches for neutron-antineutron oscillation at Super-Kamiokande [198] can be recast into a limit on the neutron-antineutron transmutation rate induced by dark matter particles in the Milky Way halo. To do this, we calculate the cross section $\sigma_{\chi n \to \chi^* \bar{n}}$ required to produce at least one event during the Super-Kamiokande exposure time. The exposure as of Ref. [198] was of 0.37 Megaton $\times$ years, and the mass of the detector 50 Megaton, which corresponds to a time of

$$t = \frac{0.37\,\mathrm{Megaton} \times \mathrm{years}}{\mathrm{Mass\,of\,detector}} \simeq 7.4\,\mathrm{years}. \tag{6.8}$$

The number of events will be given by

$$\Gamma_{\chi n \to \chi^* \bar{n}}\, N_\mathrm{T}\, t = \sigma_{\chi n \to \chi^* \bar{n}}\, n_\chi\, v_\chi\, N_\mathrm{T}\, t, \tag{6.9}$$

where $N_\mathrm{T} \approx 10^{34}$ is the total number of neutrons inside Super-Kamiokande, $n_\chi = 0.3\ (\mathrm{GeV}/m_\chi)\ \mathrm{cm}^{-3}$ is the ambient dark matter number density, and $v_\chi \approx 220\,\mathrm{km/s}$ is the typical velocity of the dark matter wind crossing Earth. By requiring at least one event, we estimate the necessary cross section to be $\sigma_{\chi n \to \chi^* \bar{n}} \lesssim 10^{-49}\,\mathrm{cm}^2$, which is significantly higher than the cross section predicted in our framework, given in Eq. (6.7).

[2] Previous works have considered similar effects in the context where N is the dark matter candidate [195–197].

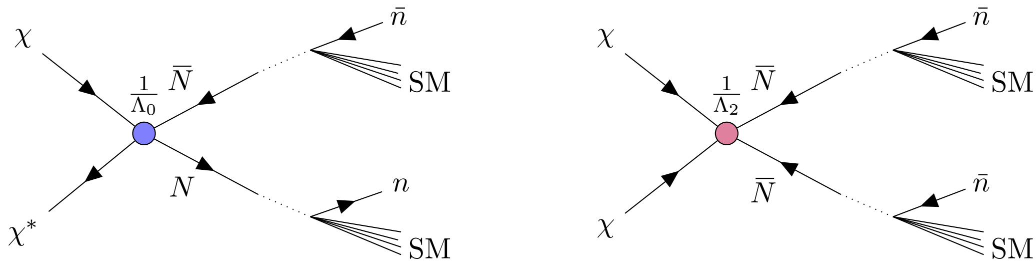

Fig. 6.4: Dark matter indirect detection processes induced by the neutron portal.

6.2.1.2 Indirect detection

For indirect detection searches, the relevant processes are illustrated in Fig. 6.4. On the right, we see processes arising from the interplay of the neutron portal term and the Λ_0 interaction. The prospects for indirect dark matter detection through this process depend heavily on whether the dark matter antiparticles were depleted during freeze-out, as the initial state involves one particle and one antiparticle of dark matter.

In the symmetric scenario, strong $\chi\chi^* \to N\overline{N}$ annihilations are expected, as χ is a light and thermal dark matter candidate. However, due to baryon number conservation, N must eventually decay into neutrons. The masses of the neutrons would account for a significant portion of the final state energy budget from the annihilation. Therefore, these decays would produce a soft cascade of hadrons and/or gamma rays with an energy $E_\gamma = m_N - m_n$. This gamma-ray signal could offer insights into the nature of dark matter and its connection to the neutron portal.

In the asymmetric case, the only available annihilation channel is $\chi\chi \to \overline{N}\overline{N}$, represented by the diagram on the right of Fig. 6.4. This process is highly suppressed in this framework due to the large effective scale Λ_2, making it unlikely to impose constraints on the model parameters. Nevertheless, it is notable that an asymmetric complex scalar dark matter candidate could still have an active direct annihilation channel today.

6.2.1.3 Neutron stars

Neutron star temperature observations have sparked growing interest as a potential dark matter detection strategy [99, 199–201]. The strong gravitational potential of neutron stars causes ambient dark matter particles to fall into them and become gravitationally bound [98]. During this process, dark matter particles scatter off the stellar matter, transferring some of their kinetic energy to the star. If dark matter is symmetric, particles and antiparticles can annihilate within the neutron star, releasing additional energy. This combined energy injection acts as a late-time heating mechanism, potentially observable as an increase in the neutron star's surface temperature, see Ref. [202].

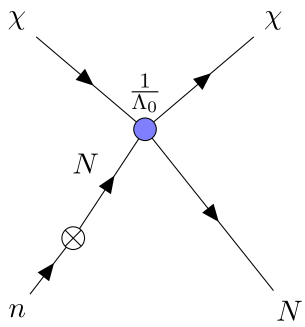

Fig. 6.5: Dark matter inelastic scattering process $\chi n \to \chi^* N$, which avoids Pauli blocking effects if present in neutron stars.

The Pauli exclusion principle from the degenerate neutrons is an important factor in studying dark matter capture in neutron stars [100], as it lowers the chances of scattering events between dark matter particles and the star's matter. This happens because the dense, degenerate matter in neutron stars limits the number of low-energy states available for scattered particles. Pauli blocking can be avoided by considering inelastic scattering processes. Typically, such processes have been explored in the context of inelastic dark matter capture in compact objects, see [203–207].

Our framework, however, introduces scatterings that are inelastic within the SM particles, $\chi n \to \chi^* \bar{n}$, as illustrated in the right diagram of Fig. 6.3. Here, the final-state particle is an antineutron rather than a neutron, which eliminates the issue of degenerate states and allows the interaction to occur. The rate of such interaction was estimated in Eq. (6.7). For comparison, the minimum cross section required for efficient dark matter trapping, equivalent to the geometric cross section of the star is

$$\sigma_{\rm th} = \pi R_\star^2 \frac{m_n}{M_\star} \simeq 10^{-45}\,{\rm cm}^2. \tag{6.10}$$

Unfortunately, the cross section of $\chi n \to \chi^* \bar{n}$ is significantly lower than this threshold, falling well below the sensitivity range of neutron stars. As a result, no meaningful constraints are expected from such processes.

Another possibility involves the process $\chi n \to \chi N$, illustrated in Fig. 6.5. In this case, dark matter scatters off a neutron in an inelastic manner, with the final state being a dark sector particle N instead of a neutron. This not only bypasses the Pauli blocking effect but is also less suppressed compared to the process $\chi n \to \chi^* \bar{n}$, as it depends on Λ_0 rather than Λ_2. Additionally, this process benefits from requiring only a single mass-mixing insertion, δm, making it more favorable than the left diagram in Fig. 6.3 considered for direct detection. The cross section of this process is

$$\sigma_{\chi n \to \chi N} \simeq 3 \times 10^{-46}\ {\rm cm}^2 \left(\frac{\rm GeV}{\Lambda_0}\right)^2 \left(\frac{10^3\,{\rm GeV}}{\Lambda_n}\right)^4, \tag{6.11}$$

which is close enough to the capture geometric cross section.

Inelastic scatterings from a lighter to a heavier state are generally kinematically forbidden in neutron stars unless the mass splitting is very small. Studies in the context of inelastic dark matter have determined a maximum mass splitting of $\Delta m_{\max} \sim 330$ MeV [206]. In the process $\chi n \to \chi N$ we can take $m_N \simeq m_n$ in order to have a smaller mass splitting. However, in the dense environment of a neutron star, medium effects, particularly the nuclear effective potential experienced by neutrons, can alter the effective mass of the neutron. In the inner region of the neutron star, the mass of the neutron is reduced by $m_n^{\rm eff} \simeq 0.6\, m_n^{\rm vac}$ [208]. This creates a substantial mass splitting between the initial neutron and the final state N, which prevents the interaction due to insufficient dark matter kinetic energy.[3]

6.2.2 Parameter space of the neutron portal

We now turn to the phenomenology of the dark sector particles N and their implications within our framework. These particles interact with the SM via the neutron portal, described in Eq. (5.3), and the mixing term generated below the QCD confinement scale, Eq. (6.5).

The particles N could influence the cosmological evolution of the universe and also be produced abundantly in collider experiments. Their mass is also subject to constraints from various physical considerations. We explore all these effects in this section. Fig. 6.6 illustrates the parameter space of the mass m_N and the neutron portal energy scale Λ_n, showing all relevant constraints. Excluded regions are shown in color, while the white area represents the allowed parameter space. Notably, the viable region can be constrained from all directions, with each boundary arising from distinct phenomenological effects.

6.2.2.1 Cosmology: early matter domination and Big Bang Nucleosynthesis

The particles N are long-lived and achieve equilibrium in the early universe through interactions with the SM thermal bath. Once the plasma temperature drops below their mass they stop being relativistic (radiation-like) and become non-relativistic (matter-like). If their lifetime is sufficiently long, they can eventually dominate the energy density of the universe, influencing its cosmological evolution.

When the particles N become non-relativistic, their energy density decreases more slowly compared to the radiation-dominated thermal plasma, whose energy density scales as T^4. If the energy density of N surpasses that of all radiation before they decay, these particles dominate the energy density of the universe, leading to an epoch of early matter domination (EMD). This phase alters the expansion rate of the universe, compared to the radiation-dominated era. The temperature at which this transition occurs, $T_{\rm dom}$, is determined by the condition $\rho_N \simeq \rho_r$. Using Eqs. (A.8) and (A.11),

[3] This effect is mitigated in the outer layers of the neutron star, where the effective mass of the neutron is closer to its vacuum mass. However, the smaller target volume counteracts the improvement in the capture rates.

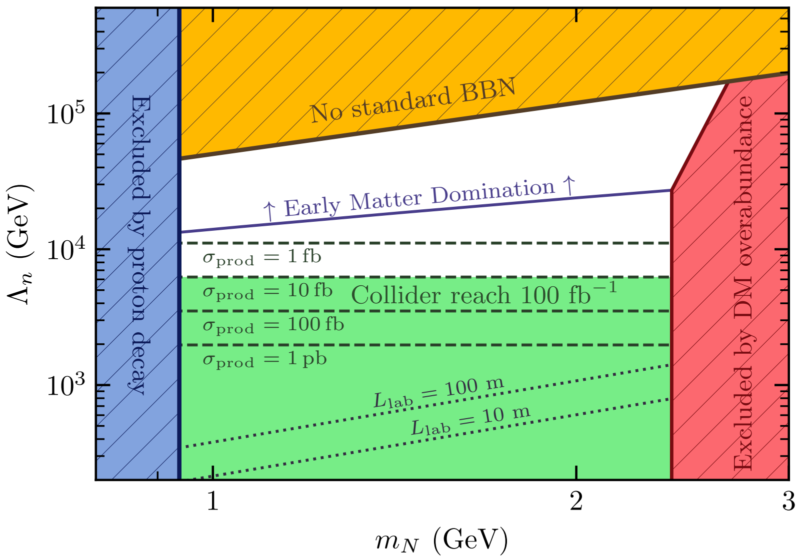

Fig. 6.6: Constraints on the neutron portal energy scale (Λ_n) and mass of N (m_N) from cosmology, proton stability, and collider experiments, along with contours of production cross section and decay length at the LHC with $\sqrt{s} = 14$ TeV. The allowed region is shown in white.

this conditon can be expressed as

$$g_N m_N \left(\frac{m_N T_{\rm dom}}{2\pi}\right)^{3/2} \simeq \frac{\pi^2}{30} g_\star(T_{\rm dom}) T_{\rm dom}^4, \tag{6.12}$$

where $g_\star(T_{\rm dom})$ represents the number of relativistic degrees of freedom at $T_{\rm dom}$ in the thermal plasma, defined in Eq. (A.12). The EMD era concludes when N decay at a temperature $T_{\rm reh}$, restoring the radiation-dominated universe that existed prior to their dominance. This decay process injects entropy into the thermal plasma, diluting all existing particle abundances and asymmetries. A similar scenario has been thoroughly explored in Refs. [182, 209].

From the moment the universe enters the matter-dominated phase, the expansion rate scales as [210]

$$H_{\rm EMD} = H_{\rm RD}(T_{\rm dom}) \left(\frac{g_\star(T)}{g_\star(T_{\rm dom})}\right)^{1/2} \left(\frac{T}{T_{\rm dom}}\right)^{3/2}, \tag{6.13}$$

where $H_{\rm RD}$ is the expansion rate during the radiation-dominated era, given in Eq. (B.10), and evaluated at the transition temperature $T_{\rm dom}$.

The condition for N and $\overline{N}$ to induce an epoch of EMD is given by

$$\Gamma_N < H_{\rm dom}, \tag{6.14}$$

where Γ_N is the decay rate of N, and $H_{\rm dom}$ is the Hubble rate at the time the universe transitions to matter domination. This condition ensures that the particles N do not decay before dominating the energy of the universe. The decay rate $N \to udd$ was provided in Eq. (5.17):

$$\Gamma_N = \frac{m_N^5}{768\pi^3 {\Lambda_n}^4}. \tag{6.15}$$

The condition in Eq. (6.14) imposes a lower bound on the energy scale Λ_n. This bound is shown as a purple line in Fig. 6.6. The parameter space above this line corresponds to scenarios where an EMD epoch would have occurred in the early universe.

As mentioned earlier, the EMD epoch also implies a later entropy injection, which dilutes all existing particle abundances and asymmetries. The degree of this dilution is quantified by a factor d, defined as

$$d \equiv \frac{\mathfrak{s}_{\rm after}}{\mathfrak{s}_{\rm before}}, \tag{6.16}$$

where $\mathfrak{s}_{\rm before}$ is the entropy density before the decay of N, and $\mathfrak{s}_{\rm after}$ is the entropy density after the N decays. Using Eq. (A.16) and Ref. [182] these are given by

$$\mathfrak{s}_{\rm before} = \frac{2\pi^2}{45} g_{\star S}(T_{\rm dom})\, T_{\rm dom}^3 \left(\frac{\Gamma_N}{H_{\rm dom}}\right)^2, \tag{6.17}$$

$$\mathfrak{s}_{\rm after} = \frac{2\pi^2}{45} g_{\star S}(T_{\rm reh})\, T_{\rm reh}^3. \tag{6.18}$$

These expressions account for the fact that the scale factor $a(t)$ evolves as $H^{-2/3}$ during the EMD epoch. The universe transitions back to a radiation-dominated phase when $\Gamma_N = H$, condition from which we can determine the reheating temperature:

$$T_{\rm reh} = \left(\frac{90}{\pi^2 g_\star(T_{\rm reh})}\right)^{1/4} \Big(\Gamma_N M_{\rm P}\Big)^{1/2}, \tag{6.19}$$

where $M_{\rm P}$ is the reduced Planck mass. Using of Eqs. (6.16)–(6.18) along with the expression for the temperature at the onset of matter domination, given by

$$T_{\rm dom} = \left(\frac{90}{\pi^2 g_\star(T_{\rm dom})}\right)^{1/4} \sqrt{H_{\rm dom}\, M_{\rm P}}, \tag{6.20}$$

which follows from the definition of the radiation-dominated expansion rate, we can express the dilution factor as

$$d = \left(\frac{g_\star(T_{\rm reh})}{g_\star(T_{\rm dom})}\right)^{1/4} \left(\frac{H_{\rm dom}}{\Gamma_N}\right)^{1/2}, \tag{6.21}$$

where we have used that $g_{\star S}(T) = g_\star(T)$ at these temperatures. In this regime, the dilution effect must be considered when selecting the initial asymmetry and the

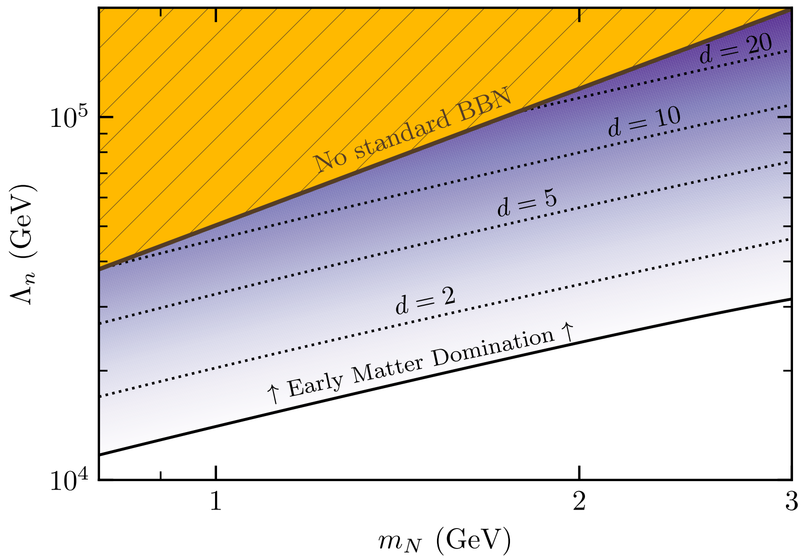

Fig. 6.7: Parameter space of the neutron portal in m_N versus Λ_n, highlighting the early matter domination domination (EMD) region. The purple solid line marks the boundary above which an EMD epoch is induced in the early universe. The dotted lines indicate benchmark values of the dilution factor ($d = 2, 5, 10, 20$). The orange hatched area above the brown solid line corresponds to parameter values excluded due to the excessive lifetime of the particle N, which conflicts with Big Bang Nucleosynthesis constraints.

parameter Λ_0 for freeze-out. The asymmetry and relic abundance should be rescaled by the factor d to account for the entropy injection during reheating. Fig. 6.7 illustrates the parameter space of the neutron portal, highlighting the EMD region along with benchmark values for the dilution factor.

Big Bang Nucleosynthesis (BBN) provides precise measurements of light element abundances. See Refs. [185, 211, 212] for reviews on the topic. To avoid disrupting the synthesis of light elements, which are highly sensitive to the universe's thermal and expansion history, the decay of N must be completed before the onset of BBN. This requires the condition

$$\Gamma_N \gtrsim H_{\rm BBN} \sim 10\,{\rm s}^{-1}, \tag{6.22}$$

or equivalently, in terms of the mean lifetime

$$\tau_N = \frac{1}{\Gamma_N} \sim 0.1\,{\rm s}. \tag{6.23}$$

The condition $\tau_N \lesssim 0.1$ s ensures that N decays well before the typical cosmic time for the onset of BBN ($t_{\rm BBN} \sim 1$ s). This allows the universe to transition back to a radiation-dominated phase and for thermal equilibrium to be restored in the thermal plasma.

Additionally, the reheating temperature following the decay of N, $T_{\rm reh}$, must exceed $T_{\rm BBN} \simeq 3$ MeV. Ensuring that the reheating temperature is high enough to restore standard thermal equilibrium, places further constraints on the decay rate through Eq. (6.19) and, consequently, on Λ_n.

Both these conditions contribute to the upper bound on Λ_n, represented by the brown line in Fig. 6.6, which defines the excluded orange hatched region. Values above this line imply that the particle N decays too late, disrupting primordial nucleosynthesis and making it inconsistent with observational data.

6.2.2.2 Constraints on m_N by baryon decays

Direct constraints on the mass of N are also present in the model. Firstly, m_N is constrained from below by exotic decays of baryons.[4] The most stringent requirement is that N must be heavier than the proton. If N were lighter than the proton, processes like $p \to N e^+ \nu_e$ would become kinematically allowed. Since this decay conserves both baryon and lepton numbers in our scenario, it would lead to observable proton decay at rates incompatible with experimental limits. Proton decay is extremely tightly constrained, with a current experimental lower limit on the proton lifetime of

$$\tau_p > 0.96 \times 10^{30}\,\text{years} \qquad 90\%\,\text{C.L.}, \tag{6.24}$$

as set by the SNO+ collaboration for invisible decay modes [214].[5] This constraint imposes $m_N \geq 938$ MeV.

Similarly, the mass of N must also be greater than that of the neutron. The neutron lifetime is also highly constrained, although slightly less than the proton. For bound neutrons undergoing invisible decay, the SNO+ collaboration has set a limit of

$$\tau_n > 0.9 \times 10^{30}\,\text{years} \qquad 90\%\,\text{C.L.}, \tag{6.25}$$

as reported in [214]. This requirement imposes then $m_N \geq 940$ MeV [17].

These limits are represented in Fig. 6.6 by the hatched blue area labeled "excluded by proton decay". While these mass constraints could, in principle, be avoided if the decay width were significantly suppressed by a large Λ_n, such scenarios are in tension with BBN.[6] As a result, this relaxation is not considered in the figure.

Constraints can also be derived from the decays of heavier baryons or mesons. Since these particles have higher masses than protons or neutrons, their decay involving N would reach higher masses. However, due to their much lower abundance, the lifetime of these heavier particles is much less constrained than those of the proton and neutron. Therefore, their bounds will relax significantly for lower values of Λ_n, overlapping with the regions excluded by experiments.

[4] Other scenarios that link dark matter and baryogenesis can also generate similar exotic decays of baryons [213].

[5] The proton decay in our scenario would produce visible particles, such as the positron. However, the constraints on $p \to e^+ +$ anything, as well as other specific decay channels, set limits of comparable order of magnitude [17], which does not affect the conclusions.

[6] In Ref. [215] they explore this scenario in a UV complete realization.

6.2.2.3 Constraints on m_N by freeze-out dynamics

In the scenario under consideration, dark matter particles χ and χ^* acquire a thermal abundance in the early universe by reaching thermal equilibrium with the SM. This occurs through interactions with N and $\bar{N}$ ($\chi\chi^* \leftrightarrow N\bar{N}$), which themselves remain in thermal equilibrium with SM quarks via the neutron portal.

Because the thermal abundance of dark matter would far exceed the observed relic density today, these particles must be depleted before the present time. The standard mechanism for this depletion is the freeze-out paradigm. If the freeze-out occurs through pair annihilation into N, specifically $\chi\chi^* \leftrightarrow N\bar{N}$, there exists a kinematic upper limit on the mass m_N. This limit ensures that the annihilation remains efficient enough to reduce the dark matter abundance to its observed value.

If the mass of the final-state particles is less than or equal to that of the initial states ($2m_\chi \geq 2m_N$), the interaction is kinematically allowed and can occur even at zero temperature. However, when the final-state particles are slightly heavier than the dark matter ($2m_\chi < 2m_N$), such annihilation processes become kinematically suppressed at zero temperature. Nevertheless, these processes can still have a significant cross section at finite temperature in the early universe due to the presence of sufficiently energetic dark matter particles in the high-energy tail of the Maxwell-Boltzmann distribution. These interactions are known as "forbidden channels", and freeze-out in such scenarios has been extensively studied in [216, 217].

The thermally averaged annihilation cross section in a forbidden channel is approximately given by [217]

$$\langle\sigma v\rangle_{\chi\chi^*\to N\bar{N}} \approx 8\pi f(\Delta)\langle\sigma v\rangle_{N\bar{N}\to\chi\chi^*}e^{-2\Delta x}, \tag{6.26}$$

where $\Delta \equiv (m_N - m_\chi)/m_\chi$ is the relative mass splitting, $x \equiv m_\chi/T$ and $f(\Delta)$ is a function of Δ defined as

$$f(\Delta) \equiv \frac{\Delta^{2/3}(2+\Delta)^{2/3}\left[2+\Delta(2+\Delta)\right]}{(1+\Delta)^4}, \tag{6.27}$$

which simplifies to $f(\Delta) \approx 1 + \Delta$ for $\Delta \gg 1$. In Eq. (6.26), the Boltzmann suppression of the dark matter annihilation cross section is explicit. This suppression arises from the equilibrium number density of non-relativistic species, as given by Eq. (A.8).

An upper limit on m_N can be derived to ensure that dark matter overproduction is avoided, for the largest possible value of the annihilation cross section. The s-wave unitarity requirement leads to a largest value of

$$\langle\sigma v\rangle_{N\bar{N}\to\chi\chi^*} \leq \frac{4\pi}{m_N^2}\left(\frac{x_{\text{f.o.}}}{\pi}\right)^{1/2}, \tag{6.28}$$

where $x_{\text{f.o.}} \simeq 30$ corresponds to the freeze-out temperature. Substituting this bound into Eq. (6.26) and ensuring that $\langle\sigma v\rangle_{\chi\chi^*\to N\bar{N}}$ is sufficient to deplete dark matter, we obtain, for $m_\chi = 1.9$ GeV,

$$m_N \lesssim 2.7\,\text{GeV}. \tag{6.29}$$

Moreover, from the milder requirement that the effective field theory remains valid, which corresponds to $\Lambda_0 \sim m_\chi$ in $\langle\sigma v\rangle_{N\bar{N}\to\chi\chi^*}$, we obtain

$$m_N \lesssim 2.4\,\mathrm{GeV}. \tag{6.30}$$

This limit has also been computed numerically using the Boltzmann equation formalism, and is shown in Fig. 6.6 as the hatched red area.

The relaxation of the constraint at large Λ_n values arises because the freeze-out of dark matter occurs during an epoch of early matter domination. In this case, the total annihilation cross section required to achieve the correct dark matter relic abundance is smaller compared to the standard WIMP paradigm, as discussed in [218]. Consequently, the mass of N can reach slightly higher values.

Notably, if the primary annihilation channel for dark matter freeze-out is not into N and $\bar{N}$, then the upper limit on m_N is no longer applicable. In this case, N could have an arbitrarily large mass without impacting the dark matter relic abundance.

6.2.2.4 Colliders

We now turn to the study of signatures and constraints from colliders that arise from the presence of the neutron portal.

The neutron portal leads to the copious production of particles N in proton-proton collisions via quark-quark partonic processes such as $ud \to N\bar{d}$ and $dd \to N\bar{u}$. The production cross section for these processes, within the EFT framework, is expressed as a function of the neutron portal energy scale Λ_n:

$$\sigma_{pp\to N+\mathrm{jet}} \approx 2\,\mathrm{fb}\left(\frac{f_{\mathrm{PDF}}}{10^{-2}}\right)\left(\frac{\sqrt{s}}{14\,\mathrm{TeV}}\right)^2\left(\frac{10^4\,\mathrm{GeV}}{\Lambda_n}\right)^4, \tag{6.31}$$

where $f_{\mathrm{PDF}} \approx 10^{-2}$ accounts for the effects of the partonic distribution functions (PDF) in the protons, as estimated using [219].

The energy scale Λ_n and the mass m_N determine the lifetime of N. From Eq. (6.15), we have

$$\tau_N = \frac{1}{\Gamma_N} \simeq \frac{768\pi^3{\Lambda_n}^4}{m_N^5}. \tag{6.32}$$

The collider signal of N depends on its lifetime, which determines the decay length. If the decay length is microscopic, N will decay promptly, producing dijets directly at the collision point. For a macroscopic decay length within the detector volume, N will decay at a displaced vertex, resulting in dijets originating from a point offset from the primary collision. If the decay length is larger than the detector size, N will escape without decaying, leading to a signature of missing transverse momentum (p_{T}).

The most likely scenario corresponds to the case where N escapes the detector before decaying. In Fig. 6.6, we illustrate this by showing dotted lines corresponding to decay lengths of $L_{\mathrm{lab}} = 100$ m and $L_{\mathrm{lab}} = 10$ m. For comparison, the ATLAS detector at CERN is 46 m in length and 25 m in diameter, and the CMS detector is 21 m in length

Fig. 6.8: On the left, monojet plus missing energy diagram generated by the neutron portal in EFT in proton proton collisions. On the right, monojet plus missing energy usual search strategy in proton proton collisions, where the jet is radiated from one of the initial states.

and 15 m in diameter. The decay length $L_{\mathrm{lab}} = v\gamma\tau_N = \beta\gamma c\tau_N$ is calculated using a Lorentz factor γ:

$$\gamma = \frac{\sqrt{\hat{s}}}{2m_N}, \tag{6.33}$$

where the partonic center-of-mass energy is taken to be $\sqrt{\hat{s}} \sim 2$ TeV.

In Fig. 6.6, we also indicate the values of Λ_n corresponding to production cross section $\sigma_{pp\to N+\mathrm{jet}} = 1$ fb, 10 fb, 100 fb and 1 pb, calculated using the expression in Eq. (6.31). These lines provide a direct comparison between the neutron portal energy scale and the predicted production rates for N at colliders, highlighting the regions of parameter space accessible to experiments.

The green region in the plot represents the values of Λ_n that can be probed at the LHC with an integrated luminosity of $\mathcal{L} = 100$ fb^{-1}. This corresponds to effective interactions with a strength of $\Lambda_n \lesssim 6$ TeV. Luminosity is a measure of a particle accelerator's capability to produce a specific number of interactions. The relation between the instantaneous luminosity L, the number of events per unit time dN/dt, and the cross section of the process σ is given by

$$\frac{dN}{dt} = L \cdot \sigma. \tag{6.34}$$

The integrated luminosity $\mathcal{L}$, obtained by integrating L over time, gives the total number of events N for a given cross section σ after a certain period of time:

$$N = \mathcal{L} \cdot \sigma. \tag{6.35}$$

Experimental results always include the integrated luminosity achieved, as it provides a process-independent measure of the collected data. For an integrated luminosity of $\mathcal{L} = 100$ fb^{-1}, achievable with current LHC experiments, we used Eq. (6.35) to calculate the green area in Fig. 6.6. We required $N = 1000$ events, which we assume is sufficient for a clear signal. This corresponds to a production cross section of 10 fb.

Existing searches have placed constraints on the EFT scale for interactions resulting in monojet plus missing energy signatures. For instance, the CMS collaboration has set a limit of $\Lambda_n \sim 436$ GeV [220]. However, these searches typically rely on the radiative emission of a jet from one of the initial states, as illustrated in the right diagram of

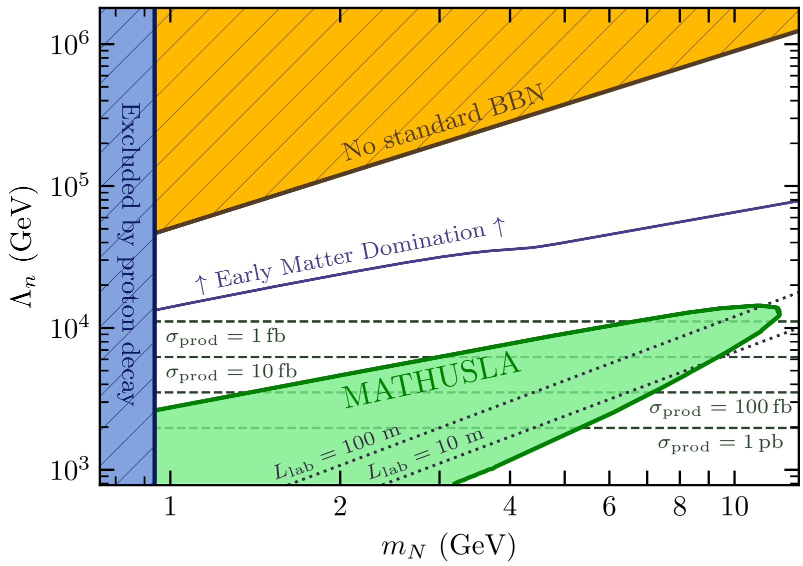

Fig. 6.9: Projected sensitivity of the proposed MATHUSLA detector to the particles N and $\overline{N}$ in the parameter space. The green region represents the reach of MATHUSLA, recast from [222]. Constraints from overabundance are not included here, as they are not present for scenarios where dark matter does not primarily freeze out into N and $\overline{N}$.

Fig. 6.8. In contrast, the process considered in this scenario corresponds to the one shown in the left diagram. Consequently, a dedicated study of this interaction would improve the current limits on the neutron portal effective scale.

We note, however, that for small values of Λ_n, the effective field theory description becomes invalid at LHC energies. In such cases, a dedicated search for the new particles mediating the neutron portal is required. This topic will be addressed in detail in Section 7.2, where we consider the UV completion of the neutron portal.

The MATHUSLA experiment could play a crucial role in probing the particle N. MATHUSLA [221,222] (Massive Timing Hodoscope for Ultra-Stable NeutraL pArticles) is a proposed detector at the LHC specifically designed to search for long-lived particles. Located above the CMS detector, MATHUSLA is optimized to detect such particles via their displaced decay signatures in a low-background environment. This makes it exceptionally well-suited for detecting N particles, which are expected to have long lifetimes and decay outside the main LHC detectors. In Fig. 6.9, we present the expected sensitivity of MATHUSLA to these particles in the parameter space, shown in green, by recasting the region given in Ref. [222], using Eqs. (6.31)–(6.33). This shows MATHUSLA's potential to explore a broad range of energy scales and masses relevant to our model. Overabundance constraints on m_N are not shown in this figure, as these limits only apply when dark matter freezes out primarily into N and $\overline{N}$. Here, we also consider regions where m_N is larger, expanding the scope of the analysis.

Finally, note that collider constraints become weaker if the portal between the dark sector and the visible sector involves second or third generation quarks, such as $\overline{N} s_R \overline{c_R^c} s_R$ or $\overline{N} b_R \overline{u_R^c} b_R$ instead of $\overline{N} d_R \overline{u_R^c} d_R$. This is because processes involving sea quarks are suppressed by their smaller partonic distribution functions within the proton, leading to reduced production rates at colliders. However, this variant of the portal could instead be probed through the decays of heavy mesons and baryons in charm and B factories such as BESIII, BElle II and LHCb [223].

Chapter 7

UV completion

In this chapter, we present a UV completion for the effective model outlined in Chapters 5 and 6, providing possible sets of matching parameters for the effective energy scales introduced in the Lagrangian terms of Eqs. (5.2) and (5.3). Section 7.1 introduces a leptogenesis-like mechanism for generating the initial asymmetry in the dark sector, highlighting its key features and identifying the viable parameter space. In Section 7.2, we develop the UV completion for the neutron portal, analyze its phenomenology, and discuss collider constraints. Finally, Section 7.3 explores mechanisms for dark matter freeze-out, including the introduction of a light dark scalar, which expands the allowed parameter space of the neutron portal and may remain as a hot subcomponent of dark matter today.

7.1 Asymmetry generation

In this section, we explore one possible mechanism for generating an asymmetry between particles and antiparticles in the χ and N sectors, which we have taken as an initial condition in the previous sections (see Fig. 5.4). Various frameworks can lead to the generation of an asymmetry in a dark sector, including those inspired by thermal leptogenesis, which we focus on here. A general discussion on alternative models for asymmetry generation in the context of asymmetric dark matter can be found in Section 4.2.2. For a general introduction to thermal leptogenesis, we refer the reader to Section 3.4.2.

We introduce two heavy Majorana fermions, φ_i $(i = 1, 2)$, which do not carry baryon number. The relevant Lagrangian terms governing their dynamics are given by

$$\mathcal{L} \supset i\overline{\varphi_i}\partial\!\!\!/\varphi_i - \frac{M_i}{2}\overline{\varphi_i^c}\varphi_i - (\lambda_i\overline{\varphi_i}N\chi + h.c)\,, \tag{7.1}$$

where the first term accounts for the kinetic term, the second represents the Majorana mass, and the term corresponds to the interaction with the dark sector particles. These interactions allow the heavy fermions to decay into final states with zero baryon number, specifically χ and N or their conjugate states χ^* and $\overline{N}$. The tree-level decay processes are illustrated in Fig. 7.1.

At one-loop level, the interference between the tree-level decays and the loop diagrams shown in Fig. 7.2 leads to CP violation, thereby generating an asymmetry in both χ and

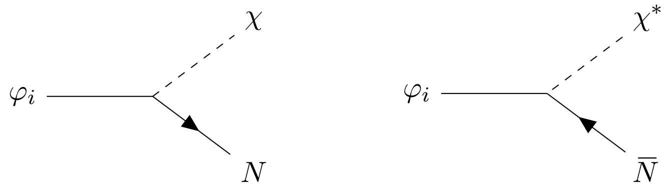

Fig. 7.1: Tree-level decays of the heavy majorana fermions φ_i.

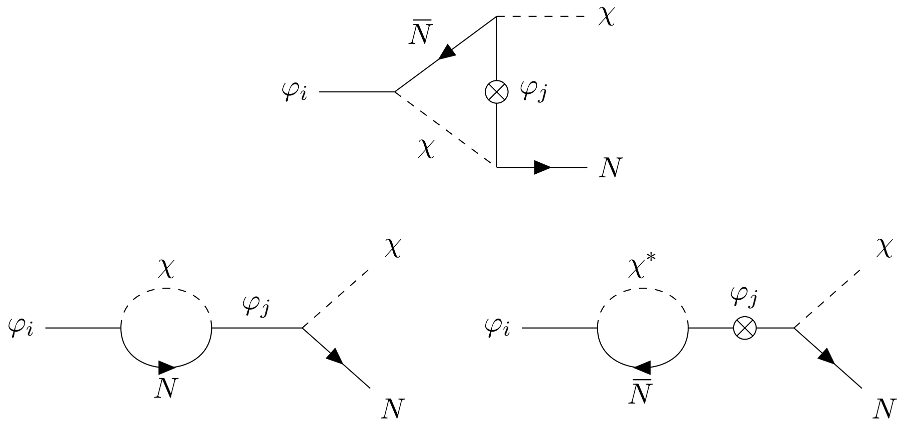

Fig. 7.2: One-loop contributions to the tree-level decay $\varphi_i \to \chi N$. The diagram above corresponds to the so-called vertex diagram, and the ones below correspond to the wave function diagrams.

N. Unlike in standard leptogenesis, where lepton number (L) is explicitly violated in decays, here the dark-sector asymmetry is generated without violating baryon number (B). Additionally, unlike traditional leptogenesis, where sphaleron processes transfer the generated lepton asymmetry into a baryon asymmetry in the SM, our scenario does not rely on sphalerons. Instead, as detailed in Chapter 5, a baryon asymmetry in the visible sector is produced through the out-of-equilibrium decays of N, establishing a direct connection between the asymmetry generated in the dark sector and the observed baryon asymmetry.

7.1.1 C and CP violation

As discussed in Section 3.2, the violation of charge conjugation (C) and the product of charge conjugation and parity (CP) are essential ingredients for generating an asymmetry between particles and antiparticles. In this section, we first demonstrate why both C and CP violation are required in our scenario. We then proceed to derive the CP violation parameter, ϵ_i, which quantifies the asymmetry generated in the decays of the heavy Majorana fermions.

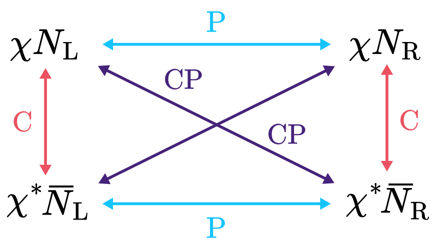

Fig. 7.3: Relation of the four different final states of the decay of φ_i by the actuation of the operators charge conjugation (C), parity (P) and the product of both (CP).

7.1.1.1 Necessary symmetry violations

To generate an asymmetry in the dark sector, the decay rates into χN and $\chi^* \overline{N}$ must differ. Since N and $\overline{N}$ are chiral, like the Majorana fermions φ_i, they each have left-handed and right-handed components related by a parity transformation. In contrast, the scalars χ and χ^* remain unchanged under parity transformations. As a result, for each φ_i, we identify four possible decay channels:

$$\begin{aligned} \varphi_{iL} &\to \chi N_R, \qquad & \varphi_{iR} &\to \chi N_L, \\ \varphi_{iL} &\to \chi^* \overline{N}_R, \qquad & \varphi_{iR} &\to \chi^* \overline{N}_L. \end{aligned}$$

For an asymmetry to arise between particles and antiparticles, the total decay rates into χN and $\chi^* \overline{N}$ must be different, leading to the condition

$$\Gamma(\chi N_R) + \Gamma(\chi N_L) \neq \Gamma(\chi^* \overline{N}_R) + \Gamma(\chi^* \overline{N}_L), \tag{7.2}$$

where $\Gamma(Y)$ represents the decay rate into a given final state Y.

Fig. 7.3 visually represents how the final states transform under C, P, and CP. To determine their impact on Eq. (7.2), we analyze how each symmetry affects the decay rates:

1. If C is conserved, the decay rates satisfy

$$\Gamma(\chi N_L) = \Gamma\left(\chi^* \overline{N}_L\right), \tag{7.3}$$
$$\Gamma(\chi N_R) = \Gamma(\chi^* \overline{N}_R). \tag{7.4}$$

   This forces both sides of Eq. (7.2) to be equal, preventing any asymmetry generation.

2. If P is conserved, we have

$$\Gamma(\chi N_L) = \Gamma(\chi N_R), \tag{7.5}$$
$$\Gamma\left(\chi^* \overline{N}_L\right) = \Gamma(\chi^* \overline{N}_R). \tag{7.6}$$

   This does not contradict Eq. (7.2), meaning that an asymmetry can still be generated. Thus, P violation is not required.

3. If CP is conserved, the decay rates satisfy

$$\Gamma(\chi N_L) = \Gamma(\chi^* \overline{N}_R), \tag{7.7}$$
$$\Gamma(\chi N_R) = \Gamma\left(\chi^* \overline{N}_L\right). \tag{7.8}$$

   This again forces both sides of Eq. (7.2) to be equal, preventing asymmetry generation. Therefore, CP violation is required.

From this analysis, we conclude that both C and CP violation are necessary to generate the dark sector asymmetries, while P violation is not essential. These violations naturally arise in our framework through the interference between tree-level and loop-level decays of the Majorana fermions. Like in standard leptogenesis, the presence of at least two Majorana fermions is required.

7.1.1.2 Derivation of the CP asymmetry parameter

Following Eq. (3.12), the CP violation parameter in our model is defined as

$$\epsilon_i \equiv \frac{\Gamma(\varphi_i \to N\chi) - \Gamma(\varphi_i \to \overline{N}\chi^*)}{\Gamma(\varphi_i \to N\chi) + \Gamma(\varphi_i \to \overline{N}\chi^*)}, \tag{7.9}$$

where $i = 1, 2$ labels the heavy Majorana fermions. At tree-level the decay rates for these two processes are identical:

$$\Gamma(\varphi_i \to N\chi) = \Gamma(\varphi_i \to \overline{N}\chi^*) = \frac{|\lambda_i|^2}{16\pi} M_i, \tag{7.10}$$

implying that no CP asymmetry is generated at this order, i.e., $\epsilon_i = 0$. However, when including loop-level contributions, CP violation arises due to the interference between tree-level and one-loop decay amplitudes. This interference generates a difference between the decay rates of φ_i into χN and $\chi^* \overline{N}$, leading to a nonzero ϵ_i.

The CP violation parameter receives contributions from two types of one-loop diagrams: the vertex correction (upper diagram in Fig. 7.2) and the wave function correction (lower two diagrams in Fig. 7.2).

The vertex correction contribution to ϵ_i is given by

$$\epsilon_i(\text{vertex}) = \frac{1}{8\pi} \sum_j f\left(\frac{M_j^2}{M_i^2}\right) \frac{\text{Im}\left[(\lambda_j^* \lambda_i)^2\right]}{|\lambda_i|^2} \tag{7.11}$$

where $j = 1, 2$ represents the Majorana fermion φ_j appearing in the loop. The function $f(a)$ is defined as

$$f(a) \equiv \sqrt{a}\left[1 - (1 + a)\ln\left(\frac{1 + a}{a}\right)\right]. \tag{7.12}$$

We observe that the contribution for $j = i$ vanishes, since

$$\text{Im}\left[(\lambda_i^* \lambda_i)^2\right] = \text{Im}\left[|\lambda_i|^2\right] = 0. \tag{7.13}$$

As a result, only terms with $j \neq i$ contribute to the sum. The expression in Eq. (7.11) is analogous to the standard leptogenesis result [224, 225], except that in their case the couplings are matrices accounting for different lepton flavours, while here they are vectors. [1]

The contribution from the wave function diagrams is

$$\begin{aligned}\epsilon_i(\text{wave}) &= -\frac{1}{2}\frac{1}{8\pi}\sum_{j\neq i}\frac{M_i M_j}{M_j^2 - M_i^2}\frac{\text{Im}\left[(\lambda_j^*\lambda_i)^2\right]}{|\lambda_i|^2} \\ &= \frac{1}{2}\frac{1}{8\pi}\sum_{j\neq i} g\left(\frac{M_j^2}{M_i^2}\right)\frac{\text{Im}\left[(\lambda_j^*\lambda_i)^2\right]}{|\lambda_i|^2},\end{aligned} \tag{7.14}$$

where the function $g(a)$ is given by

$$g(a) \equiv \frac{\sqrt{a}}{1-a}. \tag{7.15}$$

Eq. (7.14) is derived from the standard leptogenesis expression [224, 225], incorporating a factor of $1/2$ to account for the absence of $SU(2)$ doublets in the loop.

Summing both contributions, the total CP violation parameter is

$$\epsilon_i = \frac{1}{8\pi|\lambda_i|^2}\sum_{j\neq i}\text{Im}\left[(\lambda_j^*\lambda_i)^2\right]\left[f\left(\frac{M_j^2}{M_i^2}\right) + \frac{1}{2}g\left(\frac{M_j^2}{M_i^2}\right)\right]. \tag{7.16}$$

For a strong mass hierarchy $M_2 \gg M_1$, these simplify to

$$\epsilon_1 = -\frac{1}{8\pi|\lambda_1|^2}\text{Im}\left[(\lambda_2^*\lambda_1)^2\right]\left(\frac{M_1}{M_2}\right), \tag{7.17}$$

$$\epsilon_2 = \frac{1}{8\pi|\lambda_2|^2}\text{Im}\left[(\lambda_1^*\lambda_2)^2\right]\left[\frac{1}{2}\frac{M_1}{M_2}\left(3 - 2\log\left(\frac{M_2^2}{M_1^2}\right)\right)\right]. \tag{7.18}$$

Expressing the complex couplings as

$$\lambda_i \equiv |\lambda_i| \mathrm{e}^{i\phi_i}, \tag{7.19}$$

the imaginary part of their product expands as

$$\text{Im}\left[(\lambda_j^*\lambda_i)^2\right] = \text{Im}\left[\left(|\lambda_i|\mathrm{e}^{i\phi_i}|\lambda_j|\mathrm{e}^{-i\phi_j}\right)^2\right] = |\lambda_i|^2|\lambda_j|^2\sin\big(2\left(\phi_i - \phi_j\right)\big). \tag{7.20}$$

[1] Other differences, such as the reduced number of final-state degrees of freedom and the absence of a left-handed projector in our Lagrangian, also distinguish our rates from those in leptogenesis. However, these factors appear consistently in both the tree-level and loop-level decay rates, canceling out in the final expression for ϵ_i in Eq. (7.9).

To maximize CP violation, we would need

$$\phi_i - \phi_j = \pm\frac{\pi}{4}. \tag{7.21}$$

In particular, we choose the specific phase assignment

$$\lambda_1 = |\lambda_1|, \tag{7.22}$$

$$\lambda_2 = |\lambda_2| e^{i\frac{\pi}{4}}. \tag{7.23}$$

This choice ensures that the CP violation parameter is maximized, leading to the most efficient generation of an asymmetry in the dark sector.

7.1.2 Characteristic temperature for asymmetry generation

The temperature at which the dark-sector asymmetry is generated is approximately set by the decay of the lighter Majorana fermion, φ_1. If the heavier state, φ_2, has a sufficiently large mass such that it decays before inflation or reheating, any asymmetry it produces is diluted away, leaving only the contribution from φ_1 relevant for our analysis.

To estimate this characteristic temperature, we determine when the total decay rate of φ_1 becomes comparable to the Hubble expansion rate,

$$\frac{\Gamma_1^{\text{tot}}}{H} \simeq 1. \tag{7.24}$$

The total decay rate Γ_1^{tot} accounts for both decay channels, $\varphi_1 \to \chi N$ and $\varphi_1 \to \chi^* \overline{N}$. Using the tree-level decay rate from Eq. (7.10) and the Hubble rate in a radiation-dominated universe given in Eq. (B.10), we obtain

$$\frac{\frac{1}{8\pi}|\lambda_1|^2 M_1}{\frac{\pi}{\sqrt{90} M_{\text{Pl}}}\sqrt{g_\star}\, T_{\text{lepto}}^2} \simeq 1, \tag{7.25}$$

which leads to an approximate expression for the leptogenesis temperature:

$$T_{\text{lepto}}^2 \simeq \frac{\sqrt{90}\, M_{\text{Pl}}}{8\pi^2 \sqrt{g_\star}} |\lambda_1|^2 M_1. \tag{7.26}$$

This provides an estimate of the temperature at which the asymmetry is dynamically generated, setting the initial condition for the subsequent evolution of the dark sector abundances.

7.1.3 Boltzmann equations

The evolution of dark sector particle abundances and asymmetries is governed by the set of coupled Boltzmann equations that account for all relevant interactions. In Eqs. (5.21)–(5.24), (5.27), and (5.29), we previously established these equations assuming the asymmetry as an initial condition. Here, we extend the system to include the generation of the asymmetry by incorporating the additional particles and interactions.

A detailed step-by-step derivation of the Boltzmann equation for Y_{φ_i} is provided in Appendix B.4 as an example. The new processes contributing to the evolution include decays and inverse decays, shown in Fig. B.1, as well as the annihilation of two φ_i into dark sector particles, shown in Fig. B.2. Additionally, the new Majorana fermions participate in washout processes, illustrated in Fig. 7.4. The effects of washout from Majorana-mediated scatterings are already incorporated in the Boltzmann equations through the terms $\langle\sigma v\rangle_{\chi\chi\to\overline{N}\overline{N}}$ and $\langle\sigma v\rangle_{\chi N\to\chi^*\overline{N}}$, which account for the contributions of both φ_1 and φ_2. Their full expressions and thermal integration will be shown in Section 7.1.4.

We now present the full set of Boltzmann equations governing asymmetry generation. The equations for the quarks and leptons remain unchanged by the presence of the Majorana fermions and retain the same form as Eqs. (5.27) and (5.29). The notation follows the definitions introduced earlier: the yield definitions follow Eqs. (5.19) and (5.20); the thermally averaged total decay rates $\langle\Gamma\rangle_{\mathrm{D}}^{\mathrm{tot},i}$ are given by Eqs. (7.10) and (A.32); the ratio of equilibrium yields P is defined in Eq. (5.26), and the parameter λ is given in Eq. (2.12). We use the dimensionless time variable as $x = m_\chi/T$. The color code also follows the same convention previously introduced.

The Boltzmann equations without anay assumptions regarding the thermal equilibrium of N and χ are given by

$$
\begin{aligned}
\frac{dY_{\varphi_i}}{dx} = &-\frac{x}{H(1)}\langle\Gamma\rangle_{\mathrm{D}}^{\mathrm{tot},i}\left(Y_{\varphi_i} - Y_{\varphi_i}^{\mathrm{eq}}\frac{Y_\chi^{\mathrm{tot}}}{2Y_\chi^{\mathrm{eq}}}\right) \\
&-\frac{x\mathfrak{s}}{H(1)}\Bigg[2\langle\sigma v\rangle_{\varphi_i\varphi_i\to\chi\chi^*}\left(Y_{\varphi_i}^2 - \frac{Y_{\varphi_i}^{\mathrm{eq}\,2}}{Y_\chi^{\mathrm{eq}}Y_{\chi^*}^{\mathrm{eq}}}Y_\chi Y_{\chi^*}\right) \\
&\qquad +2\langle\sigma v\rangle_{\varphi_i\varphi_i\to N\overline{N}}\left(Y_{\varphi_i}^2 - \frac{Y_{\varphi_i}^{\mathrm{eq}\,2}}{Y_N^{\mathrm{eq}}Y_{\overline{N}}^{\mathrm{eq}}}Y_N Y_{\overline{N}}\right)\Bigg],
\end{aligned}
\tag{7.27}
$$

$$
\begin{aligned}
\frac{dY_{\Delta\chi}}{dx} = \frac{x}{H(1)} \sum_i \langle\Gamma\rangle_{\rm D}^{{\rm tot},i} & \left[\epsilon_i\left(Y_{\varphi_i} - Y_{\varphi_i}^{\rm eq}\frac{Y_\chi^{\rm tot}}{2Y_\chi^{\rm eq}}\right) - \frac{1}{2}Y_{\varphi_i}^{\rm eq}\frac{Y_{\Delta\chi}}{Y_\chi^{\rm eq}}\right] \\
-\frac{x\mathfrak{s}}{H(1)} & \left[2\langle\sigma v\rangle_{\chi\chi\to\bar{N}\bar{N}}\left(Y_\chi^2 - Y_{\chi^*}^2 + P(Y_N^2 - Y_{\bar{N}}^2)\right)\right. \\
& \left. + 2\langle\sigma v\rangle_{\chi N\to\chi^*\bar{N}}\left(Y_\chi Y_N - Y_{\chi^*}Y_{\bar{N}}\right)\right],
\end{aligned}
\tag{7.28}
$$

$$
\begin{aligned}
\frac{dY_{\Delta N}}{dx} = \frac{x}{H(1)} \sum_i \langle\Gamma\rangle_{\rm D}^{{\rm tot},i} & \left[\epsilon_i\left(Y_{\varphi_i} - Y_{\varphi_i}^{\rm eq}\frac{Y_\chi^{\rm tot}}{2Y_\chi^{\rm eq}}\right) - \frac{1}{2}Y_{\varphi_i}^{\rm eq}\frac{Y_{\Delta\chi}}{Y_\chi^{\rm eq}}\right] \\
-\frac{x\mathfrak{s}}{H(1)} & \left[2\langle\sigma v\rangle_{\chi\chi\to\bar{N}\bar{N}}\left(Y_\chi^2 - Y_{\chi^*}^2 + P(Y_N^2 - Y_{\bar{N}}^2)\right)\right. \\
& + 2\langle\sigma v\rangle_{\chi N\to\chi^*\bar{N}}\left(Y_\chi Y_N - Y_{\chi^*}Y_{\bar{N}}\right) \\
& + \langle\sigma v\rangle_{N\bar{d}\to ud}\left(Y_N Y_{\bar{d}}^{\rm eq} - Y_{\bar{N}}Y_d^{\rm eq} - Y_N^{\rm eq}Y_{\bar{d}}^{\rm eq} + Y_{\bar{N}}^{\rm eq}Y_d^{\rm eq}\right) \\
& + \langle\sigma v\rangle_{N\bar{u}\to dd}\left(Y_N Y_{\bar{u}}^{\rm eq} - Y_{\bar{N}}Y_u^{\rm eq} - Y_N^{\rm eq}Y_{\bar{u}}^{\rm eq} + Y_{\bar{N}}^{\rm eq}Y_u^{\rm eq}\right) \\
& \left. + \frac{1}{\mathfrak{s}}\langle\Gamma_N\rangle\left(Y_N - Y_{\bar{N}} - Y_N^{\rm eq} + Y_{\bar{N}}^{\rm eq}\right)\right],
\end{aligned}
\tag{7.29}
$$

$$
\begin{aligned}
\frac{dY_\chi^{\rm tot}}{dx} = \frac{x}{H(1)} \sum_i \langle\Gamma\rangle_{\rm D}^{{\rm tot},i} & \left(Y_{\varphi_i} - Y_{\varphi_i}^{\rm eq}\frac{Y_\chi^{\rm tot}}{2Y_\chi^{\rm eq}}\right) \\
-\frac{x\mathfrak{s}}{H(1)} & \left[-2\sum_i \langle\sigma v\rangle_{\varphi_i\varphi_i\to\chi\chi^*}\left(Y_{\varphi_i}^2 - \frac{Y_{\varphi_i}^{\rm eq\,2}}{Y_\chi^{\rm eq}Y_{\chi^*}^{\rm eq}}Y_\chi Y_{\chi^*}\right)\right. \\
& + 2\langle\sigma v\rangle_{\chi\chi^*\to N\bar{N}}\left(Y_\chi Y_{\chi^*} - P Y_N Y_{\bar{N}}\right) \\
& \left. + 2\langle\sigma v\rangle_{\chi\chi\to\bar{N}\bar{N}}\left(Y_\chi^2 + Y_{\chi^*}^2 - P\left(Y_N^2 + Y_{\bar{N}}^2\right)\right)\right],
\end{aligned}
\tag{7.30}
$$

$$
\begin{aligned}
\frac{dY_N^{\rm tot}}{dx} = & \frac{x}{H(1)}\sum_i \langle\Gamma\rangle_{\rm D}^{{\rm tot},i}\left(Y_{\varphi_i} - Y_{\varphi_i}^{\rm eq}\frac{Y_\chi^{\rm tot}}{2Y_\chi^{\rm eq}}\right) \\
& -\frac{x\mathfrak{s}}{H(1)}\left[-2\sum_i \langle\sigma v\rangle_{\varphi_i\varphi_i\to N\overline{N}}\left(Y_{\varphi_i}^2 - \frac{Y_{\varphi_i}^{\rm eq\,2}}{Y_N^{\rm eq}Y_{\overline{N}}^{\rm eq}}Y_N Y_{\overline{N}}\right)\right. \\
& \qquad -2\langle\sigma v\rangle_{\chi\chi^*\to N\overline{N}}\left(Y_\chi Y_{\chi^*} - PY_N Y_{\overline{N}}\right) \\
& \qquad -2\langle\sigma v\rangle_{\chi\chi\to\overline{N}\,\overline{N}}\left(Y_\chi^2 + Y_{\chi^*}^2 - P\left(Y_N^2 + Y_{\overline{N}}^2\right)\right) \\
& \qquad +\langle\sigma v\rangle_{N\bar{d}\to ud}\left(Y_N Y_{\bar{d}}^{\rm eq} + Y_{\overline{N}}Y_d^{\rm eq} - Y_N^{\rm eq}Y_{\bar{d}}^{\rm eq} - Y_{\overline{N}}^{\rm eq}Y_d^{\rm eq}\right) \\
& \qquad +\langle\sigma v\rangle_{N\bar{u}\to dd}\left(Y_N Y_{\bar{u}}^{\rm eq} + Y_{\overline{N}}Y_u^{\rm eq} - Y_N^{\rm eq}Y_{\bar{u}}^{\rm eq} - Y_{\overline{N}}^{\rm eq}Y_u^{\rm eq}\right) \\
& \qquad \left. +\frac{1}{\mathfrak{s}}\langle\Gamma_N\rangle\left(Y_N + Y_{\overline{N}} - Y_N^{\rm eq} - Y_{\overline{N}}^{\rm eq}\right)\right].
\end{aligned}
\tag{7.31}
$$

7.1.4 Thermally averaged cross sections and washout

As mentioned earlier, two-to-two interactions mediated by φ_i naturally arise, including $\chi\chi \leftrightarrow \overline{N}\,\overline{N}$ and $\chi N \leftrightarrow \chi^*\overline{N}$, see Fig. 7.4. While these processes do not violate baryon number, they contribute to erasing the asymmetry in the dark sector, as illustrated in Section 5.2.2 and Fig. 5.7. These interactions are analogous to the $\Delta L = 2$ processes in standard leptogenesis. However, in this framework, we do not have the equivalent of $\Delta L = 1$ processes, as their counterparts would violate baryon number in our model.

Following Ref. [226], we compute the expressions for the cross sections of these processes in the full theory. To obtain simplified analytical expressions, we assume the couplings take the form $\lambda_1 = |\lambda_1|$ and $\lambda_2 = |\lambda_2|\exp(i\pi/4)$, which maximizes CP-violation, as shown in Eq. (7.20).

The annihilation cross section for $NN \to \chi^*\chi^*$ is given by

$$
\sigma_{NN\to\chi^*\chi^*} = \frac{4\pi c_i}{s}\sum_{i=1}^{2}\left(\frac{1}{1+\frac{a_i}{x}} + \frac{1}{1+\frac{x}{2a_i}}\log\left(1+\frac{x}{a_i}\right)\right), \tag{7.32}
$$

where $i = 1, 2$ labels the mediating φ_i, and we have defined:

$$
y \equiv \frac{s}{M_1^2}, \quad a_i \equiv \left(\frac{M_i}{M_1}\right)^2, \quad c_i \equiv \left(\frac{|\lambda_i|^2}{8\pi}\right)^2. \tag{7.33}
$$

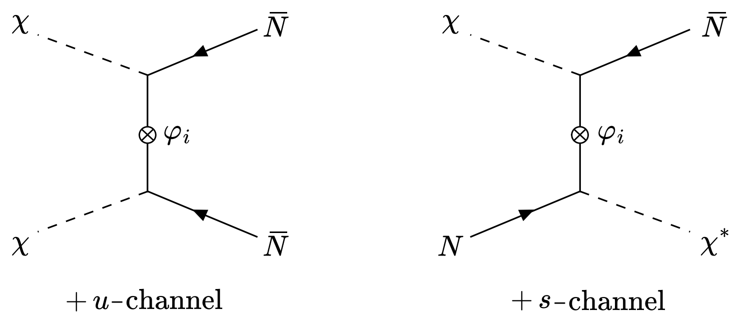

Fig. 7.4: Feynman diagrams depicting the washout processes (annihilations and scatterings) mediated by the heavy Majorana fermions φ_1 and φ_2. In the EFT framework, these interactions are characterized by the energy scale Λ_2.

Similarly, the cross section for scatterings $\chi N \to \chi^* \overline{N}$ is given by

$$\sigma_{\chi N\to\chi^*\overline{N}} = \frac{16\pi c_i}{s}\sum_{i=1}^{2}\left(\frac{y^2 - a_i^2 + a_i\left(c_i + \frac{1}{2}y\right)}{(y-a_i)^2 + a_i c_i} - \frac{3y^2 - a_i^2 - 2a_i y + a_i c_i}{(y-a_i)^2 + a_i c_i}\frac{a_i}{y}\log\frac{a_i + y}{a_i}\right). \tag{7.34}$$

To recover the EFT limit, we take $y \to 0$, corresponding to the regime $T \ll M_1$, in the full theory expressions. This yields:

$$\sigma^{y\to 0}_{NN\to\chi^*\chi^*} \simeq \frac{1}{8\pi}\left(\frac{|\lambda_1|^4}{M_1^2} + \frac{|\lambda_2|^4}{M_2^2}\right), \tag{7.35}$$

$$\sigma^{y\to 0}_{\chi N\to\chi^*\overline{N}} \simeq \frac{1}{2\pi}\left(\frac{|\lambda_1|^4}{M_1^2} + \frac{|\lambda_2|^4}{M_2^2}\right). \tag{7.36}$$

For comparison, in the EFT limit with $T \gg m_\chi$, the corresponding cross sections are:

$$\sigma^{\mathrm{EFT}}_{NN\to\chi^*\chi^*} = \frac{1}{32\pi}\frac{1}{\Lambda^2_{2,\mathrm{Ann}}}, \tag{7.37}$$

$$\sigma^{\mathrm{EFT}}_{\chi N\to\chi^*\overline{N}} = \frac{1}{32\pi}\frac{1}{\Lambda^2_{2,\mathrm{Scat}}}. \tag{7.38}$$

By matching these results, we identify the corresponding effective energy scales:

$$\Lambda_{2,\mathrm{Ann}} = \frac{1}{2\sqrt{\frac{|\lambda_1|^4}{M_1^2} + \frac{|\lambda_2|^4}{M_2^2}}}, \tag{7.39}$$

$$\Lambda_{2,\mathrm{Scat}} = \frac{1}{4\sqrt{\frac{|\lambda_1|^4}{M_1^2} + \frac{|\lambda_2|^4}{M_2^2}}}. \tag{7.40}$$

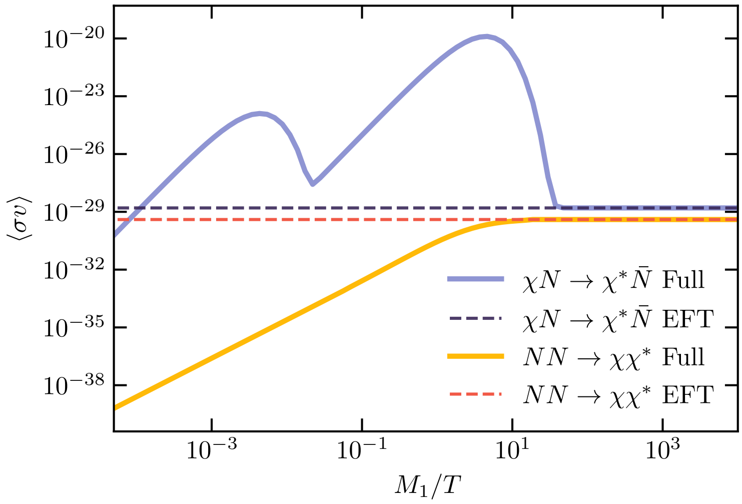

Fig. 7.5: Thermally averaged cross sections for scatterings ($\chi N \to \chi^* \overline{N}$) and annihilations ($NN \to \chi\chi^*$) as functions of M_1/T. Solid lines represent the full theory results for $M_1 = 10^6$ GeV, $M_2 = 10^9$ GeV, $\lambda_1 = 10^{-4}$, and $\lambda_2 = 10^{-4.5}$. Dashed lines show the corresponding EFT predictions. See main text for details.

To obtain the thermally averaged cross sections $\langle\sigma v\rangle$ appearing in the Boltzmann equations, we integrate following the formalism in Appendix A.4. Introducing these cross sections in Eq. (A.29), we obtain the thermally averaged rates for annihilations, $\langle\gamma^{NN}_{\chi^*\chi^*}\rangle$, and for scatterings, $\langle\gamma^{\chi N}_{\chi^*\bar{N}}\rangle$:

$$\langle\gamma^{NN}_{\chi^*\chi^*}\rangle = \frac{T}{8\pi^4}\int ds s^{3/2}\, K_1\left(\frac{\sqrt{s}}{T}\right)\lambda\left(1, \frac{m_N^2}{s}, \frac{m_N^2}{s}\right)\sigma_{NN\to\chi^*\chi^*}, \tag{7.41}$$

$$\langle\gamma^{\chi N}_{\chi^*\bar{N}}\rangle = \frac{T}{16\pi^4}\int ds s^{3/2}\, K_1\left(\frac{\sqrt{s}}{T}\right)\lambda\left(1, \frac{m_\chi^2}{s}, \frac{m_N^2}{s}\right)\sigma_{\chi N\to\chi^*\bar{N}}, \tag{7.42}$$

where $\lambda(a,b,c) = (a-b-c)^2 - 4bc$ is the Källén function, and $K_1(x)$ is the modified Bessel function of the second kind. Using Eq. (A.30), we then obtain the thermally averaged cross sections:

$$\langle\sigma v\rangle_{NN\to\chi^*\chi^*} = \frac{\langle\gamma^{NN}_{\chi^*\chi^*}\rangle}{n_N^{\rm eq} n_N^{\rm eq}}, \tag{7.43}$$

$$\langle\sigma v\rangle_{\chi N\to\chi^*\bar{N}} = \frac{\langle\gamma^{\chi N}_{\chi^*\bar{N}}\rangle}{n_\chi^{\rm eq} n_N^{\rm eq}}. \tag{7.44}$$

We perform these integrations numerically in Mathematica, and Fig. 7.5 presents an example for a given parameter set, demonstrating agreement between the full theory description and an EFT approach with matching energy scales given by Eqs. (7.39) and (7.40).

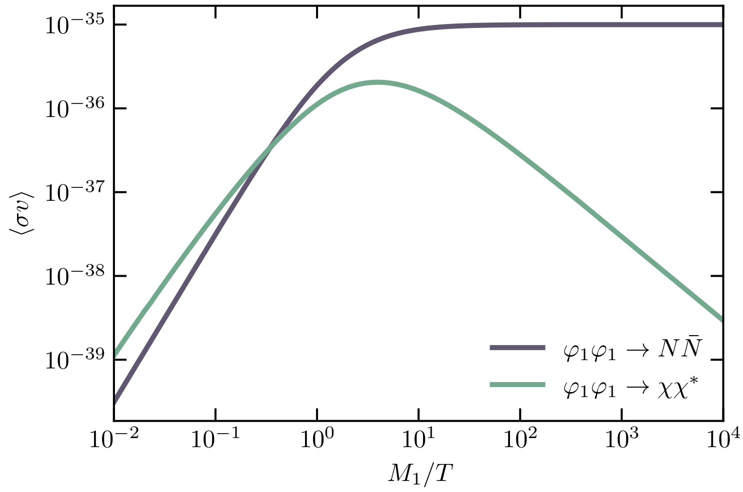

Fig. 7.6: Thermally averaged cross sections for $\varphi_1\varphi_1 \to \chi\chi^*$ and $\varphi_1\varphi_1 \to N\bar{N}$, computed for the parameter values $M_1 = 10^6$ GeV, $M_2 = 10^9$ GeV, $\lambda_1 = 10^{-4}$, and $\lambda_2 = 10^{-4.5}$.

We also derive the cross sections for the annihilation processes $\varphi_i\varphi_i \to \chi\chi^*$ and $\varphi_i\varphi_i \to N\bar{N}$. In the low-velocity limit, these simplify to:

$$\sigma^{y\to 0}_{\varphi_i\varphi_i\to\chi\chi^*} \simeq \frac{\lambda_i^4\, v}{16\pi M_i^2} + \mathcal{O}(v^3), \tag{7.45}$$

$$\sigma^{y\to 0}_{\varphi_i\varphi_i\to N\bar{N}} \simeq \frac{\lambda_i^4}{8\pi M_i^2\, v} + \mathcal{O}(v^1). \tag{7.46}$$

We numerically integrate these cross sections, and Fig. 7.6 shows the results for φ_1 annihilations using the parameter set indicated in the figure. As expected, $\varphi_i\varphi_i \to \chi\chi^*$ exhibits p-wave behavior at low temperatures, while $\varphi_i\varphi_i \to N\bar{N}$ is s-wave dominated.

Importantly, these cross sections become relevant around $T \sim M_i$, where the φ_i population is already suppressed due to Boltzmann factors from their decays. As a result, these processes are not expected to play a significant role in the dynamics of asymmetry generation within the Boltzmann equations.

7.1.5 Parameter space

In this subsection, we explore the parameter space that enables the successful generation of the dark sector asymmetry, previously treated as an initial condition. The required asymmetry, $Y^{\rm in}_{\Delta\chi} = 2.3 \times 10^{-10}$, derived in Eq. (5.62), accounts for the transfer of a portion of the dark asymmetry to SM leptons via sphaleron processes. The washout effects that influence the asymmetry occur at high temperatures and are inherently tied to the dynamics of its generation. This aligns with the derivation of $Y^{\rm in}_{\Delta\chi}$, where washout was neglected, as it is no longer active at that stage.

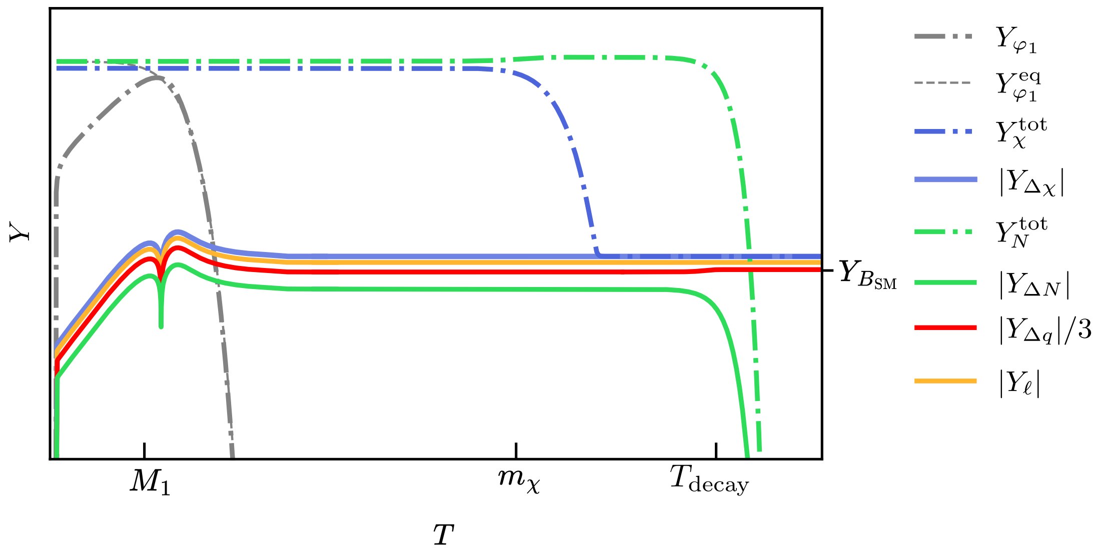

Fig. 7.7: Representative evolution of the total yields of $\chi + \chi^*$, $N + \overline{N}$, and φ_1 (dash-dotted), along with the dynamically generated asymmetries between particles and antiparticles (solid), in our leptogenesis-like scenario. A mild washout is present at high temperatures. The mass of φ_2 is taken to be above the reheating temperature.

For the precise value of the target asymmetry to be generated, $Y_{\Delta\chi}^{\rm target}$, we must account for the rescaling of the yield due to the effective entropy degrees of freedom, $g_{\star S}$, which affect its value at different temperatures. We find

$$Y_{\Delta\chi}^{\rm target} = 2.3 \times 10^{-10} \, \frac{g_{\star S}(T_{\rm today})}{g_{\star S}(T_{\rm lepto})} \simeq 8.4 \times 10^{-12}. \tag{7.47}$$

A qualitative example of the dynamical generation of the asymmetry is shown in Fig. 7.7. By solving the Boltzmann equations for different values of the model's key parameters, we identify the regions where the model successfully generates the target asymmetry, and therefore reproduce the measured quark-antiquark asymmetry. The key parameters governing asymmetry generation are the masses M_1 and M_2, along with the couplings λ_1 and λ_2, as defined in Eq. (7.1). These parameters determine the CP violation coefficients ϵ_1 and ϵ_2 through Eq. (7.16), and also control the strength of the washout processes via the cross sections in Eqs. (7.32) and (7.34).

For each set of parameters (M_1, M_2, λ_1), there might exist two possible values of λ_2 that lead to successful asymmetry generation. As illustrated in Fig. 7.8, this behavior arises from the interplay between CP violation and washout processes. Starting from small λ_2, increasing the coupling enhances the final asymmetry due to the growth of the CP violation parameter ϵ_1. However, at larger λ_2, washout processes become more efficient, eventually reducing the asymmetry. This creates a second solution where the

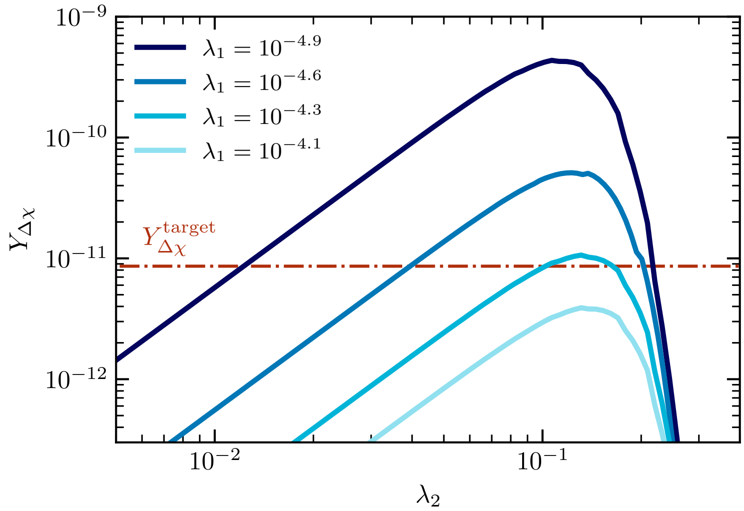

Fig. 7.8: Generated asymmetry as a function of λ_2 for fixed values of $M_1 = 10^7$ GeV, $M_2 = 10^{10}$ GeV, and different choices of λ_1 as indicated in the figure. The horizontal dash-dotted line marks the target asymmetry, $Y_{\Delta\chi}^{\text{target}}$. The inclusion of washout processes leads to a second solution for λ_2, where the initially overproduced asymmetry is reduced to the desired value.

initially overproduced asymmetry is balanced by stronger washout, yielding the target value. For certain parameter choices, no solutions exist, either because CP violation is too weak or washout effects are too strong. This is the case for example for the lightest blue curve in Fig. 7.8.

To solve the set of coupled Boltzmann equations given in Section 7.1.3, we have assumed, for simplicity, that the mass of φ_2 is greater than the reheating temperature after inflation. This assumption eliminates the contribution of φ_2 to the asymmetry generation, setting the terms with $i = 2$ in the Boltzmann equations (7.27)–(7.31) to zero. This simplification does not alter the overall picture, as the effect of φ_2 on asymmetry generation is already negligible compared to that of φ_1 when $M_2 \gg M_1$. Additionally, in the numerical analysis we have assumed that χ and φ_1 reach thermal equilibrium with N and, consequently, with the SM bath.[2] If this condition is not met, the dark sector temperature may deviate from that of the SM at early times, requiring a more detailed treatment to properly account for this effect. However, such a deviation is not expected to significantly alter the viable parameter space presented in this section.

Fig. 7.9 presents the parameter space for successful asymmetry generation. Each point in the plot corresponds to a solution of the Boltzmann equations, with the requirement that the final asymmetry matches $Y_{\Delta\chi}^{\text{target}}$. The color contours represent the values of

[2]This condition is naturally satisfied if interactions between N and χ are strong, if φ_1 couples efficiently to the SM Higgs or the neutron portal mediator (introduced in the next section), or if processes like $N\overline{N} \leftrightarrow \varphi_1\varphi_1$ are in equilibrium at the relevant temperatures, which occurs for values of $\lambda_1 \geq 6\times10^{-3}$.

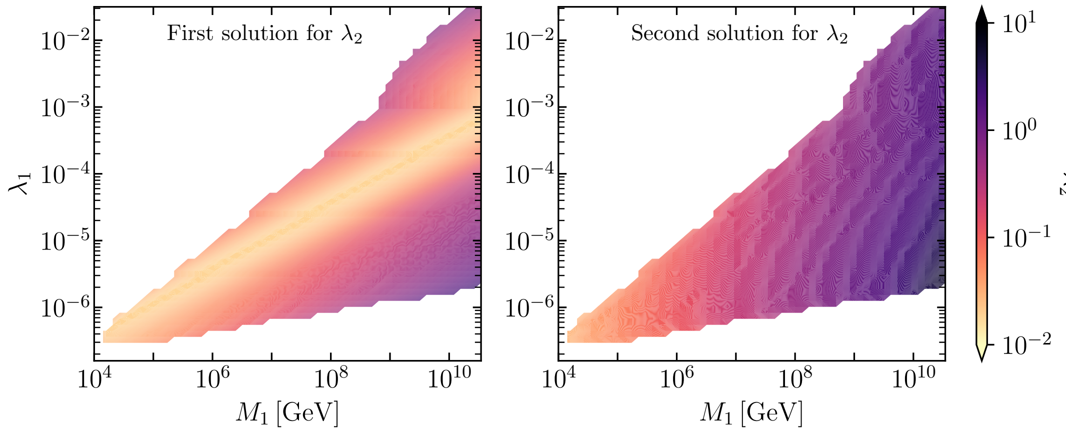

Fig. 7.9: Parameter space for successful asymmetry generation, showing the values of λ_2 (color contours) required to achieve the correct final asymmetry for the parameter set $(\lambda_1, M_1, M_2 = 10^3 M_1)$. Each panel corresponds to one of the two possible solutions for λ_2, which emerge from the balance between CP violation and washout effects. The white region represents parameter values where no viable solution exists due to either insufficient CP violation or excessive washout.

the coupling λ_2, with each panel corresponding to one of its two possible solutions. The white region in Fig. 7.9 represents parameter values where no solution for λ_2 exists that produces the correct final asymmetry. This occurs due CP violation being too weak (at smaller values of λ_1), or due to washout effects being too strong (larger values of λ_1). Additionally, the lower bound on M_1 at $M_1^{\min} \simeq 10^4$ GeV, and the decreasing range of viable λ_1 values at lower M_1 stem from the fact that smaller masses simultaneously weaken CP violation and intensify washout effects, further constraining the parameter space.

This parameter space analysis demonstrates that a large region of viable parameter space exists where the correct dark sector asymmetry can be generated, even in the presence of washout effects. These results highlight the robustness of the proposed mechanism, as successful asymmetry generation is not restricted to finely tuned regions but instead spans a wide range of physically reasonable parameters.

7.2 UV completion of the neutron portal

To achieve a UV completion of the neutron portal we introduce a complex scalar, Φ, with electromagnetic charge $Q = -1/3$, baryon number $B = -2/3$, and which transforms as a color triplet under the SM $SU(3)_C$. The kinetic, gauge and mass terms of the Langrangian are given by

$$\mathcal{L} \supset (D_\mu \Phi)^\dagger D^\mu \Phi - M_\Phi^2 |\Phi|^2 \,, \tag{7.48}$$

where D_μ is the covariant derivative, defined as $D_\mu \equiv \partial_\mu - i\frac{g'}{2}YB_\mu - i\frac{g_s}{2}\lambda_\alpha G^\alpha_\mu$, for a particle charged under both hypercharge and color interactions. The interaction terms responsible for generating the neutron portal are

$$\mathcal{L} \supset y_{ud}\,\epsilon^{ijk}\Phi_i \overline{u^c_j} d_k + y_{Nd}\,\Phi^*_i \overline{N} d_i + h.c.\,, \tag{7.49}$$

where i, j, k are color indices, and u and d are right-handed. The parameters y_{ud} and y_{Nd} are the dimensionless Yukawa couplings. Similar mediators have been explored in previous studies, particularly in scenarios where N acts as the dark matter candidate [193, 196, 197].

The particles involved in the neutron portal exhibit parallels with certain particles predicted by supersymmetry (SUSY). Specifically, N can be compared to a Dirac neutralino ($\widetilde{\chi}^0$), and Φ resembles a right-handed down-type squark ($\widetilde{d}$), with a different baryon charge. In a SUSY scenario, the coupling y_{ud} could exist only as an R-parity violating interaction, as it involves just one supersymmetric partner. This highlights a distinction from y_{Nd}, which corresponds to a more standard R-conserving supersymmetric interaction widely recognized in the literature. SUSY, being a widely studied theoretical framework [48–52], has inspired numerous experimental searches for particles like these. While the search strategies and constraints from SUSY do not map perfectly onto the neutron portal scenario, the wealth of existing literature provides a robust basis for interpreting and constraining these particles in our context.

In Section 6.2.2, we explored the constraints on the parameter space of the neutron portal within the EFT framework, identifying the allowed regions for the energy scale Λ_n. In the full theory, we can match the energy scale to the new parameters as

$$\Lambda_n = \frac{M_\Phi}{\sqrt{y_{ud}\, y_{Nd}}}. \tag{7.50}$$

Since the particle Φ carries color charge, we intuitively expect its mass to be constrained from bellow to at least several hundred GeV. From cosmological considerations, the energy scale is constrained from above to values $\Lambda_n \lesssim 10^5$ GeV.[3] These two considerations suggest that the region of interest corresponds to values of the couplings

$$y_{ud} \cdot y_{Nd} \gtrsim 5 \times 10^{-5} \left(\frac{M_\phi}{700\text{ GeV}}\right)^2, \tag{7.51}$$

where the benchmark choice of $M_\Phi = 700$ GeV will be justified below.

We aim to determine whether Φ decays promptly within the detectors volume to evaluate the expected experimental signatures. To estimate the maximum distance Φ can travel before decaying, we calculate its lifetime, accounting for the two decay channels, $\Phi \to \overline{N}d$ and $\Phi \to \bar{u}\bar{d}$. The lifetime of Φ is given by

$$\tau_\Phi = \frac{1}{\Gamma_\Phi} = \frac{16\pi}{\left(y^2_{ud} + y^2_{Nd}\right) M_\Phi}. \tag{7.52}$$

[3] Higher values of Λ_n are allowed if m_N avoids the upper limit considered in Section 6.2.2.3, which is achieved if dark matter freezes out into other particle species. This relaxes the limit in Eq. (7.51).

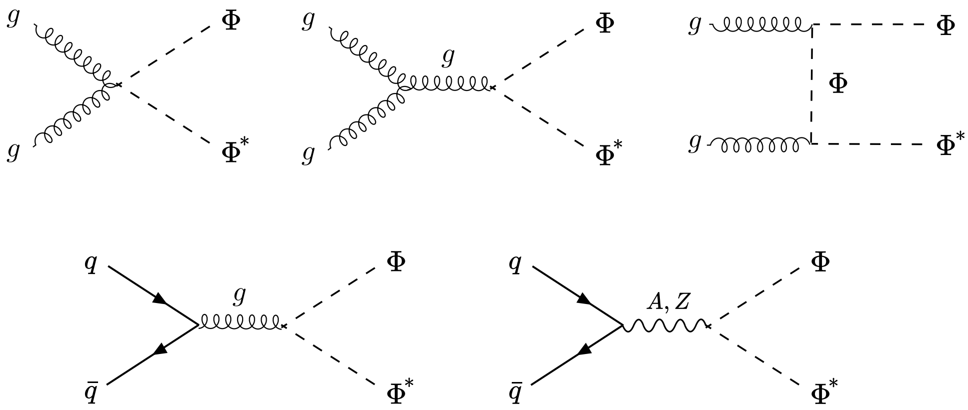

Fig. 7.10: Processes contributing to the unavoidable production of the neutron portal mediator in proton-proton collisions, driven by its gauge interactions.

The decay length in the laboratory frame is given by

$$L_\Phi = v\gamma\tau_\Phi, \tag{7.53}$$

where v is the velocity of Φ and γ is the boost factor. Unlike the lighter N particles discussed in Section 6.2.2.4, the heavier Φ particles are expected to be non-relativistic, so we approximate $\gamma \approx 1$. Using Eq. (7.51) along with the assumption that $M_\Phi \gtrsim 700$ GeV, we estimate the maximum decay length to be:[4]

$$L_\Phi^{\max} \approx 10^{-7}\mu\text{m}. \tag{7.54}$$

Consequently, we will focus on prompt decay signatures in our analysis.

7.2.1 Collider constraints: production via gauge interactions

The production of Φ and Φ^* particles via gauge interactions, illustrated in Fig. 7.10, is an unavoidable feature of the model. Since this production proceeds mainly through the strong coupling g_s, it remains highly efficient regardless of the values of the Yukawa couplings y_{ud} and y_{Nd}.

After the resonant or non-resonant gauge production of Φ and Φ^* pairs, these particles decay through their Yukawa interaction terms.[5] The branching ratios for Φ and Φ^*

[4] In our calculation, we use the simplifying assumption $v \approx c$, which significantly overestimates the decay length. Even under this approximation, we find that Φ decays promptly within the detector.

[5] If Φ is produced off-shell, there also exists a potential diphoton and digluon signature mediated solely through gauge interactions. However, due to the high SM background for these processes, they are not expected to provide meaningful sensitivity. As a result, we do not focus on these signatures.

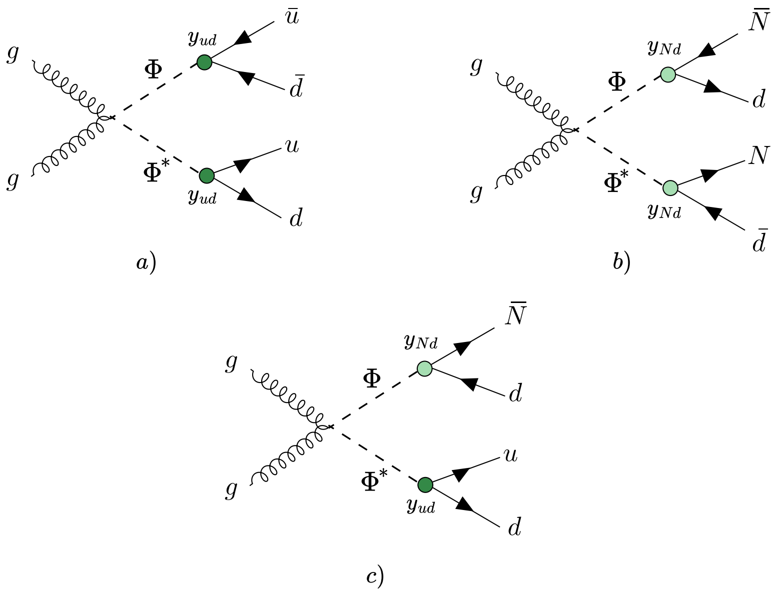

Fig. 7.11: Mixed gauge and Yukawa interaction processes mediated by the neutron portal in proton-proton collisions: *a*) Dijet paired production, dominating when $y_{ud} \gg y_{Nd}$. *b*) Monojet plus missing energy paired production, dominating when $y_{Nd} \gg y_{ud}$. *c*) Combined signature of monojet plus missing energy and dijet production, becoming significant alongside *a*) and *b*) when $y_{ud} \simeq y_{Nd}$. Notice that the gauge production shown here corresponds to the first diagram in Fig. 7.10, but the other two channels also are present.

decays are given by

$$\mathrm{Br}\left(\Phi \to \bar{u}\bar{d}\right) = \mathrm{Br}\left(\Phi^* \to ud\right) = \frac{y_{ud}^2}{y_{ud}^2 + y_{Nd}^2}\,, \tag{7.55}$$

$$\mathrm{Br}\left(\Phi \to \overline{N}d\right) = \mathrm{Br}\left(\Phi^* \to N\bar{d}\right) = \frac{y_{Nd}^2}{y_{ud}^2 + y_{Nd}^2}\,. \tag{7.56}$$

Depending on these branching ratios, there are three possible final states, as illustrated in Fig. 7.11:

a) The final state is a pair of dijets. Dominates when $y_{ud} \gg y_{Nd}$.

b) The final state consists of two jets plus missing energy. Dominates when $y_{Nd} \gg y_{ud}$.

c) The final state consists of a monojet plus missing energy and a dijet. This type of signature becomes relevant only when $y_{Nd} \approx y_{ud}$.[6]

[6] Note that in Fig. 7.11, only one of the two possible configurations is shown; the complex conjugated final state is also possible.

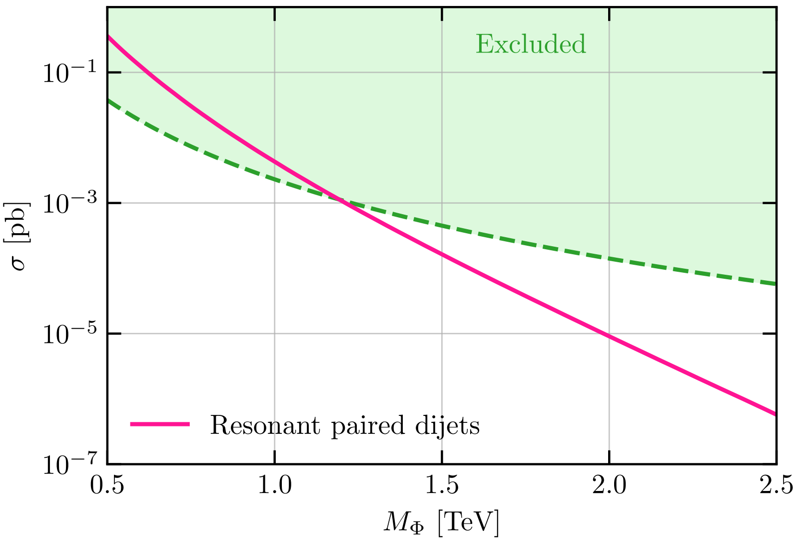

Fig. 7.12: Cross section for resonant gauge production of Φ and Φ^* decaying into a pair of dijets as a function of the mediator mass M_Φ, assuming $y_{ud} \gg y_{Nd}$. The computed cross section (pink) was obtained using MadGraph5_aMC@NLO. The green shaded region indicates the exclusion limits set by ATLAS [227, 228] and CMS [229], fitted with a polynomial function since we are interested in the overall trend. This comparison rules out mediator masses below $M_\Phi \lesssim 1.25$ TeV.

In most of the parameter space, cases a) and b) dominate, so we focus our analysis on these types of signature.

The particles Φ and Φ^* can be produced either resonantly or non-resonantly. When the mediators are off-shell, the resulting signatures are exceedingly difficult to trace back to the original collision due to the lack of a well-defined energy in the final states. These processes then suffer from hight SM backgrounds, making discrimination virtually impossible. Consequently, the prospects for detection are significantly improved if the final particles are produced through a resonance, as such events provide a distinct signal. For resonant production, applying cuts on the invariant mass of the final-state particles, centered around the mediator mass, can help isolate the signal from the large SM background.

We begin by examining the resonant pair of dijets signature, case a) in Fig. 7.11, which becomes relevant when $y_{ud} \gg y_{Nd}$. Experimental searches by ATLAS [227, 228] and CMS [229] have placed constraints on such signatures over a range of mediator masses. To evaluate the cross section for this process, we use MadGraph5_aMC@NLO [230], with model files generated using FeynRules [231] and UFO [232]. Fig. 7.12 shows the computed cross section (purple) as a function of M_Φ, alongside the region excluded by collider experiments. Note that the cross section for this process is independent of the value of y_{ud} under the assumption that Φ and Φ^* are produced resonantly and decay exclusively into dijet final states. Within this region of the Yukawa coupling parameter

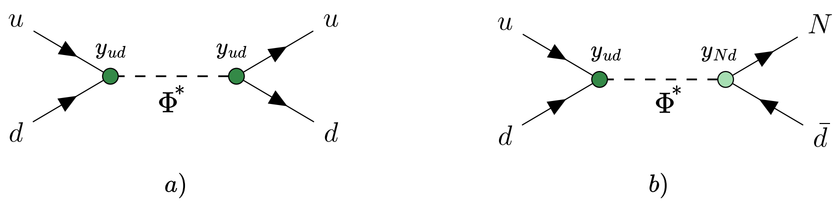

Fig. 7.13: Purely Yukawa processes mediated by the neutron portal in proton-proton collisions: a) Dijet signal, which dominates when $y_{ud} \gg y_{Nd}$. b) Monojet plus missing energy signal, which dominates when $y_{Nd} \gg y_{ud}$. In both cases, the conjugate processes are also present but are subdominant due to the parton distribution functions of the proton.

space, mediator masses below $M_\Phi \lesssim 1.25$ TeV are excluded.[7]

In the scenario where $y_{Nd} \gg y_{ud}$, corresponding to case b) in Fig. 7.11, the expected signal consists of two jets and missing energy. While there have been some searches for this type of signature, they have not been extensively explored. The CMS experiment has placed constraints on the mass of such mediators, excluding $M_\Phi \lesssim 700$ GeV [233]. This represents the weakest exclusion limit for the unavoidable production of Φ and Φ^*, making it the absolute lower bound for the mediator mass in this scenario.

7.2.2 Collider constraints: production via Yukawa interactions

In addition to the production of the mediator through gauge interactions in proton-proton collisions, Φ and Φ^* can also be produced resonantly via the $\phi \bar{u}^c d$ Yukawa interaction for sufficiently large values of y_{ud}, as illustrated in Fig. 7.13. The resulting final states depend on the branching ratios of Φ, and are:

a) A dijet, which dominates when $y_{ud} \gg y_{Nd}$.

b) A monojet plus missing energy, which dominates when $y_{Nd} \gg y_{ud}$.

To identify the values of y_{ud} and M_Φ for which Yukawa-driven production dominates, we calculate the cross section for this process using MadGraph5_aMC@NLO. Focusing on the resonant production of Φ and Φ^*, the cross section scales with y_{ud}^2. Once produced, the mediator decays into various final states, with the branching ratios determining the fraction of events in each channel. Fig. 7.14 compares the Yukawa-driven and gauge-mediated production cross sections over a range of mediator masses. The dashed lines in different shades of blue represent the Yukawa production for various

[7]Note that all cross sections generated with MadGraph5_aMC@NLO in this work are computed at leading order. Including next-to-leading order (NLO) contributions would refine the predictions and potentially strengthen the resulting constraints.

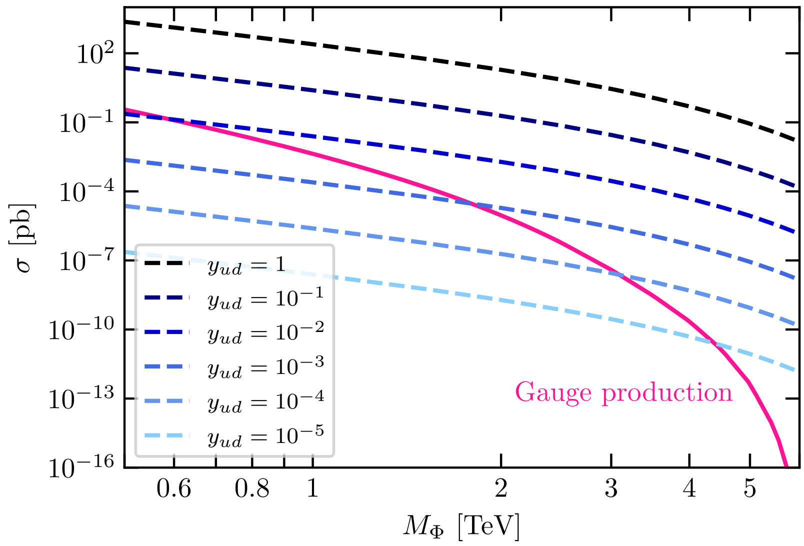

Fig. 7.14: Comparison of resonant production cross sections for Φ and Φ^* mediated by gauge interactions (solid pink line) and Yukawa interactions (dashed blue lines) across a range of mediator masses M_ϕ. The Yukawa cross sections are shown for different values of the coupling y_{ud}. The computed cross sections were obtained using MadGraph5_aMC@NLO. For sufficiently large y_{ud}, Yukawa interactions dominate.

values of the coupling y_{ud}, while the solid pink line shows the cross section for gauge-mediated production. As the figure shows, for a reasonable range of y_{ud}, Yukawa interactions can dominate the production of Φ and Φ^* particles. Hence, we aim to explore these signatures in more detail, particularly to determine whether there exists a range of couplings that are consistent with collider constraints while also satisfying the BBN limit.

When y_{ud} is relatively large, and $y_{ud} > y_{Nd}$ the dijet signature becomes dominant. In this scenario, we focus on resonant dijet production. Constraints on such signatures have been searched for by ATLAS [234] and CMS [235], which combined examine a range of mediator masses from 500 GeV to 8 TeV. Fig. 7.15 presents the excluded mass ranges for values of Yukawa couplings that yield constraints, based on a comparison between our calculated cross sections for resonant dijet signatures and the experimental exclusion limits. These experiments constrain the product of the cross section and the branching ratio, making the limits valid only under the assumption $y_{ud} \gg y_{Nd}$. We have verified that the whole constrained region can satisfy this assumption while also respecting the BBN requirement, following Eq. (7.51).

Finally, in the scenario where y_{ud} is sufficiently large for Yukawa production to dominate, and $y_{Nd} > y_{ud}$, the single jet plus missing energy signature becomes the dominant signal. While some studies have explored this type of signature [236, 237], a comprehensive systematic analysis is still lacking, which would be essential to impose

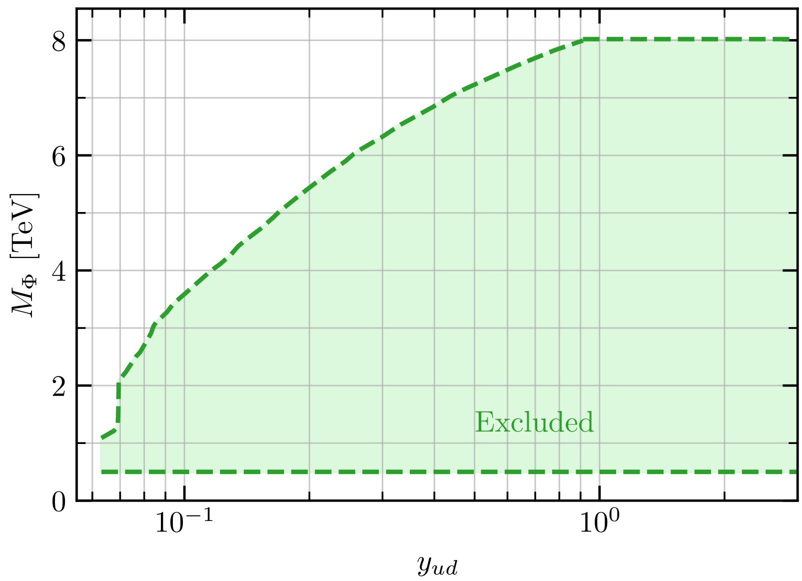

Fig. 7.15: Exclusion limits on the mediator mass M_Φ in our scenario derived from resonant dijet searches. The shaded green region indicates the parameter space excluded by experiments [234, 235]. The constraints are shown as a function of the Yukawa coupling y_{ud}, assuming $y_{ud} \gg y_{Nd}$. The constraints are consistent with BBN, see main text for details. The computed cross sections were obtained using MadGraph5_aMC@NLO.

robust constraints on the model. Notably, this signature represents the most distinctive feature of our framework.

Some studies [238, 239] analyze data on jets plus missing transverse energy from CMS [240, 241] and ATLAS [242, 243], reporting evidence of a consistent excess in both datasets with a global significance of 2.5σ. They propose that this excess could be explained by the resonant production of a heavy colored scalar decaying into a quark and an invisible particle, analogously to our scenario. Their best fit for the masses of these particles is $(M_\Phi, m_N) = (1250, 900)$ GeV. The value of M_Φ aligns well with our scenario, and m_N could also fit if dark matter primarily freezes out into particles other than N, which we explore in Section 7.3.3.

7.2.3 Collider constraints: summary

In this section, we analyzed the UV completion of the neutron portal and identified new production channels that should be included in any systematic study of this model. Our findings indicate that the model is not fully excluded and remains testable at both current and future collider experiments. Notably, the available constraints for resonant dijet signatures can encompass the entire allowed parameter space for Λ_n, shown in Fig. 6.6, for specific choices of parameters in the UV completion. Remarkably, certain key signatures have not been thoroughly explored in collider searches. In particular, the monojet plus missing energy signature, which is one of the most distinctive signals of this framework, requires more comprehensive and systematic searches. Such an approach could provide a more complete understanding of the model's viability and open new opportunities for collider-based discovery.

Finally, while we have primarily focused on the neutron portal, similar UV completions can be considered for alternative portals where Φ couples to different quark generations. If the interaction does not involve the top quark, the overall phenomenology remains largely unchanged. The strong production of Φ is unaffected, as it depends only on QCD interactions, and the decays still result in jets, regardless of the type of quark they originate from. The Yukawa-driven production channels would experience some suppression from the parton distribution functions for second- and third-generation quarks. To mitigate this suppression, studies such as [236] have considered production mechanisms involving a gluon in the initial state. Additionally, flavor constraints could impose further limitations depending on the specific generation involved. Nonetheless, the collider constraints derived in this section remain broadly applicable across different portal scenarios, making them a robust probe of this class of models.

7.3 UV completion of freeze-out

In this Section, we discuss the UV completion for dark matter to freeze out into the observed relic abundance. First, in Subsection 7.3.1, we examine whether freeze-out can be achieved using the particles already present in the model. Since these particles do not provide interactions strong enough to drive dark matter annihilation efficiently, we then consider the introduction of new particles. In Subsection 7.3.2, we explore how new heavy particles, either scalar or fermionic, can effectively reproduce the EFT dynamics for freeze-out introduced in Chapter 5. Finally, in Subsection 7.3.3, we introduce a very light scalar particle, S, into which dark matter freezes out, and which remains in the universe as a subcomponent of dark matter. We show that this scenario is compatible with cosmological measurements such as N_{eff}. Moreover, in this setup, dark matter does not need to be kinematically allowed to annihilate into N and $\overline{N}$, which lifts the upper bound on the mass of N and expands the parameter space of the neutron portal.

7.3.1 Can existing particles drive freeze-out?

Here, we investigate explicitly whether the Majorana fermions φ_i, responsible for asymmetry generation, or the colored mediator of the neutron portal Φ can drive dark matter freeze-out. However, we find that neither of these particles can provide interactions strong enough to achieve the required dark matter annihilation.

7.3.1.1 Heavy Majorana fermions φ_i

In Section 7.1, we introduced the heavy Majorana fermions φ_1 and φ_2, which can generate the asymmetry in the dark sector through a mechanism similar to leptogenesis.

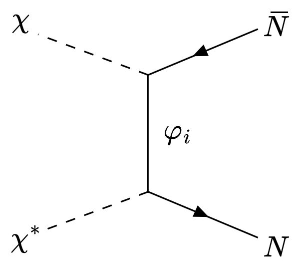

Fig. 7.16: Feynman diagram illustrating the annihilation process $\chi\chi^* \to N\bar{N}$ mediated by the heavy Majorana fermions φ_1 and φ_2. This process contributes to the generation of the effective energy scale Λ_0, which governs the dark matter freeze-out.

As discussed in Section 7.1.4, these particles also play a role in the washout processes (see Fig. 7.4), which in the EFT framework are mediated by the energy scale Λ_2.

Additionally, φ_1 and φ_2 can mediate the annihilation process $\chi\chi^* \to N\bar{N}$, which contributes to the dark matter freeze-out, as illustrated in Fig. 7.16. This process is associated with the generation of the EFT energy scale Λ_0. However, as shown in Eq. (5.47), the energy scale Λ_2 must be higher than $\sim 10^{10}$ GeV, to prevent the erasure of the dark sector asymmetry. In contrast, for dark matter freeze-out to be efficient, Λ_0 must be significantly lower. A numerical analysis solving the Boltzmann equations (5.54) and (5.55), indicates that Λ_0 should not exceed $\sim 10^4$ GeV, as shown in Fig. 5.10.

This large disparity in energy scales cannot be accommodated if both interactions originate from processes mediated by particles of the same mass. Therefore, we conclude that the contribution of φ_1 and φ_2 to the generation of Λ_0, which governs dark matter freeze-out, is negligible.

7.3.1.2 Heavy color-triplet scalar Φ

In Section 7.2, we introduced the color triplet scalar Φ as a UV completion of the neutron portal. Here, we investigate whether this particle could also drive dark matter freeze-out by mediating the annihilation process $\chi\chi^* \to N\bar{N}$.

The interaction term between dark matter and the neutron portal mediator, which is a colored and electromagnetically charged particle, is given by:

$$\mathcal{L} \supset \lambda_{\chi\Phi}|\chi|^2|\Phi|^2 \,. \tag{7.57}$$

Fig. 7.17 illustrates the loop diagram in which Φ contributes to the freeze-out into N and $\bar{N}$. This contribution arises from the interactions described in Eq. (7.57) and the second term of Eq. (7.49).

To compute the one-loop cross section for this process, we implement the relevant particles and interactions from our model on FeynRules [231] to generate the necessary model files for amplitude calculations. We then employ FeynArts [244] to generate

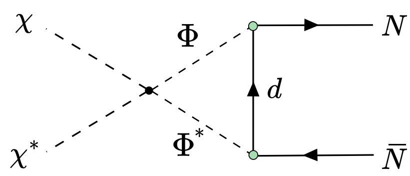

Fig. 7.17: Loop diagram illustrating the contribution of the color triplet scalar Φ to the dark matter annihilation process $\chi\chi^* \to N\bar{N}$. The interactions involved are described by the Lagrangian terms in Eqs. (7.49) and (7.57).

the Feynman diagrams and amplitudes, which are further processed with FeynCalc [245] for algebraic manipulations and simplifications. Finally, we handle loop integrals using FeynHelpers [246], which provides access to Package-X [247] for Passarino-Veltman decomposition.

We find that the cross section for this process is given by:[8]

$$\sigma^{\Phi}_{\chi\chi^*\to N\bar{N}} \simeq \frac{\lambda^2_{\chi\Phi}\, y^4_{Nd}\, m_N^2\,(m_\chi^2 - m_N^2)}{16384\,\pi^5\, M_\Phi^4\, m_\chi^2}. \tag{7.58}$$

By setting $m_\chi = 1.9$ GeV, $m_N = 1$ GeV, and using the best-case scenario values for the couplings and for the mediator mass (derived in Section 7.2), we obtain:

$$\sigma^{\Phi}_{\chi\chi^*\to N\bar{N}} \simeq 6\times 10^{-13}\,\mathrm{GeV}^{-2}\left(\frac{\lambda_{\chi\Phi}}{10}\right)^2\left(\frac{y_{Nd}}{10}\right)^4\left(\frac{700\,\mathrm{GeV}}{M_\phi}\right)^4. \tag{7.59}$$

This value is several orders of magnitude below the standard requirement for dark matter freeze-out, typically $\langle\sigma v\rangle = 10^{-9}$ GeV^{-2}. Consequently, the process $\chi\chi^* \to N\bar{N}$ mediated by Φ alone is insufficient to drive dark matter freeze-out.

An alternative possibility is to allow dark matter to freeze out into particles other than N, such as quarks, photons, or gluons. It is interesting to note that such processes were not present in the EFT framework introduced in Chapter 5, as their inclusion would have appeared somewhat ad hoc. However, within a UV-complete framework, we find that these interactions can naturally emerge under rather economical assumptions. This approach has the advantage of lifting the upper bound on m_N (see Fig. 6.6), since the annihilation process $\chi\chi^* \to N\bar{N}$ no longer needs to be kinematically allowed. Importantly, this modification does not qualitatively alter key features of the model,

[8] Since the interaction structure involves chiral projectors P_R and P_L, the loop amplitude is affected by the well-known γ_5 problem in dimensional regularization. Specifically, γ_5 is inherently four-dimensional, and its anticommutation with γ^μ is not well-defined in $d = 4-\epsilon$ dimensions. To handle this, we use the Breitenlohner-Maison-'t Hooft-Veltman (BMHV) scheme [248, 249], where γ_5 is kept in four dimensions while other gamma matrices are extended to d.

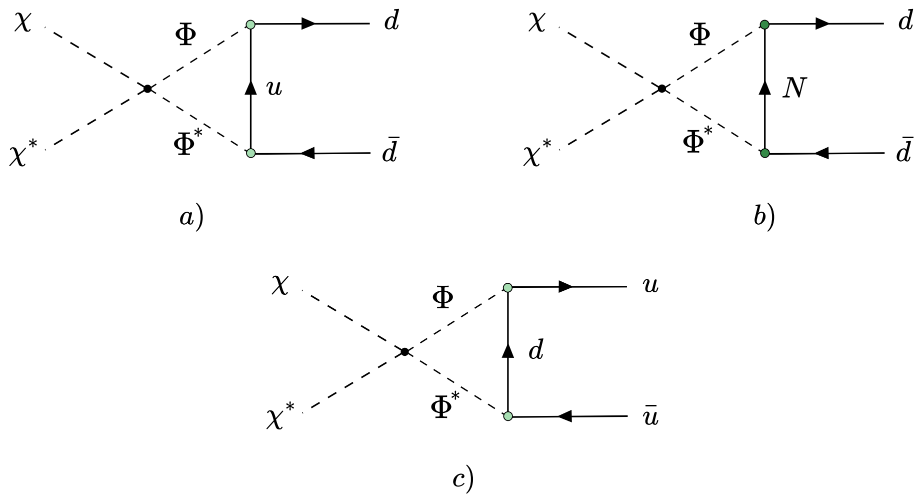

Fig. 7.18: Feynman diagrams depicting the annihilation of dark matter into quark-antiquark pairs ($\chi\chi^* \to q\bar{q}$) mediated by the neutron portal. Diagrams *a*) and *b*) show the processes for $d\bar{d}$ final states, while *c*) shows the process for $u\bar{u}$. The interactions involved are described by the Lagrangian terms in Eqs. (7.49) and (7.57).

such as asymmetry redistribution, nor does it affect the main conclusions drawn in the previous chapters.

If dark matter freezes out into quarks, the relevant processes involving the neutron portal mediator are illustrated in Fig. 7.18.

Since the quarks involved in the neutron portal interactions are right-handed, the cross sections for these final states are chirality-suppressed. Angular momentum conservation requires one of the final-state quarks to flip helicity. Since helicity flipping is mediated by the quark mass, the cross section scales as m_q^2, making it highly suppressed for light quarks. For example, considering diagram 7.18 *a*), the cross section for the process $\chi\chi^* \to d\bar{d}$ is given by:

$$\sigma^{\phi,\,a)}_{\chi\chi^*\to d\bar{d}} \simeq \frac{3\,\lambda_{\chi\Phi}^2\,y_{ud}^4\,m_d^2\,(2m_\chi^2 - m_d^2)}{8192\,\pi^5\,M_\Phi^4\,m_\chi^2}. \tag{7.60}$$

Using the same benchmark values as before and taking $m_d = 4.7$ MeV [17], we obtain:

$$\sigma^{\phi,\,a)}_{\chi\chi^*\to d\bar{d}} \simeq 2\times 10^{-16}\,\mathrm{GeV}^{-2}\left(\frac{\lambda_{\chi\Phi}}{10}\right)^2\left(\frac{y_{ud}}{10}\right)^4\left(\frac{700\,\mathrm{GeV}}{M_\phi}\right)^4. \tag{7.61}$$

This result is even more suppressed than the annihilation cross section into N and $\overline{N}$, given in Eq. (7.59). Moreover, including contributions from the remaining diagrams does not significantly improve the total cross section. As a result, this annihilation channel is too inefficient to drive dark matter freeze-out.

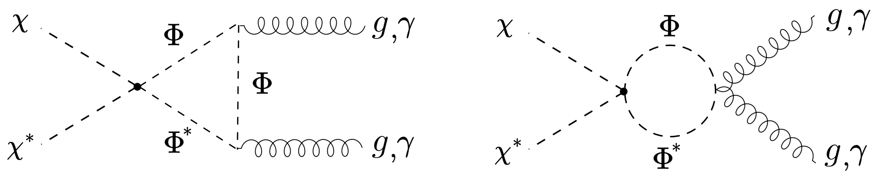

Fig. 7.19: Feynman diagrams illustrating the annihilation of dark matter into two gluons ($\chi\chi^* \to gg$) or two photons ($\chi\chi^* \to \gamma\gamma$) mediated by the neutron portal scalar Φ. The interactions involved are described by the Lagrangian term in Eqs. (7.48) and (7.57).

The chirality suppression could be lifted by considering radiative corrections to these processes, such as final states including an additional photon or gluon ($\chi\chi^* \to q\bar{q}\gamma$ or $\chi\chi^* \to q\bar{q}g$). The photon or gluon can carry angular momentum, removing the need for a helicity flip via the quark mass. As a result, the cross section could be significantly enhanced, possibly counteracting the suppression associated with the 3-body phase space.

To verify this, we compute, for example, the diagrams analogous to 7.18 a), where a photon is radiated from one of the charged particles involved, leading to the process $\chi\chi^* \to d\bar{d}\gamma$. Summing over all such diagrams, we obtain:

$$\sigma^{\phi,\,a)}_{\chi\chi^*\to d\bar{d}\gamma} \simeq \frac{e^2\,\lambda^2_{\chi\Phi}\,y^4_{ud}\,m^2_\chi}{1179648\sqrt{2}\,\pi^7\,M^4_\Phi\,v}, \tag{7.62}$$

where e is the electromagnetic charge coupling constant.[9] Evaluating this expression, we find:

$$\sigma^{\phi,\,a)}_{\chi\chi^*\to d\bar{d}\gamma}\cdot v \simeq 3\times10^{-16}\,\mathrm{GeV}^{-2}\left(\frac{\lambda_{\chi\Phi}}{10}\right)^2\left(\frac{y_{ud}}{10}\right)^4\left(\frac{700\,\mathrm{GeV}}{M_\phi}\right)^4. \tag{7.63}$$

This result shows only a marginal improvement over Eq. (7.61). Furthermore, incorporating additional diagrams that contribute to the final states $d\bar{d}\gamma$, as well as the analogous processes $u\bar{u}\gamma$, $d\bar{d}g$, and $u\bar{u}g$ while accounting for the appropriate color factors, does not bring the total cross section to the level required for efficient dark matter freeze-out.

Finally, we examine the annihilation of dark matter into two photons or gluons mediated by the scalar mediator Φ. The corresponding Feynman diagrams for this process are shown in Fig. 7.19. For the annihilation into gluons, we obtain the cross section:

$$\sigma^{\Phi}_{\chi\chi^*\to gg} \simeq \frac{g_s^4\,C_A\,C_F\,\lambda^2_{\chi\Phi}\,m^2_\chi}{18432\,\pi^5\,M^4_\Phi}, \tag{7.64}$$

[9] Infrared divergences, which typically arise from soft photon emission off external quark legs, are absent in this case. This is because such divergences are proportional to the cross section of the 2-body process $\chi\chi^* \to d\bar{d}$, which is chirality suppressed.

where g_s is the strong coupling constant, and $C_A = 3$ and $C_F = 4/3$ are the Casimir operators for the adjoint and fundamental representations of $SU(3)$, respectively. This leads to:

$$\sigma^{\phi}_{\chi\chi^*\to gg} \simeq 10^{-19}\,\mathrm{GeV}^{-2}\left(\frac{\lambda_{\chi\Phi}}{10}\right)^2\left(\frac{700\,\mathrm{GeV}}{M_\phi}\right)^4. \tag{7.65}$$

The annihilation into photons is found to be even less efficient.

We conclude that the neutron portal mediator alone does not provide a sufficient contribution to dark matter annihilation to achieve freeze-out and match the observed relic abundance. Therefore, additional particles and interactions are required to facilitate an efficient freeze-out mechanism.

7.3.2 Addition of new heavy particles

In the previous section, we explored various processes that could efficiently drive dark matter freeze-out with particles already present in our model, but found that none were sufficient. This led us to conclude that additional particles are needed to achieve the required annihilation rates.

To exactly reproduce the energy scale Λ_0 in the EFT framework presented in Chapter 5, the simplest approach is to introduce a new heavy particle that carries no baryon number or other quantum numbers. In this section we explore the freeze-out via the introduction of a heavy scalar or fermionic particle.

7.3.2.1 Heavy scalar X as an s-channel mediator

A natural candidate for this role is a real scalar X with mass M_X, whose interaction terms are described by the Lagrangian:

$$\mathcal{L}_X^{\mathrm{inter}} \supset \lambda_3 X|\chi|^2 + y_X X\overline{N}N, \tag{7.66}$$

where λ_3 is a coupling with mass dimension one, and y_X is a dimensionless coupling.

The scalar X mediates the annihilation process $\chi\chi^* \to N\overline{N}$ via the s-channel, as illustrated in Fig. 7.20 a). The corresponding cross section is:

$$\sigma^X_{\chi\chi^*\to N\overline{N}} \simeq \frac{\lambda_3^2\, y_X^2\,(s-4m_N^2)^{3/2}}{8\pi s(M_X^2-s)^2\sqrt{s-4m_\chi^2}}. \tag{7.67}$$

By comparing this result with the EFT cross section in Eq. (5.12), we identify the matching condition for the energy scale is:

$$\Lambda_0^X \simeq \frac{M_X^2}{\lambda_3\, y_X}. \tag{7.68}$$

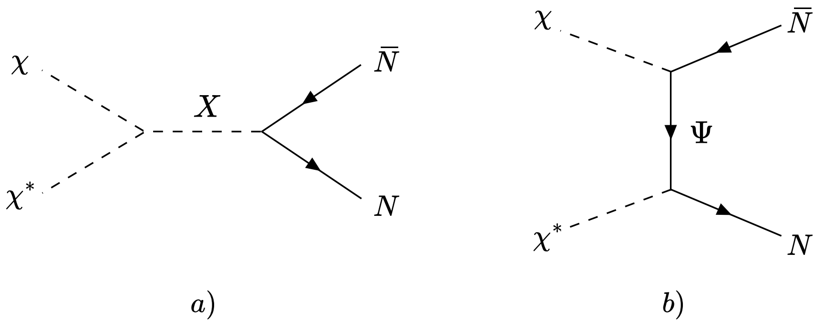

Fig. 7.20: Feynman diagrams illustrating dark matter annihilation into N and $\overline{N}$ mediated by new heavy particles. In panel $a)$ the process occurs via an s-channel exchange of a real scalar X, while in panel $b)$ it proceeds through a t-channel exchange of a heavy fermion Ψ. The interaction terms corresponding to these diagrams are given in the Lagrangians of Eq. (7.66) and Eq. (7.70).

To achieve the standard freeze-out cross section $\langle \sigma v \rangle \simeq 10^{-9}$ GeV^{-2}, the required mass for the mediator is

$$M_X \lesssim 84\,\mathrm{GeV}\left(\frac{\lambda_3}{\mathrm{GeV}}\right)^{1/2}\left(\frac{y_X}{1}\right)^{1/2} \tag{7.69}$$

for $m_\chi = 1.9$ GeV and $m_N = 1$ GeV. This mass range is feasible for an uncharged particle.

7.3.2.2 Heavy fermion Ψ as a t-channel mediator

Another possible mediator is a heavy fermion Ψ, of mass M_Ψ, which interacts with the other dark sector particles in our model as:

$$\mathcal{L}_\Psi^{\mathrm{inter}} \supset y_\Psi \bar{\Psi} N \chi + h.c.\,, \tag{7.70}$$

where y_Ψ is a dimensionless Yukawa coupling. In this scenario, Ψ mediates dark matter annihilation via a t-channel exchange, as illustrated in Fig. 7.20 $b)$. The cross section for the process is given by

$$\sigma^\Psi_{\chi\chi^*\to N\overline{N}} \simeq \frac{y_\Psi^4\,(s-4m_N^2)^{3/2}}{8\pi s M_\Psi^2\sqrt{s-4m_\chi^2}}. \tag{7.71}$$

By comparing again with the EFT cross section in Eq. (5.12), we extract the following correspondence with the energy scale

$$\Lambda_0^\Psi \simeq \frac{M_\Psi}{y_\Psi^2}. \tag{7.72}$$

To achieve a freeze-out cross section consistent with the observed relic abundance, the mediator mass must satisfy:

$$M_\Psi \lesssim 7 \times 10^3 \,\mathrm{GeV} \left(\frac{y_\Psi}{1}\right)^2. \tag{7.73}$$

This bound is significantly higher than the scalar mediator case shown in Eq. (7.69), making Ψ an even more viable realization of the required interactions.

Both mediators discussed in this section successfully reproduce the EFT description of our scenario. In the next section we explore the alternative of freeze-out into lighter dark particles.

7.3.3 Alternative scenario: very light scalar S

In this section, we explore the possibility of introducing a new dark scalar particle S, with mass $m_S < m_\chi$, which is uncharged under baryon number and does not couple to any SM gauge symmetries. Since this particle is lighter than dark matter, freeze-out can proceed through annihilation directly into a pair of S particles. As a result, the particle N no longer play a role in the freeze-out process, which removes the upper bound on m_N. This effectively expands the available parameter space for the neutron portal, which was shown in Fig. 6.6. This scenario does not reproduce the EFT presented in Chapter 5, but it remains consistent with the model's underlying principle of baryon number conservation and does not alter any of the key features of the framework.[10]

This scalar particle could in principle be real or complex; however, we focus here on the complex case.[11] We assume that this new particle interacts only with dark matter and itself, with interaction terms given by:

$$\mathcal{L}_S^{\mathrm{inter}} \supset \lambda_{S2} \, |\chi|^2 |S|^2 + \lambda_{S4} \, |S|^4, \tag{7.74}$$

where λ_{S2} and λ_{S4} are dimensionless couplings.

The particle S must either annihilate or decay into SM particles, or alternatively, it could persist in the universe until the present day as a subdominant component of dark matter. This will depend on the value of m_S and on its potential couplings to the visible sector.

Let us consider the scenario in which S is completely decoupled from the SM and remains in the dark sector until today.[12] In this case, its contribution to the radiation energy density must be evaluated to determine whether it is consistent with current

[10] If N is heavy and decays before sphalerons freeze out, this would imply a shift in the dark matter mass to $m_\chi \lesssim 1.6$ GeV.

[11] If S is a real scalar, dark matter self-interactions via t-channel exchange of S ($\chi\chi \leftrightarrow \chi\chi$) can occur. Given the light mass of S, the resulting self-interaction cross section would be substantial, likely ruled out by constraints from CMB observations and Bullet Cluster measurements [250].

[12] Another possibility is that S couples to the SM Higgs. In this case, after dark matter freezes out, S could decay into light hadrons or fermions through the Higgs mixing, and disappear. For a given range of mixing angles, this scenario can avoid cosmological constraints for masses m_S in the range 1 MeV to 1 GeV [251, 252].

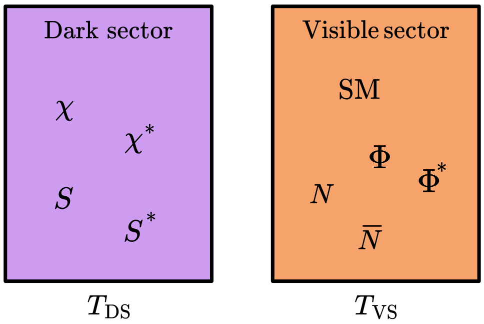

Fig. 7.21: Schematic representation of the particles composing the decoupled visible and dark sectors at high temperatures.

measurements of N_{eff}. As we will show in Section 7.3.3.3, the predicted deviation remains within the uncertainty of current Planck constraints but could be probed by next-generation experiments such as CMB-S4.

First, in Section 7.3.3.1, we review the thermal history of this dark sector. Then, in Section 7.3.3.2, we analyze the freeze-out dynamics in a secluded scenario where the dark sector temperature differs from that of the visible sector. In Section 7.3.3.3, we examine the contribution to N_{eff}, and finally, in Section 7.3.3.4, we explore the role of S as a hot relic in the dark matter density.

7.3.3.1 Thermal history of the dark sector

Here, we consider the scenario in which the particle S is very light and fully decoupled from the visible sector, allowing it to persist in the universe as a relic subcomponent of dark matter.

In order to start analyzing the thermal history of this scenario, we refer to Fig. 7.21, which provides a schematic representation of the two decoupled sectors, the visible sector (VS) and the dark sector (DS), along with their respective particle content. This depiction corresponds to temperatures below the asymmetry generation scale $T \ll T_{\mathrm{lepto}}$, as defined in Eq. (7.26), but still above the top quark mass, $T \gg m_{\mathrm{top}}$. At this stage, the heavy Majorana fermions φ_i, which generated the asymmetry and provided a connection between the two sectors, have already disappeared from the universe.

The visible sector consists of the SM particles, the neutron portal mediator Φ, and the fermion N, all in thermal equilibrium. Due to gauge interactions, as illustrated in Fig. 7.10, Φ remains in thermal equilibrium with the SM. Similarly, N maintains thermal contact with the SM through fast scattering processes such as $\Phi g \to N d$.

The dark sector, on the other hand, is composed of particles χ and S, which interact strongly enough to remain in thermal equilibrium with each other. The Majorana fermions φ_i have already decayed, but if they were in thermal equilibrium with the VS before their disappearance, their large abundance would lead to a thermal population of χ, and consequently of S. Additionally, if the interactions $\varphi_1 \leftrightarrow \chi N$ thermalize,[13] they would further enforce the thermal production of χ. Finally, a thermal population of χ could also arise from strong interactions with N.

Given this setup, it is reasonable to assume that the visible and dark sectors are initially decoupled but start off with the same temperature:

$$T_{\mathrm{DS}} = T_{\mathrm{VS}}, \tag{7.75}$$

which will evolve independently as the universe cools down.

We proceed to analyze the evolution of the dark sector temperature T_{DS}, and the dark sector energy density, ρ_{DS}. At high temperatures ($T \gg m_{\mathrm{top}}$), both species in the dark sector, χ and S, behave as relativistic particles, contributing to the total radiation energy density defined in Eq. (A.11) as:

$$\rho_{\mathrm{DS}} = \frac{\pi^2}{30}(2+2)T_{\mathrm{DS}}^4, \tag{7.76}$$

where the degrees of freedom correspond to those of complex scalars: $g_\chi = 2$ and $g_S = 2$. When dark matter freezes out, the energy density initially stored in χ and χ^* is effectively transferred to S and S^*. Thus, after freeze-out, the dark sector consists only of S and S^*, and its energy density remains:

$$\rho_{\mathrm{DS}}(T_{\mathrm{DS}} < T_{\mathrm{f.o.}}) = \rho_S(T_{\mathrm{DS}} < T_{\mathrm{f.o.}}) = \frac{\pi^2}{30}(2+2)T_{\mathrm{DS}}^4. \tag{7.77}$$

We now proceed to relate the temperature the dark and visible sectors. Once both sectors decouple, entropy conservation ensures that as various SM particles annihilate, the visible sector heats up relative to the dark sector. Following a similar procedure as in Appendix A.3 (see Eqs. (A.20)–(A.23)), we obtain:

$$T_{\mathrm{DS}} = \left(\frac{g_{\star S}(T_\gamma)}{g_{\star S}^{\mathrm{in}}}\right)^{1/3} T_\gamma, \tag{7.78}$$

where $g_{\star S}$, defined in Eq. (A.17), represents the effective relativistic degrees of freedom in the SM at a given temperature.

At the time of dark matter freeze out $T_{\mathrm{f.o.}} \sim m_\chi$, we have the contribution of the photons ($g_\gamma = 2$), the electrons and positrons ($g_e = 4$), and the neutrinos and antineutrinos ($g_\nu = 6$), all in thermal equilibrium. This gives:

$$g_{\star S}(T_\gamma \simeq m_\chi) = 2 + \frac{7}{8}\cdot(4+6) = 10.75. \tag{7.79}$$

At very high temperatures, all the SM particles are in thermal equilibrium, contributing $g_{\star S} = 106.75$ as calculated in Appendix A.2. We add the contributions of Φ ($g_\Phi = 2$) and of N ($g_N = 4$), both in thermal equilibrium with the photon plasma, obtaining:

$$g_{\star S}^{\mathrm{in}} = 106.75 + 2 + \frac{7}{8}\cdot 4 = 112.25\,. \tag{7.80}$$

[13] The thermalization of $\varphi_1 \leftrightarrow \chi N$ occurs for $\lambda_1 \geq 6\times 10^{-3}$, which is compatible with the available parameter space, see Fig. 7.9.

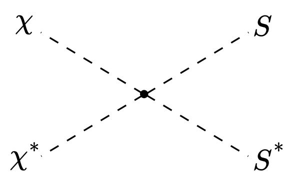

Fig. 7.22: Feynman diagram representing the annihilation of dark matter into pairs of the light scalar particles S and S^* via the interaction defined in Eq. (7.74).

Inserting these numbers into Eq. (7.78), we find

$$T_{\rm DS}(T_\gamma = m_\chi) = \left(\frac{10.75}{112.25}\right)^{1/3} T_\gamma \simeq 0.46\, T_\gamma, \tag{7.81}$$

which we must take into account when solving the Boltzmann equations for freeze-out.

7.3.3.2 Freeze-out in a colder dark sector

Fig. 7.22 illustrates the Feynman diagram contributing to dark matter freeze-out via the process $\chi\chi^* \to SS^*$. We compute the s-wave contribution to the thermally averaged cross section for this process, obtaining:

$$\langle \sigma v \rangle_{\chi\chi^* \to SS^*} \simeq \frac{\lambda_{S2}^2 \sqrt{m_\chi^2 - m_S^2}}{32\pi m_\chi^3}. \tag{7.82}$$

In the limit where $m_\chi \gg m_S$, and for the specific case of $m_\chi = 1.9$ GeV, this expression simplifies to:

$$\langle \sigma v \rangle_{\chi\chi^* \to SS^*} \simeq 10^{-9}\,\mathrm{GeV}^{-2} \left(\frac{\lambda_{S2}}{6\times 10^{-4}}\right)^2. \tag{7.83}$$

This result suggests that dark matter freeze-out can be efficiently achieved for coupling values satisfying $\lambda_{S2} \gtrsim 6 \times 10^{-4}$.

To accurately determine the values of λ_{S2} that yield the correct relic abundance, we numerically solve the coupled Boltzmann equations. In this scenario, freeze-out occurs within a secluded dark sector, meaning that the dark sector temperature differs from that of the visible sector. The temperature relation is given by Eq. (7.90), allowing us to define the variable x' in terms of the dark sector temperature:

$$x' = \frac{m_\chi}{T_{\rm DS}} = \frac{m_\chi}{0.46\, T_{\rm VS}} = \frac{x}{0.46}. \tag{7.84}$$

The Boltzmann equations governing the evolution of the total yields, $Y_\chi^{\rm tot} = Y_\chi + Y_{\chi^*}$

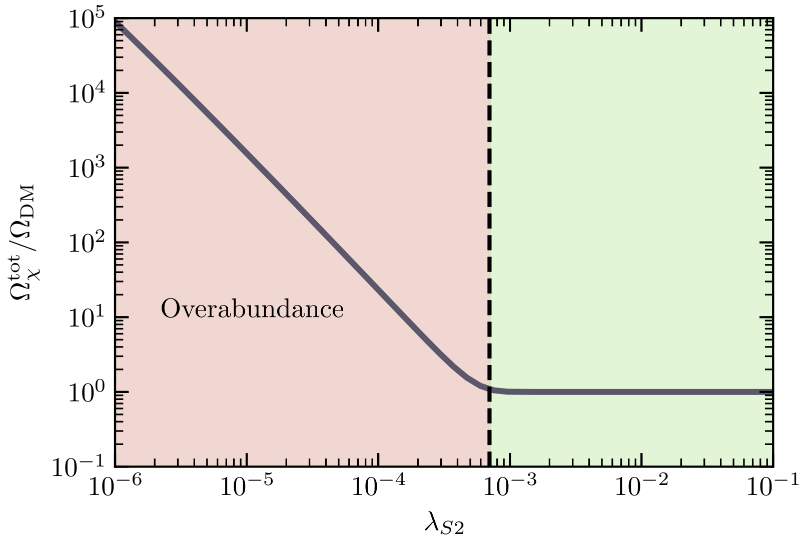

Fig. 7.23: Ratio of the energy density of the particles χ and χ^* to the observed dark matter energy density, for a range of coupling values λ_{S2}, in the case where freeze-out proceeds via the process shown in Fig. 7.22. The solution is obtained by numerically solving the coupled Boltzmann equations (7.85) and (7.86), assuming $m_\chi = 1.9$ GeV and accounting for the dark sector temperature ratio $T_{\rm DS} \simeq 0.46\,T_{\rm VS}$. For $\lambda_{S2} \lesssim 7 \times 10^{-4}$, an overabundance of χ and χ^* occurs (red region).

and $Y_S^{\rm tot} = Y_S + Y_{S^*}$ in this setup are:

$$\frac{dY_\chi^{\rm tot}}{dx} = -\,\frac{\lambda}{x^2}\left[2\langle\sigma v\rangle_{\chi\chi^*\to SS^*}\left(Y_\chi Y_{\chi^*} - \frac{Y_\chi^{\rm eq}(x')Y_{\chi^*}^{\rm eq}(x')}{Y_S^{\rm eq}(x')Y_{S^*}^{\rm eq}(x')}Y_S Y_{S^*}\right)\right], \tag{7.85}$$

$$\frac{dY_S^{\rm tot}}{dx} = +\,\frac{\lambda}{x^2}\left[2\langle\sigma v\rangle_{\chi\chi^*\to SS^*}\left(Y_\chi Y_{\chi^*} - \frac{Y_\chi^{\rm eq}(x')Y_{\chi^*}^{\rm eq}(x')}{Y_S^{\rm eq}(x')Y_{S^*}^{\rm eq}(x')}Y_S Y_{S^*}\right)\right]. \tag{7.86}$$

In Fig. 7.23, we present the numerical solution for the ratio of dark matter abundance to the observed relic abundance, across a range of values for λ_{S2}. Our results confirm that the correct relic abundance is achieved for $\lambda_{S2} \gtrsim 7 \times 10^{-4}$.

The fact that the dark sector has a lower temperature significantly impacts the freeze-out dynamics. Since the dark matter number density is proportional to $T_{\rm DS}^4$, a colder dark sector results in a lower initial density. Consequently, smaller annihilation cross sections are required to deplete dark matter to the observed relic abundance, leading to a reduced requirement for λ_{S2}.

7.3.3.3 Dark radiation and $N_{\rm eff}$

Since S remains in the universe until temperatures drop below the neutrino decoupling scale ($T \sim 1$ MeV), we need to quantify its contribution to the effective number of relativistic neutrinos, N_{eff}, and assess whether this scenario is excluded by current constraints or within the sensitivity range of future experiments. A detailed discussion on neutrino decoupling, N_{eff}, and the current bounds on ΔN_{eff} is provided in Appendix A.3.

After electron-positron annihilation, the radiation energy density of the universe, including contributions from photons and neutrinos, see Eq. (A.25), and also from S, is given by

$$\rho_r = \frac{\pi^2}{15}\left[1 + 3\frac{7}{8}\left(\frac{4}{11}\right)^{4/3}\right]T_\gamma^4 + \rho_S. \tag{7.87}$$

By comparing this to the definition of N_{eff} given in Eq. (A.26), we obtain the following expression for our scenario:

$$N_{\text{eff}} = 3 + \frac{165 \cdot 22^{1/3}}{7\pi^2}\frac{\rho_S}{T_\gamma^4}, \tag{7.88}$$

which needs to be evaluated after electron-positron annihilation.

In Eq. (7.77), we expressed the energy density ρ_S in terms of the dark sector temperature T_{DS}, expression which becomes valid after freeze-out. We now determine the relation between T_{DS} and T_γ at the relevant temperature. To do so, we recall the expression given in Eq. (7.78). After electron-positron annihilation, the radiation content consists of photons ($g_\gamma = 2$) and neutrinos ($g_\nu = 6$), which are now decoupled and contribute with a temperature ratio $T_\nu = (4/11)^{1/3}T_\gamma$, as derived in Eq. (A.24). This gives:

$$g_{\star S}(T_\gamma < m_e) = 2 + \frac{7}{8}\cdot 6 \cdot \left(\frac{4}{11}\right) \approx 3.91. \tag{7.89}$$

For $g_{\star S}^{\text{in}}$, we use the value previously obtained in Eq. (7.80). Substituting these values into Eq. (7.78), we find

$$T_{\text{DS}}(T_\gamma < m_e) = \left(\frac{3.91}{112.25}\right)^{1/3} T_\gamma \simeq 0.33\, T_\gamma, \tag{7.90}$$

and substituting this into Eq. (7.77),

$$\rho_S = \frac{2\pi^2}{15}\left(\frac{3.91}{112.25}\right)^{4/3} T_\gamma^4. \tag{7.91}$$

Finally, using Eq. (7.88), we find that in this scenario:[14]

$$N_{\text{eff}} \simeq 3.100, \tag{7.92}$$

[14] It is worth noting that our computation assumes a purely thermal distribution for S. However, half of the S particles originate from dark matter annihilation, where χ was non-relativistic. Since freeze-out occurs when $T_{\text{DS}} < m_\chi$, these annihilation-produced S particles receive a kinetic energy of approximately m_χ, which is larger than the thermal expectation. As a result, they are slightly hotter than the thermal population. This leads to a small increase in the total radiation energy density, meaning our computed N_{eff} is slightly underestimated.

which, when compared to the SM prediction $N_{\rm eff}^{\rm SM} = 3.046$ [253], gives

$$\Delta N_{\rm eff} \simeq 0.054. \tag{7.93}$$

The latest measurement from Planck 2018 [5] is

$$N_{\rm eff}^{\rm Panck} = 2.99^{+0.34}_{-0.33} \qquad (95\%\,\text{C.L.}), \tag{7.94}$$

which shows that our predicted value of $N_{\rm eff}$ lies well within the observational uncertainty, confirming the viability of this scenario. However, the next generation "Stage-4" ground-based cosmic microwave background experiment (CMB-S4) [254], which is expected to improve the uncertainty by an order of magnitude, may be able to test this prediction in the near future.

7.3.3.4 S as a hot relic and its contribution to the dark matter density

After the temperature of the dark sector falls below the mass of S, this particle will become non-relativistic. Given its stability, it may contribute to the total dark matter density. The energy density fraction of S is given by [111]:

$$\Omega_S h^2 \simeq 7.83 \times 10^{-2} \left(\frac{g_S^{\rm eff}}{g_{\star S}(T_{\rm dec})}\right) \frac{m_S}{\rm eV}, \tag{7.95}$$

where $g_S^{\rm eff}$ represents the effective number of degrees of freedom of S contributing to the energy density. In this case, we take $g_S^{\rm eff} = 4$, accounting also for the energy density transferred to S at freeze-out from dark matter. The quantity $g_{\star S}(T_{\rm dec})$ denotes the effective number of relativistic degrees of freedom in the thermal plasma when S decoupled from the SM, which, as previously argued, is $g_{\star S}(T_{\rm dec}) \approx 112.25$. Substituting these values, we obtain:

$$\Omega_S h^2 \simeq \frac{m_S}{358\,\rm eV}. \tag{7.96}$$

For comparison, the standard result for stable relic neutrinos that decouple while relativistic has a 91 eV in the denominator [111]. Since here the dark sector is colder than the neutrinos, due to its earlier decoupling, this implies a higher mass bound for S.

Given the observed total dark matter density $\Omega_{\rm DM} \simeq 0.12$ [17], we can determine the required mass of S for it to contribute a fraction $\Omega_S/\Omega_{\rm DM}$ to the total dark matter:

$$m_S \simeq 43\,\text{eV}\,\frac{\Omega_S}{\Omega_{\rm DM}}. \tag{7.97}$$

For instance, if we impose S to contribute at most 1% of the total dark matter density, its mass must satisfy:

$$m_S \lesssim 0.43\,\text{eV}. \tag{7.98}$$

This constraint ensures that S remains a subdominant dark matter component.

Chapter 8

Conclusion & Outlook

The matter-antimatter asymmetry and the nature of dark matter are two of the most fundamental open problems in modern particle physics and cosmology. In this work, we argue that since we can only measure an asymmetry within Standard Model (SM) baryons, there is no direct evidence for a baryon asymmetry in the entire universe. The unknown nature of dark matter allows it to carry the same quantum number as SM baryons, implying that the counterpart of the baryon asymmetry could be hidden within the dark sector.

A key implication of this framework is that baryon number violation is not required to account for the observed matter-antimatter asymmetry, challenging the first Sakharov condition. Instead, the necessary ingredients are C and CP violation within the dark sector, a departure from thermal equilibrium, and a portal between the dark sector and the quarks. The model presented in this work offers a minimal, baryon-conserving framework where dark matter is a baryon-charged complex scalar of mass $m_{\mathrm{DM}} \leq 1.9$ GeV, whose stability arises solely from baryon number conservation, requiring no additional symmetries.

The dark sector consists of the dark matter χ and a Dirac fermion N. An equal but opposite asymmetry is generated between the particles and antiparticles of both species. This asymmetry can arise from CP-violating decays of heavy Majorana fermions, similar to thermal leptogenesis. The asymmetry stored in N is transferred to SM quarks through scatterings and decays via the neutron portal. The UV completion of this portal involves a colored scalar mediator Φ, which is expected to be abundantly produced in colliders. This leads to distinctive experimental signatures, such as monojet events with missing energy, that apparently violate baryon number. Future analyses targeting this signal could probe the viable parameter space of the neutron portal and offer potential evidence supporting our scenario.

Dark matter freeze-out could proceed through annihilations into N or alternatively into a very light dark scalar S, which remains in the universe as a hot subcomponent of dark matter. This particle influences N_{eff} and could be tested in upcoming CMB-S4 observations.

A possible variation of this framework could involve a renormalizable neutrino portal, offering an alternative asymmetry transfer mechanism and a potential connection to neutrino mass generation.

In summary, this work connects the dark matter and quark-antiquark mysteries, demonstrating that baryon number violation is not necessary and that the universe we live in might be symmetric. The theoretical consistency, collider testability, and cosmological implications of this framework open promising directions for future research, offering a new perspective on the connection between baryonic and dark matter sectors.

Bibliography

[1] C. P. Burgess. Quantum gravity in everyday life: General relativity as an effective field theory. *Living Rev. Rel.*, 7:5–56, 2004. arXiv:gr-qc/0311082, doi:10.12942/lrr-2004-5.

[2] C. Csáki and P. Tanedo. Beyond the Standard Model. In *2013 European School of High-Energy Physics*, pages 169–268, 2015. arXiv:1602.04228, doi:10.5170/CERN-2015-004.169.

[3] A. de Gouvêa. Neutrino Mass Models. *Ann. Rev. Nucl. Part. Sci.*, 66:197–217, 2016. doi:10.1146/annurev-nucl-102115-044600.

[4] R. D. Peccei. The Strong CP problem and axions. *Lect. Notes Phys.*, 741:3–17, 2008. arXiv:hep-ph/0607268, doi:10.1007/978-3-540-73518-2_1.

[5] N. Aghanim et al. Planck 2018 results. VI. Cosmological parameters. *Astron. Astrophys.*, 641:A6, 2020. [Erratum: Astron.Astrophys. 652, C4 (2021)]. arXiv:1807.06209, doi:10.1051/0004-6361/201833910.

[6] G. Bertone, D. Hooper, and J. Silk. Particle dark matter: Evidence, candidates and constraints. *Phys. Rept.*, 405:279–390, 2005. arXiv:hep-ph/0404175, doi:10.1016/j.physrep.2004.08.031.

[7] K. Freese. Review of Observational Evidence for Dark Matter in the Universe and in upcoming searches for Dark Stars. *EAS Publ. Ser.*, 36:113–126, 2009. arXiv:0812.4005, doi:10.1051/eas/0936016.

[8] F. Zwicky. Die Rotverschiebung von extragalaktischen Nebeln. *Helv. Phys. Acta*, 6:110–127, 1933. doi:10.1007/s10714-008-0707-4.

[9] V. C. Rubin and W. K. J. Ford. Rotation of the Andromeda Nebula from a Spectroscopic Survey of Emission Regions. *Astrophysical Journal*, 159:379, 1970. doi:10.1086/150317.

[10] K. G. Begeman, A. H. Broeils, and R. H. Sanders. Extended rotation curves of spiral galaxies: dark haloes and modified dynamics. *Monthly Notices of the Royal Astronomical Society*, 249(3):523–537, 04 1991. URL: https://doi.org/10.1093/mnras/249.3.523, doi:10.1093/mnras/249.3.523.

[11] E. W. Greisen, K. Spekkens, and G. A. van Moorsel. Aperture synthesis observations of the nearby Spiral NGC 6503: modeling the thin and thick H I disks.

The Astronomical Journal, 137(6):4718–4733, apr 2009. URL: https://doi.org/10.1088/0004-6256/137/6/4718, doi:10.1088/0004-6256/137/6/4718.

[12] H. Hoekstra, H. Yee, and M. Gladders. Current status of weak gravitational lensing. *New Astron. Rev.*, 46:767–781, 2002. arXiv:astro-ph/0205205, doi:10.1016/S1387-6473(02)00245-2.

[13] D. Clowe, M. Bradac, A. H. Gonzalez, M. Markevitch, S. W. Randall, C. Jones, and D. Zaritsky. A direct empirical proof of the existence of dark matter. *Astrophys. J. Lett.*, 648:L109–L113, 2006. arXiv:astro-ph/0608407, doi:10.1086/508162.

[14] M. Markevitch. Chandra observation of the most interesting cluster in the universe. *ESA Spec. Publ.*, 604:723, 2006. arXiv:astro-ph/0511345.

[15] P. J. E. Peebles. Growth of the nonbaryonic dark matter theory. *Nature Astron.*, 1(3):0057, 2017. arXiv:1701.05837, doi:10.1038/s41550-017-0057.

[16] T.-H. Yeh, K. A. Olive, and B. D. Fields. The impact of new $d(p,\gamma)3$ rates on Big Bang Nucleosynthesis. *JCAP*, 03:046, 2021. arXiv:2011.13874, doi:10.1088/1475-7516/2021/03/046.

[17] S. Navas et al. Review of particle physics. *Phys. Rev. D*, 110(3):030001, 2024. doi:10.1103/PhysRevD.110.030001.

[18] T.-H. Yeh, J. Shelton, K. A. Olive, and B. D. Fields. Probing physics beyond the standard model: limits from BBN and the CMB independently and combined. *JCAP*, 10:046, 2022. arXiv:2207.13133, doi:10.1088/1475-7516/2022/10/046.

[19] B. D. Fields, K. A. Olive, T.-H. Yeh, and C. Young. Big-Bang Nucleosynthesis after Planck. *JCAP*, 03:010, 2020. [Erratum: JCAP 11, E02 (2020)]. arXiv:1912.01132, doi:10.1088/1475-7516/2020/03/010.

[20] L. J. Hall, K. Jedamzik, J. March-Russell, and S. M. West. Freeze-In Production of FIMP Dark Matter. *JHEP*, 03:080, 2010. arXiv:0911.1120, doi:10.1007/JHEP03(2010)080.

[21] Y. Hochberg, E. Kuflik, T. Volansky, and J. G. Wacker. Mechanism for Thermal Relic Dark Matter of Strongly Interacting Massive Particles. *Phys. Rev. Lett.*, 113:171301, 2014. arXiv:1402.5143, doi:10.1103/PhysRevLett.113.171301.

[22] K. Benakli, Y. Chen, E. Dudas, and Y. Mambrini. Minimal model of gravitino dark matter. *Phys. Rev. D*, 95(9):095002, 2017. arXiv:1701.06574, doi:10.1103/PhysRevD.95.095002.

[23] B. Carr, F. Kuhnel, and M. Sandstad. Primordial Black Holes as Dark Matter. *Phys. Rev. D*, 94(8):083504, 2016. arXiv:1607.06077, doi:10.1103/PhysRevD.94.083504.

[24] S. Dodelson. The Real Problem with MOND. *Int. J. Mod. Phys. D*, 20:2749–2753, 2011. arXiv:1112.1320, doi:10.1142/S0218271811020561.

[25] S. Joudaki et al. KiDS-450: Testing extensions to the standard cosmological model. *Mon. Not. Roy. Astron. Soc.*, 471(2):1259–1279, 2017. arXiv:1610.04606, doi:10.1093/mnras/stx998.

[26] J. L. Feng. Dark Matter Candidates from Particle Physics and Methods of Detection. *Ann. Rev. Astron. Astrophys.*, 48:495–545, 2010. arXiv:1003.0904, doi:10.1146/annurev-astro-082708-101659.

[27] G. Steigman, B. Dasgupta, and J. F. Beacom. Precise Relic WIMP Abundance and its Impact on Searches for Dark Matter Annihilation. *Phys. Rev. D*, 86:023506, 2012. arXiv:1204.3622, doi:10.1103/PhysRevD.86.023506.

[28] G. Jungman, M. Kamionkowski, and K. Griest. Supersymmetric dark matter. *Phys. Rept.*, 267:195–373, 1996. arXiv:hep-ph/9506380, doi:10.1016/0370-1573(95)00058-5.

[29] L. Roszkowski, E. M. Sessolo, and S. Trojanowski. WIMP dark matter candidates and searches—current status and future prospects. *Rept. Prog. Phys.*, 81(6):066201, 2018. arXiv:1707.06277, doi:10.1088/1361-6633/aab913.

[30] R. D. Peccei and H. R. Quinn. CP conservation in the presence of pseudoparticles. *Phys. Rev. Lett.*, 38:1440–1443, Jun 1977. URL: https://link.aps.org/doi/10.1103/PhysRevLett.38.1440, doi:10.1103/PhysRevLett.38.1440.

[31] M. Archidiacono, S. Hannestad, A. Mirizzi, G. Raffelt, and Y. Y. Y. Wong. Axion hot dark matter bounds after Planck. *JCAP*, 10:020, 2013. arXiv:1307.0615, doi:10.1088/1475-7516/2013/10/020.

[32] J. E. Kim and G. Carosi. Axions and the Strong CP Problem. *Rev. Mod. Phys.*, 82:557–602, 2010. [Erratum: Rev.Mod.Phys. 91, 049902 (2019)]. arXiv:0807.3125, doi:10.1103/RevModPhys.82.557.

[33] D. J. E. Marsh. Axion Cosmology. *Phys. Rept.*, 643:1–79, 2016. arXiv:1510.07633, doi:10.1016/j.physrep.2016.06.005.

[34] F. Chadha-Day, J. Ellis, and D. J. E. Marsh. Axion Dark Matter: What is it and Why Now? 5 2021. arXiv:2105.01406.

[35] B. Pontecorvo. Mesonium and antimesonium. *Zhur. Eksptl'. i Teoret. Fiz.* URL: https://www.osti.gov/biblio/4343073.

[36] R. N. Mohapatra. Seesaw mechanism and its implications. In *SEESAW25: International Conference on the Seesaw Mechanism and the Neutrino Mass*, pages 29–44, 12 2004. arXiv:hep-ph/0412379, doi:10.1142/9789812702210_0003.

[37] S. Dodelson and L. M. Widrow. Sterile-neutrinos as dark matter. *Phys. Rev. Lett.*, 72:17–20, 1994. arXiv:hep-ph/9303287, doi:10.1103/PhysRevLett.72.17.

[38] A. Boyarsky, M. Drewes, T. Lasserre, S. Mertens, and O. Ruchayskiy. Sterile neutrino Dark Matter. *Prog. Part. Nucl. Phys.*, 104:1–45, 2019. arXiv:1807.07938, doi:10.1016/j.ppnp.2018.07.004.

[39] M. Fabbrichesi, E. Gabrielli, and G. Lanfranchi. The Dark Photon. 5 2020. arXiv:2005.01515, doi:10.1007/978-3-030-62519-1.

[40] T. Ferber, A. Grohsjean, and F. Kahlhoefer. Dark Higgs bosons at colliders. *Prog. Part. Nucl. Phys.*, 136:104105, 2024. arXiv:2305.16169, doi:10.1016/j.ppnp.2024.104105.

[41] S. Tulin and H.-B. Yu. Dark Matter Self-interactions and Small Scale Structure. *Phys. Rept.*, 730:1–57, 2018. arXiv:1705.02358, doi:10.1016/j.physrep.2017.11.004.

[42] S. Adhikari et al. Astrophysical Tests of Dark Matter Self-Interactions. 7 2022. arXiv:2207.10638.

[43] S. Chatrchyan et al. The CMS Experiment at the CERN LHC. *JINST*, 3:S08004, 2008. doi:10.1088/1748-0221/3/08/S08004.

[44] G. Aad et al. The ATLAS Experiment at the CERN Large Hadron Collider. *JINST*, 3:S08003, 2008. doi:10.1088/1748-0221/3/08/S08003.

[45] K. Akai, K. Furukawa, and H. Koiso. SuperKEKB Collider. *Nucl. Instrum. Meth. A*, 907:188–199, 2018. arXiv:1809.01958, doi:10.1016/j.nima.2018.08.017.

[46] G. Apollinari, O. Brüning, T. Nakamoto, and L. Rossi. High Luminosity Large Hadron Collider HL-LHC. *CERN Yellow Rep.*, (5):1–19, 2015. arXiv:1705.08830, doi:10.5170/CERN-2015-005.1.

[47] D. Abercrombie et al. Dark Matter benchmark models for early LHC Run-2 Searches: Report of the ATLAS/CMS Dark Matter Forum. *Phys. Dark Univ.*, 27:100371, 2020. arXiv:1507.00966, doi:10.1016/j.dark.2019.100371.

[48] J. Wess and B. Zumino. Supergauge Transformations in Four-Dimensions. *Nucl. Phys. B*, 70:39–50, 1974. doi:10.1016/0550-3213(74)90355-1.

[49] S. Dimopoulos and H. Georgi. Softly Broken Supersymmetry and SU(5). *Nucl. Phys. B*, 193:150–162, 1981. doi:10.1016/0550-3213(81)90522-8.

[50] N. Sakai. Naturalness in Supersymmetric Guts. *Z. Phys. C*, 11:153, 1981. doi:10.1007/BF01573998.

[51] H. P. Nilles. Supersymmetry, Supergravity and Particle Physics. *Phys. Rept.*, 110:1–162, 1984. doi:10.1016/0370-1573(84)90008-5.

[52] H. E. Haber and G. L. Kane. The Search for Supersymmetry: Probing Physics Beyond the Standard Model. *Phys. Rept.*, 117:75–263, 1985. doi:10.1016/0370-1573(85)90051-1.

[53] G. Busoni, A. De Simone, E. Morgante, and A. Riotto. On the Validity of the Effective Field Theory for Dark Matter Searches at the LHC. *Phys. Lett. B*, 728:412–421, 2014. arXiv:1307.2253, doi:10.1016/j.physletb.2013.11.069.

[54] G. Busoni, A. De Simone, T. Jacques, E. Morgante, and A. Riotto. On the Validity of the Effective Field Theory for Dark Matter Searches at the LHC Part III: Analysis for the t-channel. *JCAP*, 09:022, 2014. arXiv:1405.3101, doi:10.1088/1475-7516/2014/09/022.

[55] D. Goncalves, P. A. N. Machado, and J. M. No. Simplified Models for Dark Matter Face their Consistent Completions. *Phys. Rev. D*, 95(5):055027, 2017. arXiv:1611.04593, doi:10.1103/PhysRevD.95.055027.

[56] P. Agnes et al. Low-Mass Dark Matter Search with the DarkSide-50 Experiment. *Phys. Rev. Lett.*, 121(8):081307, 2018. arXiv:1802.06994, doi:10.1103/PhysRevLett.121.081307.

[57] Y. Meng et al. Dark Matter Search Results from the PandaX-4T Commissioning Run. *Phys. Rev. Lett.*, 127(26):261802, 2021. arXiv:2107.13438, doi:10.1103/PhysRevLett.127.261802.

[58] W. Ma et al. Search for Solar B8 Neutrinos in the PandaX-4T Experiment Using Neutrino-Nucleus Coherent Scattering. *Phys. Rev. Lett.*, 130(2):021802, 2023. arXiv:2207.04883, doi:10.1103/PhysRevLett.130.021802.

[59] J. Aalbers et al. First Dark Matter Search Results from the LUX-ZEPLIN (LZ) Experiment. *Phys. Rev. Lett.*, 131(4):041002, 2023. arXiv:2207.03764, doi:10.1103/PhysRevLett.131.041002.

[60] G. Aad et al. Constraints on simplified dark matter models involving an s-channel mediator with the ATLAS detector in pp collisions at $\sqrt{s} = 13$ TeV. *Eur. Phys. J. C*, 84(10):1102, 2024. arXiv:2404.15930, doi:10.1140/epjc/s10052-024-13215-5.

[61] F. Kahlhoefer. Review of LHC Dark Matter Searches. *Int. J. Mod. Phys. A*, 32(13):1730006, 2017. arXiv:1702.02430, doi:10.1142/S0217751X1730006X.

[62] A. Boveia and C. Doglioni. Dark Matter Searches at Colliders. *Ann. Rev. Nucl. Part. Sci.*, 68:429–459, 2018. arXiv:1810.12238, doi:10.1146/annurev-nucl-101917-021008.

[63] M. W. Goodman and E. Witten. Detectability of Certain Dark Matter Candidates. *Phys. Rev. D*, 31:3059, 1985. doi:10.1103/PhysRevD.31.3059.

[64] S. Ahlen, F. Avignone, R. Brodzinski, A. Drukier, G. Gelmini, and D. Spergel. Limits on cold dark matter candidates from an ultralow background germanium spectrometer. *Physics Letters B*, 195:603–608, 09 1987. doi:10.1016/0370-2693(87)91581-4.

[65] D. O. Caldwell, R. M. Eisberg, D. M. Grumm, M. S. Witherell, B. Sadoulet, F. S. Goulding, and A. R. Smith. Laboratory Limits on Galactic Cold Dark Matter. *Phys. Rev. Lett.*, 61:510, 1988. doi:10.1103/PhysRevLett.61.510.

[66] A. K. Drukier, K. Freese, and D. N. Spergel. Detecting Cold Dark Matter Candidates. *Phys. Rev. D*, 33:3495–3508, 1986. doi:10.1103/PhysRevD.33.3495.

[67] R. Bernabei et al. Recent Results from DAMA/LIBRA and Comparisons. *Moscow Univ. Phys. Bull.*, 77(2):291–300, 2022. doi:10.3103/S0027134922020138.

[68] E. Armengaud et al. Searching for low-mass dark matter particles with a massive Ge bolometer operated above-ground. *Phys. Rev. D*, 99(8):082003, 2019. arXiv:1901.03588, doi:10.1103/PhysRevD.99.082003.

[69] R. Agnese et al. Results from the Super Cryogenic Dark Matter Search Experiment at Soudan. *Phys. Rev. Lett.*, 120(6):061802, 2018. arXiv:1708.08869, doi:10.1103/PhysRevLett.120.061802.

[70] E. Aprile et al. First Dark Matter Search with Nuclear Recoils from the XENONnT Experiment. 3 2023. arXiv:2303.14729.

[71] P. Agnes et al. DarkSide-50 532-day Dark Matter Search with Low-Radioactivity Argon. *Phys. Rev. D*, 98(10):102006, 2018. arXiv:1802.07198, doi:10.1103/PhysRevD.98.102006.

[72] C. Amole et al. Dark Matter Search Results from the Complete Exposure of the PICO-60 C_3F_8 Bubble Chamber. *Phys. Rev. D*, 100(2):022001, 2019. arXiv:1902.04031, doi:10.1103/PhysRevD.100.022001.

[73] J. Billard, L. Strigari, and E. Figueroa-Feliciano. Implication of neutrino backgrounds on the reach of next generation dark matter direct detection experiments. *Phys. Rev. D*, 89(2):023524, 2014. arXiv:1307.5458, doi:10.1103/PhysRevD.89.023524.

[74] J. Billard, L. E. Strigari, and E. Figueroa-Feliciano. Solar neutrino physics with low-threshold dark matter detectors. *Phys. Rev. D*, 91(9):095023, 2015. arXiv:1409.0050, doi:10.1103/PhysRevD.91.095023.

[75] I. Alkhatib et al. Light Dark Matter Search with a High-Resolution Athermal Phonon Detector Operated Above Ground. *Phys. Rev. Lett.*, 127:061801, 2021. arXiv:2007.14289, doi:10.1103/PhysRevLett.127.061801.

[76] A. Aguilar-Arevalo et al. Results on low-mass weakly interacting massive particles from a 11 kg-day target exposure of DAMIC at SNOLAB. *Phys. Rev. Lett.*, 125:241803, 2020. arXiv:2007.15622, doi:10.1103/PhysRevLett.125.241803.

[77] J. I. Collar. Search for a nonrelativistic component in the spectrum of cosmic rays at Earth. *Phys. Rev. D*, 98(2):023005, 2018. arXiv:1805.02646, doi:10.1103/PhysRevD.98.023005.

[78] D. S. Akerib et al. Results of a Search for Sub-GeV Dark Matter Using 2013 LUX Data. *Phys. Rev. Lett.*, 122(13):131301, 2019. arXiv:1811.11241, doi:10.1103/PhysRevLett.122.131301.

[79] E. Armengaud et al. Search for sub-GeV dark matter via the Migdal effect with an EDELWEISS germanium detector with NbSi transition-edge sensors. *Phys. Rev. D*, 106(6):062004, 2022. arXiv:2203.03993, doi:10.1103/PhysRevD.106.062004.

[80] E. Aprile et al. Search for Light Dark Matter Interactions Enhanced by the Migdal Effect or Bremsstrahlung in XENON1T. *Phys. Rev. Lett.*, 123(24):241803, 2019. arXiv:1907.12771, doi:10.1103/PhysRevLett.123.241803.

[81] Z. Z. Liu et al. Constraints on Spin-Independent Nucleus Scattering with sub-GeV Weakly Interacting Massive Particle Dark Matter from the CDEX-1B Experiment at the China Jinping Underground Laboratory. *Phys. Rev. Lett.*, 123(16):161301, 2019. arXiv:1905.00354, doi:10.1103/PhysRevLett.123.161301.

[82] Z. Z. Liu et al. Studies of the Earth shielding effect to direct dark matter searches at the China Jinping Underground Laboratory. *Phys. Rev. D*, 105(5):052005, 2022. arXiv:2111.11243, doi:10.1103/PhysRevD.105.052005.

[83] M. F. Albakry et al. Search for low-mass dark matter via bremsstrahlung radiation and the Migdal effect in SuperCDMS. *Phys. Rev. D*, 107(11):112013, 2023. arXiv:2302.09115, doi:10.1103/PhysRevD.107.112013.

[84] G. Angloher et al. Results on light dark matter particles with a low-threshold CRESST-II detector. *Eur. Phys. J. C*, 76(1):25, 2016. arXiv:1509.01515, doi:10.1140/epjc/s10052-016-3877-3.

[85] R. Essig, J. Mardon, and T. Volansky. Direct Detection of Sub-GeV Dark Matter. *Phys. Rev. D*, 85:076007, 2012. arXiv:1108.5383, doi:10.1103/PhysRevD.85.076007.

[86] R. Essig, M. Fernandez-Serra, J. Mardon, A. Soto, T. Volansky, and T.-T. Yu. Direct Detection of sub-GeV Dark Matter with Semiconductor Targets. *JHEP*, 05:046, 2016. arXiv:1509.01598, doi:10.1007/JHEP05(2016)046.

[87] R. Bernabei et al. On electromagnetic contributions in WIMP quests. *Int. J. Mod. Phys. A*, 22:3155–3168, 2007. arXiv:0706.1421, doi:10.1142/S0217751X07037093.

[88] M. Ibe, W. Nakano, Y. Shoji, and K. Suzuki. Migdal Effect in Dark Matter Direct Detection Experiments. *JHEP*, 03:194, 2018. arXiv:1707.07258, doi:10.1007/JHEP03(2018)194.

[89] R. Essig, M. Sholapurkar, and T.-T. Yu. Solar Neutrinos as a Signal and Background in Direct-Detection Experiments Searching for Sub-GeV Dark Matter With Electron Recoils. *Phys. Rev. D*, 97(9):095029, 2018. arXiv:1801.10159, doi:10.1103/PhysRevD.97.095029.

[90] J. Wyenberg and I. M. Shoemaker. Mapping the neutrino floor for direct detection experiments based on dark matter-electron scattering. *Phys. Rev. D*, 97(11):115026, 2018. arXiv:1803.08146, doi:10.1103/PhysRevD.97.115026.

[91] G. Herrera. A neutrino floor for the Migdal effect. *JHEP*, 05:288, 2024. arXiv:2311.17719, doi:10.1007/JHEP05(2024)288.

[92] J. E. Gunn, B. W. Lee, I. Lerche, D. N. Schramm, and G. Steigman. Some astrophysical consequences of the existence of a heavy stable neutral lepton. *Astrophys. J.*, 223:1015–1031, August 1978. doi:10.1086/156335.

[93] F. W. Stecker. The cosmic gamma -ray background from the annihilation of primordial stable neutral heavy leptons. *Astrophys. J.*, 223:1032–1036, August 1978. doi:10.1086/156336.

[94] J. Silk and M. Srednicki. Cosmic-Ray Antiprotons as a Probe of a Photino-Dominated Universe. *Phys. Rev. Lett.*, 53(6):624–627, August 1984. doi:10.1103/PhysRevLett.53.624.

[95] L. M. Krauss, K. Freese, D. N. Spergel, and W. H. Press. Cold dark matter candidates and the solar neutrino problem. *Astrophys. J.*, 299:1001–1006, December 1985. doi:10.1086/163767.

[96] M. Mateo. Dwarf galaxies of the Local Group. *Ann. Rev. Astron. Astrophys.*, 36:435–506, 1998. arXiv:astro-ph/9810070, doi:10.1146/annurev.astro.36.1.435.

[97] M. Ackermann et al. Searching for Dark Matter Annihilation from Milky Way Dwarf Spheroidal Galaxies with Six Years of Fermi Large Area Telescope Data. *Phys. Rev. Lett.*, 115(23):231301, 2015. arXiv:1503.02641, doi:10.1103/PhysRevLett.115.231301.

[98] I. Goldman and S. Nussinov. Weakly Interacting Massive Particles and Neutron Stars. *Phys. Rev. D*, 40:3221–3230, 1989. doi:10.1103/PhysRevD.40.3221.

[99] C. Kouvaris and P. Tinyakov. Can Neutron stars constrain Dark Matter? *Phys. Rev. D*, 82:063531, 2010. arXiv:1004.0586, doi:10.1103/PhysRevD.82.063531.

[100] B. Bertoni, A. E. Nelson, and S. Reddy. Dark Matter Thermalization in Neutron Stars. *Phys. Rev. D*, 88:123505, 2013. arXiv:1309.1721, doi:10.1103/PhysRevD.88.123505.

[101] J. Bramante and T. Linden. Detecting Dark Matter with Imploding Pulsars in the Galactic Center. *Phys. Rev. Lett.*, 113(19):191301, 2014. arXiv:1405.1031, doi:10.1103/PhysRevLett.113.191301.

[102] J. L. Feng, A. Rajaraman, and F. Takayama. Superweakly interacting massive particles. *Phys. Rev. Lett.*, 91:011302, 2003. arXiv:hep-ph/0302215, doi:10.1103/PhysRevLett.91.011302.

[103] J. Preskill, M. B. Wise, and F. Wilczek. Cosmology of the invisible axion. *Physics Letters B*, 120(1):127–132, 1983. URL: https://www.sciencedirect.com/science/article/pii/0370269383906378, doi:https://doi.org/10.1016/0370-2693(83)90637-8.

[104] L. Abbott and P. Sikivie. A cosmological bound on the invisible axion. *Physics Letters B*, 120(1):133–136, 1983. URL: https://www.sciencedirect.com/science/article/pii/037026938390638X, doi:https://doi.org/10.1016/0370-2693(83)90638-X.

[105] M. Dine and W. Fischler. The not-so-harmless axion. *Physics Letters B*, 120(1):137–141, 1983. URL: https://www.sciencedirect.com/science/article/pii/0370269383906391, doi:https://doi.org/10.1016/0370-2693(83)90639-1.

[106] Y. Ema, K. Nakayama, and Y. Tang. Production of Purely Gravitational Dark Matter. *JHEP*, 09:135, 2018. arXiv:1804.07471, doi:10.1007/JHEP09(2018)135.

[107] A. Vilenkin and E. P. S. Shellard. *Cosmic Strings and Other Topological Defects*. Cambridge University Press, 7 2000.

[108] H. Iminniyaz, M. Drees, and X. Chen. Relic Abundance of Asymmetric Dark Matter. *JCAP*, 07:003, 2011. arXiv:1104.5548, doi:10.1088/1475-7516/2011/07/003.

[109] M. Aguilar et al. Antiproton Flux, Antiproton-to-Proton Flux Ratio, and Properties of Elementary Particle Fluxes in Primary Cosmic Rays Measured with the Alpha Magnetic Spectrometer on the International Space Station. *Phys. Rev. Lett.*, 117(9):091103, 2016. doi:10.1103/PhysRevLett.117.091103.

[110] J. Heisig, M. Korsmeier, and M. W. Winkler. Dark matter or correlated errors: Systematics of the AMS-02 antiproton excess. *Phys. Rev. Res.*, 2(4):043017, 2020. arXiv:2005.04237, doi:10.1103/PhysRevResearch.2.043017.

[111] E. W. Kolb and M. S. Turner. *The Early Universe*, volume 69. 1990.

[112] A. G. Cohen, A. De Rujula, and S. L. Glashow. A Matter - antimatter universe? *Astrophys. J.*, 495:539–549, 1998. arXiv:astro-ph/9707087, doi:10.1086/305328.

[113] A. D. Sakharov. Violation of CP Invariance, C asymmetry, and baryon asymmetry of the universe. *Pisma Zh. Eksp. Teor. Fiz.*, 5:32–35, 1967. doi:10.1070/PU1991v034n05ABEH002497.

[114] G. 't Hooft. Symmetry breaking through bell-jackiw anomalies. *Phys. Rev. Lett.*, 37:8–11, Jul 1976. URL: https://link.aps.org/doi/10.1103/PhysRevLett.37.8, doi:10.1103/PhysRevLett.37.8.

[115] N. S. Manton. Topology in the Weinberg-Salam Theory. *Phys. Rev. D*, 28:2019, 1983. doi:10.1103/PhysRevD.28.2019.

[116] F. R. Klinkhamer and N. S. Manton. A saddle-point solution in the weinberg-salam theory. *Phys. Rev. D*, 30:2212–2220, Nov 1984. URL: https://link.aps.org/doi/10.1103/PhysRevD.30.2212, doi:10.1103/PhysRevD.30.2212.

[117] M. D'Onofrio, K. Rummukainen, and A. Tranberg. Sphaleron Rate in the Minimal Standard Model. *Phys. Rev. Lett.*, 113(14):141602, 2014. arXiv:1404.3565, doi:10.1103/PhysRevLett.113.141602.

[118] A. G. Cohen, D. B. Kaplan, and A. E. Nelson. Progress in electroweak baryogenesis. *Ann. Rev. Nucl. Part. Sci.*, 43:27–70, 1993. arXiv:hep-ph/9302210, doi:10.1146/annurev.ns.43.120193.000331.

[119] D. Bodeker and W. Buchmuller. Baryogenesis from the weak scale to the grand unification scale. *Rev. Mod. Phys.*, 93(3):035004, 2021. arXiv:2009.07294, doi:10.1103/RevModPhys.93.035004.

[120] J. A. Harvey and M. S. Turner. Cosmological baryon and lepton number in the presence of electroweak fermion number violation. *Phys. Rev. D*, 42:3344–3349, 1990. doi:10.1103/PhysRevD.42.3344.

[121] P. Langacker. Grand Unified Theories and Proton Decay. *Phys. Rept.*, 72:185, 1981. doi:10.1016/0370-1573(81)90059-4.

[122] E. W. Kolb, A. D. Linde, and A. Riotto. GUT baryogenesis after preheating. *Phys. Rev. Lett.*, 77:4290–4293, 1996. arXiv:hep-ph/9606260, doi:10.1103/PhysRevLett.77.4290.

[123] I. Affleck and M. Dine. A New Mechanism for Baryogenesis. *Nucl. Phys. B*, 249:361–380, 1985. doi:10.1016/0550-3213(85)90021-5.

[124] V. Kuzmin, V. Rubakov, and M. Shaposhnikov. On anomalous electroweak baryon-number non-conservation in the early universe. *Physics Letters B*, 155(1):36–42, 1985. URL: https://www.sciencedirect.com/science/article/pii/0370269385910287, doi:https://doi.org/10.1016/0370-2693(85)91028-7.

[125] K. Kajantie, M. Laine, K. Rummukainen, and M. E. Shaposhnikov. The Electroweak phase transition: A Nonperturbative analysis. *Nucl. Phys. B*, 466:189–258, 1996. arXiv:hep-lat/9510020, doi:10.1016/0550-3213(96)00052-1.

[126] M. B. Gavela, P. Hernandez, J. Orloff, and O. Pene. Standard model CP violation and baryon asymmetry. *Mod. Phys. Lett. A*, 9:795–810, 1994. arXiv:hep-ph/9312215, doi:10.1142/S0217732394000629.

[127] D. E. Morrissey and M. J. Ramsey-Musolf. Electroweak baryogenesis. *New J. Phys.*, 14:125003, 2012. arXiv:1206.2942, doi:10.1088/1367-2630/14/12/125003.

[128] M. Fukugita and T. Yanagida. Baryogenesis Without Grand Unification. *Phys. Lett. B*, 174:45–47, 1986. doi:10.1016/0370-2693(86)91126-3.

[129] R. N. Mohapatra and G. Senjanovic. Neutrino Mass and Spontaneous Parity Nonconservation. *Phys. Rev. Lett.*, 44:912, 1980. doi:10.1103/PhysRevLett.44.912.

[130] S. L. Glashow. The future of elementary particle physics. In M. Lévy, J.-L. Basdevant, D. Speiser, J. Weyers, R. Gastmans, and M. Jacob, editors, *Quarks and Leptons*, pages 687–713, Boston, MA, 1980. Springer US.

[131] T. Yanagida. Horizontal gauge symmetry and masses of neutrinos. *Conf. Proc. C*, 7902131:95–99, 1979.

[132] M. Gell-Mann, P. Ramond, and R. Slansky. Complex Spinors and Unified Theories. *Conf. Proc. C*, 790927:315–321, 1979. arXiv:1306.4669.

[133] S. Nussinov. Technocosmology — could a technibaryon excess provide a "natural" missing mass candidate? *Physics Letters B*, 165(1):55–58, 1985. URL: https://www.sciencedirect.com/science/article/pii/0370269385906896, doi:https://doi.org/10.1016/0370-2693(85)90689-6.

[134] D. N. Spergel and W. H. Press. Effect of hypothetical, weakly interacting, massive particles on energy transport in the solar interior. *Astrophys. J.*, 294:663–673, 1985. doi:10.1086/163336.

[135] G. B. Gelmini, L. J. Hall, and M. J. Lin. What Is the Cosmion? *Nucl. Phys. B*, 281:726, 1987. doi:10.1016/0550-3213(87)90424-X.

[136] D. E. Kaplan, M. A. Luty, and K. M. Zurek. Asymmetric Dark Matter. *Phys. Rev. D*, 79:115016, 2009. arXiv:0901.4117, doi:10.1103/PhysRevD.79.115016.

[137] S. M. Barr, R. S. Chivukula, and E. Farhi. Electroweak Fermion Number Violation and the Production of Stable Particles in the Early Universe. *Phys. Lett. B*, 241:387–391, 1990. doi:10.1016/0370-2693(90)91661-T.

[138] S. M. Barr. Baryogenesis, sphalerons and the cogeneration of dark matter. *Phys. Rev. D*, 44:3062–3066, 1991. doi:10.1103/PhysRevD.44.3062.

[139] D. B. Kaplan. A Single explanation for both the baryon and dark matter densities. *Phys. Rev. Lett.*, 68:741–743, 1992. doi:10.1103/PhysRevLett.68.741.

[140] S. B. Gudnason, C. Kouvaris, and F. Sannino. Towards working technicolor: Effective theories and dark matter. *Phys. Rev. D*, 73:115003, 2006. arXiv:hep-ph/0603014, doi:10.1103/PhysRevD.73.115003.

[141] S. B. Gudnason, C. Kouvaris, and F. Sannino. Dark Matter from new Technicolor Theories. *Phys. Rev. D*, 74:095008, 2006. arXiv:hep-ph/0608055, doi:10.1103/PhysRevD.74.095008.

[142] S. M. Barr. The Unification and Cogeneration of Dark Matter and Baryonic Matter. *Phys. Rev. D*, 85:013001, 2012. arXiv:1109.2562, doi:10.1103/PhysRevD.85.013001.

[143] J. J. Heckman and S.-J. Rey. Baryon and Dark Matter Genesis from Strongly Coupled Strings. *JHEP*, 06:120, 2011. arXiv:1102.5346, doi:10.1007/JHEP06(2011)120.

[144] R. Foot and R. R. Volkas. Was ordinary matter synthesized from mirror matter? An Attempt to explain why Omega(Baryon) approximately equal to 0.2 Omega(Dark). *Phys. Rev. D*, 68:021304, 2003. arXiv:hep-ph/0304261, doi:10.1103/PhysRevD.68.021304.

[145] R. Foot and R. R. Volkas. Explaining Omega(Baryon) approximately 0.2 Omega(Dark) through the synthesis of ordinary matter from mirror matter: A More general analysis. *Phys. Rev. D*, 69:123510, 2004. arXiv:hep-ph/0402267, doi:10.1103/PhysRevD.69.123510.

[146] N. Bernal, C. S. Fong, and N. Fonseca. Sharing but not Caring: Dark Matter and the Baryon Asymmetry of the Universe. *JCAP*, 09:005, 2016. arXiv:1605.07188, doi:10.1088/1475-7516/2016/09/005.

[147] G. R. Farrar and G. Zaharijas. Dark matter and the baryon asymmetry. *Phys. Rev. Lett.*, 96:041302, 2006. arXiv:hep-ph/0510079, doi:10.1103/PhysRevLett.96.041302.

[148] T. Bringmann, J. M. Cline, and J. M. Cornell. Baryogenesis from neutron-dark matter oscillations. *Phys. Rev. D*, 99(3):035024, 2019. arXiv:1810.08215, doi:10.1103/PhysRevD.99.035024.

[149] J. Shelton and K. M. Zurek. Darkogenesis: A baryon asymmetry from the dark matter sector. *Phys. Rev. D*, 82:123512, 2010. arXiv:1008.1997, doi:10.1103/PhysRevD.82.123512.

[150] D. G. E. Walker. Dark Baryogenesis. 2 2012. arXiv:1202.2348.

[151] A. G. Cohen and D. B. Kaplan. SPONTANEOUS BARYOGENESIS. *Nucl. Phys. B*, 308:913–928, 1988. doi:10.1016/0550-3213(88)90134-4.

[152] A. G. Cohen, D. B. Kaplan, and A. E. Nelson. Spontaneous baryogenesis at the weak phase transition. *Phys. Lett. B*, 263:86–92, 1991. doi:10.1016/0370-2693(91)91711-4.

[153] J. March-Russell and M. McCullough. Asymmetric Dark Matter via Spontaneous Co-Genesis. *JCAP*, 03:019, 2012. arXiv:1106.4319, doi:10.1088/1475-7516/2012/03/019.

[154] N. Haba and S. Matsumoto. Baryogenesis from Dark Sector. *Prog. Theor. Phys.*, 125:1311–1316, 2011. arXiv:1008.2487, doi:10.1143/PTP.125.1311.

[155] A. Falkowski, J. T. Ruderman, and T. Volansky. Asymmetric Dark Matter from Leptogenesis. *JHEP*, 05:106, 2011. arXiv:1101.4936, doi:10.1007/JHEP05(2011)106.

[156] V. A. Kuzmin. A Simultaneous solution to baryogenesis and dark matter problems. *Phys. Part. Nucl.*, 29:257–265, 1998. arXiv:hep-ph/9701269, doi:10.1134/1.953070.

[157] R. Kitano and I. Low. Dark matter from baryon asymmetry. *Phys. Rev. D*, 71:023510, 2005. arXiv:hep-ph/0411133, doi:10.1103/PhysRevD.71.023510.

[158] N. Cosme, L. Lopez Honorez, and M. H. G. Tytgat. Leptogenesis and dark matter related? *Phys. Rev. D*, 72:043505, 2005. arXiv:hep-ph/0506320, doi:10.1103/PhysRevD.72.043505.

[159] P.-H. Gu and U. Sarkar. Common Origin of Visible and Dark Universe. *Phys. Rev. D*, 81:033001, 2010. arXiv:0909.5463, doi:10.1103/PhysRevD.81.033001.

[160] H. An, S.-L. Chen, R. N. Mohapatra, and Y. Zhang. Leptogenesis as a Common Origin for Matter and Dark Matter. *JHEP*, 03:124, 2010. arXiv:0911.4463, doi:10.1007/JHEP03(2010)124.

[161] E. J. Chun. Leptogenesis origin of Dirac gaugino dark matter. *Phys. Rev. D*, 83:053004, 2011. arXiv:1009.0983, doi:10.1103/PhysRevD.83.053004.

[162] H. Davoudiasl, D. E. Morrissey, K. Sigurdson, and S. Tulin. Hylogenesis: A Unified Origin for Baryonic Visible Matter and Antibaryonic Dark Matter. *Phys. Rev. Lett.*, 105:211304, 2010. arXiv:1008.2399, doi:10.1103/PhysRevLett.105.211304.

[163] C. Arina and N. Sahu. Asymmetric Inelastic Inert Doublet Dark Matter from Triplet Scalar Leptogenesis. *Nucl. Phys. B*, 854:666–699, 2012. arXiv:1108.3967, doi:10.1016/j.nuclphysb.2011.09.014.

[164] K.-Y. Choi, E. J. Chun, and C. S. Shin. Dark matter asymmetry in supersymmetric Dirac leptogenesis. *Phys. Lett. B*, 723:90–94, 2013. arXiv:1211.5409, doi:10.1016/j.physletb.2013.04.020.

[165] G. Elor, M. Escudero, and A. Nelson. Baryogenesis and Dark Matter from *B* Mesons. *Phys. Rev. D*, 99(3):035031, 2019. arXiv:1810.00880, doi:10.1103/PhysRevD.99.035031.

[166] A. E. Nelson and H. Xiao. Baryogenesis from B Meson Oscillations. *Phys. Rev. D*, 100(7):075002, 2019. arXiv:1901.08141, doi:10.1103/PhysRevD.100.075002.

[167] G. Alonso-Álvarez, G. Elor, and M. Escudero. Collider signals of baryogenesis and dark matter from B mesons: A roadmap to discovery. *Phys. Rev. D*, 104(3):035028, 2021. arXiv:2101.02706, doi:10.1103/PhysRevD.104.035028.

[168] K. Enqvist and J. McDonald. Q balls and baryogenesis in the MSSM. *Phys. Lett. B*, 425:309–321, 1998. arXiv:hep-ph/9711514, doi:10.1016/S0370-2693(98)00271-8.

[169] K. Enqvist and J. McDonald. B - ball baryogenesis and the baryon to dark matter ratio. *Nucl. Phys. B*, 538:321–350, 1999. arXiv:hep-ph/9803380, doi:10.1016/S0550-3213(98)00695-6.

[170] I. M. Shoemaker and A. Kusenko. Gravitino dark matter from Q-ball decays. *Phys. Rev. D*, 80:075021, 2009. arXiv:0909.3334, doi:10.1103/PhysRevD.80.075021.

[171] M. L. Graesser, I. M. Shoemaker, and L. Vecchi. A Dark Force for Baryons. 7 2011. arXiv:1107.2666.

[172] C. Cheung and K. M. Zurek. Affleck-Dine Cogenesis. *Phys. Rev. D*, 84:035007, 2011. arXiv:1105.4612, doi:10.1103/PhysRevD.84.035007.

[173] B. Dutta and J. Kumar. Asymmetric Dark Matter from Hidden Sector Baryogenesis. *Phys. Lett. B*, 699:364–367, 2011. arXiv:1012.1341, doi:10.1016/j.physletb.2011.04.036.

[174] K. Petraki, M. Trodden, and R. R. Volkas. Visible and dark matter from a first-order phase transition in a baryon-symmetric universe. *JCAP*, 02:044, 2012. arXiv:1111.4786, doi:10.1088/1475-7516/2012/02/044.

[175] C. Cheung and Y. Zhang. Electroweak Cogenesis. *JHEP*, 09:002, 2013. arXiv:1306.4321, doi:10.1007/JHEP09(2013)002.

[176] K. Kamada and M. Yamaguchi. Asymmetric Dark Matter from Spontaneous Cogenesis in the Supersymmetric Standard Model. *Phys. Rev. D*, 85:103530, 2012. arXiv:1201.2636, doi:10.1103/PhysRevD.85.103530.

[177] S. Dodelson and L. M. Widrow. Baryogenesis in a Baryon Symmetric Universe. *Phys. Rev. D*, 42:326–342, 1990. doi:10.1103/PhysRevD.42.326.

[178] D. H. Oaknin and A. Zhitnitsky. Baryon asymmetry, dark matter and quantum chromodynamics. *Phys. Rev. D*, 71:023519, 2005. arXiv:hep-ph/0309086, doi:10.1103/PhysRevD.71.023519.

[179] W.-Z. Feng and P. Nath. Cogenesis in a universe with vanishing $B - L$ within a gauged $U(1)_x$ extension. *Phys. Lett. B*, 731:43–50, 2014. arXiv:1312.1334, doi:10.1016/j.physletb.2014.02.020.

[180] C. Cheung and K. Ishiwata. Baryogenesis with Higher Dimension Operators. *Phys. Rev. D*, 88(1):017901, 2013. arXiv:1304.0468, doi:10.1103/PhysRevD.88.017901.

[181] R. Allahverdi et al. The First Three Seconds: a Review of Possible Expansion Histories of the Early Universe. 6 2020. arXiv:2006.16182, doi:10.21105/astro.2006.16182.

[182] R. Allahverdi and J. K. Osiński. Early matter domination from long-lived particles in the visible sector. *Phys. Rev. D*, 105(2):023502, 2022. arXiv:2108.13136, doi:10.1103/PhysRevD.105.023502.

[183] N. Terasawa and K. Sato. Lepton and Baryon Number Asymmetry of the Universe and Primordial Nucleosynthesis. *Prog. Theor. Phys.*, 80:468, 1988. doi:10.1143/PTP.80.468.

[184] E. Castorina, U. Franca, M. Lattanzi, J. Lesgourgues, G. Mangano, A. Melchiorri, and S. Pastor. Cosmological lepton asymmetry with a nonzero mixing angle θ_{13}.

Phys. Rev. D, 86:023517, 2012. arXiv:1204.2510, doi:10.1103/PhysRevD.86.023517.

[185] C. Pitrou, A. Coc, J.-P. Uzan, and E. Vangioni. Precision big bang nucleosynthesis with improved Helium-4 predictions. *Phys. Rept.*, 754:1–66, 2018. arXiv:1801.08023, doi:10.1016/j.physrep.2018.04.005.

[186] P. Gondolo and G. Gelmini. Cosmic abundances of stable particles: Improved analysis. *Nucl. Phys. B*, 360:145–179, 1991. doi:10.1016/0550-3213(91)90438-4.

[187] G. Arcadi, A. Djouadi, and M. Raidal. Dark Matter through the Higgs portal. *Phys. Rept.*, 842:1–180, 2020. arXiv:1903.03616, doi:10.1016/j.physrep.2019.11.003.

[188] G. Aad et al. Constraints on new phenomena via Higgs boson couplings and invisible decays with the ATLAS detector. *JHEP*, 11:206, 2015. arXiv:1509.00672, doi:10.1007/JHEP11(2015)206.

[189] G. Aad et al. Search for invisible Higgs-boson decays in events with vector-boson fusion signatures using 139 fb^{-1} of proton-proton data recorded by the ATLAS experiment. *JHEP*, 08:104, 2022. arXiv:2202.07953, doi:10.1007/JHEP08(2022)104.

[190] P. Agnes et al. Search for low-mass dark matter WIMPs with 12 ton-day exposure of DarkSide-50. *Phys. Rev. D*, 107(6):063001, 2023. arXiv:2207.11966, doi:10.1103/PhysRevD.107.063001.

[191] J. M. Cline, K. Kainulainen, P. Scott, and C. Weniger. Update on scalar singlet dark matter. *Phys. Rev. D*, 88:055025, 2013. [Erratum: Phys.Rev.D 92, 039906 (2015)]. arXiv:1306.4710, doi:10.1103/PhysRevD.88.055025.

[192] J. McDonald. Gauge singlet scalars as cold dark matter. *Phys. Rev. D*, 50:3637–3649, 1994. arXiv:hep-ph/0702143, doi:10.1103/PhysRevD.50.3637.

[193] B. Fornal and B. Grinstein. Neutron's dark secret. *Mod. Phys. Lett. A*, 35(31):2030019, 2020. arXiv:2007.13931, doi:10.1142/S0217732320300190.

[194] Y. Aoki, T. Izubuchi, E. Shintani, and A. Soni. Improved lattice computation of proton decay matrix elements. *Phys. Rev. D*, 96(1):014506, 2017. arXiv:1705.01338, doi:10.1103/PhysRevD.96.014506.

[195] J. Huang and Y. Zhao. Dark Matter Induced Nucleon Decay: Model and Signatures. *JHEP*, 02:077, 2014. arXiv:1312.0011, doi:10.1007/JHEP02(2014)077.

[196] M. Jin and Y. Gao. Nucleon - Light Dark Matter Annihilation through Baryon Number Violation. *Phys. Rev. D*, 98(7):075026, 2018. arXiv:1808.10644, doi:10.1103/PhysRevD.98.075026.

[197] B. Fornal, A. Hewitt, and Y. Zhao. Baryonic and Leptonic GeV Dark Matter. *Phys. Lett. B*, 815:136151, 2021. arXiv:2011.09014, doi:10.1016/j.physletb.2021.136151.

[198] K. Abe et al. Neutron-antineutron oscillation search using a 0.37 megaton-years exposure of Super-Kamiokande. *Phys. Rev. D*, 103(1):012008, 2021. arXiv:2012.02607, doi:10.1103/PhysRevD.103.012008.

[199] C. Kouvaris. WIMP Annihilation and Cooling of Neutron Stars. *Phys. Rev. D*, 77:023006, 2008. arXiv:0708.2362, doi:10.1103/PhysRevD.77.023006.

[200] G. Bertone and M. Fairbairn. Compact Stars as Dark Matter Probes. *Phys. Rev. D*, 77:043515, 2008. arXiv:0709.1485, doi:10.1103/PhysRevD.77.043515.

[201] A. de Lavallaz and M. Fairbairn. Neutron Stars as Dark Matter Probes. *Phys. Rev. D*, 81:123521, 2010. arXiv:1004.0629, doi:10.1103/PhysRevD.81.123521.

[202] R. Garani, Y. Genolini, and T. Hambye. New Analysis of Neutron Star Constraints on Asymmetric Dark Matter. *JCAP*, 05:035, 2019. arXiv:1812.08773, doi:10.1088/1475-7516/2019/05/035.

[203] M. McCullough and M. Fairbairn. Capture of Inelastic Dark Matter in White Dwarves. *Phys. Rev. D*, 81:083520, 2010. arXiv:1001.2737, doi:10.1103/PhysRevD.81.083520.

[204] D. Hooper, D. Spolyar, A. Vallinotto, and N. Y. Gnedin. Inelastic Dark Matter As An Efficient Fuel For Compact Stars. *Phys. Rev. D*, 81:103531, 2010. arXiv:1002.0005, doi:10.1103/PhysRevD.81.103531.

[205] M. Blennow, S. Clementz, and J. Herrero-Garcia. Pinning down inelastic dark matter in the Sun and in direct detection. *JCAP*, 04:004, 2016. arXiv:1512.03317, doi:10.1088/1475-7516/2016/04/004.

[206] N. F. Bell, G. Busoni, and S. Robles. Heating up Neutron Stars with Inelastic Dark Matter. *JCAP*, 09:018, 2018. arXiv:1807.02840, doi:10.1088/1475-7516/2018/09/018.

[207] G. Alvarez, A. Joglekar, M. Phoroutan-Mehr, and H.-B. Yu. Heating neutron stars with inelastic dark matter and relativistic targets. *Phys. Rev. D*, 107(10):103024, 2023. arXiv:2301.08767, doi:10.1103/PhysRevD.107.103024.

[208] F. Anzuini, N. F. Bell, G. Busoni, T. F. Motta, S. Robles, A. W. Thomas, and M. Virgato. Improved treatment of dark matter capture in neutron stars III:

nucleon and exotic targets. *JCAP*, 11(11):056, 2021. arXiv:2108.02525, doi:10.1088/1475-7516/2021/11/056.

[209] R. Allahverdi, N. P. D. Loc, and J. K. Osiński. Dark matter and baryogenesis from visible-sector long-lived particles. *Phys. Rev. D*, 107(12):123510, 2023. arXiv:2212.11303, doi:10.1103/PhysRevD.107.123510.

[210] M. Dutra and Y. Wu. EvoEMD: cosmic evolution with an early matter-dominated era. *Phys. Dark Univ.*, 40:101198, 2023. arXiv:2111.15665, doi:10.1016/j.dark.2023.101198.

[211] D. N. Schramm and M. S. Turner. Big Bang Nucleosynthesis Enters the Precision Era. *Rev. Mod. Phys.*, 70:303–318, 1998. arXiv:astro-ph/9706069, doi:10.1103/RevModPhys.70.303.

[212] R. H. Cyburt, B. D. Fields, K. A. Olive, and T.-H. Yeh. Big Bang Nucleosynthesis: 2015. *Rev. Mod. Phys.*, 88:015004, 2016. arXiv:1505.01076, doi:10.1103/RevModPhys.88.015004.

[213] J. Berger and G. Elor. Dark Matter Induced Nucleon Decay Signals in Mesogenesis. 1 2023. arXiv:2301.04165.

[214] A. Allega et al. Improved search for invisible modes of nucleon decay in water with the SNO+detector. *Phys. Rev. D*, 105(11):112012, 2022. arXiv:2205.06400, doi:10.1103/PhysRevD.105.112012.

[215] D. McKeen, M. Pospelov, and N. Raj. Cosmological and astrophysical probes of dark baryons. *Phys. Rev. D*, 103(11):115002, 2021. arXiv:2012.09865, doi:10.1103/PhysRevD.103.115002.

[216] K. Griest and D. Seckel. Three exceptions in the calculation of relic abundances. *Phys. Rev. D*, 43:3191–3203, 1991. doi:10.1103/PhysRevD.43.3191.

[217] R. T. D'Agnolo and J. T. Ruderman. Light Dark Matter from Forbidden Channels. *Phys. Rev. Lett.*, 115(6):061301, 2015. arXiv:1505.07107, doi:10.1103/PhysRevLett.115.061301.

[218] S. Hamdan and J. Unwin. Dark Matter Freeze-out During Matter Domination. *Mod. Phys. Lett. A*, 33(29):1850181, 2018. arXiv:1710.03758, doi:10.1142/S021773231850181X.

[219] D. B. Clark, E. Godat, and F. I. Olness. ManeParse : A Mathematica reader for Parton Distribution Functions. *Comput. Phys. Commun.*, 216:126–137, 2017. arXiv:1605.08012, doi:10.1016/j.cpc.2017.03.004.

[220] V. Khachatryan et al. Search for dark matter, extra dimensions, and unparticles in monojet events in proton–proton collisions at $\sqrt{s} = 8$ TeV. *Eur. Phys. J. C*, 75(5):235, 2015. arXiv:1408.3583, doi:10.1140/epjc/s10052-015-3451-4.

[221] D. Curtin and M. E. Peskin. Analysis of Long Lived Particle Decays with the MATHUSLA Detector. *Phys. Rev. D*, 97(1):015006, 2018. arXiv:1705.06327, doi:10.1103/PhysRevD.97.015006.

[222] D. Curtin et al. Long-Lived Particles at the Energy Frontier: The MATHUSLA Physics Case. *Rept. Prog. Phys.*, 82(11):116201, 2019. arXiv:1806.07396, doi:10.1088/1361-6633/ab28d6.

[223] J. Heeck. Light particles with baryon and lepton numbers. *Phys. Lett. B*, 813:136043, 2021. arXiv:2009.01256, doi:10.1016/j.physletb.2020.136043.

[224] J. Liu and G. Segre. Reexamination of generation of baryon and lepton number asymmetries by heavy particle decay. *Phys. Rev. D*, 48:4609–4612, 1993. arXiv:hep-ph/9304241, doi:10.1103/PhysRevD.48.4609.

[225] L. Covi, E. Roulet, and F. Vissani. CP violating decays in leptogenesis scenarios. *Phys. Lett. B*, 384:169–174, 1996. arXiv:hep-ph/9605319, doi:10.1016/0370-2693(96)00817-9.

[226] A. Pilaftsis and T. E. J. Underwood. Resonant leptogenesis. *Nucl. Phys. B*, 692:303–345, 2004. arXiv:hep-ph/0309342, doi:10.1016/j.nuclphysb.2004.05.029.

[227] G. Aad et al. Search for pair-produced massive coloured scalars in four-jet final states with the ATLAS detector in proton-proton collisions at $\sqrt{s} = 7$ TeV. *Eur. Phys. J. C*, 73(1):2263, 2013. arXiv:1210.4826, doi:10.1140/epjc/s10052-012-2263-z.

[228] M. Aaboud et al. A search for pair-produced resonances in four-jet final states at $\sqrt{s} = 13$ TeV with the ATLAS detector. *Eur. Phys. J. C*, 78(3):250, 2018. arXiv:1710.07171, doi:10.1140/epjc/s10052-018-5693-4.

[229] Search for resonant and nonresonant production of pairs of dijet resonances in proton-proton collisions at $\sqrt{s} = 13$ TeV. 6 2022. arXiv:2206.09997.

[230] J. Alwall, R. Frederix, S. Frixione, V. Hirschi, F. Maltoni, O. Mattelaer, H. S. Shao, T. Stelzer, P. Torrielli, and M. Zaro. The automated computation of tree-level and next-to-leading order differential cross sections, and their matching to parton shower simulations. *JHEP*, 07:079, 2014. arXiv:1405.0301, doi:10.1007/JHEP07(2014)079.

[231] A. Alloul, N. D. Christensen, C. Degrande, C. Duhr, and B. Fuks. FeynRules 2.0 - A complete toolbox for tree-level phenomenology. *Comput. Phys. Commun.*, 185:2250–2300, 2014. arXiv:1310.1921, doi:10.1016/j.cpc.2014.04.012.

[232] C. Degrande, C. Duhr, B. Fuks, D. Grellscheid, O. Mattelaer, and T. Reiter. UFO - The Universal FeynRules Output. *Comput. Phys. Commun.*, 183:1201–1214, 2012. arXiv:1108.2040, doi:10.1016/j.cpc.2012.01.022.

[233] A. M. Sirunyan et al. Search for natural and split supersymmetry in proton-proton collisions at $\sqrt{s} = 13$ TeV in final states with jets and missing transverse momentum. *JHEP*, 05:025, 2018. arXiv:1802.02110, doi:10.1007/JHEP05(2018)025.

[234] M. Aaboud et al. Search for low-mass dijet resonances using trigger-level jets with the ATLAS detector in pp collisions at $\sqrt{s} = 13$ TeV. *Phys. Rev. Lett.*, 121(8):081801, 2018. arXiv:1804.03496, doi:10.1103/PhysRevLett.121.081801.

[235] A. M. Sirunyan et al. Search for narrow and broad dijet resonances in proton-proton collisions at $\sqrt{s} = 13$ TeV and constraints on dark matter mediators and other new particles. *JHEP*, 08:130, 2018. arXiv:1806.00843, doi:10.1007/JHEP08(2018)130.

[236] B. Dutta, Y. Gao, and T. Kamon. Probing Light Nonthermal Dark Matter at the LHC. *Phys. Rev. D*, 89(9):096009, 2014. arXiv:1401.1825, doi:10.1103/PhysRevD.89.096009.

[237] S. Undleeb. *Search for Non-thermal Dark Matter in Monojet Events in Proton-Proton Collisions at $\sqrt{s} = 13$ TeV*. PhD thesis, Texas Tech., 2017. doi:10.2172/1413084.

[238] P. Asadi, M. R. Buckley, A. DiFranzo, A. Monteux, and D. Shih. Digging Deeper for New Physics in the LHC Data. *JHEP*, 11:194, 2017. arXiv:1707.05783, doi:10.1007/JHEP11(2017)194.

[239] P. Asadi, M. R. Buckley, A. DiFranzo, A. Monteux, and D. Shih. An Update on the LHC Monojet Excess. *JHEP*, 03:130, 2018. arXiv:1712.04939, doi:10.1007/JHEP03(2018)130.

[240] A. M. Sirunyan et al. Search for supersymmetry in multijet events with missing transverse momentum in proton-proton collisions at 13 TeV. *Phys. Rev. D*, 96(3):032003, 2017. arXiv:1704.07781, doi:10.1103/PhysRevD.96.032003.

[241] A. M. Sirunyan et al. Search for new phenomena with the M_{T2} variable in the all-hadronic final state produced in proton–proton collisions at $\sqrt{s} = 13$ TeV. *Eur. Phys. J. C*, 77(10):710, 2017. arXiv:1705.04650, doi:10.1140/epjc/s10052-017-5267-x.

[242] M. Aaboud et al. Search for squarks and gluinos in final states with jets and missing transverse momentum using 36 fb^{-1} of $\sqrt{s} = 13$ TeV pp collision data with the ATLAS detector. *Phys. Rev. D*, 97(11):112001, 2018. arXiv:1712.02332, doi:10.1103/PhysRevD.97.112001.

[243] M. Aaboud et al. Search for dark matter and other new phenomena in events with an energetic jet and large missing transverse momentum using the ATLAS

detector. *JHEP*, 01:126, 2018. arXiv:1711.03301, doi:10.1007/JHEP01(2018)126.

[244] T. Hahn. Generating Feynman diagrams and amplitudes with FeynArts 3. *Comput. Phys. Commun.*, 140:418–431, 2001. arXiv:hep-ph/0012260, doi:10.1016/S0010-4655(01)00290-9.

[245] V. Shtabovenko, R. Mertig, and F. Orellana. New Developments in FeynCalc 9.0. *Comput. Phys. Commun.*, 207:432–444, 2016. arXiv:1601.01167, doi:10.1016/j.cpc.2016.06.008.

[246] V. Shtabovenko. FeynHelpers: Connecting FeynCalc to FIRE and Package-X. *Comput. Phys. Commun.*, 218:48–65, 2017. arXiv:1611.06793, doi:10.1016/j.cpc.2017.04.014.

[247] H. H. Patel. Package-X 2.0: A Mathematica package for the analytic calculation of one-loop integrals. *Comput. Phys. Commun.*, 218:66–70, 2017. arXiv:1612.00009, doi:10.1016/j.cpc.2017.04.015.

[248] G. 't Hooft and M. J. G. Veltman. Regularization and Renormalization of Gauge Fields. *Nucl. Phys. B*, 44:189–213, 1972. doi:10.1016/0550-3213(72)90279-9.

[249] P. Breitenlohner and D. Maison. Dimensional Renormalization and the Action Principle. *Commun. Math. Phys.*, 52:11–38, 1977. doi:10.1007/BF01609069.

[250] S. W. Randall, M. Markevitch, D. Clowe, A. H. Gonzalez, and M. Bradac. Constraints on the Self-Interaction Cross-Section of Dark Matter from Numerical Simulations of the Merging Galaxy Cluster 1E 0657-56. *Astrophys. J.*, 679:1173–1180, 2008. arXiv:0704.0261, doi:10.1086/587859.

[251] J. Berger, K. Jedamzik, and D. G. E. Walker. Cosmological Constraints on Decoupled Dark Photons and Dark Higgs. *JCAP*, 11:032, 2016. arXiv:1605.07195, doi:10.1088/1475-7516/2016/11/032.

[252] A. Fradette, M. Pospelov, J. Pradler, and A. Ritz. Cosmological beam dump: constraints on dark scalars mixed with the Higgs boson. *Phys. Rev. D*, 99(7):075004, 2019. arXiv:1812.07585, doi:10.1103/PhysRevD.99.075004.

[253] G. Mangano, G. Miele, S. Pastor, T. Pinto, O. Pisanti, and P. D. Serpico. Relic neutrino decoupling including flavor oscillations. *Nucl. Phys. B*, 729:221–234, 2005. arXiv:hep-ph/0506164, doi:10.1016/j.nuclphysb.2005.09.041.

[254] K. N. Abazajian et al. CMB-S4 Science Book, First Edition. 10 2016. arXiv:1610.02743.

[255] S. Davidson, E. Nardi, and Y. Nir. Leptogenesis. *Phys. Rept.*, 466:105–177, 2008. arXiv:0802.2962, doi:10.1016/j.physrep.2008.06.002.

[256] A. D. Dolgov. Neutrinos in cosmology. *Phys. Rept.*, 370:333–535, 2002. arXiv:hep-ph/0202122, doi:10.1016/S0370-1573(02)00139-4.

Appendix A

Thermal universe

A.1 Equilibrium thermodynamics and abundances

In the early universe, particles formed a hot, dense plasma in thermal equilibrium. At temperatures exceeding a few GeV, the energy of most SM particles was significantly greater than their rest mass. Their energies can be approximated as

$$E \approx \sqrt{m^2 + |\vec{p}|^2} \approx |\vec{p}| \,, \tag{A.1}$$

meaning they behaved as relativistic particles, similar to radiation. In this regime, the plasma's temperature, T, dominates as the primary thermodynamic parameter.

For species in kinetic equilibrium, the phase-space distributions are described by either the Fermi-Dirac (fermions) or Bose-Einstein (bosons) distributions:

$$f_\pm = \frac{1}{e^{(E-\mu)/T} \pm 1} \,, \tag{A.2}$$

where μ is the chemical potential of the particle species. The + sign corresponds to fermions, while the − sign applies to bosons. In many scenarios, particularly in the early universe, the chemical potential μ of SM particles can be approximated as negligible compared to the temperature, $\mu \approx 0$. This assumption implies an equal number of particles and antiparticles, although slight asymmetries are present.

To understand the distribution and energy properties of particle species in equilibrium, we calculate the number density n and the energy density ρ. For a species with g internal degrees of freedom, these quantities are derived from the phase-space distribution. The number density n is given by:

$$n = \frac{g}{(2\pi)^3} \int f(E)\, d^3p \,, \tag{A.3}$$

which accounts for the total number of particles per unit volume. The energy density ρ, which represents the total energy per unit volume, is calculated as

$$\rho = \frac{g}{(2\pi)^3} \int E f(E)\, d^3p \,. \tag{A.4}$$

We assume the Maxwell-Boltzmann (MB) approximation, which treats bosons and fermions equally. This is valid at high temperatures, where quantum effects are negligible. The MB distribution is given by:

$$f_{\rm MB} = \exp\left(-\frac{E-\mu}{T}\right). \tag{A.5}$$

Using this distribution and Eq. (A.3), the number density becomes

$$n_{\rm MB} = \frac{g}{(2\pi)^3}\, e^{\mu/T} \int d^3p\, e^{-E/T}. \tag{A.6}$$

Below, we outline the derivation of $n_{\rm MB}$ for three cases: relativistic, non-relativistic, and general.

a) For relativistic particles, where $E \approx |\vec{p}|$, the number density simplifies to

$$\begin{aligned} n_{\rm MB}^{\rm rel} &= \frac{g}{(2\pi)^3}\, e^{\mu/T} \int d^3p\, e^{-p/T} = \frac{g}{(2\pi)^3}\, e^{\mu/T} 4\pi \int_0^\infty dp\, p^2\, e^{-p/T} = \\ &= \frac{g}{(2\pi)^3}\, e^{\mu/T} 4\pi\, 2T^2 = \frac{g}{\pi^2} T^3 e^{\mu/T}. \end{aligned} \tag{A.7}$$

b) For non-relativistic particles, where $E \approx m + |\vec{p}|^2/(2m)$, the number density is

$$\begin{aligned} n_{\rm MB}^{\rm NR} &= \frac{g}{(2\pi)^3}\, e^{\mu/T} \int d^3p\, e^{-m/T}\, e^{-p^2/(2mT)} = \frac{g}{(2\pi)^3}\, e^{-m/T}\, e^{\mu/T} 4\pi \int_0^\infty dp\, p^2\, e^{-p^2/(2mT)} = \\ &= \frac{g}{(2\pi)^3}\, e^{-m/T}\, e^{\mu/T} 4\pi \sqrt{\frac{\pi}{2}} (mT)^{\frac{3}{2}} = g\, e^{-(m-\mu)/T} \left(\frac{mT}{2\pi}\right)^{\frac{3}{2}}. \end{aligned} \tag{A.8}$$

c) For the general case, where $E = \sqrt{m^2 + |\vec{p}|^2}$, the number density involves a modified Bessel function of the second kind, $K_2(x)$, and is given by

$$\begin{aligned} n_{\rm MB} &= \frac{g}{(2\pi)^3}\, e^{\mu/T} 4\pi \int_0^\infty dp\, p^2\, e^{-E/T} = \frac{g}{(2\pi)^3}\, e^{\mu/T} 4\pi m^2 T K_2\left(\frac{m}{T}\right) = \\ &= \frac{g}{2\pi^2} m^2 T K_2\left(\frac{m}{T}\right) e^{\mu/T} = \frac{g}{2\pi^2} x^2 T^3 K_2\left(x\right) e^{\mu/T}, \end{aligned} \tag{A.9}$$

with $x \equiv m/T$.

A.2 Effective number of relativistic species

In the relativistic limit, the energy density given in Eq. (A.4) takes the form

$$\rho^{\rm rel} = \frac{\pi^2}{30} g T^4 \begin{cases} 1 & \text{bosons,} \\ \frac{7}{8} & \text{fermions.} \end{cases} \tag{A.10}$$

The total radiation energy density at a given photon temperature T is obtained by summing over all relativistic particle species,

$$\rho_r = \sum_i \rho_i = \frac{\pi^2}{30} g_\star(T) T^4, \tag{A.11}$$

where $g_\star(T)$ represents the "effective number of relativistic degrees of freedom" at temperature T. The sum over particle species is expressed as

$$g_\star(T) \equiv \sum_{i=\mathrm{b}} g_i \left(\frac{T_i}{T}\right)^4 + \frac{7}{8} \sum_{i=\mathrm{f}} g_i \left(\frac{T_i}{T}\right)^4, \tag{A.12}$$

where the subscripts b and f denote bosons and fermions, respectively. For particles in thermal equilibrium with the photon bath ($T_i = T$), the temperature fraction simplifies to one. However, for relativistic species that have decoupled from the plasma, this factor remains relevant.

At high temperatures, specifically for $T \gg 173$ GeV, all SM particles are relativistic. Summing their internal degrees of freedom, we obtain

$$g_\mathrm{b} = 28 \qquad \text{photons}\,(2),\ \mathrm{W}^\pm\ \text{and}\ \mathrm{Z}^0\,(3\cdot 3),\ \text{gluons}\,(8\cdot 2),\ \text{and Higgs}\,(1), \tag{A.13}$$

$$g_\mathrm{f} = 90 \qquad \text{quarks}\,(6\cdot 12),\ \text{charged leptons}\,(3\cdot 4),\ \text{and neutrinos}\,(3\cdot 2). \tag{A.14}$$

Thus, the total relativistic degrees of freedom at these temperatures is given by

$$g_\star = g_\mathrm{b} + \frac{7}{8} g_\mathrm{f} = 106.75\,. \tag{A.15}$$

As the universe cools, different particle species transition to a non-relativistic state and subsequently annihilate. To determine $g_\star$ at a particular temperature T, we sum the contributions of all remaining relativistic degrees of freedom at that epoch.

Similarly, the total entropy density for a system with multiple particle species is given by

$$\mathfrak{s} = \frac{2\pi^2}{45} g_{\star S}(T) T^3, \tag{A.16}$$

where $g_{\star S}(T)$, defined as the "effective number of degrees of freedom in entropy," is expressed as

$$g_{\star S}(T) \equiv \sum_{i=\mathrm{b}} g_i \left(\frac{T_i}{T}\right)^3 + \frac{7}{8} \sum_{i=\mathrm{f}} g_i \left(\frac{T_i}{T}\right)^3. \tag{A.17}$$

For particle species in thermal equilibrium ($T_i = T$), their contributions to $g_{\star S}$ and $g_\star$ are identical. At high temperatures, we also have

$$g_{\star S} = 106.75\,. \tag{A.18}$$

However, for relativistic species that have decoupled from the thermal bath, their entropy contribution follows a different scaling behavior. In Fig. A.1 we find the evolution of $g_\star(T)$ and $g_{\star S}(T)$.

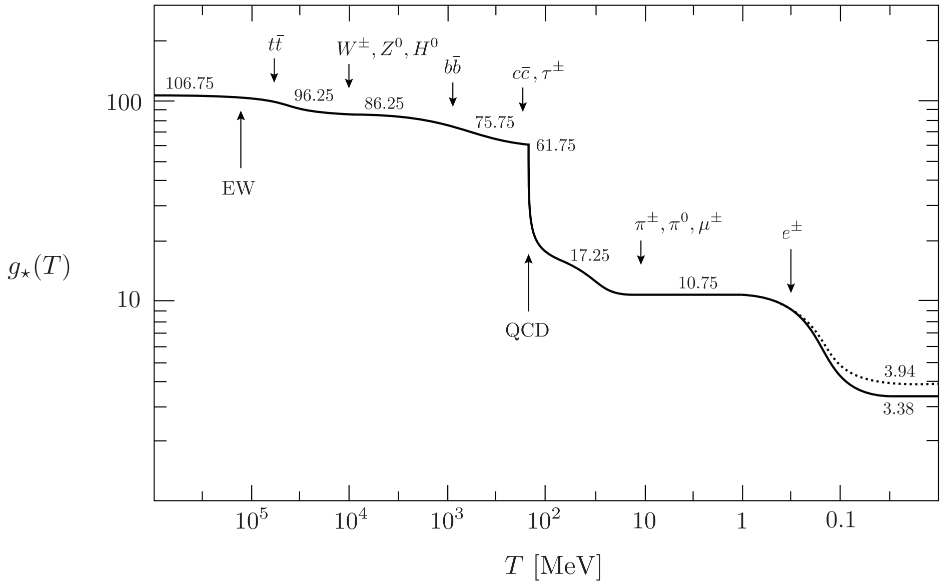

Fig. A.1: Evolution of relativistic degrees of freedom $g_\star(T)$ assuming the SM particle content. The dotted line stands for the number of effective degrees of freedom in entropy $g_{\star S}(T)$. Taken from Daniel Baumann's Cosmology lectures.

A.3 Neutrino decoupling and effective neutrino number $N_{\rm eff}$

At very high temperatures, all SM particles in the early universe were in thermal equilibrium due to frequent and efficient interactions. Since their masses were much smaller than the ambient temperature, they behaved as relativistic radiation. As the universe expanded and cooled, the temperature decreased, causing different particle species to become non-relativistic and to decouple from the thermal plasma.

One of the most significant decoupling events in this context is neutrino decoupling. In the early universe, neutrinos were kept in thermal equilibrium primarily through weak interactions with electrons and positrons

$$e^- + e^+ \leftrightarrow \nu_e + \bar{\nu}_e \,. \tag{A.19}$$

However, as the temperature dropped below $T \sim 1$ MeV, the weak interaction rate fell below the expansion rate of the universe, causing neutrinos to decouple. From this point onward, neutrinos evolved independently from the remaining particle species still in thermal equilibrium. We will simplify the discussion by assuming that neutrinos decoupled instantaneously before electron-positron annihilation.

Shortly after neutrino decoupling, electron-positron annihilation occurred, transferring entropy to the photon bath. Since neutrinos were already decoupled, they did not receive this entropy injection, leading to a difference between the neutrino and photon temperatures. This difference can be derived by considering the conservation of comoving entropy density, given by

$$a^3 \mathfrak{s}(T) = \text{constant}, \tag{A.20}$$

where a is the scale factor, which scales as $a \sim T^{-1}$. We impose this conservation before and after electron-positron annihilation. The relativistic degrees of freedom contributing to entropy in the thermal plasma before annihilation include two photon spin states and two electron-positron spin states. Following Eq. (A.17), this gives

$$g_{\star S}^{\text{before}} = 2 + \frac{7}{8}(2+2) = \frac{11}{2}. \tag{A.21}$$

After electron positron annihilation, only the photons remain in equilibrium, reducing the entropy degrees of freedom to

$$g_{\star S}^{\text{after}} = 2. \tag{A.22}$$

Applying comoving entropy conservation from Eq. (A.20), we obtain:

$$\frac{g_{\star S}^{\text{before}}\, T^3_{\gamma,\,\text{before}}}{T^3_{\nu,\,\text{before}}} = \frac{g_{\star S}^{\text{after}}\, T^3_{\gamma,\,\text{after}}}{T^3_{\nu,\,\text{after}}}. \tag{A.23}$$

Using the fact that $T_{\gamma,\,\text{before}} = T_{\nu,\,\text{before}}$, this simplifies to

$$T_{\nu,\,\text{after}} = \left(\frac{4}{11}\right)^{1/3} T_{\gamma,\,\text{after}} \simeq 0.71\, T_{\gamma,\,\text{after}}\,, \tag{A.24}$$

which quantifies the relative cooling of neutrinos compared to photons after electron-positron annihilation.

Following electron-positron annihilation and assuming three families of neutrinos and antineutrinos, the total radiation energy density in the universe, using Eqs. (A.11), (A.12) and (A.24), is given by

$$\rho_r = \frac{\pi^2}{30}\left[2\,T_\gamma^4 + 6\frac{7}{8}T_\nu^4\right] = \frac{\pi^2}{15}\left[1 + 3\frac{7}{8}\left(\frac{4}{11}\right)^{4/3}\right]T_\gamma^4. \tag{A.25}$$

To express this radiation density in terms of an effective number of neutrino species, the parameter N_{eff} is introduced. It is defined such that

$$\rho_r \equiv \frac{\pi^2}{15}\left[1 + \frac{7}{8}\left(\frac{4}{11}\right)^{4/3} N_{\text{eff}}\right]T_\gamma^4. \tag{A.26}$$

In the simplified scenario where neutrinos decouple instantaneously, the SM prediction is $N_{\text{eff}}^{\text{SM}} = 3$. However, in reality, neutrino decoupling occurs over a finite period of time, and the weak residual interactions between neutrinos and the thermal plasma during electron-positron annihilation lead to $N_{\text{eff}}^{\text{SM}} = 3.046$.

To account for deviations from the SM prediction of the effective number of neutrino species, $\Delta N_{\rm eff}$ is defined as

$$\Delta N_{\rm eff} \equiv N_{\rm eff} - N_{\rm eff}^{\rm SM}. \tag{A.27}$$

A non-zero value of $\Delta N_{\rm eff}$ could arise due to additional contributions to the radiation energy density. Cosmological observations place stringent constraints on $\Delta N_{\rm eff}$. Planck 2018 measurements of the cosmic microwave background anisotropies, combined with baryon acoustic oscillations, provide the most precise limits up to date [5]:

$$N_{\rm eff} = 2.99^{+0.34}_{-0.33} \qquad (95\%\,\text{C.L.}). \tag{A.28}$$

The next generation "Stage-4" ground-based cosmic microwave background experiment, CMB-S4 [254], is expected to improve these constraints by one order of magnitude.

A.4 Thermal average of cross sections and rates

Thermally averaged cross sections and decay rates account for the thermal distribution of particles and the temperature-dependent dynamics of interactions. They are crucial for solving Boltzmann equations, as the interaction terms are proportional to these quantities, see Appendix B.1.

The thermally averaged rate for a two-to-two process ($i + j \to m + n$) is given by the following integral of the cross section $\sigma(s)$ [255]:

$$\langle \gamma^{ij}_{mn} \rangle = \frac{g_i g_j T}{32\pi^4} \int ds s^{3/2}\, K_1\left(\frac{\sqrt{s}}{T}\right) \lambda\left(1, \frac{m_i^2}{s}, \frac{m_j^2}{s}\right) \sigma(s), \tag{A.29}$$

where $\lambda(a, b, c) = (a - b - c)^2 - 4bc$ is the Kallen function, $K_1(x)$ is a modified Bessel function of the second kind, s is the Mandelstam variable, and g_i are the degrees of freedom of particle species i.

To obtain the thermally averaged cross section $\langle \sigma v \rangle$, we divide this rate by the equilibrium number densities of the incoming particles:

$$\langle \sigma v \rangle_{ij \to mn} = \frac{\langle \gamma^{ij}_{mn} \rangle}{n_i^{\rm eq}\, n_j^{\rm eq}}. \tag{A.30}$$

For the thermally averaged decay rate of a particle species into two particles ($i \to m + n$), the total rate is given by [255]:

$$\langle \gamma^{i}_{mn} \rangle = \frac{g_i T^3}{2\pi^2} x^2\, K_1\left(x\right) \Gamma(i \to m + n), \tag{A.31}$$

where $x = m_i/T$, and $\Gamma(i \to m + n)$ is the decay width. The thermally averaged decay rate is then

$$\langle \Gamma \rangle = \frac{\langle \gamma^{i}_{mn} \rangle}{n_i^{\rm eq}} = \Gamma(i \to m + n) \frac{K_1\left(x\right)}{K_2\left(x\right)}, \tag{A.32}$$

where $K_2(x)$ is another modified Bessel function of the second kind.

Appendix B

Boltzmann Equations

B.1 Boltzmann equations formalism

The Boltzmann equation provides a fundamental framework for studying the evolution of particle abundances in the early universe. While particles in equilibrium with the thermal plasma are well described by equilibrium distributions, understanding their behavior during and around the epoch of decoupling is more complex. This is because decoupling is not instantaneous, and the particle abundances evolve dynamically as the universe expands and cools. In this appendix, we derive the Boltzmann equation, its simplifications under common assumptions, and its form in terms of comoving variables.

The Boltzmann equation generically describes the time evolution of a particle's phase-space distribution f and is expressed as

$$\hat{L}[f] = \hat{C}[f], \tag{B.1}$$

where $\hat{L}$ is the Liouville operator, and $\hat{C}$ is the collision operator. For the Friedmann-Lemaître-Robertson-Walker metric, the Liouville operator takes the form

$$\hat{L}[f(E,t)] = E\frac{\partial f}{\partial t} - \frac{\dot{a}}{a}|\vec{p}|^2\frac{\partial f}{\partial E}. \tag{B.2}$$

Using the definition of the number density in terms of the phase-space density (A.3), dividing by E, and integrating by parts, this expression leads to the evolution equation for the number density

$$\dot{n} + 3Hn = \frac{g}{(2\pi)^3}\int \frac{d^3p}{E}\hat{C}[f], \tag{B.3}$$

where H is the Hubble parameter.

To account for the collision term $\hat{C}[f]$ for a generic interaction ($\psi + a + b + \ldots \leftrightarrow i + j + \ldots$), where the focus is on the particle ψ, we write

$$\begin{aligned}
\frac{g_\psi}{(2\pi)^3}\int \hat{C}[f]\frac{d^3p_\psi}{E_\psi} = -g_\psi \int & d\Pi_\psi d\Pi_a d\Pi_b ... d\Pi_i d\Pi_j ... \\
& \times (2\pi)^4\delta^4\left(p_\psi + p_a + p_b + ... - p_i - p_j ...\right) \\
& \times \Big[|M|^2_{\psi+a+b...\to i+j...} f_\psi f_a f_b ... (1\pm f_i)(1\pm f_j)... \\
& -|M|^2_{i+j...\to\psi+a+b...} f_i f_j ... \left(1\pm f_\psi\right)\left(1\pm f_a\right)(1\pm f_b)...\Big],
\end{aligned} \tag{B.4}$$

where f_ψ, f_a, etc. are the phase-space distributions for each particle, given by (A.2). The $+$ sign applies to bosons and the $-$ sign to fermions. The delta function ensures energy-momentum conservation, while $|M|^2$ represents the squared matrix element averaged over spins and symmetrized for identical particles. The Lorentz-invariant phase-space element is defined as

$$d\Pi \equiv \frac{1}{(2\pi)^3}\frac{d^3p}{2E}. \tag{B.5}$$

To simplify the Boltzmann equation, we make the following assumptions:

1. Time-reversal invariance (or CP invariance): This implies

$$|M|^2_{\psi+a+b...\to i+j...} = |M|^2_{i+j...\to\psi+a+b...} \equiv |M|^2. \tag{B.6}$$

   Even if CP is broken, the equilibrium distributions remain unchanged, and this relation can still be effectively applied [256].

2. High-temperature approximation: At high temperatures, $E-\mu \gg T$, which happens for high temperatures, so the exponential in the Bose-Einstein or Fermi-Dirac distributions dominates, leading to:

$$f \approx \mathrm{e}^{-(E-\mu)/T}, \quad 1 \pm f \approx 1. \tag{B.7}$$

   Even if we are not in the high temperature regime, this assumption will translate into a correction of less than ~ 20 % in the rate.

Under these assumptions, the Boltzmann equation for the number density simplifies to

$$\begin{aligned}\dot{n}_\psi + 3Hn_\psi = &- g_\psi \int d\Pi_\psi d\Pi_a d\Pi_b ... d\Pi_i d\Pi_j ... (2\pi)^4 |M|^2 \times \\ &\times \delta^4\left(p_\psi + p_a + p_b + ... - p_i - p_j ...\right)\left[f_\psi f_a f_b ... - f_i f_j ...\right],\end{aligned} \tag{B.8}$$

where the term $3Hn_\psi$ accounts for the dilution of the number density due to the expansion of the universe, and the right-hand side encompasses the change in particle number due to the interactions with other particles. It is usual to write the Boltzmann equation in terms of the comoving number density, or yield, removing in this way the expansion term. This quantity is defined as $Y \equiv n/\mathfrak{s}$, where $\mathfrak{s}$ is the entropy density, given by Eq. (2.6).

Using the conservation of entropy, see Eq. A.20, the Boltzmann equation can be rewritten as

$$\begin{aligned}\frac{dY_\psi}{dx} = &-\frac{x g_\psi}{H(1)\mathfrak{s}} \int d\Pi_\psi d\Pi_a d\Pi_b ... d\Pi_i d\Pi_j ... (2\pi)^4 |M|^2 \times \\ &\times \delta^4\left(p_\psi + p_a + p_b + ... - p_i - p_j ...\right)\left[f_\psi f_a f_b ... - f_i f_j ...\right],\end{aligned} \tag{B.9}$$

where $x \equiv m_\psi/T$ and $H(1)$ is the Hubble parameter at $T = m_\psi$. During the radiation-dominated epoch, the Hubble parameter is given by

$$H_{\mathrm{RD}} = \pi\sqrt{\frac{g_\star(T)}{90}}\frac{T^2}{M_{\mathrm{Pl}}}, \tag{B.10}$$

with $M_{\rm Pl}$ the reduced Planck mass, and $g_\star(T)$ the effective number of relativistic degrees of freedom, defined in Eq. (A.12). This final form of the Boltzmann equation provides a comprehensive description of the evolution of a particle species in the early universe.

B.2 Boltzmann equations for dark matter freeze-out

The freeze-out process describes the decoupling of dark matter particles from the thermal plasma of the early universe, marking the point when their abundances cease to follow equilibrium distributions. To study this process in detail, we consider dark matter particles χ that are stable, massive, and weakly interacting with SM particles. These particles undergo annihilation and production processes of the form

$$\chi\,\bar{\chi} \longleftrightarrow \psi\,\bar{\psi}, \tag{B.11}$$

where ψ represents all possible species that χ can annihilate into. Each interaction changes the number of dark matter particles by two units.

At temperatures relevant for dark matter freeze-out, we assume that SM particles remain in thermal equilibrium with the plasma due to their stronger interactions with other particles. Consequently, ψ and $\bar{\psi}$ can be described by thermal distributions with effectively zero chemical potentials.

The Boltzmann equation for the evolution of χ particles, particularizing Eq. (B.9), is given by

$$\begin{aligned}\frac{dY_\chi}{dx} = -\frac{x g_\chi}{H(1)\mathfrak{s}}\int & d\Pi_\chi d\Pi_{\bar{\chi}} d\Pi_\psi d\Pi_{\bar{\psi}} (2\pi)^4 |M|^2 \\ & \times \delta^4\left(p_\chi + p_{\bar{\chi}} - p_\psi - p_{\bar{\psi}}\right)\left[f_\chi f_{\bar{\chi}} - f_\psi f_{\bar{\psi}}\right].\end{aligned} \tag{B.12}$$

For the SM particles ψ and $\bar{\psi}$, which are in thermal equilibrium, their phase-space distributions become

$$\begin{aligned} f_\psi &= f_\psi^{\rm eq} = \exp\left(-E_\psi/T\right), \\ f_{\bar{\psi}} &= f_{\bar{\psi}}^{\rm eq} = \exp\left(-E_{\bar{\psi}}/T\right). \end{aligned} \tag{B.13}$$

The energy component of the delta function in Eq. (B.12) enforces energy conservation, $E_\chi + E_{\bar{\chi}} = E_\psi + E_{\bar{\psi}}$. This leads to the relation

$$f_\psi^{\rm eq} f_{\bar{\psi}}^{\rm eq} = \exp\left(-\frac{E_\psi + E_{\bar{\psi}}}{T}\right) = \exp\left(-\frac{E_\chi + E_{\bar{\chi}}}{T}\right) = f_\chi^{\rm eq} f_{\bar{\chi}}^{\rm eq}. \tag{B.14}$$

This property, known as "detailed balance", allows the substitution

$$\left[f_\chi f_{\bar{\chi}} - f_\psi f_{\bar{\psi}}\right] \quad \longrightarrow \quad \left[f_\chi f_{\bar{\chi}} - f_\chi^{\rm eq} f_{\bar{\chi}}^{\rm eq}\right]. \tag{B.15}$$

Using this, one can further develop the collision term and arrive to the simplified form of the Boltzmann equation

$$\dot{n}_\chi + 3Hn\chi = -\langle\sigma v\rangle_{\rm ann}\left[n_\chi^2 - n_{\chi,{\rm eq}}^2\right], \tag{B.16}$$

where $\langle\sigma v\rangle_{\rm ann}$ is the thermally averaged annihilation cross section times velocity, summed over all final states. Alternatively, in terms of the yield Y_χ, the equation becomes

$$\frac{dY_\chi}{dx} = -\frac{x\mathfrak{s}\langle\sigma v\rangle_{\rm ann}}{H(1)}\big[Y_\chi^2 - Y_{\chi,\rm eq}^2\big]. \tag{B.17}$$

In these expressions, we have assumed no asymmetry between χ and $\bar{\chi}$, setting $n_\chi = n_{\bar{\chi}}$. The thermally averaged annihilation cross section $\langle\sigma v\rangle_{\rm ann}$ can be computed from the annihilation cross section σ following the formalism shown in Appendix A.4.

B.3 Inclusion of sphalerons in the Boltzmann equations

In this appendix, we detail the inclusion of sphalerons in the Boltzmann equations for the SM quarks and leptons, in the context of our framework.

Let $g(x)$ denote the contributions from the neutron portal interactions that change the quark asymmetry. The evolution equations for the relevant asymmetries are then

$$\frac{dY_{\Delta N}}{dx} = -g(x), \tag{B.18}$$
$$\frac{dY_{\Delta q}}{dx} = 3g(x) + 3\left(\frac{dY_{B_{\rm SM}}}{dx}\right)_{\rm sph}, \tag{B.19}$$
$$\frac{dY_{\Delta l}}{dx} = \left(\frac{dY_{L_{\rm SM}}}{dx}\right)_{\rm sph}, \tag{B.20}$$

where the terms $(dY_{B_{\rm SM}}/dx)_{\rm sph}$ and $(dY_{L_{\rm SM}}/dx)_{\rm sph}$ correspond to the change to the SM baryon and lepton asymmetries induced by the sphaleron processes. These terms satisfy the relation

$$\left(\frac{dY_{B_{\rm SM}}}{dx}\right)_{\rm sph} = \left(\frac{dY_{L_{\rm SM}}}{dx}\right)_{\rm sph}, \tag{B.21}$$

due to the conservation of $(B-L)_{\rm SM} = 0$ in the SM. Substituting Eq. (B.20) into Eq. (B.19) gives

$$\frac{dY_{\Delta q}}{dx} = 3\left(g(x) + \frac{dY_{\Delta l}}{dx}\right). \tag{B.22}$$

The equilibrium relation between the baryon and lepton asymmetries in the presence of sphaleron processes, given by Eq. (3.11), is rewritten as

$$Y_{B_{\rm SM}} = -\frac{c}{1-c}Y_{L_{\rm SM}} = -\frac{c}{1-c}Y_{\Delta l}. \tag{B.23}$$

And differentiating, we find

$$\frac{dY_{B_{\rm SM}}}{dx} \equiv \frac{1}{3}\frac{dY_{\Delta q}}{dx} = -\frac{c}{1-c}\frac{dY_{\Delta l}}{dx}. \tag{B.24}$$

Substituting Eq. (B.24) into Eq. (B.22) and rearranging terms:

$$\frac{dY_{\Delta q}}{dx} = 3g(x) + \left(\frac{c-1}{c}\right)\frac{dY_{\Delta q}}{dx}, \tag{B.25}$$

and finally

$$\frac{dY_{\Delta q}}{dx} = 3\,c\,g(x). \tag{B.26}$$

This result provides the evolution of the quark asymmetry, including contributions from the neutron portal and sphaleron processes. The parameter c encapsulates the relative influence of sphalerons on the baryon and lepton asymmetries. We see that c acts as an overall factor in the equation rather than introducing an additional term. Analogously for the leptons

$$\frac{dY_{\Delta\ell}}{dx} = (c-1)\,g(x). \tag{B.27}$$

B.4 Derivation of the Boltzmann equations for asymmetry generation

This appendix provides the derivation of the Boltzmann equation terms for the the particles and processes involved in generating the asymmetry within the mechanism explored in Section 7.1.

The relevant tree-level decays and inverse decays are depicted in Fig. B.1, together with the notation used for their rates. Note that these rates include higher-order contributions, shown in Fig. 7.2, which induce CP violation, so that $\Gamma^i_{\mathrm{D}} \neq \bar{\Gamma}^i_{\mathrm{D}}$. We define the total decay rate as

$$\Gamma^{\mathrm{tot},i}_{\mathrm{D}} \equiv \Gamma^i_{\mathrm{D}} + \bar{\Gamma}^i_{\mathrm{D}}. \tag{B.28}$$

The thermally averaged cross sections for these processes are related to their thermally averaged rates as

$$\langle\Gamma\rangle^i_{\mathrm{ID}} = \langle\sigma v\rangle^i_{\mathrm{ID}} n_N = \langle\sigma v\rangle^i_{\mathrm{ID}} Y_N \mathfrak{s}, \tag{B.29}$$

$$\langle\bar{\Gamma}\rangle^i_{\mathrm{ID}} = \langle\overline{\sigma v}\rangle^i_{\mathrm{ID}} n_{\bar{N}} = \langle\overline{\sigma v}\rangle^i_{\mathrm{ID}} Y_{\bar{N}} \mathfrak{s}, \tag{B.30}$$

where $\mathfrak{s}$ is the entropy density. The thermally averaged rates are related to the decay rates as already shown in Eq. (A.32)

$$\langle\Gamma\rangle = \Gamma\,\frac{K_1(x)}{K_2(x)}. \tag{B.31}$$

Without any assumptions on thermal equilibrium, the contribution of decays and inverse decays to the Boltzmann equation for the abundance of φ_i is

$$\frac{dY_{\varphi_i}}{dx} \supset \frac{x}{H(x=1)}\Big[-\langle\Gamma\rangle^i_{\mathrm{D}} Y_{\varphi_i} - \langle\bar{\Gamma}\rangle^i_{\mathrm{D}} Y_{\varphi_i} + \mathfrak{s}\langle\sigma v\rangle^i_{\mathrm{ID}} Y_N Y_\chi + \mathfrak{s}\langle\overline{\sigma v}\rangle^i_{\mathrm{ID}} Y_{\bar{N}} Y_{\chi^*}\Big]. \tag{B.32}$$

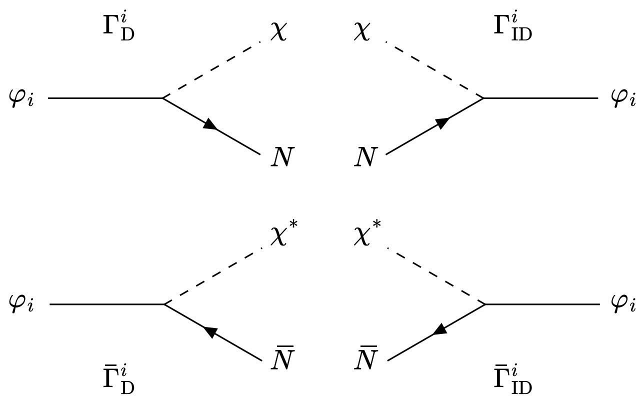

Fig. B.1: Schematic representation of the tree-level decay and inverse decay processes for φ_i, which contribute to the generation of the asymmetry.

Now we use Eqs. (B.29)–(B.30) to simplify this expression:

$$\frac{dY_{\varphi_i}}{dx} \supset \frac{x}{H(x=1)}\Big[-\langle\Gamma\rangle^i_{\rm D} Y_{\varphi_i} - \langle\bar{\Gamma}\rangle^i_{\rm D} Y_{\varphi_i} + \langle\Gamma\rangle^i_{\rm ID} Y_\chi + \langle\bar{\Gamma}\rangle^i_{\rm ID} Y_{\chi^*}\Big]. \tag{B.33}$$

The yields of χ and χ^* can be rewritten as

$$Y_\chi = \frac{1}{2}(Y_\chi + Y_{\chi^*}) + \frac{1}{2}(Y_\chi - Y_{\chi^*}) = \frac{Y^{\rm tot}_\chi}{2} + \frac{Y_{\Delta\chi}}{2}, \tag{B.34}$$

$$Y_{\chi^*} = \frac{1}{2}(Y_\chi + Y_{\chi^*}) - \frac{1}{2}(Y_\chi - Y_{\chi^*}) = \frac{Y^{\rm tot}_\chi}{2} - \frac{Y_{\Delta\chi}}{2}. \tag{B.35}$$

Using these expressions, together with Eq. (B.28), and substituting into Eq. (B.33), we get:

$$\frac{dY_{\varphi_i}}{dx} \supset \frac{x}{H(x=1)}\left[-\langle\Gamma\rangle^{{\rm tot},i}_{\rm D} Y_{\varphi_i} + \left(\langle\Gamma\rangle^i_{\rm ID} + \langle\bar{\Gamma}\rangle^i_{\rm ID}\right)\frac{Y^{\rm tot}_\chi}{2} + \left(\langle\Gamma\rangle^i_{\rm ID} - \langle\bar{\Gamma}\rangle^i_{\rm ID}\right)\frac{Y_{\Delta\chi}}{2}\right]. \tag{B.36}$$

Now we use a definition analogous to Eq. (B.28) for inverse decays

$$\Gamma^i_{\rm ID} + \bar{\Gamma}^i_{\rm ID} \equiv \Gamma^{{\rm tot},i}_{\rm ID}, \tag{B.37}$$

and the definition in Eq. (7.9) to express the asymmetry between inverse decay rates as

$$\Gamma^i_{\rm ID} - \bar{\Gamma}^i_{\rm ID} = \epsilon_i\, \Gamma^{{\rm tot},i}_{\rm ID}, \tag{B.38}$$

where ϵ_i represents the CP-violating parameter for the process. We further relate the total inverse decay rate to the total decay rate through the equilibrium yields

$$\Gamma_{\mathrm{ID}}^{\mathrm{tot},i} = \Gamma_{\mathrm{D}}^{\mathrm{tot},i} \frac{Y_{\varphi_i}^{\mathrm{eq}}}{Y_{\chi}^{\mathrm{eq}}}. \tag{B.39}$$

Substituting Eqs. (B.37)–(B.39) into Eq. (B.36), the Boltzmann equation becomes

$$\begin{aligned} \frac{dY_{\varphi_i}}{dx} &\supset \frac{x}{H(x=1)}\left[-\langle\Gamma\rangle_{\mathrm{D}}^{\mathrm{tot},i} Y_{\varphi_i} + \langle\Gamma\rangle_{\mathrm{D}}^{\mathrm{tot},i} \frac{Y_{\varphi_i}^{\mathrm{eq}}}{Y_{\chi}^{\mathrm{eq}}} \frac{Y_{\chi}^{\mathrm{tot}}}{2} + \epsilon_i \langle\Gamma\rangle_{\mathrm{D}}^{\mathrm{tot},i} \frac{Y_{\varphi_i}^{\mathrm{eq}}}{Y_{\chi}^{\mathrm{eq}}} \frac{Y_{\Delta\chi}}{2} \right] \\ &= -\frac{x}{H(x=1)} \langle\Gamma\rangle_{\mathrm{D}}^{\mathrm{tot},i} \left[Y_{\varphi_i} - Y_{\varphi_i}^{\mathrm{eq}} \frac{Y_{\chi}^{\mathrm{tot}}}{2Y_{\chi}^{\mathrm{eq}}} - \frac{1}{2}\epsilon_i Y_{\varphi_i}^{\mathrm{eq}} \frac{Y_{\Delta\chi}}{Y_{\chi}^{\mathrm{eq}}} \right]. \end{aligned} \tag{B.40}$$

If the dark matter particles are also in thermal equilibrium, such as when their interactions with N and $\overline{N}$ are strong at these temperatures, then the total dark matter yield can be approximated as $Y_{\chi}^{\mathrm{tot}} \simeq 2Y_{\chi}^{\mathrm{eq}}$. Under this assumption, the Boltzmann equation simplifies to

$$\frac{dY_{\varphi_i}}{dx} \supset -\frac{x}{H(x=1)} \langle\Gamma\rangle_{\mathrm{D}}^{\mathrm{tot},i} \left[Y_{\varphi_i} - Y_{\varphi_i}^{\mathrm{eq}} \left(1 + \frac{1}{2}\epsilon_i \frac{Y_{\Delta\chi}}{Y_{\chi}^{\mathrm{eq}}} \right) \right], \tag{B.41}$$

where the term proportional to $\epsilon_i Y_{\Delta\chi}/Y_{\chi}^{\mathrm{eq}}$ is typically negligible and can be dropped. This simplification highlights that, in the equilibrium regime, the evolution of Y_{φ_i} is predominantly governed by the equilibrium yield and the total decay rate.

The two-to-two annihilation processes affecting φ_i are depicted in Fig. B.2, and also need to be taken into account. The contribution to the Boltzmann equation is

$$\begin{aligned} \frac{dY_{\varphi_i}}{dx} \supset -\frac{x\mathfrak{s}}{H(x=1)} 2\Big[&\langle\sigma v\rangle_{\varphi_i\varphi_i\to\chi\chi^*} Y_{\varphi_i}^2 - \langle\sigma v\rangle_{\chi\chi^*\to\varphi_i\varphi_i} Y_{\chi} Y_{\chi^*} \\ &+ \langle\sigma v\rangle_{\varphi_i\varphi_i\to N\overline{N}} Y_{\varphi_i}^2 - \langle\sigma v\rangle_{N\overline{N}\to\varphi_i\varphi_i} Y_N Y_{\overline{N}} \Big] \end{aligned} \tag{B.42}$$

The first two terms in the equation correspond to the processes depicted in the first diagram in Fig. B.2, representing $\varphi_i\varphi_i \to \chi\chi^*$ (left to right) and its reverse process, $\chi\chi^* \to \varphi_i\varphi_i$ (right to left). Similarly, the last two terms arise from the second diagram in Fig. B.2, corresponding to $\varphi_i\varphi_i \to N\overline{N}$ and its reverse process, $N\overline{N} \to \varphi_i\varphi_i$.

Using the principle of detailed balance, we can relate the thermally averaged cross sections for the forward and reverse processes as follows:

$$\langle\sigma v\rangle_{\chi\chi^*\to\varphi_i\varphi_i} = \langle\sigma v\rangle_{\varphi_i\varphi_i\to\chi\chi^*} \frac{Y_{\varphi_i}^{\mathrm{eq}\,2}}{Y_{\chi}^{\mathrm{eq}} Y_{\chi^*}^{\mathrm{eq}}}, \tag{B.43}$$

$$\langle\sigma v\rangle_{N\overline{N}\to\varphi_i\varphi_i} = \langle\sigma v\rangle_{\varphi_i\varphi_i\to N\overline{N}} \frac{Y_{\varphi_i}^{\mathrm{eq}\,2}}{Y_{N}^{\mathrm{eq}} Y_{\overline{N}}^{\mathrm{eq}}}, \tag{B.44}$$

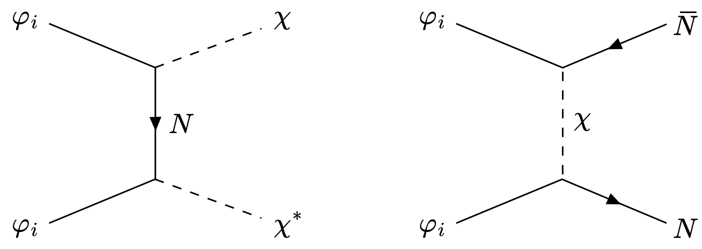

Fig. B.2: Two-to-two annihilation processes affecting the abundance of φ_i.

and rewrite Eq. (B.42) as

$$\frac{dY_{\varphi_i}}{dx} \supset -\frac{x\mathfrak{s}}{H(x=1)} 2\Bigg[\langle\sigma v\rangle_{\varphi_i\varphi_i\to\chi\chi^*}\left(Y_{\varphi_i}^2 - \frac{Y_{\varphi_i}^{\text{eq}\,2}}{Y_\chi^{\text{eq}}Y_{\chi^*}^{\text{eq}}}Y_\chi Y_{\chi^*}\right) + \langle\sigma v\rangle_{\varphi_i\varphi_i\to N\overline{N}}\left(Y_{\varphi_i}^2 - \frac{Y_{\varphi_i}^{\text{eq}\,2}}{Y_N^{\text{eq}}Y_{\overline{N}}^{\text{eq}}}Y_N Y_{\overline{N}}\right)\Bigg]. \tag{B.45}$$

Combining the decay, inverse decay, and two-to-two processes, the full Boltzmann equation for φ_i is

$$\begin{aligned}\frac{dY_{\varphi_i}}{dx} = &-\frac{x}{H(x=1)}\langle\Gamma\rangle_{\text{D}}^{\text{tot},i}\left[Y_{\varphi_i} - Y_{\varphi_i}^{\text{eq}}\left(1+\frac{1}{2}\epsilon_i\frac{Y_{\Delta\chi}}{Y_\chi^{\text{eq}}}\right)\right]\\ &-\frac{x\mathfrak{s}}{H(x=1)}2\Bigg[\langle\sigma v\rangle_{\varphi_i\varphi_i\to\chi\chi^*}\left(Y_{\varphi_i}^2 - \frac{Y_{\varphi_i}^{\text{eq}\,2}}{Y_\chi^{\text{eq}}Y_{\chi^*}^{\text{eq}}}Y_\chi Y_{\chi^*}\right)\\ &\qquad + \langle\sigma v\rangle_{\varphi_i\varphi_i\to N\overline{N}}\left(Y_{\varphi_i}^2 - \frac{Y_{\varphi_i}^{\text{eq}\,2}}{Y_N^{\text{eq}}Y_{\overline{N}}^{\text{eq}}}Y_N Y_{\overline{N}}\right)\Bigg].\end{aligned} \tag{B.46}$$

The remaining equations are derived in a similar manner and are presented in Eqs. (7.27)–(7.31).

Appendix C

Chemical equilibration and asymmetry redistribution

To understand the equilibrium relation between the asymmetries in $\Delta\chi$, ΔN, $B_{\rm SM}$ and $L_{\rm SM}$, we analyze the constraints imposed on the chemical potentials by different interactions in the thermal plasma, basing ourselves on Ref. [120].

When particle species are in chemical equilibrium, their chemical potentials obey relations dictated by particle interactions. For example, in a reaction of the type $a+b \to c+d$, the chemical potentials satisfy:

$$\mu_a + \mu_b = \mu_c + \mu_d\,. \tag{C.1}$$

Also, particle asymmetries can be expressed in terms of their chemical potentials. Assuming that all the particles are ultra-relativistic, which at temperatures above the electroweak phase transition is a good approximation, this relation is given by

$$n_a - n_{\bar{a}} = \frac{g_a T^3}{6} \begin{cases} \mu_a/T + \mathcal{O}\big((\mu_a/T)^3\big) & \text{for fermions,} \\ 2\mu_a/T + \mathcal{O}\big((\mu_a/T)^3\big) & \text{for bosons,} \end{cases} \tag{C.2}$$

where n_a is the equilibrium number density of a given particle species, $n_{\bar{a}}$ that of the CP-conjugate species, g_a its internal degrees of freedom and μ_a its chemical potential. We also assume that $|\mu/T| \ll 1$, as the baryon and lepton chemical potentials are expected to be of order $|\mu| \sim 10^{-10}\,T$, due to the tiny baryon asymmetry observed in the universe.

C.1 Standard Model and sphalerons

In this section, we focus exclusively on the SM interactions and sphaleron processes, deriving the value of the constant c in the sphaleron equilibrium relation shown in Eq (3.11).

The SM interactions enforce the following relations among the chemical potentials of the particles:

$$\begin{aligned}
\mu_W &= \mu_- + \mu_0 && (W^- \leftrightarrow \phi^- + \phi^0), && \text{(C.3)}\\
\mu_{d_L} &= \mu_{u_L} + \mu_W && (W^- \leftrightarrow \bar{u}_L + d_L), && \text{(C.4)}\\
\mu_{iL} &= \mu_i + \mu_W && (W^- \leftrightarrow \bar{\nu}_{iL} + e_{iL}), && \text{(C.5)}\\
\mu_{u_R} &= \mu_{u_L} + \mu_0 && (\phi^0 \leftrightarrow \bar{u}_L + u_R), && \text{(C.6)}\\
\mu_{d_L} &= \mu_{d_R} + \mu_0 && (\phi^0 \leftrightarrow \bar{d}_R + d_L), && \text{(C.7)}\\
\mu_{iL} &= \mu_{iR} + \mu_0 && (\phi^0 \leftrightarrow \bar{e}_{iR} + e_{iL}). && \text{(C.8)}
\end{aligned}$$

Here, μ_0 and μ_- refer to the neutral and charged components of the Higgs field (ϕ^0 and ϕ^-), and μ_W to W^-. The chemical potentials μ_{iL} and μ_{iR} correspond to the left- and right-handed charged lepton in the family i, while μ_i refer to the left-handed neutrinos in the family i. Further, the quark potentials μ_{u_R}, μ_{d_R}, μ_{u_L} and μ_{d_L} are the same for each generation due to the CKM mixing, and also the same for all colors due to the vanishing chemical potential of gluons.

The electroweak sphalerons, introduced in Section 3.3, impose the following equilibrium condition

$$3(\mu_{u_L} + 2\mu_{d_L}) + \mu_\nu = 0, \tag{C.9}$$

where $\mu_\nu = \sum_i \mu_i$, accounting for three generations of leptons. We can use Eq. (C.4) to rewrite this condition as

$$9\mu_{u_L} + 6\mu_W + \mu_\nu = 0. \tag{C.10}$$

Now we express the baryon and lepton number densities of the SM in terms of the chosen chemical potentials, making use of (C.2) and the relations (C.4), (C.6) and (C.7). From now on we will use the common notation $n_B \equiv B_{\text{SM}}$ and $n_L \equiv L_{\text{SM}}$. We arrive to

$$B_{\text{SM}} = \frac{T^2}{3}(12\mu_{u_L} + 3\mu_W), \tag{C.11}$$

$$L_{\text{SM}} = \frac{T^2}{3}(3\mu_\nu + 6\mu_W - 3\mu_0). \tag{C.12}$$

The number density of electric charge Q, which must vanish, can be expressed as

$$Q = \frac{4T^2}{3}(3\mu_{u_L} - \mu_\nu - 9\mu_W + 7\mu_0) = 0, \tag{C.13}$$

where the relations (C.3)–(C.8) have been used to reduce the number of independent variables. Since sphalerons remain active below the electroweak phase transition temperature [117], when the Higgs field acquires a vacuum expectation value, we set its chemical potential to zero:

$$\mu_0 = 0. \tag{C.14}$$

By combining (C.10), (C.13), and (C.14), we can rewrite (C.11) and (C.12) in terms of a single chemical potential

$$B_{\mathrm{SM}} = 12\,T^2 \mu_{u_L}, \tag{C.15}$$

$$L_{\mathrm{SM}} = -25\,T^2 \mu_{u_L}. \tag{C.16}$$

This leads to the well-known relation

$$B_{\mathrm{SM}} = \frac{12}{37}(B-L)_{\mathrm{SM}}, \tag{C.17}$$

providing the value of c in the sphaleron equilibrium relation.

C.2 Equilibration of the neutron portal

We now extend the analysis to the neutron portal, which introduces new interactions connecting the dark sector to the visible sector. These interactions do not alter the chemical potential relations derived in the previous section. Instead, our focus is on understanding how the SM processes and sphaleron interactions influence the equilibrium of the neutron portal, and consequently, the asymmetries stored in $\Delta\chi$ and ΔN.

The neutron portal imposes the following relation among the chemical potentials:

$$\mu_N = 2\mu_{d_R} + \mu_{u_R}. \tag{C.18}$$

The relations Eq. (C.4), (C.6) and (C.7), together with $\mu_0 = 0$, lead to

$$\mu_{u_R} = \mu_{u_L}, \tag{C.19}$$

$$\mu_{d_R} = \mu_{d_L}, \tag{C.20}$$

$$\mu_{d_R} = \mu_{u_R} + \mu_W. \tag{C.21}$$

Combining the sphaleron relation (C.10), the vanishment of Q (C.13), and relations (C.4) and (C.21), we find:

$$\mu_{d_L} = 5\mu_{u_L}, \tag{C.22}$$

$$\mu_{d_R} = 5\mu_{d_R}, \tag{C.23}$$

which reduce the neutron portal relation (C.18) to

$$\mu_N = 11\mu_{u_R}. \tag{C.24}$$

Now, sing the correspondence between chemical potentials and asymmetries in Eq. (C.2), we translate this relation to

$$Y_{\Delta N} = \frac{11}{3} Y_{\Delta u_R}, \tag{C.25}$$

where we have used $g_N = 2$ and $g_{u_R} = g_{d_R} = 6$, accounting for spin and color. Here, $Y_{\Delta u_R}$ and $Y_{\Delta d_R}$ represent the asymmetries for each individual generation. By definition, the total asymmetry stored in all quarks is

$$Y_{\Delta q} = 3(Y_{\Delta u_R} + Y_{\Delta d_R} + Y_{\Delta u_L} + Y_{\Delta d_R}), \tag{C.26}$$

$$Y_{\Delta q} = 3Y_{B_{\rm SM}}, \tag{C.27}$$

which using the relations (C.19), (C.20), (C.22), (C.23) and (C.25) leads to

$$Y_{\Delta q} = 36Y_{\Delta u_R}, \tag{C.28}$$

$$Y_{\Delta N} = \frac{11}{3}\frac{1}{36}Y_{\Delta q} = \frac{11}{36}Y_{B_{\rm SM}}. \tag{C.29}$$

Using the relation imposed by sphalerons after symmetry breaking, see Eqs. (C.11) and (C.12),

$$Y_{B_{\rm SM}} = -\frac{12}{25}Y_{L_{\rm SM}}, \tag{C.30}$$

and the $B - L$ conservation relation,

$$Y^{\rm in}_{\Delta N} = Y_{\Delta N} + Y_{B_{\rm SM}} - Y_{L_{\rm SM}}, \tag{C.31}$$

we can solve the resulting system of three equations. This yields the following asymmetries:

$$Y_{\Delta N}(T) = \frac{11}{122}Y^{\rm in}_{\Delta N}, \tag{C.32}$$

$$Y_{\Delta q}(T) = \frac{54}{61}Y^{\rm in}_{\Delta N}, \tag{C.33}$$

$$Y_{\Delta \ell}(T) = -\frac{75}{122}Y^{\rm in}_{\Delta N}, \tag{C.34}$$

which are used in Section. 5.2.3 of this thesis.

We can also consider the case where sphalerons are out of equilibrium at the time the asymmetry ΔN is generated. In this scenario, instead of the sphaleron equilibrium condition (C.9), we impose that lepton number is never violated. Consequently, the chemical potential associated with lepton number must vanish:

$$\mu_L = \sum(\mu_i + \mu_{iL} + \mu_{iR}) = 3\mu + 6\mu_W - 3\mu_0 = 0, \tag{C.35}$$

where we have used the relations (C.5) and (C.8). With this, and by imposing $\mu_W = 0$, since $SU(2)$ is a conserved symmetry prior to symmetry breaking and all interactions are equilibrated in this regime, we arrive at the following relations (keeping in mind that $\mu_0 = 0$ as the Higgs has not yet acquired a vacuum expectation value):

$$Y_{\Delta N}(T) = \frac{7}{31}Y^{\rm in}_{\Delta N}, \tag{C.36}$$

$$Y_{\Delta q}(T) = \frac{24}{31}Y^{\rm in}_{\Delta N}, \tag{C.37}$$

$$Y_{\Delta \ell}(T) = 0. \tag{C.38}$$

Since no asymmetry is transferred to the leptons in this case, the resulting dark matter mass and initial asymmetry are given by $m_\chi = 5\,\mathrm{GeV}$ and $Y^{\mathrm{in}}_{\Delta\chi} = Y^0_{B_{\mathrm{SM}}}$, the same as in the standard case of asymmetric dark matter, see Section. 2.4.2.